Path-resolved electron transport in a triangular triple quantum dot system

Von der QUEST-Leibniz-Forschungsschule der
Gottfried Wilhelm Leibniz Universität Hannover
zur Erlangung des Grades
Doktor der Naturwissenschaften
Dr. rer. nat.
genehmigte Dissertation
von

M.Sc. Monika Kotzian
geboren am 26. Februar 1986 in Wolfsburg

2016

Referent: Prof. Dr. Rolf J. Haug
Korreferent: Prof. Dr. Gloria Platero
Korreferent: apl. Prof. Dr. Stefan Süllow

Tag der Disputation: 19.07.2016

Abstract

In this thesis electronic transport through a lateral triple quantum dot with triangular geometry and two double-dot transport paths sharing one dot is investigated. The work combines experimental and theoretical approaches to transport in this complex multi-dot network. In order to enable path-resolved measurements and a thorough study of interactions between the transport paths two source contacts are used to apply AC voltages with different frequencies to the paths. The system is characterized by means of charge detection using a nearby quantum point contact and transport spectroscopy investigating linear and non-linear transport through the two double dot paths of the device simultaneously but separately. The tunability of the triple quantum dot into double and triple dot resonances is shown in both charge and transport measurements. If the device is tuned into a serial dot configuration two different charging mechanisms of the central dot arise which are analyzed by detector measurements. Interference effects between electrons coming from the two different paths of the dot system are observed in the total transport through the system. Path-resolved transport measurements show an inter-channel blockade effect induced by Coulomb correlations in the shared quantum dot leading to non-linear transport even around zero bias voltage. Second-order cotunneling is discussed as an intra-channel double dot transport property which combines with these inter-channel effects. Making use of the two-path setup, the formation of hybridized states in one double dot path is detected within the same device by probing the states with a more localized single dot level in the other path. The characterization of the device and the analysis of its special transport properties are supported by a simulation of transport through the system using a quantum mechanical model.

Keywords: triple quantum dots, path-resolved transport, Coulomb correlations

Kurzzusammenfassung

In dieser Arbeit wird der elektronische Transport durch ein laterales Dreifachquantenpunktsystem mit triangularer Geometrie und zwei Transportpfaden untersucht. Die Transportpfade bestehen jeweils aus einem seriellen Doppelquantenpunkt und sind über einen gemeinsamen Quantenpunkt gekoppelt. Die Arbeit umfasst Transportuntersuchungen dieses komplexen Mehrfachquantenpunktsystems mittels experimenteller und theoretischer Analysen. Zwei Source Zuleitungen mit angelegten AC Spannungen unterschiedlicher Frequenzen ermöglichen pfadaufgelöste Transportmessungen und die Untersuchung von Wechselwirkungen zwischen den Pfaden im Transport. Das System wird charakterisiert mittels Ladungsdetektion mit einem naheliegenden Quantenpunktkontakt und Transportspektroskopie, welche den Transport durch das System pfadaufgelöst im (nicht-)linearen Regime untersucht. Es zeigen sich Doppel- und Dreifachquantenpunktresonanzen sowohl in Detektor- als auch in Transportmessungen. Bei Transformation in eine serielle Quantenpunktkonfiguration ergeben sich zwei unterschiedliche Ladungsmechanismen für den mittleren Quantenpunkt, die mittels Ladungsmessung analysiert werden. Interferenzeffekte zwischen Elektronen aus verschiedenen Pfaden zeigen sich in den Transportmessungen des Gesamtsystems. Pfadaufgelöste Transportmessungen zeigen den Effekt einer Pfadblockade im Transport als Resultat der Coulomb-Wechselwirkung zwischen den Elektronen verschiedener Transportpfade. Dies führt zu nicht-linearem Transportverhalten des Systems. Im Zuge der Analyse der Transporteigenschaften der einzelnen Pfade werden Effekte aufgrund von Tunnelprozessen höherer Ordnung und ihre Kombination mit Pfadkorrelationseffekten untersucht. Durch den Doppelpfadaufbau können hybridisierte Zustände der Quantenpunkte in einem Pfad im Transport durch den anderen Pfad mittels Abtastung mit einem lokalisierteren Quantenpunktzustand detektiert werden. Die Charakterisierung der Probe und die Untersuchung der speziellen Transporteigenschaften werden unterstützt durch eine Simulation des Systems mittels eines quantenmechanischen Modells.

Schlagworte: Dreifachquantenpunkte, pfadaufgelöster Transport, Coulomb-Korrelationen

Contents

Nomenclature

C	Capacitance
$C_{\Sigma \mathrm{X}}$	Sum capacitance of dot X, X $\in$ {A,B,C}
$C_{\mathrm{GX,Y}}$	Capacitive coupling between gate GX with X $\in$ {1,...,4} and dot Y $\in$ {A,B,C}
$C_{\mathrm{L,X}}$	Capacitive coupling between lead L $\in$ {S1,S2,D} and dot X $\in$ {A,B,C}
C_{XY}	Inter-dot capacitive coupling XY $\in$ {AB,AC,BA,BC}
D	Drain lead
$D_{\mathrm{xD}}(E)$	Electronic density of states for an n-dimensional system n $\in$ {0,...,3} in dependence of energy E
E	Energy
E^*_{N}	Total energy of a quantum dot with N electrons with excited electrons
E_{C} ($E_{\mathrm{C},i}$)	Charging energy of a quantum dot (of quantum dot i, $i \in \{A,B,C\}$)
E_{N}	Total energy of a quantum dot with N electrons, all electrons in ground state
E_{el}	Electrostatic energy
G	Differential conductance in (e^2/h)
G_{X}	Gate X $\in$ {1,..,4,QPC}
I	Current
I_{AC}	AC current

I_{DC}	DC current
L	Length
Q	Charge
Q_{X}	Charge on quantum dot X, X $\in$ {A,B,C}
S_{X}	Source lead X $\in$ {1,2}
T	Temperature
U	Voltage
U_{GX}	Voltage applied at gate X $\in$ {1,...,4,QPC}
U_{SX}	Bias voltage applied at source lead X $\in$ {1,2,QPC}
$\hbar$	$h/(2\pi)$
$\mathcal{H}$	Hilbert space
H	Hamilton operator
a^*	Complex conjugate of complex number a
e	Elementary charge ($1.602 \cdot 10^{-19}$ C)
$f(E)$	Fermi distribution function
h	Planck constant ($4.136 \cdot 10^{-15}$ eV $\cdot$ s)
k_{B}	Boltzmann constant ($8.617 \cdot 10^{-5}$ eV/K)
m^*	Effective electron mass
n_{e}	Electron concentration
Δ_{XY}	Energy level detuning between the on-site states of dot X and Y
Γ_{X}	Tunnel coupling between dot X $\in$ {A,B,C} and neighboring lead
Φ	Coherent state wave function (for one electron in the system)

Ψ	Coherent state wave function
Θ	Heaviside function
$\langle\Psi\vert$	Bra-vector, element of the dual Hilbert space $\mathcal{H}^*$ (Dirac notation)
$\langle\Psi\vert A\vert\Psi\rangle$	Expectation value of the operator A
$\dot{\rho}$	Partial time derivative of the density operator
ε_i	Eigenenergies of a single electron in a quantum dot
$\vert\Psi\rangle$	Ket-vector, element of a given Hilbert space $\mathcal{H}$ (Dirac notation)
λ_i	Eigenenergies corresponding to coherent states of coupled quantum dots
$\mathbb{I}$	Identity matrix
$\mathcal{G}$	Conductance
$\mathcal{L}$	Liouvillian superoperator
μ_{N}^*	Chemical potential of an excited state of the dot
μ_{N}	Chemical potential of a dot for the transition N-1$\rightarrow$ N electrons
μ_{X}	Chemical potential of lead X, X $\in$ {S,D}
μ_{e}	Electron mobility
∇	Nabla operator $(\frac{\partial}{\partial x_1},...,\frac{\partial}{\partial x_n})$
ω_0	Radial frequency
ϕ	Electronic wave function of localized single quantum dot states
ρ	Density operator
τ_{XY}	Inter-dot tunnel coupling XY $\in$ {AB,AC}
Tr	Trace
2DEG	Two-dimensional electron gas

AC	Active current
AFM	Atomic force microscope
DAC	Digital-to-analog converter
DC	Direct current
DOS	Electronic density of states
LAO	Local anodic oxidation
QCA	Quantum cellular automata
QP	Quadruple point
QPC	Quantum point contact
TP	Triple point
TQD	Triple quantum dot
UHV	Ultra high vacuum

1 Introduction

The quest for a continuous miniaturization of classical transistors as components of integrated circuits drives modern microtechnology. The exponentially increasing chip complexity was early on described by Moore's law [1] and inevitably leads to a fundamental quantum limit. This in turn ultimately limits the processing power of classical computers. Even before reaching this fundamental limit the miniaturization causes major issues. The increasingly high packing density of the integrated circuits leads to quantum mechanical leakage currents resulting in high energy loss and heat production. The revolutionary idea of developing a quantum computer [2–4] circumvents these problems and leads to exponentially increasing computational power with the system size. This can be achieved by exploiting the axioms of quantum mechanics such as superposition and entanglement.

A classical bit as the basic information unit in a classical computer can only be in either of two different states, 0 or 1 and is typically represented by voltage or current pulses. The quantum mechanical analogon, a quantum bit or qubit, instead, is based on a quantum mechanical state and represents all possible superpositions of these two states. The advantages emerge when coupling several qubits obtaining a qubit register. While a classical register containing N bits stores only one of N possible numbers, a register of N qubits simultaneously stores 2^N numbers, the wave function amplitudes of the basis states in the superposition, so the information stored increases exponentially with the register size. The growing field of quantum information processing is focusing on the utilization of this information in a quantum computer with qubits as basic information units. A promising candidate for the physical realization of a qubit register are coupled quantum dots [5–7].

Quantum dots are artificial structures in the nanometer to micrometer range containing only a small number of electrons. These electrons are confined in all spatial directions to a region of the order of their wavelength in size which results in a discrete electronic density of states [8, 9]. Thus, quantum dots can be seen as artificial mesoscopic atoms [10], or molecules in

case of multiple quantum dots, with controllable physical properties. These structures allow the realization of experiments like spectroscopy known from atomic physics in a mesoscopic regime. In the realization of qubits based on quantum dots the charge state or the electron spin state serves as the quantum two-level system [6, 11]. Triple quantum dots (TQDs) are a step towards more complex quantum architectures as they are the smallest possible qubit chain. They have been proposed to work as exchange-controlled spin qubits [12–14] and current rectifiers [15–17], for instance. As a characteristic feature TQDs provide the possibility to implement quantum cellular automata processes, which are both a charging and reconfiguration process and a crucial element in quantum information processing [18, 19]. Further advantages of TQDs compared to double quantum dots are the purely electrical implementation of all quantum gates without using a magnetic field and the reduction of decoherence originating from charge fluctuations (decoherence free subspace) [13, 20].

On a general level the realization of quantum dots opened up a new chapter in both fundamental physics and the development of new devices with novel properties due to their tunability and versatility. Other prominent research applications aside from qubits are single electron transistors and quantum dot solar cells. A double quantum dot setup can serve as a single-electron ammeter for metrology applications [21]. Current commercial applications are quantum dot lasers and the implementation in display technology (QD LED).

For the purpose of electronic transport investigations in fundamental research quantum dots are most commonly fabricated as lateral structures defined by metallic top gates with electron beam lithography or by oxide lines with an atomic force microscope. The basis is a two-dimensional electron gas in a semiconductor heterostructure. The preparation of TQDs, especially of fully tunable lateral few-electron TQDs, has been made possible only a few years ago [15, 22–24] due to significant improvement in these fabrication methods.

TQDs offer the possibility of analyzing new fascinating properties [25] which are not present in double quantum dot systems. A TQD is the smallest molecule where different topologies are possible [25]. It can serve as a model system to study correlated electrons and three-level systems. TQDs show interference between different transport channels causing dark states

in triangular [26–29] and linear [30] dot distributions and long-distance coherent states [30–34]. Establishing a deep understanding of quantum interference is crucial for the coherent control of quantum states in quantum computation [25, 28, 35]. The triangular dot configuration in particular brings the opportunity to study the combination of quantum interference and electron-electron interaction [25, 36]. This configuration furthermore allows the exploration and utilization of a great variety of unique phenomena, such as entanglement and spin properties like spin frustration and chirality [25, 37]. For the investigation of properties manifesting themselves in electronic transport the flexibility of this setup is beneficial. Both charge detection by quantum point contacts (QPCs) and transport spectroscopy serve as essential tools for the characterization of system parameters and investigation of the described fundamental properties [22, 23].

In this thesis the electronic transport properties of such a triangular-shaped TQD are investigated in order to explore the electronic interactions between the two transport paths in this complex system. The device is a multi-terminal lateral TQD defined by oxide lines and with one lead attached to each dot. Two of the leads are used as sources and the remaining lead as a drain. This configuration has not been implemented before and enables both the simultaneous but separate investigation of transport through the two different double dot paths and the analysis of transport through the whole TQD system by measuring the total transport through the system or by a combination of the path-resolved measurements. By applying two different AC voltages to the sources a thorough study of electronic interactions between the electrons flowing through the two paths is allowed. It manifests itself in the path-resolved transport measurements. The transport is furthermore investigated with regard to interference effects between the electrons from different paths. These studies are based on a characterization of transport through the double dot paths separately, as well as of transport through the whole TQD system by a combination of the path-resolved measurements. The two-path setup allows the investigation of transitions from triple to quadruple points in transport. Charge measurements by using a quantum point contact as a charge sensor support the system characterization and are used to analyze the tunability of the charging properties of the device.

The experimental results are supported by a numerical simulation of electronic transport on the basis of a quantum mechanical model of the system.

Within a collaboration with the working group Theoretical Group on Quantum Transport on the Nanoscale from the Instituto de Ciencias de Materiales de Madrid, CSIC, Spain, F. Gallego-Marcos under supervision of Professor Gloria Platero provided the model and its implementation in a Mathematica simulation code. The model includes the quantum mechanical dynamics within the system and includes all quantum correlations. It treats the on-site states of all three dots coherently coupled so that the simulated transport involves quantum coherences. A first characterization of basic transport properties and fundamental tunability of this TQD sample combined with an electrostatic model can be found in [19, 24, 38–41].

This thesis gives an introduction into theoretical and experimental approaches and covers a thorough analysis of the transport properties in a triangular-shaped TQD by combining both. In the following the content of each chapter will be introduced in more detail.

The presentation of results is preceded by two introductory chapters. **Chapter 2** describes the theoretical background including an electrostatic and a quantum mechanical model of transport through single and multiple quantum dots. In **Chapter 3** the experimental techniques regarding the sample fabrication process are explained. These comprise optical lithography and local anodic oxidation by atomic force microscope. The measurement techniques for the conducted charge and transport measurements are described and the experimental setup is presented. The latter includes the cryogenic setup as all measurements were performed at a temperature of a few mK to enable the observation of quantum mechanical effects and the electrical measurement setup used for measuring electronic transport and for charge detection.

In the following chapters results obtained within this thesis are presented and discussed. **Chapter 4** covers the basic sample characterization by charge measurements showing modification possibilities of the charging properties by the tuning of tunneling barriers. In addition, linear and non-linear transport of the two paths separately is analyzed and discussed regarding the basic properties of a two-path device.

Chapter 5 focuses on the transport properties arising from the interaction between the two transport channels of the sample in greater detail. A numerical simulation of the electronic transport using a master equation

ansatz enables the determination of system parameters and supports the interpretation of the observed channel blockade effect in transport which substantially defines the transport characteristics of the device. Non-linear transport properties are revealed and discussed. The tunability of the device is utilized to form a double dot molecule in one path and a single dot in the other, giving rise to the possibility of probing hybridized states in one path with localized states in the other. Additionally, effects in transport concerning the separate double dot paths only, like elastic and inelastic cotunneling, are discussed.

Chapter 6 highlights the obtained results and presents conclusions which can been drawn from this work.

2 Theoretical background

The transport through an array of quantum dots as a spectroscopic characterization method is based on the knowledge of the electronic density of states of such low-dimensional systems. Therefore the spectrum of electronic states of quantum dots is introduced in this chapter. Controlling parameters which enable transport spectroscopy by tuning of a quantum dot are introduced within the framework of an electrostatic capacitance model of the dot. This model is also used to explain basic quantum dot transport properties like Coulomb blockade and to predict the charging properties of a dot system by a calculation of the stability diagram.

2.1 Electronic density of states

The electronic density of states (DOS) is a key parameter in the determination of electronic and optical properties of a material. It is defined as the number of electronic states in an energy interval [E, E+dE] and per unit volume V. It is used for determination of the carrier concentration and energy distribution of carriers within a material, for instance a semiconductor. Applying the simplified model of a free electron gas for the electrons in a semiconductor, the DOS of a three-, two-, one- and zero-dimensional electron system can be derived by modeling the crystal as a potential well with infinite walls (energy barriers).

2.1.1 Density of states in three dimensions

Solving the Schrödinger equation for electrons in three dimensions in a box with edge length L, the possible energy states

$$E\left(\vec{k}\right) = \sum_{i\in\{\mathrm{x,y,z}\}} E_i\left(k_i\right) = \frac{\hbar^2 k_\mathrm{x}^2}{2m_\mathrm{x}^*} + \frac{\hbar^2 k_\mathrm{y}^2}{2m_\mathrm{y}^*} + \frac{\hbar^2 k_\mathrm{z}^2}{2m_\mathrm{z}^*} \tag{2.1}$$

with wavevector $\vec{k}$ and effective electron mass m^* for each spatial direction

x,y,z are obtained.

The density of states in energy space is derived from the density of states in k-space via this dispersion relation $E(\vec{k})$. The states are evenly spaced in k-space with π/L, resulting from the restriction for the wave number $k_i = \pi/L \cdot n_i$, with $n_i \in \{1,2,...,\infty\}$, $i = \mathrm{x,y,z}$ which follows from the fixed boundary conditions for the potential box with infinite walls. One state then occupies a volume of $V_\mathrm{k} = (\pi/L)^3$ in k-space. We get sphere-surfaces of constant energy in k-space. As all values of k are positive, the states occupy only the positive octant of the Fermi sphere, thus a volume of $V_\mathrm{k,sum} = 1/8 \cdot 4/3\pi k^3$. This leads to a number of states at energy E of

$$N = 2 \cdot \frac{V_\mathrm{k,sum}}{V_\mathrm{k}} = 2 \cdot \frac{1}{8} \cdot \frac{4/3\pi k^3}{(\pi/L)^3}. \tag{2.2}$$

The factor 2 takes account of the two possible spin states of an electron.

We obtain by derivation

$$\mathrm{d}N^* = 2\frac{4\pi k^2 dk}{(2\pi/L)^3} = L^3 \frac{(2m)^{(3/2)}}{2\pi^2\hbar^3}\sqrt{E}\mathrm{d}E \tag{2.3}$$

with the transformation $\mathrm{d}E = \left(\hbar^2 k/m\right)\mathrm{d}k$ given by the dispersion relation Eq.(2.1).

After normalization to the volume of the cube L^3 it follows

$$\mathrm{d}N = \frac{(2m)^{(3/2)}}{2\pi^2\hbar^3}\sqrt{E}\mathrm{d}E, \tag{2.4}$$

with $\mathrm{d}N^* = L^3\mathrm{d}N$. Thus, the density of states in 3D is

$$D_\mathrm{3D}(E) = \frac{\mathrm{d}N}{\mathrm{d}E} = \frac{(2m)^{(3/2)}}{2\pi^2\hbar^3}\sqrt{E}. \tag{2.5}$$

The DOS is continuous in energy and proportional to $\sqrt{E}$ (Fig. 2.1 (a)).

2.1.2 Density of states in low dimensions

For lower dimensional systems the density of states is calculated analogously to the situation in three dimensions above in section 2.1.1. The DOS for

two, one and zero dimensions will be presented with a short derivation in the following.

2.1.2.1 Density of states in two dimensions

Application of a potential confining the electrons of the order of their wavelength in z-direction leads to energy quantization in this direction. The eigenenergies are

$$E_{\mathrm{2D}}\left(k_{\mathrm{x}},k_{\mathrm{y}},n_{\mathrm{z}}\right)=\frac{\hbar^2k_{\mathrm{x}}^2}{2m_{\mathrm{x}}^*}+\frac{\hbar^2k_{\mathrm{y}}^2}{2m_{\mathrm{y}}^*}+E_{\mathrm{z}}(n_{\mathrm{z}}). \tag{2.6}$$

$n\in\{1,2,...,\infty\}$ is the number of occupied states. We write $E_{\mathrm{z}}(n_{\mathrm{z}})=E_{\mathrm{z}}^n$ in the following. With one state occupying a volume of $V_{\mathrm{k}}=\left(\pi/L\right)^2$ in k-space we calculate the 2D density of states analogously to the 3D case. We get $N\propto E$ and the density of states is

$$D_{\mathrm{2D}}(E)=\frac{m^*}{\pi\hbar^2}, \tag{2.7}$$

which is energy independent.

In real systems electrons are always not ideally confined. They are confined of the order of their wavelength by a confinement potential. When the electrons are confined in this way in z-direction we get a quantum well with discrete energies E_{z}^n, so called subbands, with $E_{\mathrm{z}}^1>0$ for the lowest subband. The low dimensionality comes per subband. Systems with more then one occupied subband are called quasi-low-dimensional. When only the lowest subband is occupied the system is low-dimensional. For a system with several occupied subbands we have to use the Heaviside function Θ to introduce a stepfunction for the total occupation of the subbands. The DOS is

$$D_{\mathrm{2D}}(E)=\frac{m^*}{\pi\hbar^2}\sum_n\Theta\left(E-E_{\mathrm{z}}^n\right). \tag{2.8}$$

The DOS with respect to energy is depicted in Fig. 2.1 (b). A step in the DOS for each quantized state n_i is obtained.

2.1.2.2 Density of states in one dimension

One-dimensional systems are described analogously. We get the energy-eigenstates

$$E_{1\mathrm{D}}\left(k_{\mathrm{x}},n_{\mathrm{y}},n_{\mathrm{z}}\right)=\frac{\hbar^2k_{\mathrm{x}}^2}{2m_{\mathrm{x}}^*}+E_{\mathrm{y}}(n_{\mathrm{y}})+E_{\mathrm{z}}(n_{\mathrm{z}}). \tag{2.9}$$

One state occupies a volume of $V_{\mathrm{k}}=\pi/L$ in k-space. On this basis the DOS in one dimension is expressed by

$$D_{1\mathrm{D}}(E)=\frac{\sqrt{2m^*}}{\pi\hbar}\frac{1}{\sqrt{E}}. \tag{2.10}$$

In the case of a quasi-one-dimensional system with a confinement potential in y- and z-direction subbands E_{y}^m and E_{z}^n, with $n,m\in\{1,2,...,\infty\}$ arise and the DOS is given by

$$D_{1\mathrm{D}}(E)=\frac{\sqrt{2m^*}}{\pi\hbar}\sum_{m,n}\sqrt{\frac{\hbar^2}{2m^*\left(E-E_{\mathrm{y}}^m-E_{\mathrm{z}}^n\right)}}\Theta\left(E-E_{\mathrm{y}}^m-E_{\mathrm{z}}^n\right). \tag{2.11}$$

The DOS with respect to energy is depicted in Fig. 2.1 (c). A peak is obtained at each quantized state n_i.

2.1.2.3 Density of states in zero dimensions

If the electron motion is confined in x-, y- and z-direction, we get energy quantization in all spacial directions. The energy-eigenstates are

$$E_{0\mathrm{D}}\left(n_{\mathrm{x}},n_{\mathrm{y}},n_{\mathrm{z}}\right)=E_{\mathrm{x}}(n_{\mathrm{x}})+E_{\mathrm{y}}(n_{\mathrm{y}})+E_{\mathrm{z}}(n_{\mathrm{z}}). \tag{2.12}$$

For parabolic confinement potentials the energy is

$$E_{0\mathrm{D}}\left(n_{\mathrm{x}},n_{\mathrm{y}},n_{\mathrm{z}}\right)=\hbar\omega_{\mathrm{x}}\left(n_{\mathrm{x}}+\frac{1}{2}\right)+\hbar\omega_{\mathrm{y}}\left(n_{\mathrm{y}}+\frac{1}{2}\right)+\hbar\omega_{\mathrm{z}}\left(n_{\mathrm{z}}+\frac{1}{2}\right). \tag{2.13}$$

The DOS for a quasi-zero-dimensional system is fully discretized and can be written as a summation over Dirac δ-functions

$$D_{0\mathrm{D}}(E) = 2 \sum_{n_\mathrm{x},n_\mathrm{y},n_\mathrm{z}} \delta\left(E - E\left(n_\mathrm{x},n_\mathrm{y},n_\mathrm{z}\right)\right) \tag{2.14}$$

with the factor of 2 coming from the spin degeneracy of the energy levels. The fully discretized DOS is depicted in Fig. 2.1 (d).

The energetic structure of a quasi-zero-dimensional system, named quantum dot, is a sequence of discrete energy states $E\left(n_\mathrm{x},n_\mathrm{y},n_\mathrm{z}\right)$, comparable to the energy quantization in an atom. This is why quantum dots are also called artificial atoms.

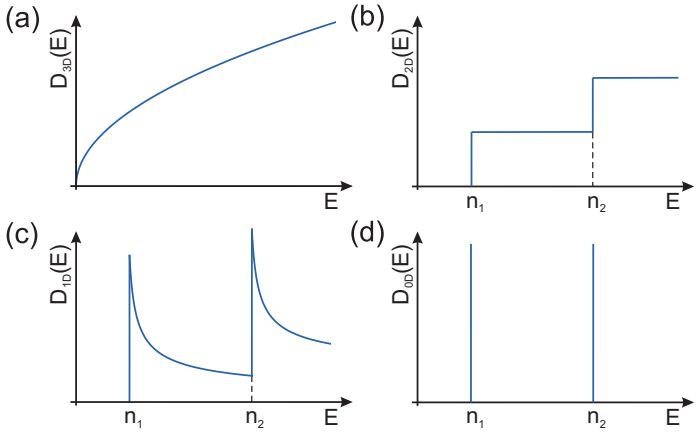

Figure 2.1: Electronic density of states in 3D, 2D, 1D and 0D systems. While the DOS in 3D is continous in energy (a), it exhibits quantized states, so called subbands, in lower dimensions, which leads to a step (2D) (b) or a peak (1D) (c) in the DOS for each quantized state. In case of a 0D system, the electronic states only exist at discrete energies (d). The first two quantized states n_1 and n_2 are shown for each case.

2.2 Electronic states in quantum dots

As described above a quantum dot is a quasi-zero-dimensional system and exhibits a discrete energy spectrum (Fig. 2.1 (d)). This energy spectrum will be explained in detail in the following. Within the scope of this work lateral

quantum dots are discussed. These are artificially defined quantum dots created by lateral patterning of a two-dimensional electron gas (2DEG). A confining potential is introduced by means of electrical gates on the surface of the heterostructure including the 2DEG. It confines the electrons in the remaining two dimensions. A zero-dimensional electron system is formed. Other types of quantum dots, like self-organized dots, are fabricated and controlled in a different way but exhibit the same discrete energy spectrum.

2.2.1 Excitation spectrum

The energy spectrum of a quantum dot is obtained by solving the Schrödinger equation. We consider the confinement potential $V(x,y)$ of a circular shaped quantum dot to be of parabolic form

$$V(x,y) = \frac{1}{2} m^* w_0^2 \left|\vec{r}\right|^2 \tag{2.15}$$

with the radial frequency ω_0 and the dot radius $\left|\vec{r}^2\right| = x^2 + y^2$. In a lateral quantum dot defined on the basis of a 2DEG electrons are already confined in z-direction. They are further confined by a gate structure in a parabolic potential, which is considered a good approximation for the common gate geometries [42, 43]. Therefore, the Hamilton operator H of the two dimensional harmonical oscillator

$$\mathrm{H} = -\frac{\hbar^2}{2m}\nabla^2 + V(\vec{r}) \tag{2.16}$$

is used. We obtain the eigenenergies

$$\varepsilon_{n,l} = \hbar\omega_0(2n + |l| + 1) \tag{2.17}$$

with the radial quantum number $n \in \{1,2,...,\infty\}$ and the orbital quantum number $l = 0, \pm 1, \pm 2$ and $2n + |l| = n_\mathrm{x} + n_\mathrm{y} = j$ being the shell number j. Thus, equidistant energy levels are located at $(j+1)\hbar\omega_0 = ((n_\mathrm{x}+n_\mathrm{y})+1)\hbar\omega_0$ with distance $\hbar\omega_0$. In this notation the eigenenergies are

$$\varepsilon_{n_\mathrm{x},n_\mathrm{y}} = \hbar\omega_0((n_\mathrm{x} + n_\mathrm{y}) + 1) \tag{2.18}$$

This is the energy spectrum of a single electron in a 2D harmonic potential.

The 2DEG which is used as a basis to define the quantum dot is a real two-dimensional system. Only the first subband E_z^1 is occupied in z-direction. This first subband energy adds up to the energy spectrum 2.18. The energies of an electron in a quantum dot are therefore

$$\varepsilon_{n_x,n_y} = \hbar\omega_0((n_x + n_y) + 1) + E_z^1 \tag{2.19}$$

2.2.2 Addition spectrum

While the electron spectrum discussed above refers to a dot occupied by a single electron, the following section considers the energy spectrum of a dot occupied by several electrons. This is the addition spectrum of the dot. If a dot is charged with more than one electron we have to consider the electron-electron interaction in form of the Coulomb repulsion between the electrons. The constant interaction model considers the Coulomb repulsion which has to be overcome when adding one more electron to the system to be independent of the number of electrons on the dot. This model disregards other effects, like screening, exchange and correlation effects between electrons. The Coulomb repulsion is taken into account by a constant charging energy E_C. The electrostatic part of the total energy of a quantum dot with N electrons is expressed by

$$E_{el} = \frac{1}{2}N(N-1)E_C. \tag{2.20}$$

The electrons added to the dot will successively occupy the Fock-Darwin states (Eq.(2.18)), their respective ground state energy. The total energy of the dot is the sum of these quantum-mechanical energies of the electrons in the dot and their electrostatic energies (Eq.(2.20))

$$E_N = \frac{1}{2}N(N-1)E_C + \sum_{i=1}^{N}\varepsilon_i. \tag{2.21}$$

E_1 is the energy of the ground state ε_i of the Fock-Darwin spectrum. When for instance the N-th electron occupies not its ground state ε_N, but a higher state, say ε_{N+1}, the dot is in an excited state, denoted as E_N^*, with $E_N^* > E_N$. Thus, the system has a higher total energy.

The energy which has to be spent to raise the electron number by one from N-1 to N is the chemical potential

$$\mu_{\mathrm{N}} = E_{\mathrm{N}} - E_{\mathrm{N}-1} = (N-1)E_{\mathrm{C}} + \varepsilon_{\mathrm{N}} \tag{2.22}$$

for the transition $N-1 \rightarrow N$ electrons on the dot. For consecutive electron numbers the respective chemical potentials have an energy distance of

$$\mu_{\mathrm{N}+1} - \mu_{\mathrm{N}} = E_{\mathrm{C}} + \varepsilon_{\mathrm{N}+1} - \varepsilon_{\mathrm{N}}. \tag{2.23}$$

Especially lateral quantum dots are relatively large, so most commonly the charging energy E_{C} is much larger than the energy distance between the quantum mechanical states of the dot. Consequently the dot has equally spaced chemical potentials in distance E_{C}. Thus, in good approximation the charging energy E_{C} is the energy which is necessary to load one electron on the dot.

2.3 Electronic transport through quantum dots

Transport spectroscopy is used for the characterization and further analysis of a lateral quantum dot system. For spectroscopy of a system, the electronic structure of the system under investigation is scanned with a testing energy that is applied to the system and the reaction of the system is measured. In transport spectroscopy of a quantum dot this testing energy is the kinetic energy of electrons which are fed into the dot by the leads of the system. The reaction of the system is then reflected by the observed current through the system flowing one lead (source) to the other (drain).

The energies of electrons coming from the leads are given by the population of the two-dimensional density of states of the leads. When their energy equals μ_{N}, the addition energy to add one more electron to the system, the energy can be absorbed by the dot. Thus, the dot can be charged with the N-th electron, if one of the chemical potentials of the leads, μ_{S} (chemical potential of the source lead) or μ_{D} (chemical potential of the drain lead), is higher than the energy to add the N-th electron to the dot, the potential μ_{N}: $\mu_{\mathrm{S}} \geq \mu_{\mathrm{N}}$ or $\mu_{\mathrm{D}} \geq \mu_{\mathrm{N}}$. The difference of the chemical potentials μ_{S} and μ_{D} defines a so-called transport window. If the chemical potential of the dot μ_{N} is located inside this transport window, transport through the dot from lead to lead is possible and a current I flows. This requires that the tunneling barriers between the dot and the leads are transparent enough to allow transport. The chemical potential of the source

lead is tuned by applying a voltage U_S to the source. The drain lead is usually grounded. Therefore the size of the transport window is controlled by U_S applied to the source. This voltage is also called bias voltage. In order to measure the energy spectrum of the quantum dot, parameters which control the positions of $\mu_{S,D}$ and μ_N relative to each other have to be varied.

In lateral quantum dots these parameters are the voltage U_S applied to the source lead, which directly varies its chemical potential, and the gate voltage U_G controlling the potential of the dot itself, which is applied at gates coupling capacitively to the dot. The electrical control of the quantum dot by gates is a characteristic property of structured quantum dots. These dependencies are explained in an electrostatic capacitance model of the quantum dot and its environment, namely the leads and gates, in the following section.

2.3.1 Electrostatic model

The electrostatic model of a quantum dot system is able to explain Coulomb blockade phenomena observed in electronic transport through the dot. It completely neglects the spacial quantization effects of the quantum dots and only takes into account the capacitive couplings in the system. Figure 2.2 shows a schematic of the electrostatic model for a single quantum dot. The source and drain leads are tunnel coupled to the dot, which leads to the resistance R_S and R_D, respectively, between the dot and the leads. In addition, the voltage U_S applied to the source is affecting the potential of the dot by a capacitive coupling C_S. Thus, the source voltage U_S also has a gate effect on the dot. Analogously the drain lead is capacitively coupled to the dot by C_D. The gate is only capacitively coupled by C_G as it is electrically isolated from the dot. The capacitive coupling raises linearly with the inverse distance between dot and gate. An applied gate voltage U_G is influencing the dot potential by the capacitance C_G. The total capacitance C_Σ between dot and its environment then is

$$C_\Sigma = C_S + C_D + C_G \tag{2.24}$$

and the corresponding charging energy E_C of the dot is

$$E_C = \frac{e^2}{C_\Sigma}. \tag{2.25}$$

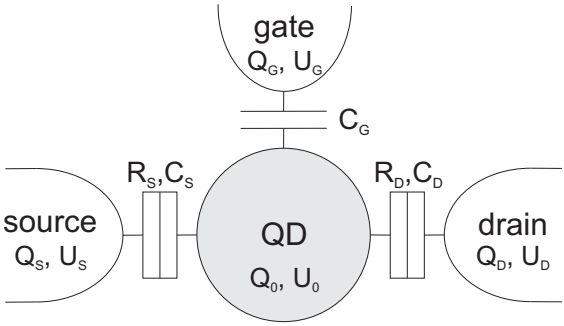

Figure 2.2: Electrostatic model for a single dot coupled capacitively to a gate, a source- and drain lead by C_G, C_S and C_D, respectively. R_S and R_D denote, only for the sake of completeness, the additional tunnel resistance between the dot and the leads. The system can be handled as a network of metallic discs with charges Q and voltages U connected by capacitors.

With behalf of the electrostatic capacitance model of a dot the charging energy of the dot can be derived. The dot can be described as a small metallic island of radius r with a self-capacitance of $C = 8\varepsilon_r\varepsilon_0 r$ with relative dielectric constant ε_r and the vacuum permittivity ε_0, which is the capacitance against the infinity and as such marks the upper limit of the disc capacitance. This disc is connected by capacitors to a network of other metallic discs. The metallic discs are electrodes, voltage sources, modeling the dot and the capacitive coupled leads and gates (Fig. 2.2).

The charge state of the system is expressed in terms of the electrostatic potentials of the electrodes (dot, gates and leads) by [44]

$$\vec{Q} = C\vec{U} \tag{2.26}$$

with the elements Q_i of the charge vector $\vec{Q}$ being the charge on electrode i. C is the capacitance matrix. A diagonal element C_{ii} is the total capacitance of electrode i and a non-diagonal element C_{ij} is the negative capacitance between electrode i and j. The voltage vector $\vec{U} = (U_0,U_\mathrm{S},U_\mathrm{G},U_\mathrm{D})$ consists of elements U_j, with $j \in \{0,\mathrm{S},\mathrm{G},\mathrm{D}\}$ being the electrostatic potential of electrode j. The electrostatic potential of the dot, U_0, in dependence of the electrostatic potentials of the gates and leads is

$$U_0 = \frac{Q_0}{C_\Sigma} + \sum_j \frac{C_{0j}}{C} U_j \tag{2.27}$$

with C_{0j} being the capacitance between lead/gate j ($j \in \{G,S,D\}$) and the dot. U_j is the voltage on electrode (lead/gate) j. The sum capacitance of the dot is given by the sum over the capacitances of all leads $C_\Sigma = \sum_{j=1}^{n} C_{0j}$ (Eq. (2.24)). The electrostatic energy of the dot charged with N electrons is

$$E_\mathrm{N} = \int_0^{\mathrm{N}e} U_0(Q_0)\mathrm{d}Q_0 = \frac{N^2 e^2}{2C_\Sigma} + Ne \sum_j \frac{C_{0j}}{C_\Sigma} U_j. \tag{2.28}$$

The summand $Ne\sum_{j=1}(C_{0j}/C_\Sigma)\cdot U_j$ is the electrostatic potential of the dot charged with N electrons and $(N^2e^2)/(2C_\Sigma)$ is the energy needed to charge the dot with N electrons. The chemical potential μ_N of the dot is its change in electrostatic energy with its charge:

$$\mu_\mathrm{N} = \frac{\delta E_\mathrm{N}}{\delta N} = N\frac{e^2}{C_\Sigma} + e\sum_j \frac{C_{0j}}{C_\Sigma} U_j \tag{2.29}$$

and the difference in chemical potentials equals the charging energy E_C (Eq. (2.25)) of the dot, the energy needed to load one electron on the dot

$$E_\mathrm{C} = \mu_{\mathrm{N}+1} - \mu_\mathrm{N} = \frac{e^2}{C_\Sigma}. \tag{2.30}$$

A voltage U coupling to the system by a capacitance C is not only affecting the potential of the dot, it is also varying the tunnel couplings R_S, R_D in the system. This fact is ignored in the introduced capacitive model. The influence of a voltage U on the chemical potentials μ_N of the dot is

$$\Delta\mu_\mathrm{N} = -eU\frac{C}{C_\Sigma}. \tag{2.31}$$

In this way a gate voltage U_G controls the chemical potentials μ_N of the dot via C_G, while it is not affecting the chemical potentials μ_S and μ_D of the leads. Thus their relative position can be tuned by U_G which enables a change in the electron number on the dot. The chemical potentials of the dot are also changed by U_S via C_S in the same manner (Eq. (2.31)). In addition, U_S influences the chemical potential μ_S of the source lead by

$$\Delta\mu_S = -eU_S. \tag{2.32}$$

The drain lead is grounded. This opens a transport window which enables transport through more than one transport channel. All chemical potentials of the dot located within the transport window spanned by μ_S and μ_D: $\mu_S \geq \mu_N \geq \mu_D$ or $\mu_S \leq \mu_N \leq \mu_D$ participate in transport. To sum up, the relation between the change of the chemical potential of the dots and the control parameters U_G and U_S is

$$\Delta\mu_N = -eU_G\frac{C_G}{C_\Sigma} - eU_S\frac{C_S}{C_\Sigma}. \tag{2.33}$$

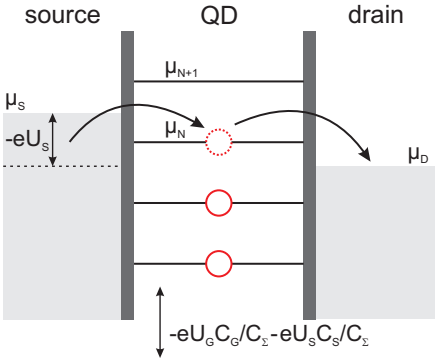

Figure 2.3: Model of a quantum dot connected to source and drain by tunneling barriers. It shows, how the control parameters U_G and U_S change the relation between the chemical potentials μ_N of the dot and the chemical potentials μ_S and μ_D of the source and drain lead. U_S additionally opens a transport window.

Fig. 2.3 shows how these control parameters tune the chemical potentials of the dot and of the leads. The source voltage shifts the chemical potential of the source lead according to Eq. (2.32) opening a transport window and both the gate and the source voltage control the chemical potentials of the dot according to Eq. (2.33). This way the transport through the dot is controlled.

With Eq. (2.33) and Eq. (2.25) a conversion from gate voltages to energy scales is obtained by

$$E = eU_{\mathrm{G}}\frac{C_{\mathrm{G}}}{C_{\Sigma}} = eU_{\mathrm{G}}C_{\mathrm{G}}\frac{E_{\mathrm{C}}}{e^2}. \tag{2.34}$$

This capacitive model can easily be extended for the description of multiple quantum dots. Besides the described relations for each of the single dots, two different coupling effects between the dots have to be taken into account in a system consisting of multiple quantum dots. These are the inter-dot tunnel coupling and the inter-dot capacitive coupling. As we focus on capacitive models in this section, only the capacitive coupling is taken into account.

We consider the example of a triple quantum dot in triangle configuration with each dot capacitively coupled to the other two in advance of the measurement setup discussed later. For spectroscopy of the electronic structure of one dot one gate was sufficient. For a multiple quantum dot system a gate number equaling the number of dots is needed when we want to control each of the dots independently and shift their potentials with respect to each other. Thus, each dot has its specific gate. In this example of a triple quantum dot system each dot is additionally coupled to a lead. Cross-capacitances are neglected for better clarity in this ideal model. This means that each dot is capacitively coupled to only one specific gate. Capacitive couplings to the other gates are neglected. However, in real systems cross-capacitances are always relevant and the model has to be expanded in a straight forward manner. A schematic of the considered system setup based on a capacitive model is shown in Figure 2.4. It includes the inter-dot capacitances C_{ij} (i,$j \in$ {A,B,C} and $i \neq j$), the dot-gate capacitances $C_{\mathrm{G}i,j}$ ($i = j$), the dot-lead capacitances $C_{\mathrm{S1,B}}$, $C_{\mathrm{S2,C}}$, $C_{\mathrm{D,A}}$, and the voltages $U_{\mathrm{G}i}$ and U_{S1}, U_{S2}, U_{D} applied to the gates G_i and leads S_1, S_2, D, respectively. Additionally, there are the cross-capacitances $C_{\mathrm{G}i,j}$ ($i \neq j$), which are $C_{\mathrm{S1,A}}$, $C_{\mathrm{S2,A}}$, $C_{\mathrm{S2,B}}$, $C_{\mathrm{D,B}}$, $C_{\mathrm{S1,C}}$, $C_{\mathrm{D,C}}$. They are not marked in the figure.

The total energies for zero up to one electron on each dot according to the energy needed to charge an empty dot with one electron (Eq. (2.31)) without considering cross-capacitances and the capacitive influence of the leads, are

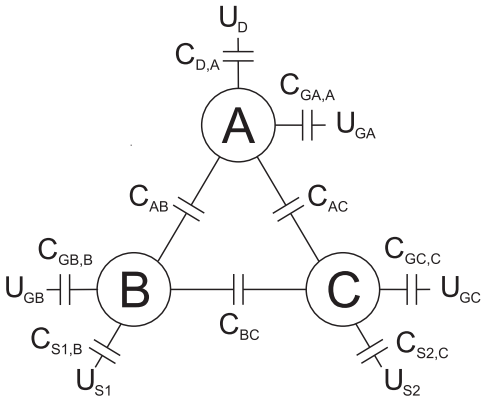

Figure 2.4: Schematic of a triple quantum dot described within the capacitive model including inter-dot capacitances C_{ij} (i,j = A,B,C,$i \neq j$), dot-gate capacitances $C_{\mathrm{G}i,j}$ ($i = j$), dot-lead capacitances $C_{\mathrm{D,A}}$, $C_{\mathrm{S1,B}}$, $C_{\mathrm{S2,C}}$ and voltages $U_{\mathrm{G}i}$, U_{S1}, U_{S2}, U_{D}.

$$\begin{aligned} E_{000} &= 0 \\ E_i &= -\frac{e}{C_{\Sigma i}} \left(C_{\mathrm{G}i,i} U_{\mathrm{G}i}\right) \\ E_{i,j} &= E_i + E_j + e^2 \frac{C_{ij}}{C_{\Sigma i} C_{\Sigma j}} \\ E_{i,j,k} &= E_{i,j} + E_{i,k} + E_{j,k} - E_i - E_j - E_k. \end{aligned} \tag{2.35}$$

with i,j,$k \in$ {A,B,C}, $i \neq j \neq k$ and E_i denoting the electrostatic energy for one electron on dot i. $E_{i,j}$ is the electrostatic energy for two electrons in the system, one on dot i and one on dot j. Analogously, $E_{i,j,k}$ is the electrostatic energy for three electrons in the system. $C_{\mathrm{GA},i}$, $C_{\mathrm{GB},i}$, $C_{\mathrm{GC},i}$ is the capacitive coupling between dot i to gate G_{A}, G_{B}, G_{C}, respectively, and C_{ij} is the capacitive inter-dot coupling between dot i and j. $C_{\Sigma i}$ is the total capacitance of dot i.

Considering cross-capacitances, which means taking into account the capacitive coupling of the dots to each gate and lead, E_i becomes

$$\begin{aligned} E_i = &- \frac{e}{C_{\Sigma i}}(C_{\mathrm{GA},i}U_{\mathrm{GA}} + C_{\mathrm{GB},i}U_{\mathrm{GB}} + C_{\mathrm{GC},i}U_{\mathrm{GC}} \\ &+ \quad C_{\mathrm{S1},i}U_{\mathrm{S1}} + C_{\mathrm{S2},i}U_{\mathrm{S2}} + C_{\mathrm{D},i}U_{\mathrm{D}}). \end{aligned} \tag{2.36}$$

When a certain set of gate voltages U_{GA}, U_{GB}, U_{GB} is applied, the system favors the charge configuration (i,j,k) with the smallest energy $E_{i,j,k}$. The charge configuration of the system is tunable by varying the gate voltages. A parameter area for which the charge configuration is fixed is called stability region. At the borders of these stability regions charge transitions take place. For a fully tunable system of N quantum dots N gates are needed, as the N dot system consists of N linearly independent energy spectra. Thus, for a system of N quantum dots a full stability diagram is N-dimensional [22]. On basis of this electrostatic model the three-dimensional stability diagram of the dot system can be calculated [19].

Another possible way to plot a stability diagram of a quantum dot system is the evaluation of the chemical potential of each dot. In the following this is discussed for the triple quantum dot system shown in Fig. 2.4. However, cross-capacitances are neglected for reasons of clarity. They are a natural extension of the described model and can easily be included. The relevant capacitances are only $C_{\mathrm{G}i,i}$ (in the following in short written as $C_{\mathrm{G}i}$), as in Eq. (2.35). In the following the approach of van der Wiel et al. [44] is followed and extended to a three dot system [45].

The electrostatic energy E_{el} of the system is

$$E_{\mathrm{el}} = \frac{1}{2}\vec{U}C\vec{U} \tag{2.37}$$

with the capacitance matrix C of the system and the voltage vector $\vec{U}$. $\vec{U}$ is calculated on the basis of Eq. (2.26). The voltages on the gates and leads are known and the voltages on the dots U_{A}, U_{B}, U_{C} have to be determined only. Thus, with the partition of $\vec{Q}$ and $\vec{U}$ into two parts referring to the dots and gates/leads, marked with indices c and v, respectively

$$\begin{pmatrix} \vec{Q}_{\mathrm{c}} \\ \vec{Q}_{\mathrm{v}} \end{pmatrix} = \begin{pmatrix} C_{\mathrm{cc}} & C_{\mathrm{cv}} \\ C_{\mathrm{vc}} & C_{\mathrm{vv}} \end{pmatrix} \begin{pmatrix} \vec{U}_{\mathrm{c}} \\ \vec{U}_{\mathrm{v}} \end{pmatrix} \tag{2.38}$$

Eq. (2.26) can thus be written as

$$\vec{Q}_\mathrm{c} = C_\mathrm{cc}\vec{U}_\mathrm{c} + C_\mathrm{cv}\vec{U}_\mathrm{v} \tag{2.39}$$

with $\vec{Q}_\mathrm{c} = (Q_\mathrm{A},Q_\mathrm{B},Q_\mathrm{C})$ and $\vec{U}_\mathrm{c}$ being the charge and the voltage on the dots, respectively, and $\vec{U}_\mathrm{v}$ being the voltage on the gates/leads. $\vec{U}_\mathrm{c}$ then is

$$\vec{U}_\mathrm{c} = C_\mathrm{cc}^{-1}\left(\vec{Q}_\mathrm{c} - C_\mathrm{cv}\vec{U}_\mathrm{v}\right). \tag{2.40}$$

The elements of $\vec{Q}_\mathrm{c}$ are

$$\begin{aligned} Q_\mathrm{A} =& Q_\mathrm{D} + Q_\mathrm{GA} + Q_\mathrm{AB} + Q_\mathrm{AC} = C_\mathrm{D}\left(U_\mathrm{A} - U_\mathrm{D}\right) \\ &+ C_\mathrm{GA}\left(U_\mathrm{A} - U_\mathrm{GA}\right) + C_\mathrm{AB}\left(U_\mathrm{A} - U_\mathrm{B}\right) + C_\mathrm{CA}\left(U_\mathrm{A} - U_\mathrm{C}\right) \end{aligned} \tag{2.41}$$

$$\begin{aligned} Q_\mathrm{B} =& Q_\mathrm{S1} + Q_\mathrm{GB} + Q_\mathrm{AB} + Q_\mathrm{BC} = C_\mathrm{S1}\left(U_\mathrm{B} - U_\mathrm{S1}\right) \\ &+ C_\mathrm{GB}\left(U_\mathrm{B} - U_\mathrm{GB}\right) + C_\mathrm{AB}\left(U_\mathrm{B} - U_\mathrm{A}\right) + C_\mathrm{BC}\left(U_\mathrm{B} - U_\mathrm{C}\right) \end{aligned} \tag{2.42}$$

and

$$\begin{aligned} Q_\mathrm{C} =& Q_\mathrm{S2} + Q_\mathrm{GC} + Q_\mathrm{AC} + Q_\mathrm{BC} = C_\mathrm{S2}\left(U_\mathrm{C} - U_\mathrm{S2}\right) \\ &+ C_\mathrm{GC}\left(U_\mathrm{C} - U_\mathrm{GC}\right) + C_\mathrm{AC}\left(U_\mathrm{C} - U_\mathrm{A}\right) + C_\mathrm{BC}\left(U_\mathrm{C} - U_\mathrm{B}\right). \end{aligned} \tag{2.43}$$

The matrix form is

$$\begin{pmatrix} Q_\mathrm{A} \\ Q_\mathrm{B} \\ Q_\mathrm{C} \end{pmatrix} = \begin{pmatrix} C_\mathrm{A} & -C_\mathrm{AB} & -C_\mathrm{CA} \\ -C_\mathrm{AB} & C_\mathrm{B} & -C_\mathrm{BC} \\ -C_\mathrm{AC} & -C_\mathrm{BC} & C_\mathrm{C} \end{pmatrix} \begin{pmatrix} U_\mathrm{A} \\ U_\mathrm{B} \\ U_\mathrm{C} \end{pmatrix} \tag{2.44}$$

with $C_\mathrm{A} = C_\mathrm{D} + C_\mathrm{GA} + C_\mathrm{AB} + C_\mathrm{AC}$, $C_\mathrm{B} = C_\mathrm{S1} + C_\mathrm{GB} + C_\mathrm{AB} + C_\mathrm{BC}$ and $C_\mathrm{C} = C_\mathrm{S2} + C_\mathrm{GC} + C_\mathrm{BC} + C_\mathrm{AC}$. The matrix corresponds to C_cc. The electrostatic energy E_el can be calculated using Eq. (2.37). It can now be reduced to

$$E_\mathrm{el} = \frac{1}{2}\vec{U}_\mathrm{c}C_\mathrm{cc}\vec{U}_\mathrm{c}. \tag{2.45}$$

The chemical potentials μ_A, μ_B, μ_C of dots A, B, C, respectively, are

$$\begin{aligned}\mu_{\mathrm{A}}(n,m,l) &= E_{\mathrm{el}}(n,m,l) - E_{\mathrm{el}}(n-1,m,l)\\ \mu_{\mathrm{B}}(n,m,l) &= E_{\mathrm{el}}(n,m,l) - E_{\mathrm{el}}(n,m-1,l)\\ \mu_{\mathrm{C}}(n,m,l) &= E_{\mathrm{el}}(n,m,l) - E_{\mathrm{el}}(n,m,l-1),\end{aligned} \tag{2.46}$$

with n, m, l being the number of electrons on dot A, B, C, respectively. Inserting the respective electrostatic energies E_{el} we obtain

$$\begin{aligned}\mu_{\mathrm{A}}(n,m,l) = |e|^2 CD_{\mathrm{AA}}&\left(n - \frac{1}{2} - T_{\mathrm{UC,A}}\right)\\ &+ D_{\mathrm{AB}}(m - T_{\mathrm{UC,B}}) + D_{\mathrm{AC}}(l - T_{\mathrm{UC,C}})\end{aligned} \tag{2.47}$$

$$\begin{aligned}\mu_{\mathrm{B}}(n,m,l) = |e|^2 CD_{\mathrm{AB}}&(n - T_{\mathrm{UC,A}})\\ &+ D_{\mathrm{BB}}\left(m - \frac{1}{2} - T_{\mathrm{UC,B}}\right) + D_{\mathrm{BC}}(l - T_{\mathrm{UC,C}})\end{aligned} \tag{2.48}$$

$$\begin{aligned}\mu_{\mathrm{C}}(n,m,l) = |e|^2 CD_{\mathrm{AC}}&(n - T_{\mathrm{UC,A}})\\ &+ D_{\mathrm{BC}}(m - T_{\mathrm{UC,B}}) + D_{\mathrm{CC}}\left(l - \frac{1}{2} - T_{\mathrm{UC,C}}\right)\end{aligned} \tag{2.49}$$

with $D = C_{\mathrm{cc}}^{-1}$ and D_{ij} being the elements of D with $i,j \in \{A,B,C\}$. The terms $T_{\mathrm{UC,A}}$, $T_{\mathrm{UC,B}}$, $T_{\mathrm{UC,C}}$ stand for

$$\begin{aligned}T_{\mathrm{UC,A}} &= C_{\mathrm{D}}U_{\mathrm{D}} + C_{\mathrm{GA}}U_{\mathrm{GA}},\\ T_{\mathrm{UC,B}} &= C_{\mathrm{S1}}U_{\mathrm{S1}} + C_{\mathrm{GB}}U_{\mathrm{GC}},\\ T_{\mathrm{UC,C}} &= C_{\mathrm{S2}}U_{\mathrm{S2}} + C_{\mathrm{GC}}U_{\mathrm{GC}},\end{aligned} \tag{2.50}$$

respectively. The charge on the dots is substituted by the electron number by using the factor $|e|^2$. The voltages are consequently given by $U/|e|$. When the capacitances between the dots, between dot and its respective gate and lead, and the voltages applied to the gates and leads are known, the chemical potential of the dots can be calculated with these formulas [45].

In order to calculate the three-dimensional stability diagram of the triple dot system in dependence of the three gate voltages we want to know the stable charge configuration of the system for a certain gate-voltage-domain. The chemical potentials of the leads are $\mu_{S1} = \mu_{S2} = \mu_D = 0$ for the no bias case. The charge on the dots in equilibrium is the solution of $\mu_{S1}, \mu_{S2}, \mu_D \leq 0$ with maximum N_1, N_2, N_3. The borders of the stable regions, the charging lines, are the solutions of the equations $\mu_i\,(n,m,l) = 0, (i \in \{\mathrm{A,B,C}\})$ in terms of gate voltages. Appropriate border conditions determine which solution to take and where the charging lines are supposed to start and end. In this way the stability diagram can be computed. [44, 45] As an example a two-dimensional cut through the stability diagram of a triple quantum dot system is shown in Fig. 2.5 which is computed according to the instructions above. The lines with different slopes marked with A, B and C correspond to the charging lines of dots A, B and C, respectively. They are connected by charge reconfiguration lines at the dot resonances of which two (A-B and B-C) are seen in this section of the diagram. In the charge stability regions the number of electrons on the dots is denoted.

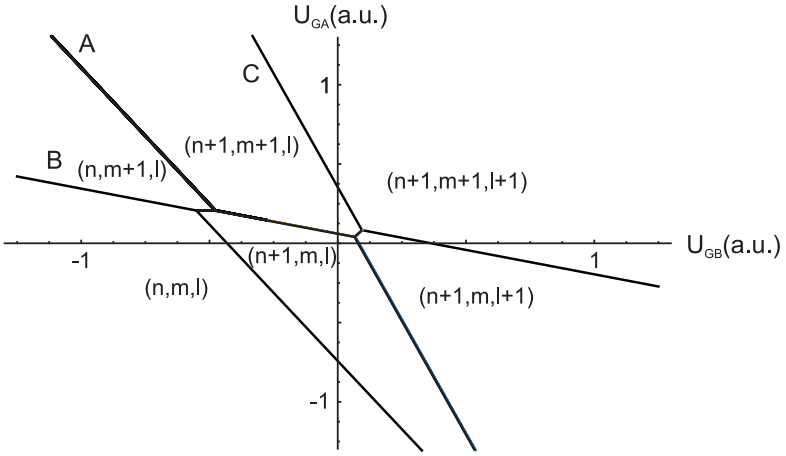

Figure 2.5: Calculated 2D cut of the stability diagram of a triple quantum dot system in dependence of U_{GA} and U_{GB}. The charging lines of dots A, B and C are marked with A, B, C, respectively.

A problem by calculating the chemical potentials following van der Wiel is, that the discretness of charge is not kept to full extent when substituting the charges Q by the voltages U in Eq. (2.41)-(2.43). This becomes evident when looking exemplarly at the expression for U_A (solving Eq.(2.41) by U_A):

$$U_\mathrm{A} = Q_\mathrm{A} + C_\mathrm{AB} \cdot U_\mathrm{B} + C_\mathrm{CA} \cdot U_\mathrm{C} + C_\mathrm{GA} \cdot U_\mathrm{GA}. \tag{2.51}$$

The voltage on dot A, U_A, depends continuously on the voltage at the gate coupled capacitively to the dot, U_GA. U_B is included via $C_\mathrm{AB} \cdot U_\mathrm{B}$. U_B depends linearly on U_GB. Consequently, U_A depends linearly on U_GB as well. However, U_A should only depend on Q_B, which does not depend continuously on U_GB. Using the continuous dot-voltages U_i ($i \in \{\mathrm{A,B,C}\}$) to calculate the other dot-voltages thus leads to the loss of discretness of charge, while there is no problem when directly calculating the energy. This problem becomes obvious for a system without cross-capacitances. While we expect the charging lines of a dot in a measured 2D cut through the stability diagram to be parallel to the axis where the gate voltage is varied the dot is not coupled to, we always obtain a finite slope in this model. One has to make sure that U_i does not follow the outer voltages $U_{\mathrm{G}j}$ with $j \in \{\mathrm{A,B,C}\}$ and $j \neq i$, continuously, but in a quantized manner because with continuous voltages there is an influence between the dots via $C_\mathrm{AB}, C_\mathrm{AC}, C_\mathrm{BC}$ even though the electron numbers on the dots do not change.

2.3.2 Transport properties

The conductance through the system oscillates in dependence of the relation between the chemical potentials μ_i of the dot to the chemical potentials of the leads $\mu_\mathrm{S}, \mu_\mathrm{D}$. If $\mu_\mathrm{N} \leq \mu_\mathrm{S}$ or $\mu_\mathrm{N} \leq \mu_\mathrm{D}$, there are electrons in the population of the 2D density of states of the source or of the drain which provide enough energy, μ_N, to populate the dot with N electrons. Transport through the dot is only possible if there is a chemical potential μ_N of the dot with $\mu_\mathrm{N} \leq \mu_\mathrm{S}$, $\mu_\mathrm{N} \geq \mu_\mathrm{D}$, or $\mu_\mathrm{N} \geq \mu_\mathrm{S}$, $\mu_\mathrm{N} \leq \mu_\mathrm{D}$, meaning when μ_N lies in the so-called transport window spanned by μ_S and μ_D. Otherwise, the transport is blocked as there are no electrons in the leads with enough energy to overcome the charging energy of the dot and no non-occupied states in the other lead. The Coulomb repulsion between the electrons leads to a restriction of tunneling onto the dot due to energy conservation and thus is responsible for the charging energy. This is why this blockade of transport is

known as Coulomb blockade. Consequently, for increasing detuning between μ_S and μ_D the energy levels of the dot successively enter the transport window. The current through the system in dependence of the detuning between μ_S and μ_D exhibits a step whenever a new dot energy level enters. The detuning of the chemical potentials of the leads is controlled by a bias voltage U_S. Another possibility to tune the conductance through the system is the variation of a gate voltage shifting the energy levels of the dot. It results in a current through the dot whenever an energy level of the dot is in the transport window. The differential conductance $G = \mathrm{d}I_{SD}/\mathrm{d}U_S$ exhibits a peak whenever an energy level of the dot comes into resonance with the source or drain chemical potential, $\mu_N = \mu_S$ or $\mu_N = \mu_D$. This makes the differential conductance G (in e^2/h) a good measurand to detect resonances in transport. At $T = 0\,\mathrm{K}$ this peak in the differential conductance is a delta peak. The conductivity $\mathcal{G}$ of one transport channel does not exceed $\mathcal{G}_0 = e^2/h$, where $\mathcal{G}_0$ is the conductance quantum.

The transport properties of a system are significantly affected by charging effects if the charging energy of the system is large compared to the thermal energy. [46] Consequently, for transport spectroscopy the thermal energy $k_B T$ has to be smaller than the energy level spacing of the dot, which is the charging energy E_C, in order to resolve the quantized states of the dot

$$k_B T << E_C = e^2/C_\Sigma. \tag{2.52}$$

Thus, for a good resolution at an achievable temperature small dots with a small sum capacitance C_Σ are necessary. When the temperature is very high, $E_C << k_B T$, the differential conductance through the system, G_{highT}, is simply given by the sum of the differential conductances across the two barriers (1,2) of the dot to the leads, $1/G_{highT} = 1/G_1 + 1/G_2$, independent of the dot size. Mesoscopic systems are sufficiently small to observe charging effects but also large enough to be easily coupled to macroscopic probes for application of voltages and current measurement of the system. For tunnel junctions with capacitances of the order of $10^{-15}\,\mathrm{F}$, which can easily be fabricated today, the charging energy of the system is around $E_C = 0.1\,\mathrm{meV}$, which corresponds to an energy scale of $E_C/k_B = 1\,\mathrm{K}$. Consequently, for structures of such size charging effects are significant in the transport properties for temperatures in the sub-kelvin regime. In case of quantum dots typical capacitances even reach values of the order of aF.

Additionally, the energy uncertainty has to be much smaller than the charging energy of the dot to observe effects showing the quantization of charge. With the Heisenberg uncertainty relation

$$\Delta E \Delta t = (e^2/C_\Sigma) R_t C > h \tag{2.53}$$

with the typical (dis-)charging time $\Delta t = R_t C_\Sigma$ of the dot it follows that the tunnel resistance R_t of the barriers between the dot and the leads has to be much larger than the resistance quantum,

$$R_t >> h/e^2 \cong 25.81\,\mathrm{k\Omega}, \tag{2.54}$$

in order to meet this criterion. [47] This can be fulfilled by coupling the dot weakly to the leads, so that weak tunneling through the system is obtained. If both Eq. 2.52 and 2.54 are fulfilled single electron effects, meaning effects regarding the quantization of charge, can be observed. *Sequential tunneling* through the system and Coulomb blockade are observed. This transport is described by the so-called orthodox theory which was developed by Averin and Likharev [48]. It treats electron tunneling in the first-order perturbation theory, where the transition rates in the system are described by Fermi's Golden rule. This transition rate for an electron from an energy state l on the dot to the state i in the leads in general form is

$$\Gamma_{i \leftarrow l} = 2\pi/\hbar |\, \langle i |\, \mathrm{H}' \,| l \rangle \,|^2 \rho \tag{2.55}$$

with $|\, \langle i |\, \mathrm{H}' \,| l \rangle \,|$ being the matrix element of the perturbation H' between final and initial state and ρ being the density of the final states. [49] Fermi's Golden rule gives the transition rate from an energy eigenstate of a system into a continuum of other energy eigenstates, caused by pertubation of the system. For the derivation of Fermi's Golden rule second-order perturbation in the tunnel Hamiltonian describing the electron tunneling between dot system and leads is taken into account. This results in first-order perturbation in the tunneling rates. The coupling to the leads is the perturbation of the system. The current through the dot arising from this single electron tunneling is then derived by a master equation ansatz taking into account the tunneling rates obtained by this first-order perturbation theory, which is described in sections 2.3.3.2 and 2.3.3.3.

Sequential tunneling is a non-coherent process, where the phase memory of the transmitted electron is lost due to inelastic scattering events inside the

quantum well during the transport. It can be described as a process where an electron tunnels from a lead into a quantum well, where it is scattered inelastically and possibly changes its energy, and then tunnels out through the lead on the other side. The tunneling events through the two barriers are considered as uncorrelated events. The conductance peak at resonance is decreased and broadened in case of inelastic scattering. [50] *Resonant tunneling* is present if the electron tunnels coherently from one lead across the quantum well to the other lead. [51, 52] The transmission peak is higher compared to sequential tunneling, as the back and forth propagating electron wave inside the quantum well can interfere constructively as it is coherent and forms the transmission peak (Fabry-Perot Interferometer analogon). When the time constant for this process τ_0 is smaller than the scattering time τ, and consequently the intrinsic resonance width $\Gamma_0 = \hbar/\tau_0$ being larger than the broadening due to the scattering, $\Gamma = \hbar/\tau$, as for instance with thin tunneling barriers, the condition for coherent tunneling is fulfilled. [50]

For $T > 0\,\mathrm{K}$ a broadened peak in the differential conductance instead of a delta peak is obtained. The reason is that the Fermi function of the leads is smeared out and the electronic states of the dot are broadened due to temperature. One can distinguish between two different transport regimes, the weak ($\hbar\Gamma << k_BT$) and the strong coupling regime ($k_BT \lesssim \hbar\Gamma$), with the dot-lead tunnel rate Γ. In the weak coupling regime the dot energy levels can be treated as delta peaks in the density of states. Two regimes can be distinguished, the classical Coulomb blockade regime, where $\Delta E << k_BT << E_C$ and the quantum Coulomb blockade regime, where $k_BT << \Delta E < E_C$, with ΔE being the excitation energy of the dot and E_C the dot charging energy. [47] While in the classical regime several energy levels can participate in transport due to thermal electron excitations, in the quantum regime only one energy level of the dot participates in transport. In the quantum regime the Coulomb peak has the form $G \propto \cosh^{-2}(\delta E/2k_BT)$, with δE being the energy level detuning. [47] Reason is that for high temperatures the temperature broadening of the leads is large compared to the intrinsic width of the electronic states of the dot. Consequently, by performing transport spectroscopy the well defined dot state scans the density of states of the leads and the Coulomb peak has the form of the derivation of the Fermi function at temperature T. At very low temperatures the Fermi function of the leads is approximately a step function. Now the intrinsic width of the energy state with finite lifetime τ

of the dot becomes important, as $k_B T \lesssim \hbar\Gamma$. The chemical potentials of the leads serve well as a testing energy for the broadened dot level. The Coulomb peak can be described by a Lorentzian function (Breit-Wigner distribution) of the form

$$G = \frac{2e^2}{h}(\hbar\Gamma)^2/((\hbar\Gamma)^2 + (\delta E)^2) \tag{2.56}$$

with $\Gamma = 1/\tau$ and the intrinsic half-width of the Lorentz peak $2\hbar\Gamma$ and a peak height at the resonance ($\delta E = 0$) of $2e^2/h$, the conductance quantum. [47] This formula applies for the case of $T = 0\,\mathrm{K}$. As a consequence for transport spectroscopy of the quantum dot energy levels low temperatures are used.

We distinguish between two different transport regimes defined by the current-voltage characteristic the dot exhibits. They are the linear and the non-linear transport regime and are described in the following.

2.3.2.1 Linear transport

The linear transport regime is defined as the parameter area in which the measured current is proportional to the applied bias voltage. This is fulfilled when the bias voltage is small compared to the thermal energy of the electrons $\Delta\mu_{\mathrm{SD}} << k_{\mathrm{B}}T$ [53, 54]. Then the conductance $\mathcal{G}$ of a dot is independent of the voltage so the current $I = \mathcal{G} \cdot U_S$ is linear.

For typical quantum dots E_{C} is in the order of some $100\,\mu\mathrm{eV}$ ($\equiv 1.16\,\mathrm{K}$). Thus $\Delta\mu_{\mathrm{SD}}$ has to be well below $100\,\mu\mathrm{eV}$ to achieve linear transport.

Figure 2.6 shows a schematic of linear transport through a quantum dot. The differential conductance $G = \mathrm{d}I_{\mathrm{SD}}/\mathrm{d}U_{\mathrm{S}}$ is plotted in dependence of a gate voltage U_{G1} and shows an equidistant sequence of the described Lorentzian shaped Coulomb peaks. For $\mu_{\mathrm{S}} = \mu_{\mathrm{D}}$ G equals the conductance through the dot. The distance between them is the constant charging energy of the dot. From the distance in gate voltage ΔU_{G} between the charging lines the capacitive coupling C_{G} between the dot and the gate can be calculated by

$$C_{\mathrm{G}} = \frac{e}{\Delta U_{\mathrm{G}}}. \tag{2.57}$$

If the dot is coupled to more than one gate, the Coulomb peaks can be displayed in a 2D-charging diagram (Fig. 2.6). The peaks become parallel charging lines. Their slope m can be expressed by

$$m = \frac{\Delta U_{G2}}{\Delta U_{G1}} = \frac{C_{G1}}{C_{G2}}. \tag{2.58}$$

It is the ratio between the two capacitive dot-gate couplings.

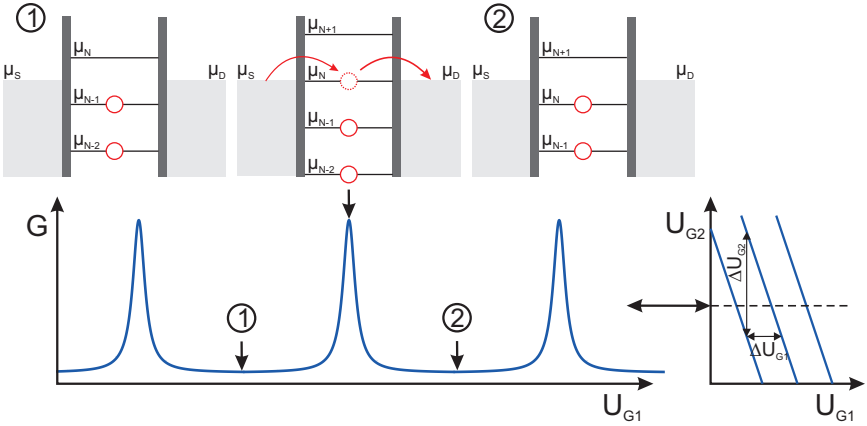

Figure 2.6: Schematic of linear transport through a single dot. If an energy level of the dot comes into resonance with the chemical potential of the leads, a Lorentz-peak in the conductance G of the system is obtained, which becomes a charging line in 2D. The slope given by the ratio between the respective dot-gate capacitive couplings.

2.3.2.2 Non-linear transport

Transport measurements with higher applied bias voltage U_S between source and drain exhibit a non-linear current-voltage characteristic. The reason is that excited states of the dot, and for a larger transport window even more than one ground state of the dot, play a role in transport. A staircase-like behavior in the current through the dot with a step for every new state entering the transport window is obtained. This step in current corresponds to a peak in differential conductance. If a dot energy level comes into resonance with the chemical potential of one of the leads a peak in the differential conductance is observed. In a diagram showing the differential

conductance in dependence of U_S and U_G straight resonance lines of high differential conductance for $\mu_N = \mu_S$ and $\mu_N = \mu_D$ are obtained. This results in a Coulomb-diamond-pattern as seen in Figure 2.7.

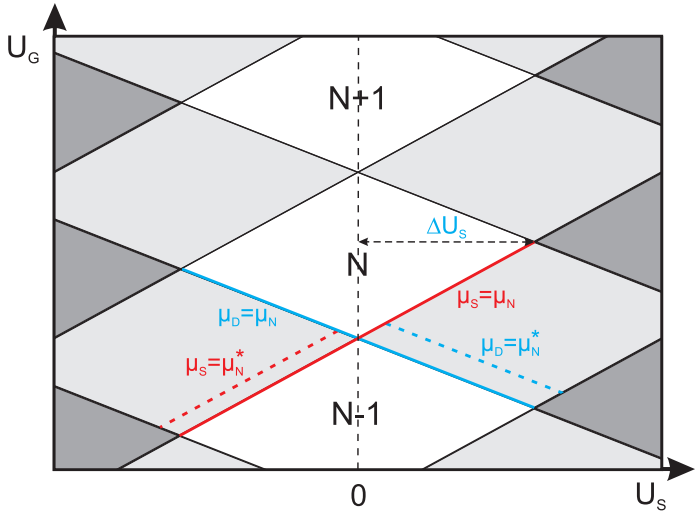

Figure 2.7: Schematic of non-linear transport through a single dot. Coulomb diamonds are formed by the charging lines of the resonances between leads and dot $\mu_S = \mu_N$ and $\mu_D = \mu_N$. Between the diamonds the electron number on the dot changes by one. Resonances between chemical potentials of the leads and excited states of the dot $\mu_S = \mu_N^*$ and $\mu_D = \mu_N^*$ appear as parallel lines to these. Via $e\Delta U_S = E_C$ the charging energy of the dot can be calculated from half the width of the Coulomb diamonds.

A cut at $U_S = 0$ shows the known resonances of the dot chemical potentials with the identical chemical potentials of source and drain. The resonances for each μ_N split into two for $|U_S| > 0$, a resonance with source and a resonance with drain. Thus, a sequence of diamonds for consecutive electron numbers $N, N+1, N+2,...$ is observed in direction of varied gate voltage. The slopes of the resonance lines with source result from the effect of U_S on the source potential and the capacitive influence of U_S on the dot energy levels, the slopes of the resonance lines with drain result from the capacitive influence of U_S on the dot energy levels only. The slopes of the resonance

line $\mu_N = \mu_S$ is

$$m = (C_\Sigma - C_S)/C_G \tag{2.59}$$

and the slope for $\mu_N = \mu_D$ is

$$m = -C_S/C_G. \tag{2.60}$$

Inside the Coulomb diamonds the transport window is smaller than the charging energy and no transport takes place. The dot is in Coulomb blockade. At the corners of the diamonds are the crossing points of the resonances $\mu_N = \mu_S$ and $\mu_N = \mu_D$. For the ones lying at $U_S = 0\,\mathrm{mV}$ we have $\mu_S = \mu_D = \mu_N$, as explained before. At the other two corners we have the condition $\mu_S - \mu_D = \mu_{N+1} - \mu_N$ and thus

$$e\Delta U_S = E_C. \tag{2.61}$$

In these points and in the dark gray marked area in Fig. 2.7 two ground states lie in the transport window and participate in transport. Half the width of a Coulomb diamond corresponds to the charging energy E_C of the dot. Outside the Coulomb diamonds, in the light grey regions in Fig. 2.7, there is one ground state energy level of the dot inside the transport window.

In the non-Coulomb-blocked regions excited states of the dot can participate in transport as well. The resonances of source and drain with the excited state μ_N^* lead to the same crossing pattern as for the ground states. However, they are only visible when μ_N lies inside the transport window. As the distance between the ground state μ_N and its excited state μ_N^* is the quantum mechanical level spacing $\Delta\varepsilon_N$, the resonances of μ_N^* with the leads occur as a parallel line in distance of $\Delta\varepsilon_N$ from the resonances of the ground state μ_N. In the region where $eU_S < E_C$ ground and corresponding excited state can not be occupied simultaneously. This leads to a small resonance peak for the excited state.

A stability diagram with constant $U_S > 0$ in dependence of two gate voltages is a cut through the Coulomb diamond diagram for a certain $U_S > 0$. Consequently, it shows parallel double lines. Each double line originates from a charging line at zero bias split into two lines, one line for resonance μ_N with the source lead, the other with the drain lead. The distance between them depends on the bias voltage.

2.3.2.3 Cotunneling

In single electron tunneling as treated before the tunnel rate is derived from first order perturbation theory and given by Fermi's Golden rule Eq. (2.55). In the Coulomb blockade regime of a dot single electron tunneling is exponentially suppressed, as the first-order tunnel current decreases exponentially with the detuning [55, 56]. In this regime higher order tunnel processes gain relevance. They become especially important if the tunneling barriers are so small that their tunnel resistance lies in the order of h/e^2. In this case the requirement $R_t >> h/e^2$ (Eq. (2.54)) for single electron tunneling and charge quantization effects is not satisfied anymore. When R_t is approaching the value of h/e^2 quantum fluctuations cause broadening of the energy levels which leads to more charge transfer channels. Higher order tunneling gains importance, called cotunneling [46, 57]. Due to these quantum fluctuations in macroscopic charge a finite tunneling current can flow although the dot is in Coulomb blockade and first order tunnel processes are forbidden due to the energy conservation law. Taking into account second-order perturbation theory results in a transition rate Γ_{co} for cotunneling electrons. The underlying tunnel process can be considered as tunneling through the Coulomb energy barrier. As this barrier stems from the interaction of a macroscopically large number of electrons, the tunneling through the barrier is sometimes also referred to as macroscopic quantum tunneling of charge [55, 56, 58]. The tunneling process leads to a decay of the Coulomb blockade energy barrier. The cotunneling process is described in general as follows. The electron virtually tunnels through a charge state which is energetically forbidden as it lies at a certain energy E above the chemical potentials of the leads. The tunneling process occurs on a short time scale allowed by the time-energy uncertainty relation (Eq. (2.53)). For instance, for a forbidden charge state at energy $E = e^2/(2C_\Sigma)$ in the middle between two Coulomb peaks the maximum allowed time scale for the virtual process is $t = h/E$. E decreases to zero towards the Coulomb peaks.

One distinguishes between elastic and inelastic cotunneling. In the elastic tunneling process only one electron tunnels and the inelastic process is described as two different electrons involved in the tunneling sequence. Sometimes the term *co*-tunneling is only used for the inelastic tunneling, as it refers to two tunneling electrons.

An elastic tunneling process can be described as one electron tunneling in and out of a virtual state of the quantum dot. This process is possible while first-order single-electron tunneling over a non-virtual state of the dot is forbidden due to Coulomb blockade. These processes already take place close to equilibrium where the bias voltage is arbitrarily low and does not exceed the energy difference between ground and excited state ΔE of the dot ($e\,|U_\mathrm{S}| < \Delta E$) and small temperatures ($k_\mathrm{B}T < E_\mathrm{C}$). Elastic cotunneling is always occurring. It manifests itself in the tails of lifetime-broadened Coulomb peaks and is thus also responsible for the residual conductance between the peaks [46, 59]. An electron from a state below the chemical potentials of the leads tunnels to the drain lead, leaving the dot in a virtual state (N-1). It is immediately replaced by an electron from the source lead. This is called the hole-like process. Another possible process is that an electron tunnels from the source lead to a state of the dot lying above the chemical potentials of the lead and immediately tunnels out to the drain lead. During this process the dot is in a virtual (N+1)-state. It is called the electron-like process. Initial and final state of the system have the same energy. This is why the tunneling process is called elastic. The process is shown schematically in Fig. 2.8. Elastic cotunneling is a coherent process, where at least two tunneling processes are coherent, so that coherent transport from source lead to drain lead is possible. It only dominates for small temperatures and small bias voltages.

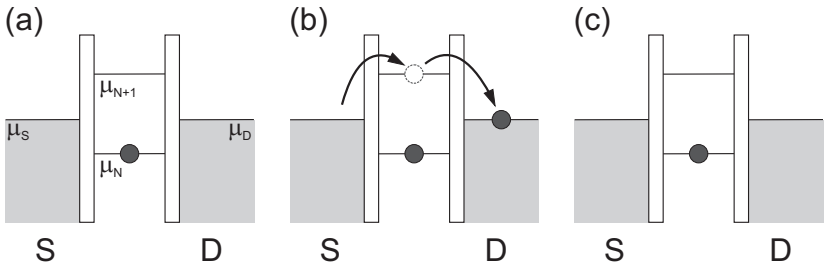

Figure 2.8: Schematic showing the elastic tunneling process via the virtual (N-1)-state of the dot. The process using the virtual (N+1)-state is analogous with the dot energy level detuned above the chemical potentials of the leads.

Inelastic cotunneling appears if the dot is driven out of equilibrium by a

bias voltage equal to or larger than the energy difference between ground state and excited state of the dot, $e\,|U_\mathrm{S}| \geq \Delta E$. It also dominates for $k_\mathrm{B}T > \Delta E$. Two different electrons are involved in the process. There are two cotunneling channels, a hole-like process and an electron-like process which both contribute to the cotunneling current. An electron tunnels from a ground state of the dot which is located below the chemical potentials of the leads to the drain lead and within a very short time scale another electron tunnels from the source lead to the excited state of the dot. As the first electron tunnels out of the dot, violating the energy conservation law for a very short time allowed by the Heisenberg uncertainity principle another one tunnels into the dot, so that the energy is conserved for the whole process (hole-like process). For a short time interval the QD is in an intermediate virtual state with an energy which lies outside the classically allowed range. The virtual intermediate state of the dot is an (N-1)-state. The energy difference $\mu_\mathrm{D} - \mu_\mathrm{N}$ is called blockade energy for this process. [59] This tunneling sequence can be switched which results in the electron-like process. In this case an electron tunnels first from the source lead to a ground state of the dot located above the chemical potentials of the leads and another electron tunnels from an excited state of the dot to the drain lead. The virtual intermediate state of the dot is then an (N+1)-state. The blockade energy is $\mu_{\mathrm{N}+1} - \mu_\mathrm{S}$. [59] Both processes are depicted schematically in Fig. 2.9. These two cotunneling processes are called inelastic as they leave the dot in an excited state.

The dot relaxes into ground state by sequential tunneling, photon emission, or another cotunneling process. In contrast to elastic tunneling processes inelastic cotunneling is an incoherent process. Inelastic cotunneling is seen in transport through the quantum dot as a finite current onset at $e\,|U_\mathrm{S}| \geq \Delta E$ inside the Coulomb diamond, a current step parallel to the $U_\mathrm{S} = 0\,\mathrm{mV}$ axis. At the diamond boundary it intersects the line corresponding to first-order tunneling at the resonance of a lead with an excited state of the dot inside the single-electron tunneling region. This becomes obvious considering the energy configurations.

The cotunneling rate $\Gamma_\text{inel-co}$ for the inelastic cotunneling process can be derived analogously to the tunneling rate for sequential tunneling, and starting with Fermi's Golden rule describing first-order sequential tunneling (Eq. (2.55)). The total matrix element for the two-electron tunneling process

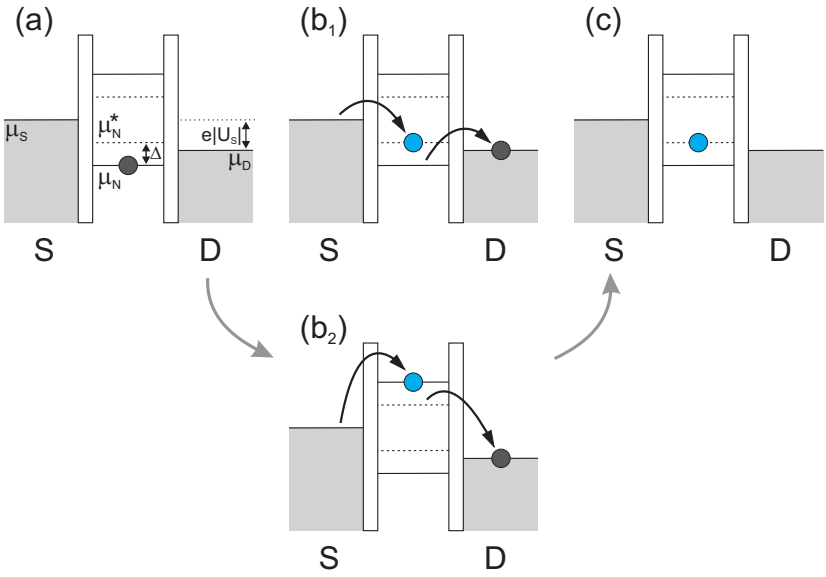

Figure 2.9: Schematic showing the inelastic tunneling process over the virtual dot state (N-1) (b_1) (hole-like process) and the virtual dot state (N+1) (b_2) (electron-like process). Both contribute to the inelastic cotunneling current.

$$\langle i|\,\mathrm{H}'\,|l\rangle = T^{(1)}T^{(2)}\left(\frac{1}{\Delta E_1}\frac{1}{\Delta E_2}\right) \tag{2.62}$$

consists of the matrix elements $T^{(1)}$ and $T^{(2)}$ for the tunneling through the first and the second barrier, respectively, and a factor taking into account the energy difference between the initial and the virtual state ΔE. The electron can go via two different virtual states, as described above, one with the energy difference ΔE_1 referring to the electron tunneling into the dot first (electron-like process), and the other one described by ΔE_2 referring to the electron tunneling out of the dot first (hole-like process). Following Eq. (2.55) one obtains for the cotunneling rate between two states l and i [55]

$$\Gamma^{\text{inel-co}}_{i\leftarrow l} = \frac{2\pi}{\hbar}\left|T^{(1)}\right|^2\left|T^{(2)}\right|^2\left(\frac{1}{\Delta E_1}+\frac{1}{\Delta E_2}\right)^2\delta\left(E_i - E_l\right). \tag{2.63}$$

Inelastic cotunneling is an incoherent process, so the total tunneling rate $\Gamma_{\text{total}}^{\text{inel-co}}$ through the dot is obtained by summing up the rates for the tunneling processes, weighted by the Fermi function, over all possible initial and final states afterwards. The cotunneling current for $T \neq 0$ is derived from the total tunneling rate $\Gamma_{\text{total}}^{\text{inel-co}}$ by a summation of the currents induced by the forward (+) and backward total tunneling rate (-)

$$I_{\text{inel-co}} = e\left(\Gamma_{\text{total}}^{\text{inel-co},(+)} - \Gamma_{\text{total}}^{\text{inel-co},(-)}\right). \tag{2.64}$$

Consequently, the inelastic cotunneling conductance $(I_{\text{inel-co}}/U_{\text{S}})$ is expressed by [56]

$$G_{\text{inel-co}} = \frac{\hbar G_1 G_2}{12\pi e^2}\left(\frac{1}{E_1} + \frac{1}{E_2}\right)^2 \left[(eU_{\text{S}})^2 + (2\pi k_{\text{B}}T)^2\right] \tag{2.65}$$

with E_1 (E_2) being the energy associated with adding (removing) an electron to (from) the dot ($E_1 + E_2 \approx E_{\text{C}}$) and G_1 (G_2) is the conductance through the left (right) tunneling barrier of the dot. The inelastic cotunneling current thus rises linearly with the inverse energies for tunneling in and out of the dot and with the product of conductances through the tunneling barriers. It additionally strongly depends on the bias voltage and temperature and vanishes for $U_{\text{S}} \to 0$ and $T \to 0$, as there is no energy available for excitations of the dot.

The tunneling rate for elastic cotunneling has to be derived by perturbation theory in the tunnel Hamiltonians describing the electron tunneling across the barriers [55], as it is a coherent process where the approach for the derivation of the inelastic current, where the rates corresponding to different energy states are summed up incoherently, is not applicable. Fourth order perturbation in the tunnel Hamiltonian results in a second-order perturbation in the tunneling rate. One obtains for the elastic cotunneling conductance $(I_{\text{el-co}}/U_{\text{S}})$ [56]

$$G_{\text{el-co}} = \frac{\hbar G_1 G_2 \Delta}{4\pi e^2}\left(\frac{1}{E_1} + \frac{1}{E_2}\right). \tag{2.66}$$

The parameter Δ^{-1} is the electronic denisity of states of the leads. The formula is valid for small dots where the electrons go through a virtual state of the dot, as the time the electron classically needs to cross the dot is small compared to the time the electron stays in the virtual state ($t = h/E$). The

elastic cotunneling current thus also rises linearly with the inverse energies for tunneling in and out of the dot and with the product of the conductances through the tunneling barriers.

In general, the detuning between dot and leads determines the strength of the cotunneling current. The appearance of cotunneling itself is independent of the detuning.

2.3.2.4 Multiple quantum dots

A multiple quantum dot system consists of $N > 1$ quantum dots in close proximity to one another, so that coupling effects between the dots play a role. There are various arrangement and coupling possibilities in a multiple quantum dot system, as seen in Fig. 2.10. The most basic coupling possibility between the dots is the pure capacitive coupling which is caused by the classical electrostatic repulsion, the Coulomb repulsion, between the dots. Additionally, the dots can be tunnel coupled. The tunnel coupling between the dots is caused by an inter-dot finite overlap of the electronic wave functions of the electrons. The arrangement of the dots in transport can thus be a parallel circuit, a series circuit, or combinations of both.

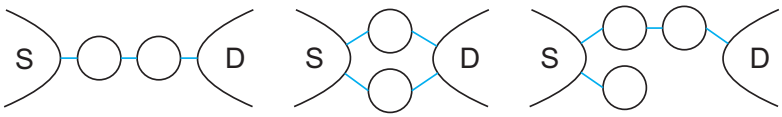

Figure 2.10: Examples of different dot configurations: linear, parallel and a combination of both, where two tunnel coupled dots are in series configuration and another dot is capacitively coupled to these dots. The inter-dot- and dot-lead capacitive coupling is present due to the small spacial range in the setups. The additional tunnel coupling between the dots and between dots and leads is depicted as a line between the dots.

The appearance of the stability diagram of a multiple quantum dot system depends on this coupling between the dots. A system of n quantum dots has an n-dimensional charging diagram. Analogously to a gate voltage influencing the potential of a quantum dot capacitively, the potential is also influenced capacitively by the potential of a nearby dot. The capacitive coupling raises linearly with the inverse distance between the dots. The

potential of a quantum dot (2) gives rise to the shift of the chemical potentials of a capacitive coupled other dot (1). With a capacitive coupling of C_{12} between the dots the chemical potential μ_1 of dot (1) shift by

$$\Delta\mu_1 = -eQ_2 \frac{C_{12}}{C_{\Sigma 1} C_{\Sigma 2}} \tag{2.67}$$

according to Eq. (2.31). The difference between the potential of a gate and the potential of a quantum dot is that the potential of the gate is varied continuously with applied voltage, whereas the potential of a quantum dot depends on the electron number on the dot. The potential of the dot is the sum of the potentials of each electron on the dot and as the dot is charged in a quantized manner, the potential is quantized, too. So only when the charging energy is overcome and dot 2 is charged, the potential of dot 2 is changed and this shifts the potential of dot 1.

For the described double dot system the stability diagram is two-dimensional. It shows the differential conductance through the system in dependence of two gate voltages. For a parallel dot configuration the charging of each dot is marked by a line of finite differential conductance. The slope of the lines depend on the ratio between the respective dot-gate capacitive couplings. As the lines have different slopes they cross each other, meaning there are points in the stability diagram where more than one dot is in resonance with source and drain. At theses points the dots themselves are in resonance. Both dots are charged at this point. At the resonance between two dots the resulting shift in the chemical potential of dot 1 due to the capacitive coupling of dot 2 is Eq. (2.67) with $Q_2 = e$:

$$\Delta\mu_1 = -e\,(\pm e)\,\frac{C_{12}}{C_{\Sigma 1} C_{\Sigma 2}} \tag{2.68}$$

The factor $\pm e$ denotes the charging and decharging of dot 2 with one electron. Analogously $\Delta\mu_2$ for dot 2 is calculated. Consequently, the gate voltages at which the dot level is in resonance with the leads shift, so we obtain a shift in the charging lines of both dots with respect to the gate voltages. Altogether a hexagonal pattern of charging lines is obtained. This shift due to the capacitive coupling between the dots is depicted schematically in Figure 2.11. As the charging lines of both dots shift due to this interaction, we obtain a splitting with two crossing points which connect three different charging configurations. These two points are thus called triple points. Across the

connection line between the triple points, named charge reconfiguration line, the total charge of the system is constant and there is charge transfer between the quantum dots only. Along this line the dots are in resonance with each other. In a system with two serial dots being negligibly tunnel coupled, there is finite conductance through the system only at these two points. For purely capacitively coupled parallel dots coupled to the same leads the stability diagram shows transport in the full hexagonal pattern. When only one dot (1) is connected to both leads and the other one (2) is capacitively coupled to it and only tunnel coupled to source so it can be charged, the stability diagram shows the full charging lines of the single dot (1), but with shifts in gate voltage marking the charging of dot (2). The charging of dot (2) is not directly seen as no transport through the dot is possible.

Using Eq. (2.31) with inserted Eq. (2.68) the shift of the charging line of dot 1 in gate voltage U_{G1} due to $\Delta\mu_1$ can be calculated by

$$\Delta U_{\mathrm{G1},1} = \pm e \frac{C_{12}}{C_{\mathrm{G1},1} C_{\Sigma 2}}, \tag{2.69}$$

where $C_{\mathrm{G1},1}$ is the capacitive coupling between gate G_1 and dot (1). The shift of the charging line regarding other gate voltages (e.g. $\Delta U_{\mathrm{G2},2}$ in Fig. 2.11) is calculated analogously, as well as the shifting of the charging lines of the other dot. Thus, in this example the inter-dot capacitive coupling C_{12} can be calculated by reading the shift $\Delta U_{\mathrm{G1},1}$ from the stability diagram and knowing $C_{\mathrm{G1},1}$ and $C_{\Sigma 2}$.

In the non-linear transport regime, we get an overlay, a combination of the Coulomb diamonds of the different dots depending on the coupling arrangement of the dots for varying bias voltage and a gate voltage. For serial multiple dots, as there is only transport when all three dots are in resonance, the smallest Coulomb diamonds, which are the ones of of the biggest dot, are modulated by the bigger Coulomb diamonds. A sawtooth-like pattern emerges. In case of quantum dots in a parallel circuit the Coulomb diamond of the dots are lying on top of each other without interacting. Transport inside a diamond of one Coulomb blockaded dot is still possible when an energy level of another dot is inside the transport window.

In case of constant bias voltage the stability diagram shows lines along

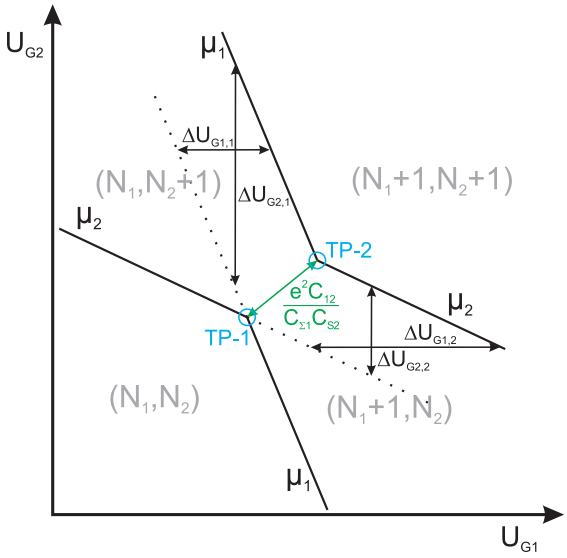

Figure 2.11: Schematic stablity diagram for capacitively coupled quantum dots. The shift of the charging lines of dot 1 and 2 in gate voltage by $\Delta U_{\mathrm{G1,1}}$, $\Delta U_{\mathrm{G2,1}}$ and $\Delta U_{\mathrm{G1,2}}$, $\Delta U_{\mathrm{G2,2}}$, respectively due to the capacitive coupling between the dots leads to two triple points TP-1 and TP-2. They connect three charge configurations of the system.

which the chemical potentials of dot (1) and (2) are aligned, $\mu_{\mathrm{N},1} = \mu_{\mathrm{N},2}$, instead of triple points (see Fig. 2.12). They span the rhombic feature which arises where the described double lines for the single dots with $\mu_{\mathrm{N},1} = \mu_{\mathrm{S}}$, $\mu_{\mathrm{N},1} = \mu_{\mathrm{D}}$ and $\mu_{\mathrm{N},2} = \mu_{\mathrm{S}}$, $\mu_{\mathrm{N},2} = \mu_{\mathrm{D}}$ cross each other. These two lines with $\mu_{\mathrm{N},1} = \mu_{\mathrm{N},2}$ are the only lines where transport over ground states of the dot is possible in serial dot configuration. Adjacent triangular regions above and below these triple lines are formed where $\mu_{\mathrm{N},1}$ and $\mu_{\mathrm{N},2}$ lie inside the transport window. In the upper triangle $\mu_{\mathrm{N},1} \leq \mu_{\mathrm{N},2}$ and in the lower triangle $\mu_{\mathrm{N},1} \geq \mu_{\mathrm{N},2}$. In these regions inelastic tunneling processes are possible, giving rise to transport. Transport is visible in the upper triangle for $U_{\mathrm{S}} > 0$ (gray marked areas in Fig. 2.12) and in the lower triangle for $U_{\mathrm{S}} < 0$. Resonances between the dots involving excited states are visible inside the triangles as lines parallel to the triple lines.

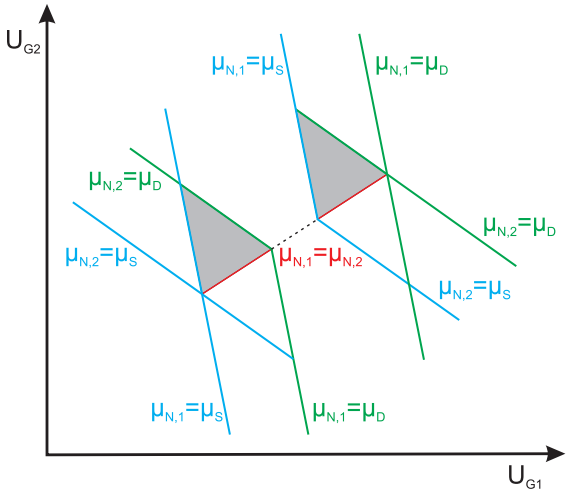

Figure 2.12: Schematic stablity diagram for capacitively coupled double quantum dots showing the influence of an applied bias voltage $U_S > 0$. Ground state resonances of dots 1 and 2 with the source (marked in blue) and the drain lead (marked in green) result in twice as many resonance lines than for $U_S = 0$ (see Fig. 2.11). The triplepoints have evolved to triple lines (marked in red) along which $\mu_{N,1} \geq \mu_{N,2}$. Above and below these lines triangular regions are formed. Inside these regions $\mu_{N,1}$ and $\mu_{N,2}$ lie inside the transport window. For $U_S > 0$ transport is possible inside the upper triangles (grey colored areas) due to inelastic processes. In this area resonances involving excited states of the dots can be seen in transport as lines parallel to the triple lines.

For a system of three quantum dots the stability diagram is three-dimensional. A model of such a stability diagram calculated by the electrostatic model described in section 2.3.1 is shown in Figure 2.13. In order to measure the full stability diagram three gate voltages have to be varied, one for each dot. Instead of charging lines, we have charging planes and at their crossing line the respective two dots are in resonance. In the middle of the stability diagram, where all three planes cross, we get a plane (yellow in Fig. 2.13) along which all three dots are in resonance. In a triple dot system we have quadruple points, where four charge configurations meet. In a general case six quadruple points exist at a triple dot resonance. Four of them span a plane of rhomboidal shape and two points lie above and below (Fig. 2.13,

insert). This plane separates two charge states of the system. Across the plane the system is charged by one electron and the electron number of each of the dots changes by one. This internal charge rearrangement combined with the charging of the whole system by one electron is only possible across this plane and unique for a quantum dot system with $N \geq 3$ dots. In a triple quantum dot system the states connected by the plane are (1,0,0) and (0,1,1), (0,1,0) and (1,0,1), or (0,0,1) and (1,1,0), depending on the capacitive arrangement of the dots [19]. The process is called quantum cellular automata (QCA) process and is a crucial element in quantum information processing.

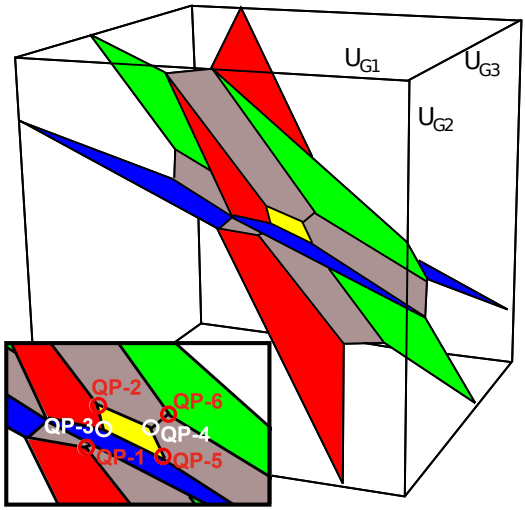

Figure 2.13: Model of the three-dimensional stability diagram of a TQD in dependence of three different gate voltages U_{G1}, U_{G2}, U_{G3}. Each plane marks the charging of one of the dots. At the crossing line of two planes the respective two dots are in resonance, and where in the center of the model all three planes meet, a plane (yellow) is formed, across which QCA processes are possible. The insert shows the central region with the QCA plane and the location of the six quadruple points QP-1 - QP-6. [19]

For reasons of clarity and to simplify data presentation and analysis, usually a two dimensional cut through the three-dimensional stability diagram is measured. Thus, to show the development of a triple dot resonance as

the joining of two double dot resonances, one spacial direction has to be quantized by measuring several cuts at different gate voltages, scanning the three-dimensional space. In such a stability diagram the resonance between all three dots is reflected by the crossing of all three charging lines.

In Figure 2.14 schemes of parallel two-dimensional cuts through the stability diagram of a TQD system are shown measured for different gate voltages. Figure 2.14 (a) shows the anticrossings of three double dot resonances. With varying the third gate voltage the double dot resonances shift with respect to each other until they align, as shown in Fig. 2.14 (b). Here, all three dots are in resonance. The triple points have developed into quadruple points. In principle, four quadruple points can be seen in such a cut by choosing a measurement plane with the appropriate cutting angle, as they lie in one plane. The total number of quadruple points is marked in the full 3D stability diagram (Fig. 2.13) for comparison. However, in general not all of these four quadruple points are perfectly crossed by a measurement plane. In this case they are not or poorly seen in the stability diagram. The stability regions (1,0,1) and (0,1,0) only coexist at a triple dot resonance, otherwise only one of them is visible. The transition between these two regions is a QCA process. In case of larger gate voltage the triple dot resonance splits up again into three double dot resonances, see Fig. 2.14 (c).

Tunnel coupling

The described transport between the dots is only allowed by a finite tunnel coupling between two dots in the first place. The tunnel coupling results from a finite overlap between the electron wave functions of the different dots lying close to each other. The electrons of the dots are moving in the dots' joint potential, comparable to the electronic bonding situation of atoms in molecules. This is why multiple tunnel coupled quantum dots are also called artificial molecules in extension to artificial atoms for single dots. The wave function overlap allows the electron transfer between the dots.

Starting from a double dot system with two separate dots (1) and (2), described by a Hamiltonian H_0. The eigenstates of these two non-coupled dots are $|\phi_1\rangle$ and $|\phi_2\rangle$ with eigenenergies E_1 and E_2. When a tunnel coupling is introduced between the dots described by a tunnel matrix T, with

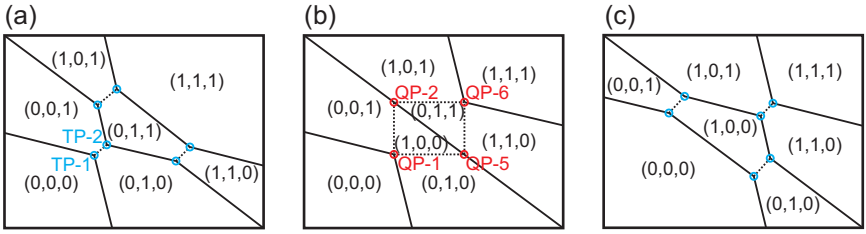

Figure 2.14: Schematics of a 2D cut through the stability diagram in dependence of two gate voltages. From (a) to (c) a third gate voltage is swept in steps and the double dot resonances are shifted with respect to each other. (a) Three double dot resonances and the stability region (0,1,1) are visible. (b) The double dot resonances align to a triple dot resonance. Only then both stability regions (0,1,1) and (1,0,0) are visible. Four quadruplepoints QP-1, QP-2, QP-5, QP-6 are depicted here, corresponding to the ones marked in Fig. 2.13. Only four of them can be measured simultaneously by choosing the appropriate 2D measurement plane. (c) For further sweeping of the third gate voltage we again have three double dot resonances, this time with the stability region (1,0,0).

$$T = \begin{pmatrix} 0 & t \\ t & 0 \end{pmatrix} \tag{2.70}$$

and the tunnel amplitude t, the system is described by the Hamiltonian $\mathrm{H} = \mathrm{H}_0 + \mathrm{T}$ with the two delocalized eigenstates $|\Psi_\mathrm{A}\rangle$ and $|\Psi_\mathrm{B}\rangle$ with eigenvalues E_A and E_B. These two wave functions of the electron in the joint potential of the two dots are the superposition of the single electron wave function ϕ_1 and ϕ_2, so there is an symmetric superposition state, $|\Psi_\mathrm{A}\rangle$, and an anti-symmetric superposition state, $|\Psi_\mathrm{B}\rangle$:

$$\begin{aligned} \Psi_\mathrm{A} &= c_1 \cdot (\phi_1 + \phi_2) \\ \Psi_\mathrm{B} &= c_2 \cdot (\phi_1 - \phi_2) \end{aligned} \tag{2.71}$$

with the coefficients c_1, c_2 resulting from normalization. The corresponding eigenenergies E_A and E_B described in terms of the two single dot eigenvalues E_1 and E_2 are [44, 57]

$$E_{\mathrm{A}} = \frac{E_1 + E_2}{2} + \sqrt{\frac{1}{4}\left(E_1 - E_2\right)^2 + t^2}$$
$$E_{\mathrm{B}} = \frac{E_1 + E_2}{2} - \sqrt{\frac{1}{4}\left(E_1 - E_2\right)^2 + t^2} \tag{2.72}$$

with the separation between them being

$$\Delta E = \sqrt{\left(E_1 - E_2\right)^2 + (2t)^2}. \tag{2.73}$$

The state with lower energy is called bonding state and the one with higher energy anti-bonding state. It follows, that in case of resonance ($E_1 = E_2$) the distance between the atomic states and the molecular states is the tunnel amplitude t and the distance between the bonding and anti-bonding state is the tunnel splitting $2t$. Thus, the stronger the tunnel coupling between the dots, the larger the splitting. For decreasing tunnel coupling the distance between the two molecular states decreases and they more and more resemble localized states. In resonance both wave functions have the same weight and the wave function is delocalized over both dot potentials in equal measure. By detuning the states by energy $\delta E = E_1 - E_2$ one of the single dots becomes more weight then the other. The bigger the detuning δE between E_1 and E_2, the better the molecular states approximate the atomic states as the overlap of the wave functions is decreasing. In this case the coupling between them is only weakly affecting the two systems. [57] Figure 2.15 shows a schematic of the original single-dot wave function and the resulting bonding and anti-bonding states for two resonant states.

The new energies for the molecular states Ψ_0 for zero electrons on the molecule, Ψ_{A}, Ψ_{B} and Ψ_2 for two electrons on the molecule, lead to different chemical potentials. The transition $\Psi_0 \rightarrow \Psi_{\mathrm{B}}$ is described by $\mu_{0\rightarrow B}$ and the transition $\Psi_{\mathrm{B}} \rightarrow \Psi_2$ by $\mu_{B\rightarrow 2}$. The same applies for the same transitions involving the anti-bonding state. The chemical potentials for the atomic and the molecular states in comparison in dependence of the detuning δ between the dots are depicted in Figure 2.16. The chemical potentials $\mu_{0\rightarrow B}$ and $\mu_{B\rightarrow 2}$ for the bonding state are represented by the lower and upper black solid line, respectively, and the chemical potentials $\mu_{0\rightarrow A}$ and $\mu_{A\rightarrow 2}$ for the anti-bonding state are represented by the lower and upper black dashed line, respectively.

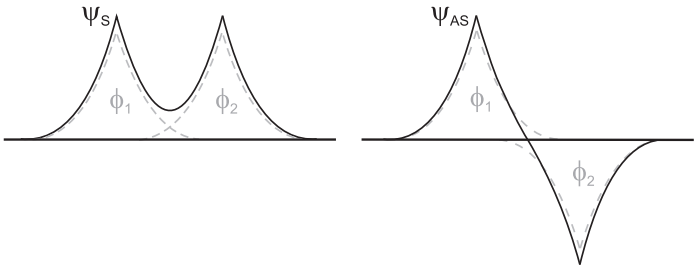

Figure 2.15: Schematic of the superposition of two electronic wave functions and the resulting bonding (left) and anti-bonding (right) states. One superposition case leads to a finite electron probability density in the middle of the two potentials, a bonding state. The probability is zero in the other superposition case, the anti-bonding state.

For a non-zero tunnel coupling an additional energy splitting of t at each of the triple points at the resonance between the states appears. Therefore the total tunnel splitting is $2t$. Far from the resonance the additional tunnel coupling is not affecting the energies of the states. As a consequence a rounding of the meeting charging lines at the triple points is occurring in the stability diagram for a tunnel coupled dot system. This is shown in the schematic of the stability diagram of a tunnel coupled double quantum dot in Figure 2.17 (a). For increasing tunnel coupling the energy spectrum of the states approaches the spectrum of one big single dot formed out of the two dots. For decreasing tunnel coupling the energy spectrum of the double dot approaches the spectrum of two single dots. Hence the stability diagrams for very big and very small inter-dot tunnel coupling resemble the ones for one big single dot and two capacitively coupled single dots, respectively.

Figure 2.17 (b) shows the stability diagram for a tunnel coupled double dot with applied bias voltage $U_S > 0\,\mathrm{mV}$. The resonances of the dot states with the leads split into two resonances, one with the source and one with the drain lead, analogously to the case for a purely capaitively coupled dot system (Fig. 2.12). If the bias voltage is large enough, not only the ground state resonances $\mu_{0\to B} = \mu_S$, $\mu_{0\to B} = \mu_D$, and $\mu_{B\to 2} = \mu_S$, $\mu_{B\to 2} = \mu_D$ are visible in transport, but the resonances of the excited state of the molecule,

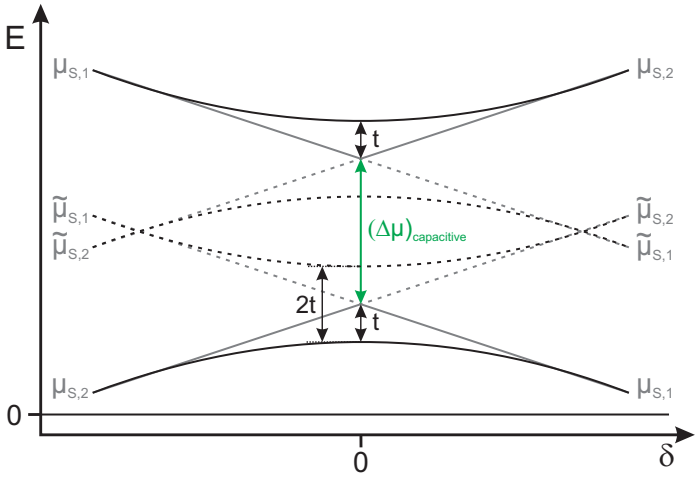

Figure 2.16: Chemical potentials for a double dot system (dot (1), dot (2)) at a resonance for pure capacitive inter-dot-coupling (grey; $\mu_{S,1} \equiv \mu_S = \mu_1$ and $\mu_{S,2} \equiv \mu_S = \mu_2$) and with additional tunnel coupling between the dots (solid black) in dependence of the detuning between the dots. The solid black lines are the symmetric superposition binding states, the ground states of the double dot molecule. The dashed grey lines ($\tilde{\mu}$) are excited states of the single dots, where the electron is on one dot, although the other would be energetic more favourable, dashed black lines are the antisymmetric states, which are also excited. At resonance the additional splitting caused by the tunnel coupling reaches its maximum $2t$.

the anti-bonding state, with the leads appear as well. They become visible in transport as differential conductance lines being roughly parallel to the ground state resonance lines and thus transversely to the axis of the charge reconfiguration line.

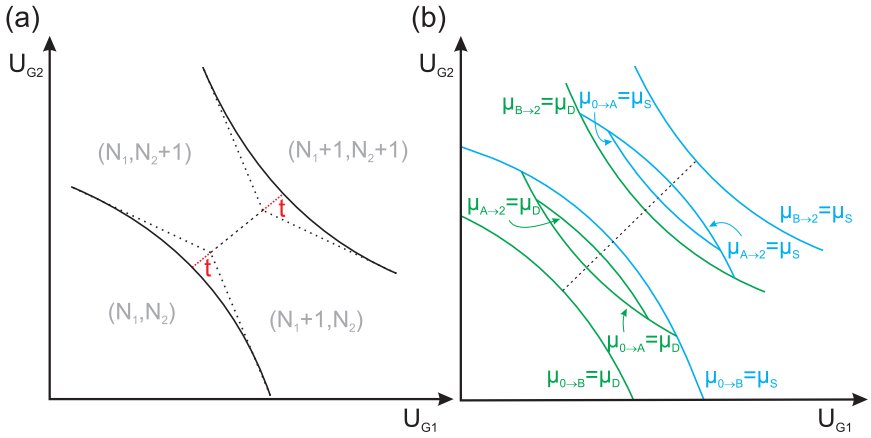

Figure 2.17: (a) Schematic stability diagram for tunnel coupled double quantum dots. The charging lines of the dots are represented by solid lines for the case of a non-zero tunnel coupling and by dotted lines for the case of no tunnel coupling for comparison. The crossing points of the charging lines obtain a rounded shape due to the additional tunnel splitting which has its maximum value of $2t$ at the triple points. (b) Schematic stablity diagram for tunnel coupled double quantum dots with a bias voltage $U_S > 0\,\mathrm{mV}$. The ground state resonances with the leads split into two separate resonances with source (blue lines) and drain (green lines). Resonances of the anti-bonding excited state of the double dot molecule with source and drain are also seen in transport if the bias voltage is large enough for them to lie inside the transport window as well.

2.3.3 Quantum mechanical model

2.3.3.1 Introduction to density matrix formalism and master equation

The *Master equation* is a first order differential equation which describes the time evolution of probabilities of random events as a stochastic evolution. It is intrinsic for quantum systems. Thus, for the time evolution of a system described by a statistical mixture of states the determining equation is the Master equation. [60]

Often, and also within the scope of this work, the considered problems involve a small system S of interest which is in contact with a larger environment R, e.g. a reservoir (Fig. 2.18). This setup is the general description used for treating open quantum systems.

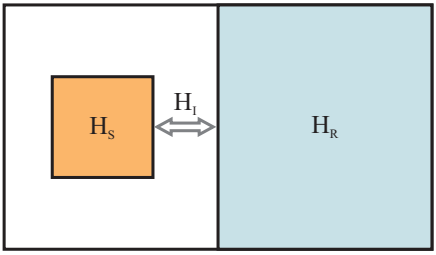

Figure 2.18: Schematic of a small system S (with Hamiltonian H_S) coupled to a larger reservoir R (with Hamiltonian H_R). The interaction is described by the Hamiltonian H_I.

We consider a system S, which is described by the Hamiltonian H_S, coupled to a reservoir R, which is described by the Hamiltonian H_R. The interaction between the systems, considered by the Hamiltonian H_I, is assumed to be weak. The Hamiltonian H for the whole system is

$$H = H_S \otimes \mathbb{I} + \mathbb{I} \otimes H_R + H_I. \tag{2.74}$$

The system Hamiltonian $H_S \in \mathcal{H}_S$ only acts on the system Hilbert space $\mathcal{H}_S$ and the reservoir Hamiltonian $H_R \in \mathcal{H}_S$ only acts on the reservoir Hilbert space $\mathcal{H}_R$. The interaction Hamiltonian $H_I \in \mathcal{H}_S \otimes \mathcal{H}_R$ acts on both Hilbert spaces and can be decomposed as

$$\mathrm{H_I} = \sum_\alpha A_\alpha \otimes B_\alpha \tag{2.75}$$

with the coupling operators $A_\alpha \in \mathcal{H}_\mathrm{S}$ and $B_\alpha \in \mathcal{H}_\mathrm{R}$.

We introduce the total density operator $\rho(t)$ of the whole system, with an ensemble of eigenstates $|\psi_n\rangle$ of H. p_n is the probability of the whole system to be in state $|\psi_n\rangle$, with $0 \leq p_n \leq 1$ and $\sum_n p_n = 1$. The density operator is

$$\rho = \sum_n p_n \left|\psi_n\right\rangle \left\langle\psi_n\right| . \tag{2.76}$$

It describes the system as a statistical mixture of states $\{\psi_n\}$. For instance, mixed superpositions of states are formed if the system of interest is coupled to an environment like in measurement problems and transport. The diagonal elements of the density matrix fulfill the normalization condition $\mathrm{Tr}\rho = \Sigma_n p_n \mathrm{Tr}\left\{|\psi_n\rangle \langle\psi_n|\right\} = 1$. If the system is in a pure state $\rho^2 = \rho$ and $\mathrm{Tr}\rho^2 = 1$ and if the system is in a mixed state $\rho^2 \neq \rho$ and $\mathrm{Tr}\rho^2 < 1$.

The diagonal elements for an orthonormal basis $\{|\phi_i\rangle\}$ are

$$\rho_{ii} = \langle\phi_i|\rho|\phi_i\rangle = \sum_n p_n \langle\phi_i|\psi_n\rangle \langle\psi_n|\phi_i\rangle = \sum_n p_n \left|c_{ni}\right|^2 \tag{2.77}$$

with $c_{ni} = \langle\psi_n|\phi_i\rangle$. They represent the occupations, which are the probability of finding the system in the state $|\phi_i\rangle$.

The off-diagonal elements

$$\langle\phi_j|\rho|\phi_i\rangle = \sum_n p_n \langle\phi_j|\psi_n\rangle \langle\psi_n|\phi_i\rangle = \sum_n p_n c_{nj}^* c_{ni} \tag{2.78}$$

are the coherences. $|\psi_n\rangle$ is a coherent superposition of $|\phi_i\rangle$, thus ρ_{ij} is in general non-zero. Consequently, their time evolution describes the coherent dynamics and interference effects in the system. The equation of motion (von-Neumann equation) [61] for the total density operator is

$$\frac{\partial\rho(t)}{\partial t} = -\frac{i}{\hbar}\left[\mathrm{H_S} \otimes \mathbb{I} + \mathbb{I} \otimes \mathrm{H_R} + \mathrm{H_I}, \rho\right] . \tag{2.79}$$

The von-Neumann equation describes the time evolution of the density

matrix. It is convenient to consider the interaction picture which treats the interaction as a pertubation of the Hamiltonian $\mathrm{H}_0 = \mathrm{H_S} \otimes \mathbb{I} + \mathbb{I} \otimes \mathrm{H_R}$. After transformation to the interaction picture it follows with the interaction Hamiltonian

$$\begin{aligned} \mathrm{H_I}(t) &= e^{+i(\mathrm{H_S}+\mathrm{H_R})t} \mathrm{H_I} e^{-i(\mathrm{H_S}+\mathrm{H_R})t} \\ &= e^{+i\mathrm{H_S}t} A_\alpha e^{-i\mathrm{H_S}t} \otimes e^{+i\mathrm{H_R}t} B_\alpha e^{-i\mathrm{H_R}t} \end{aligned} \tag{2.80}$$

and with the density matrix

$$\rho_\mathrm{I}(t) = e^{+i(\mathrm{H_S}+\mathrm{H_R})t} \rho(t) e^{-i(\mathrm{H_S}+\mathrm{H_R})t} \tag{2.81}$$

the von-Neumann equation

$$\frac{\partial \rho_\mathrm{I}(t)}{\partial t} = -\frac{i}{\hbar} \left[\mathrm{H_I}(t), \rho_\mathrm{I}(t)\right]. \tag{2.82}$$

As we will stay in the interaction picture we will identify $\rho_\mathrm{I} \equiv \rho$ for reasons of notation simplification.

The time-dependent Schrödinger equation

$$i\hbar \frac{\partial}{\partial t} |\psi_n(t)\rangle = \mathrm{H}(t) |\psi_n(t)\rangle \tag{2.83}$$

describes the special case of the time evolution of a system being in a pure state ψ_n at an initial time t_0. It can be derived from the time evolution of the corresponding density operator.

In case of composed systems one often wants to study the evolution of only one of the systems. In these cases it is not necessary to have the information of the total system in the density matrix but the information on the particular subsystem only, in our example system S. A density matrix which encodes the information on one subsystem is called the *reduced density matrix*. We introduce the reduced density operator $\rho_\mathrm{S}(t)$ for the system S by

$$\rho_\mathrm{S}(t) = \mathrm{Tr_R}\left[\rho(t)\right] \tag{2.84}$$

where $\mathrm{Tr_R}$ means that we trace over the reservoir variables.

In order to find the equation of motion for the reduced density matrix analogous to Eq. (2.82), we perform the partial trace over the reservoir variables and obtain from Eq. (2.82)

$$\begin{aligned}\frac{\partial \rho_{\mathrm{S}}(t)}{\partial t} =& -i\mathrm{Tr}_{\mathrm{R}}\left\{[\mathrm{H}_{\mathrm{I}}(t),\rho_0]\right\} \\ &- \int_t^0 \mathrm{Tr}_{\mathrm{R}}\left\{[\mathrm{H}_{\mathrm{I}}(t),[\mathrm{H}_{\mathrm{I}}(t'),\rho(t')]]\,\mathrm{d}t'\right\}.\end{aligned} \tag{2.85}$$

When S and R are initially uncorrelated at time $t = 0$, we can factorize the initial total density matrix $\rho(0)$

$$\rho(0) = \rho_{\mathrm{S}}(0) \otimes \rho_{\mathrm{R}} \tag{2.86}$$

with ρ_{R} being the density operator of the reservoir. When the reservoir R is large it is negligibly affected by the presence of the system S. Hence only S is affected by the interaction and R remains in equilibrium. This means there will be no or negligible reaction of R on S. With $\mathrm{H}_{\mathrm{I}}(t) = O\{\lambda\}$, while λ is a small dimensionless pertubation parameter we obtain

$$\rho(t) = \rho_{\mathrm{S}}(t) \otimes \rho_{\mathrm{R}} + O\{\lambda\}. \tag{2.87}$$

All higher orders in perturbation theory are neglected as they have a smaller effect. This approximation is called **Born-approximation** and accounts for the irreversibility of the interaction process. Inserting Eq. (2.87) in the equation of motion for the reduced density matrix Eq. (2.85) we obatain

$$\begin{aligned}\frac{\partial \rho_{\mathrm{S}}(t)}{\partial t} =& -i\mathrm{Tr}_{\mathrm{R}}\left\{[\mathrm{H}_{\mathrm{I}}(t),\rho_0]\right\} \\ &- \int_t^0 \mathrm{Tr}_{\mathrm{R}}\left\{[\mathrm{H}_{\mathrm{I}}(t),[\mathrm{H}_{\mathrm{I}}(t'),\rho_{\mathrm{S}}(t') \otimes \rho_{\mathrm{R}}]]\,\mathrm{d}t'\right\} + O\left\{\lambda^3\right\}.\end{aligned} \tag{2.88}$$

With the interaction Hamiltonian H_{I} decomposed as Eq. (2.75) we get

$$\begin{aligned}\frac{\partial \rho_{\mathrm{S}}(t)}{\partial t} = &- i \sum_{\alpha} A_{\alpha}(t)\rho_{\mathrm{S}}(0)\mathrm{Tr}\left\{B_{\alpha}(t)\rho_{\mathrm{R}}\right\} \\ &+ i \sum_{\alpha} \rho_{\mathrm{S}}(0)A_{\alpha}(t)\mathrm{Tr}\left\{\rho_{\mathrm{R}}B_{\alpha}(t)\right\} \\ &- \sum_{\alpha\beta} \int_{0}^{t} \left[A_{\alpha}(t)A_{\beta}(t')\rho_{\mathrm{S}}(t')\mathrm{Tr}\left\{B_{\alpha}(t)B_{\beta}(t')\rho_{\mathrm{R}}\right\}\right. \\ &- A_{\alpha}(t)\rho_{\mathrm{S}}(t')A_{\beta}(t')\mathrm{Tr}\left\{B_{\alpha}(t)\rho_{\mathrm{R}}B_{\beta}(t')\right\} \\ &- A_{\beta}(t')\rho_{\mathrm{S}}(t')A_{\alpha}(t)\mathrm{Tr}\left\{B_{\beta}(t')\rho_{\mathrm{R}}B_{\alpha}(t)\right\} \\ &\left.+\rho_{\mathrm{S}}(t')A_{\beta}(t')A_{\alpha}(t)\mathrm{Tr}\left\{\rho_{\mathrm{R}}B_{\beta}(t')B_{\alpha}(t)\right\}\right] \mathrm{d}t'.\end{aligned} \tag{2.89}$$

Without loss of generality the expectation value of a single coupling operator is zero

$$\mathrm{Tr}\left\{B_{\alpha}(t)\rho_{\mathrm{R}}\right\} = 0 \tag{2.90}$$

and we define the reservoir correlation function $C_{\alpha\beta}$ by

$$C_{\alpha\beta} = \mathrm{Tr}\left\{B_{\alpha}(t_1)B_{\beta}(t_2)\rho_{\mathrm{B}}\right\}. \tag{2.91}$$

Consequently we obtain from for the equation of motion for the reduced density matrix

$$\begin{aligned}\frac{\partial \rho_{\mathrm{S}}(t)}{\partial t} = &- \sum_{\alpha\beta} \int_{0}^{t} \mathrm{d}t' \left[C_{\alpha\beta}(t,t')\left[A_{\alpha}(t),A_{\beta}(t')\rho_{\mathrm{S}}(t')\right]\right. \\ &\left.+C_{\beta\alpha}(t',t)\left[\rho_{\mathrm{S}}(t')A_{\beta}(t'),A_{\alpha}(t)\right]\right].\end{aligned} \tag{2.92}$$

In order to solve this equation for a general case further approximations have to be made. We assume that the correlation time is much shorter in the reservoir than the time in which system S is significantly damped due to the interaction with the reservoir, so that the reservoir correlation functions decay much quicker than the density matrix varies. Thus, there is no influence of the past time on the evolution of the system. Memory is not preserved and consequently the time derivative of the density matrix only depends on its present value and not on former times t':

$$\rho_{\mathrm{S}}(t') \approx \rho_{\mathrm{S}}(t) \tag{2.93}$$

For the same reason we can furthermore extend the upper integration bound in the equation of motion to infinity to remove time dependence. With the substitution $\tau = t - t'$ we obtain from Eq. (2.88) with including Eq. (2.90)

$$\frac{\partial \rho_{\mathrm{S}}(t)}{\partial t} = -\int_0^\infty \mathrm{Tr}_{\mathrm{B}} \left\{ [\mathrm{H}_{\mathrm{I}}(t), [\mathrm{H}_{\mathrm{I}}(t-\tau), \rho_{\mathrm{S}}(t) \otimes \rho_{\mathrm{R}}]] \right\} d\tau. \tag{2.94}$$

This is the Markovian master equation. Equation (2.93) and the extention of the intergration bound are called the first and second **Markov-approximation**, respectively. In the Schrödinger picture the Markovian master equation reads

$$\begin{aligned} \frac{\partial \rho_{\mathrm{S}}(t)}{\partial t} =& -i\,[\mathrm{H}_{\mathrm{S}}, \rho_{\mathrm{S}}(t)] \\ & - \sum_{\alpha\beta} \int_0^\infty C_{\alpha\beta}(\tau) \left[A_\alpha, e^{-i\mathrm{H}_{\mathrm{S}}\tau} A_\beta e^{+i\mathrm{H}_{\mathrm{S}}\tau} \rho_{\mathrm{S}}(t) \right] d\tau \\ & - \sum_{\alpha\beta} \int_0^\infty C_{\beta\alpha}(-\tau) \left[\rho_{\mathrm{S}}(t) e^{-i\mathrm{H}_{\mathrm{S}}\tau} A_\beta e^{+i\mathrm{H}_{\mathrm{S}}\tau}, A_\alpha \right] d\tau \\ =& -i\,[\mathrm{H}_{\mathrm{S}}, \rho_{\mathrm{S}}(t)] + M_\Gamma. \end{aligned} \tag{2.95}$$

The Master equation of Lindblad form can be written as

$$\frac{\partial \rho_{\mathrm{S}}(t)}{\partial t} = \mathcal{L}\rho(t) \tag{2.96}$$

with $\mathcal{L}$ being the Liouvillian superoperator containing all information about the system. In order to obtain a Lindblad type master equation from Eq. (2.95) for the general case, the **secular approximation** has to be applied, meaning to perform a long-time average so that terms that are quickly oscillating in time are neglected.

2.3.3.2 Example of a single quantum dot

In order to demonstrate how the Liouvillian is set up and the current through the system are calculated, we consider a system consisting of one single quantum dot. For transport through a single dot classical rate equations are used. First we consider the dot coupled to one fermionic lead with a tunnel rate Γ as the simplest example. The quantum dot has one single level at energy ε. The energy level can be occupied by one electron only due to strong Coulomb repulsion, so no spin is considered in the following. The occupation of the dot varies depending on the Fermi energy of the lead. The Fermi function of the lead at energy ε is $f(\varepsilon)$. The system is depicted schematically in Fig. 2.19.

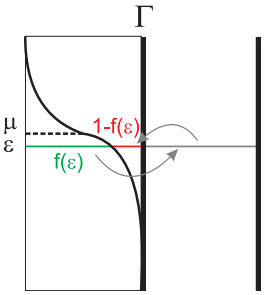

Figure 2.19: Schematic of a single dot coupled to one tunnel junction by Γ. The occupation of the lead is described by the Fermi distribution function f at temperature T. μ denotes the chemical potential of the lead and the dot level is at energy ε.

The transition rate Γ^+ for electrons tunneling from lead to dot is the tunneling rate Γ weighted by the probability to have an electron of the required energy in the lead which can tunnel onto the dot, $\Gamma^+ = \Gamma f(\varepsilon)$. The inverse transition rate for electrons leaving the state is $\Gamma^- = \Gamma(1 - f(\varepsilon))$, so one has to multiply the tunneling rate with the the probability to have a corresponding hole in the lead. The transition rate between dot and lead is given by Fermi's Golden rule, which is for incoming electrons to the dot system

$$\Gamma^{(+)} = 2\pi/\hbar|\gamma|^2 f(\mu - \varepsilon) \tag{2.97}$$

and electrons leaving the dot to the lead

$$\Gamma^{(-)} = 2\pi/\hbar|\gamma|^2\,[1 - f(\mu - \varepsilon)] \tag{2.98}$$

Thus, it is $\Gamma = 2\pi/\hbar\,|\gamma|^2$ with the hopping parameter γ. The probability that the dot is occupied with one electron at time $t + \Delta t$ is $\Gamma \Delta t f(\varepsilon)$.

The classical master equations are classical rate equations for the two states of the dot, $|0\rangle$ and $|1\rangle$. They are

$$\begin{aligned} \dot{\rho}_{00} &= -\Gamma f(\varepsilon)\rho_{00} + \Gamma(1 - f(\varepsilon))\rho_{11} \\ \dot{\rho}_{11} &= +\Gamma f(\varepsilon)\rho_{00} - \Gamma(1 - f(\varepsilon))\rho_{11}, \end{aligned} \tag{2.99}$$

with the occupation probabilities ρ_{00} and ρ_{11} of the dot being empty or charged by one electron, respectively.
The Liouvillian becomes

$$\mathcal{L} = \begin{pmatrix} -\Gamma f & +\Gamma(1-f) \\ +\Gamma f & -\Gamma(1-f) \end{pmatrix}. \tag{2.100}$$

In case of a single level of a quantum dot coupled to two leads with different Fermi distribution functions due to different chemical potentials or temperature the Liouvillian has to be extended. The energy level of the dot lies at an energy ε in the transport window between the chemical potentials of the leads. We have $\Gamma^{+} = \Gamma^{+}_{0\leftarrow \mathrm{L}} + \Gamma^{+}_{0\leftarrow \mathrm{R}}$ for electron transitions onto the dot containing the rates $\Gamma^{+}_{0\leftarrow i} = \Gamma_i f_i(\varepsilon)$, with lead $i \in \{\mathrm{L},\mathrm{R}\}$, and $\Gamma^{-} = \Gamma^{-}_{\mathrm{L}\leftarrow 0} + \Gamma^{-}_{\mathrm{R}\leftarrow 0}$ for electron transitions off the dot with the rates $\Gamma^{-}_{i\leftarrow 0} = \Gamma_i(1 - f_i(\varepsilon))$. The tunnel rates are $\Gamma_{\mathrm{L}} = 2\pi/\hbar\,|\gamma_{\mathrm{L}}|$ and $\Gamma_{\mathrm{R}} = 2\pi/\hbar\,|\gamma_{\mathrm{R}}|$ for the coupling to the left and right lead, respectively, and the Fermi functions $f_{\mathrm{L}}(\varepsilon) = f_{\mathrm{L}}(\mu_{\mathrm{L}} - \varepsilon)$ and $f_{\mathrm{R}}(\varepsilon) = f_{\mathrm{R}}(\mu_{\mathrm{R}} - \varepsilon)$ for the left and right lead, respectively. μ_{L} and μ_{R} are the chemical potentials of the left and right lead, respectively. We get for the equations of motion for the two states of the dot, $|0\rangle$ and $|1\rangle$, expressed with the rates Γ_{L} and Γ_{R}

$$\begin{aligned} \dot{\rho}_{00} =& (-\Gamma_{\mathrm{L}} f_{\mathrm{L}}(\varepsilon) - \Gamma_{\mathrm{R}} f_{\mathrm{R}}(\varepsilon))\rho_{00} \\ &+ (\Gamma_{\mathrm{L}}(1 - f_{\mathrm{L}}(\varepsilon)) + \Gamma_{\mathrm{R}}(1 - f_{\mathrm{R}}(\varepsilon)))\rho_{11} \\ \dot{\rho}_{11} =& (+\Gamma_{\mathrm{L}} f_{\mathrm{L}}(\varepsilon) + \Gamma_{\mathrm{R}} f_{\mathrm{R}}(\varepsilon))\rho_{00} \\ &- (\Gamma_{\mathrm{L}}(1 - f_{\mathrm{R}}(\varepsilon)) + \Gamma_{\mathrm{R}}(1 - f_{\mathrm{R}}(\varepsilon)))\rho_{11}. \end{aligned} \tag{2.101}$$

and consequently for the Liouvillian

$$\mathcal{L} = \begin{pmatrix} -\Gamma_{\mathrm{L}} f_{\mathrm{L}}(\varepsilon) - \Gamma_{\mathrm{R}} f_{\mathrm{R}}(\varepsilon) & +\Gamma_{\mathrm{L}}(1 - f_{\mathrm{L}}(\varepsilon)) + \Gamma_{\mathrm{R}}(1 - f_{\mathrm{R}}(\varepsilon)) \\ +\Gamma_{\mathrm{L}} f_{\mathrm{L}}(\varepsilon) + \Gamma_{\mathrm{R}} f_{\mathrm{R}}(\varepsilon) & -\Gamma_{\mathrm{L}}(1 - f_{\mathrm{R}}(\varepsilon)) - \Gamma_{\mathrm{R}}(1 - f_{\mathrm{R}}(\varepsilon)) \end{pmatrix}.$$

The stationary current is calculated with $\dot{\rho}_{ij}(t) = 0$. Consequently $\dot{\rho}_{00} = \dot{\rho}_{11}$. Solving the equation for ρ_{11} and using the normalization condition $\rho_{00} + \rho_{11} = 1$ results in

$$\rho_{11} = \frac{\Gamma_{\mathrm{L}} f_{\mathrm{L}} + \Gamma_{\mathrm{R}} f_{\mathrm{R}}}{\Gamma_{\mathrm{L}} + \Gamma_{\mathrm{R}}} \tag{2.102}$$

The current through the system is proportional to the occupation of the dot, in case of a multiple dot system of the dot coupled to the drain. Thus we have in this case

$$I = e\Gamma_{\mathrm{R}}\rho_{11} \tag{2.103}$$

With Eq. (2.102) this gives for the stationary current

$$I = e\frac{\Gamma_{\mathrm{R}}\Gamma_{\mathrm{L}} f_{\mathrm{L}} + \Gamma_{\mathrm{R}}^2 f_{\mathrm{R}}}{\Gamma_{\mathrm{L}} + \Gamma_{\mathrm{R}}} \tag{2.104}$$

In case of a high bias voltage $\mu_{\mathrm{L}} >> \varepsilon >> \mu_{\mathrm{R}}$ driving the electron current from left to right lead we have $\Gamma_{0\mathrm{L}} = \Gamma_{\mathrm{R}0} = 0$, as the Fermi functions for a large (infinite) bias voltage are $f_{\mathrm{L}} = 1$ and $f_{\mathrm{R}} = 0$. The only non-zero tunneling rates are the ones for electrons tunneling from left to right. With these values for the Fermi functions we obtain from Eq. (2.104) for the current through a system with infinite bias

$$I_{\mathrm{inf.bias}} = e\frac{\Gamma_{\mathrm{R}}\Gamma_{\mathrm{L}}}{\Gamma_{\mathrm{L}} + \Gamma_{\mathrm{R}}}. \tag{2.105}$$

2.3.3.3 Example of serial double quantum dots

Transport through a tunnel coupled multiple quantum dot system can be approximated with classical master equations if the tunnel coupling is very low. For strong tunnel coupling compared to the inter-dot energy level detuning the electrons are delocalized over the dot system and the states resemble molecular states rather than localized atomic states and a bonding and anti-bonding state results with distance $2t$ between them, with

t being the tunneling amplitude between the dots (see section 2.3.2.4). Thus, in case of appreciable tunnel coupling between the dots, phase-coherent tunneling through the dot system is dominating. These coherent effects from the inter-dot tunneling have then to be taken into account in the master equations. The larger the detuning between the energy levels of the dots, the less the electrons occupying the states are delocalized. The inter-dot tunneling rate is exponentially suppressed. For a large energy level detuning compared to the inter-dot tunnel coupling the energy states can be approximated as localized states. The distance Δ between the hybridized states in dependence of energy level detuning Δ_{AC} and inter-dot tunnel coupling τ_{AC} is (see Eq. (2.73))

$$\Delta = \sqrt{\Delta_{\mathrm{AC}}^2 + 4\tau_{\mathrm{AC}}^2}. \tag{2.106}$$

The transport through a multiple quantum dot is described by a quantum master equation instead of a classical rate equation, where the superposition between the states of the two dots are included. The system is conveniently described in a molecular (delocalized) basis, which is derived from the atomic (localized) one by basis transformation. For a double dot system instead of the basis states $|\mathrm{L}\rangle$ and $|\mathrm{R}\rangle$ describing the occupation of the left and right dot with one electron, respectively, the basis states now are the molecular states named Ψ_1 and Ψ_2 in the following for the electron being delocalized between the dots. The density matrix is then diagonal, as the basis states now contain the coherences between the dot states. [62]

In the following two examples are presented showing how to derivate and solve a Master equation for a double dot system with infinite and small bias voltage.

Infinite bias voltage
In case of infinite bias, or a weak coupling between the dots and the leads compared to the inter-dot coupling, $\Gamma < \tau$, however, the system can be treated in a localized basis and the transport can be reduced to the description by classical rate equations. An approximation of the transport in the localized basis of the system is also applicable for a large energy level detuning between the dots, as the molecular states resemble atomic states for a large level detuning. If the bias voltage is finite, one has to take into account the energy difference between the localized dot states and the delocalized molecular states coupling to the density of states of the leads.

The Fermi function then can not be regarded as 1 for the source and 0 for the drain (for non-zero temperature) and the exact energetic position of the dot states plays a role.

For a double quantum dot in the infinite bias regime with a tunnel coupling t_{LR} between the dots and a lead coupled to the left dot with Γ_{L} and a lead coupled to the right dot with Γ_{R} the master equations in the localized basis are [63]

$$\begin{aligned}
\dot{\rho}_{00} &= -\Gamma_{\mathrm{L}}\rho_{00} + \Gamma_{\mathrm{R}}\rho_{\mathrm{RR}} \\
\dot{\rho}_{\mathrm{LL}} &= \Gamma_{\mathrm{L}}\rho_{00} - it_{\mathrm{LR}}\rho_{\mathrm{RL}} + it_{\mathrm{LR}}\rho_{\mathrm{LR}} \\
\dot{\rho}_{\mathrm{RR}} &= -\Gamma_{\mathrm{R}}\rho_{\mathrm{RR}} - it_{\mathrm{LR}}\rho_{\mathrm{LR}} + it_{\mathrm{LR}}\rho_{\mathrm{RL}} \\
\dot{\rho}_{\mathrm{LR}} &= i\varepsilon\rho_{\mathrm{LR}} - \frac{1}{2}\Gamma_{\mathrm{R}}\rho_{\mathrm{LR}} - it_{\mathrm{LR}}\rho_{\mathrm{RR}} + it_{\mathrm{LR}}\rho_{\mathrm{LL}}
\end{aligned} \tag{2.107}$$

where ρ_{LL} (ρ_{RR}) is the probability of the left (right) dot being occupied by one electron, ε is the detuning between the dot energy levels. With $\dot{\rho}_{00} = \dot{\rho}_{\mathrm{LL}} = \dot{\rho}_{\mathrm{RR}} = 0$ the stationary state is calculated by the normalization condition $\rho_{00} + \rho_{\mathrm{RR}} + \rho_{\mathrm{LL}} = 1$. From this the stationary current is obtained by $I = e\Gamma_{\mathrm{R}}\rho_{\mathrm{RR}}$. This gives the Lorentzian resonance current peak of the form [63]

$$I = \frac{I_0 W^2}{W^2 + \varepsilon^2} \tag{2.108}$$

and the height of the peak

$$I_0 = e\Gamma_{\mathrm{L}}\Gamma_{\mathrm{R}}\frac{4t_{\mathrm{LR}}^2}{4t_{\mathrm{LR}}^2(\Gamma_{\mathrm{R}} + 2\Gamma_{\mathrm{L}}) + \Gamma_{\mathrm{L}}\Gamma_{\mathrm{R}}^2} \tag{2.109}$$

and the half width at half maximum

$$W^2 = \frac{4t_{\mathrm{LR}}^2(\Gamma_{\mathrm{R}} + 2\Gamma_{\mathrm{L}}) + \Gamma_{\mathrm{L}}\Gamma_{\mathrm{R}}^2}{4\Gamma_{\mathrm{L}}}. \tag{2.110}$$

Small bias voltage

As a short example of derivating and solving such a Master equation for a specific open quantum system, the case of two tunnel-coupled serial quantum dots with one lead attached to each dot will be written down in detail. Up to two electrons are allowed in the system. The system is studied in the

regime of small bias analogous to the triple dot experiment discussed in this thesis. A schematic of this system is shown in Fig. 2.20.

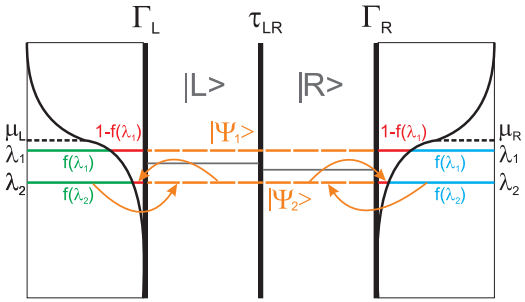

Figure 2.20: Schematic of a serial double dot with the left and right dot coupled each to a tunnel junction with the tunneling rates Γ_L and Γ_R, respectively and an inter-dot tunnel coupling τ_LR. The occupation of the lead is described by the Fermi function f at temperature T. μ_L and μ_R denote the chemical potentials of the leads and λ_1 and λ_2 denote the eigenenergies of the coherent states Ψ_1 and Ψ_2, respectively. $|\mathrm{L}\rangle$ and $|\mathrm{R}\rangle$ are the single dot states.

The left and right dot have a tunnel junction to their lead with the tunneling rate Γ_L and Γ_R, respectively. The electronic occupation of the lead is well described by the Fermi distribution function f at a certain temperature T. The leads have the chemical potential μ_L and μ_R which lie close to each other due to very small bias.

Due to the tunneling rate Γ to the leads, the occupation of the dots will fluctuate depending on the chemical potential of the lead. The transition rate between dot $i \in \{\mathrm{L},\mathrm{R}\}$ and lead $l \in \{\mathrm{L},\mathrm{R}\}$ is calculated by Fermi's Golden rule, analogously to the single dot example Eq. (2.97)

$$\Gamma^{(+)}_{i\leftarrow l} = 2\pi/\hbar|\gamma_l|^2 f(\mu_l - \varepsilon_i) \tag{2.111}$$

for incoming electrons to the dot system, with the Fermi distribution function $f(\alpha) = 1/(e^{-\alpha/(k_\mathrm{B}T)}+1)$ and the hopping parameter γ_l with $2\pi/\hbar\,|\gamma_l|^2 = \Gamma_l$. The hopping parameter γ_l is given in energy units. So, we have for the transition rate $\Gamma^+ = \Gamma f(\varepsilon)$. The tunneling rate Γ is weighted by the probability to have an electron of the required energy in the lead which can tunnel onto the dot. The inverse transition rate for electrons leaving the

state is $\Gamma^- = \Gamma(1 - f(\varepsilon))$. This corresponds to Fermi's Golden rule (Eq. (2.97))

$$\Gamma^{(-)}_{l \leftarrow i} = 2\pi/\hbar |\gamma_l|^2 [1 - f(\mu_l - \varepsilon_i)]. \tag{2.112}$$

The dot system Hamiltonian H_0 reads

$$\mathrm{H}_0 = \left[\begin{array}{c|cc|c} 0 & 0 & 0 & 0 \\ \hline 0 & \varepsilon_\mathrm{L} & \tau & 0 \\ 0 & \tau & \varepsilon_\mathrm{R} & 0 \\ \hline 0 & 0 & 0 & \varepsilon_\mathrm{L} + \varepsilon_\mathrm{R} + V \end{array}\right] \tag{2.113}$$

containing the energies ε_L and ε_R of the left and right dot, respectively, the tunnel coupling between the dots τ and the inter-dot electron Coulomb interaction V. As we want to analyze the system in the vicinity of zero bias, we have to work in the delocalized basis. Thus, the Hamiltonian needs to be diagonalized. The middle section of H_0 is not diagonal yet and has to be diagonalized by $\mathrm{H}_\Psi = D\mathrm{H}_0 D^+$ so that we can work in the coherent basis. For the case of the dots being in resonance one has $\varepsilon_\mathrm{L} = \varepsilon_\mathrm{R} = \varepsilon$ in H_0 and we obtain the coherent states

$$\begin{aligned} \lambda_1 : &\quad |\Psi_1\rangle = |00\rangle \\ \lambda_2 : &\quad |\Psi_2\rangle = \frac{1}{\sqrt{2}} \left(|\mathrm{L}\rangle + |\mathrm{R}\rangle\right) \\ \lambda_3 : &\quad |\Psi_3\rangle = \frac{1}{\sqrt{2}} \left(|\mathrm{L}\rangle - |\mathrm{R}\rangle\right) \\ \lambda_4 : &\quad |\Psi_4\rangle = |11\rangle \end{aligned} \tag{2.114}$$

with $|\mathrm{L}\rangle \equiv |10\rangle$, $|\mathrm{R}\rangle \equiv |01\rangle$ and the eigenenergies λ_i corresponding to the respective coherent states.

The dot system density matrix

$$\rho_\mathrm{S} = \begin{pmatrix} \rho_{|00\rangle} & \rho_{|00\rangle,|\mathrm{L}\rangle} & \rho_{|00\rangle,|\mathrm{R}\rangle} & \rho_{|00\rangle,|11\rangle} \\ \rho_{|\mathrm{L}\rangle,|00\rangle} & \rho_{|\mathrm{L}\rangle} & \rho_{|\mathrm{L}\rangle,|\mathrm{R}\rangle} & \rho_{|\mathrm{L}\rangle,|11\rangle} \\ \rho_{|\mathrm{R}\rangle,|00\rangle} & \rho_{|\mathrm{R}\rangle,|\mathrm{L}\rangle} & \rho_{|\mathrm{R}\rangle} & \rho_{|\mathrm{R}\rangle,|11\rangle} \\ \rho_{|11\rangle,|00\rangle} & \rho_{|11\rangle,|\mathrm{L}\rangle} & \rho_{|11\rangle,|\mathrm{R}\rangle} & \rho_{|11\rangle} \end{pmatrix} \tag{2.115}$$

contains the population of the states as diagonal elements and the coherences

between the states as off-diagonal elements. ρ_{S} undergoes the same basis transformation as H_0 and we obtain $\tilde{\rho} = D\rho_{\mathrm{S}}D^{+}$. The equation to solve is the von-Neumann equation with Born-Markov approximation

$$\frac{\partial\tilde{\rho}(t)}{\partial t} = -\frac{i}{\hbar}\left[\mathrm{H}_{\Psi},\tilde{\rho}(t)\right] + M_{\Gamma} \tag{2.116}$$

with the dot system Hamiltonian H_0 and M_{Γ}, which contains the tunnel couplings Γ of the dot system to the leads.

We can map to the matrix - vector notation

$$\frac{\partial\tilde{\rho}(t)}{\partial t} = \mathcal{L}\tilde{\rho}(t) \tag{2.117}$$

with $\tilde{\rho}$ now being a vector. Its dimension mostly is dimension d^2, with d being the dimension of the system Hilbert space. $\mathcal{L}$ is the Liouvillian superoperator which is a square matrix of dimension $d^2 \times d^2$ which contains all the information of the system. In general, the density matrix is mapped to a density vector containing all the entries from the matrix. These are d populations and $d(d-1)$ coherences. If one is only interested in the occupations of the states, one can use the decomposability of the Liovillian superoperator. $\mathcal{L}$ can be separated in blocks and one takes the block, which is of dimension $d \times d$, which corresponds to the diagonal elements ρ_{ii}, which is a vector of dimension d. We obtain

$$\begin{pmatrix} \dot{\tilde{\rho}}_{|\Psi_1\rangle} \\ \dot{\tilde{\rho}}_{|\Psi_2\rangle} \\ \dot{\tilde{\rho}}_{|\Psi_3\rangle} \\ \dot{\tilde{\rho}}_{|\Psi_4\rangle} \end{pmatrix} = \begin{pmatrix} \mathcal{L}_{11} & \mathcal{L}_{12} & \mathcal{L}_{13} & \mathcal{L}_{14} \\ \mathcal{L}_{21} & \mathcal{L}_{22} & \mathcal{L}_{23} & \mathcal{L}_{24} \\ \mathcal{L}_{31} & \mathcal{L}_{32} & \mathcal{L}_{33} & \mathcal{L}_{34} \\ \mathcal{L}_{41} & \mathcal{L}_{42} & \mathcal{L}_{43} & \mathcal{L}_{44} \end{pmatrix} \cdot \begin{pmatrix} \tilde{\rho}_{|\Psi_1\rangle} \\ \tilde{\rho}_{|\Psi_2\rangle} \\ \tilde{\rho}_{|\Psi_3\rangle} \\ \tilde{\rho}_{|\Psi_4\rangle} \end{pmatrix} \tag{2.118}$$

where $\mathcal{L}_{ij}$ describes how the probability of the system being in a certain state j will change depending on the probability of the system being in a certain state i with the electron on state i being able to leave the state with a certain rate Γ. It contains the transition rates $\Gamma^{+} = \Gamma f(\varepsilon)$, with the Fermi energy $f(\varepsilon)$, and the inverse transition rates $\Gamma^{-} = \Gamma(1 - f(\varepsilon))$ for the electrons multiplied by the probability of an electron going from state Ψ_i to state Ψ_j, $\left|\langle\Psi_i|\mathcal{J}|\Psi_j\rangle\right|^2$. Here $\mathcal{J}$ is a 4x4 matrix containing the tunnel rates of the dots to the leads γ_{L}, γ_{R}, with $\Gamma = \frac{2\pi}{\hbar}\left|\gamma\right|^2$. The entries $\mathcal{L}_{ij}$ are

$$\mathcal{L}_{ij} = f(\varepsilon_{ij}) \left| \left\langle \Psi_i \left| \tilde{\mathcal{J}}^{(+)} \right| \Psi_j \right\rangle \right|^2 + (1 - f(\varepsilon_{ij})) \left| \left\langle \Psi_i \left| \tilde{\mathcal{J}}^{(-)} \right| \Psi_j \right\rangle \right|^2 \quad (2.119)$$

with $\varepsilon_{ij} = |\lambda_i - \lambda_j|$ being the energy difference between state $|\Psi_i\rangle$ and $|\Psi_j\rangle$ and $\tilde{\mathcal{J}}^{(+)} = D\mathcal{J}^{(+)}D^+$. The expression for $\mathcal{J}^{(-)}$ follows analogously. Additionally, it is $\sum_{i=1}^{4} \mathcal{L}_{i,j} = 0$, $j \in \{1,...4\}$.

We have $\langle m|D^+D\mathcal{J}D^+D|n\rangle = \langle \Psi_i|\tilde{\mathcal{J}}|\Psi_j\rangle$, with the states $\langle m|$ and $|n\rangle$. $\mathcal{J}^{(+)}$ describes the tunneling of electrons from the leads to the dots and $\mathcal{J}^{(-)}$ the tunneling from the dots to the leads. For example, with $\langle 0| = (1,0,0,0)$, $\langle \mathrm{L}| = (0,1,0,0)$, $\langle \mathrm{R}| = (0,0,1,0)$, $\langle 2| = (0,0,0,1)$ and $|0\rangle = (1,0,0,0)^T$, $|\mathrm{L}\rangle = (0,1,0,0)^T$, $|\mathrm{R}\rangle = (0,0,1,0)^T$, $|2\rangle = (0,0,0,1)^T$, $\mathcal{J}^{(+)}$ and $\mathcal{J}^{(-)}$ are

$$\begin{aligned} \mathcal{J}^{(+)} &= \begin{pmatrix} 0 & 0 & 0 & 0 \\ \gamma_\mathrm{L} & 0 & 0 & 0 \\ \gamma_\mathrm{R} & 0 & 0 & 0 \\ 0 & \gamma_\mathrm{R} & \gamma_\mathrm{L} & 0 \end{pmatrix} \\ \mathcal{J}^{(-)} &= \begin{pmatrix} 0 & \gamma_\mathrm{L} & \gamma_\mathrm{R} & 0 \\ 0 & 0 & 0 & \gamma_\mathrm{R} \\ 0 & 0 & 0 & \gamma_\mathrm{L} \\ 0 & 0 & 0 & 0 \end{pmatrix}. \end{aligned} \quad (2.120)$$

Thus, for instance we get $\langle i|\mathcal{J}^{(+)}|0\rangle = \gamma_i$ and $\langle 0|\mathcal{J}^{(-)}|i\rangle = \gamma_i$, with $(i \in \{\mathrm{L},\mathrm{R}\})$.

As an example, for $\mathcal{L}_{12}$ we obtain

$$\begin{aligned} \mathcal{L}_{12} &= (1 - f(\varepsilon_{12})) \left| \langle \Psi_1 | \tilde{\mathcal{J}}^{(-)} | \Psi_2 \rangle \right|^2 \\ &= \left| \frac{1}{\sqrt{2}} (\gamma_\mathrm{L} + \gamma_\mathrm{R}) \right|^2 \cdot (1 - f(\varepsilon_{12})) \\ &= \frac{1}{2} \left| \gamma_\mathrm{L} + \gamma_\mathrm{R} \right|^2 \cdot (1 - f(\varepsilon_{12})). \end{aligned} \quad (2.121)$$

Thus, the entries of $\mathcal{L}$ can be extracted from experiment and the Master equation Eq. (2.118) can be solved in the following to obtain the occupations.

The steady state occupations of the doube dot are calculated by solving the kernel of the master equation $\rho^{\mathrm{ss}} = \ker[\mathcal{L}]$, meaning $\mathcal{L}\tilde{\rho}(t) = 0$.

3 Experimental techniques

The experimental analysis of a TQD system requires a variety of technologies and techniques to fabricate the sample, set up the requirements to investigate quantum mechanical phenomena and measure the sample. The investigated lateral TQD sample was fabricated by M. C. Rogge in the course of his PhD thesis. Within this chapter the used materials and fabrication techniques regarding the used heterostructure wafer and the lithography are shortly described, as these are common techniques used to fabricate lateral quantum dots. Detector and transport measurements on the TQD sample are performed within this work and thus the experimental measurement setup and measurement techniques for these purposes are explained in the following.

The following section 3.1 introduces the structure and properties of the used heterostructure wafer and the optical and atomic force microscope lithographic steps to structure the surface. The measurement techniques for the detector measurements by using the quantum point contact on the sample are presented in section 3.2 and the measurement method for performing transport spectroscopy on the sample is shown in section 3.3. The experimental setup including cryogenic and electrical measurement setup are introduced in section 3.4.

3.1 Sample preparation

The fabrication of lateral quantum dots requires a 2DEG, which is structured by lithographic methods to produce quasi-zero dimensional electronic structures with two-dimensional leads. For our sample a heterostructure based on the well-known III-V-semiconductor GaAs is used. Si is predominantly used in industry due to many advantages, whereas GaAs is not as commonly used. However, GaAs plays an important role in basic research and high-frequency applications due to its higher electron mobility.

3.1.1 Heterostructures

Semiconductor heterostructures are epitaxial grown structures consisting of more than one semiconductor material with different band gaps. This can be achieved by varying the chemical composition from layer to layer. The simplest heterostructure is a heterojunction, which is an interface within a crystal occurring between two layers of different crystalline semiconductors [64]. Heterostructures for basic research are commonly produced using molecular beam epitaxy (MBE) [64]. The considered GaAs-based heterostructure is made of epitaxial growth of combinations of layers of GaAs and $Al_xGa_{1-x}As$. The parameter x controls the ratio between Al and Ga and in this way the band gap, which can vary between 1.424 eV (GaAs) and 2.168 eV (AlAs) [65]. In addition to having very different band gaps, combinations of GaAs and AlGaAs have a minimal lattice mismatch due to very similar lattice constants of $a_{\mathrm{GaAs}} = 5.6533$Å and $a_{\mathrm{AlGaAs}} = 5.6611$Å [65], which makes the two semiconductors perfectly suitable for realization of various electronic structures with high crystalline quality and electron mobility.

The band gap of AlGaAs is greater than that of GaAs, with different electron affinities referring to the position of the band edges relative to the vacuum energy. As a consequence, band offsets appear. The Fermi energy of the two materials is set by doping. When the materials are brought together, the band diagram follows the rule that the Fermi energy is constant across the layers in equilibrium. Far from the junction the bulk properties are maintained. In consequence, electrons flow from AlGaAs to GaAs, the Fermi energies align and the bands bend. The band bending leads to a triangular potential well which confines the electrons in GaAs if the width of the potential in growth direction is of the same order of magnitude as the electron wavelength. 2D subbands are formed within the potential well. As the Fermi energy is controlled by doping, AlGaAs is n-doped by Si. The Si density is chosen such that only the lowest subband of the potential well is occupied and the electrons form a 2DEG (Fig. 3.1). Only a small percentage of the doping electrons relax into the potential well, the rest is thermally excited and occupies the surface states close by [43]. This makes the electronic structure very surface-sensitive. In the heterostructure considered in the following, this modulation doping is realized via Si δ-doping. Here the Si donor atoms are located within a single monolayer of AlGaAs several nm separated from the potential well by a spacer layer. This separation leads

to an enhanced electron mobility in the 2DEG as the screened Coulomb potentials of the ionized donors influence the electron gas only weakly over this distance, which leads to mostly small-angle scattering [43].

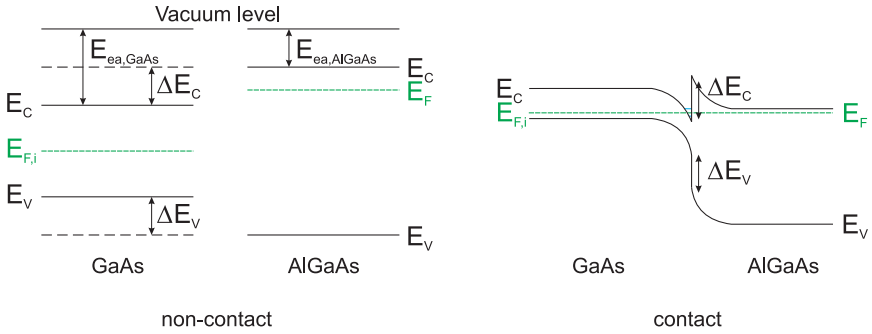

Figure 3.1: Schematic band diagram of GaAs and AlGaAs apart and in contact, showing the formation of a triangle potential well. In potential well 2D subbands are formed (blue lines). The lowest subband lies below the Fermi energy due to specific doping.

The lateral triple quantum dot sample used within the scope of this work is made using such a GaAs/AlGaAs-heterostructure wafer as a basis. Figure 3.2 shows the layer sequence including a GaAs buffer layer separating the structure from the bulk material, an AlGaAs spacer layer and the Si-doped AlGaAs layer. The structure is closed at the top by a cap layer of GaAs. The 2DEG has an electron concentration of $n_e = 3.47 \cdot 10^{15}\,\mathrm{m}^{-2}$ at 4.2 K and is located in 33 nm depth below the surface. The electron mobility is $\mu_e = 42.1\,\mathrm{m}^2/\mathrm{Vs}$ at 4.2 K.

3.1.2 Lithography

In order to fabricate zero-dimensional systems starting from the 2DEG in the heterostructure, the wafer is structured in basically two lithographic steps. Via optical lithography electronically separated conducting paths are created in the 2DEG and contacted for connection to external devices. In a second step the 0D system itself is formed using local anodic oxidation (LAO) with an atomic force microscope (AFM). In the following the two techniques are presented.

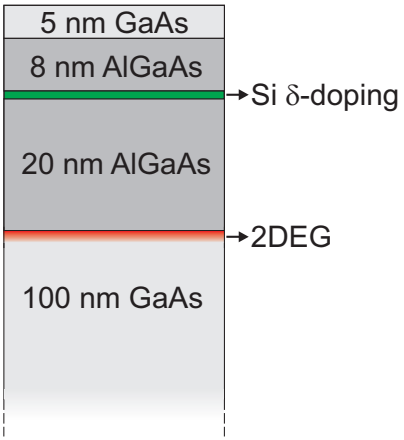

x	0.329
2DEG depth	33 nm
Doping	Si δ
n_e (4.2 K)	$3.47*10^{15}$ m^{-2}
μ_e (4.2 K)	42.1 m^2/Vs

Figure 3.2: Layer sequence of the used heterostructure. It was grown by M. Bichler and G. Abstreiter, Walter Schottky Institut, TU Muenchen, and W. Wegscheider, Universitaet Regensburg

3.1.2.1 Optical lithography

Optical lithography is used for connection of the nanoscale sample structures to the macroscopic environment. The first step is defining the separate conducting paths, the usable area of the 2DEG, called mesa. For the structuring of the heterostructure wafer a 4.5 mm × 4.5 mm piece is cut from the wafer to fit into the chip carrier later. It is coated with a special UV-sensitive positive photo resist in a spin coater. The mesa structure is transferred onto the wafer by bringing it into contact with a quartz glass mask with UV-opaque chrome metallization in the considered geometry and using UV light to expose the resist only under the non-metallized parts of the mask. After developing the resist only the non-exposed parts of the structure remain. The wafer is etched down to a few nm below the 2DEG by chemical wet etching while the remaining resist serves as an etching mask. Thus, only the area protected by the resist, the mesa, remains conducting. The resist is removed by acetone afterwards. The mask used for our geometries has a chrome metallization for 16 conduction paths arranged in a star shape. Figure 3.3 (1) shows optical microscopy of the mesa structure on the wafer piece.

In order to establish electrical contacts between the 2DEG and the surface,

ohmic contacts are placed on the conducting paths. To do so the wafer is again coated, but this time with a negative resist, which is resistant to the developer only after being exposed to UV light. The sample is irradiated with UV light through a mask with a chrome metallization for ohmic contacts fitting on the mesa structure. The considered mask has a chrome metallization for 16 ohmic contacts arranged in a ring fitting on the mesa. After developing, the non-exposed parts of the structure are resist-free and can be selectively processed. The wafer piece is metalized with a layer sequence of germanium, gold and nickel in an ultra high vacuum (UHV) evaporation chamber. Afterwards the resist is removed in an acetone bath (lift-off process) and the metallization only remains on the resist-free areas. Due to a gradient in the UV radiation dose on the borders of the UV-opaque structures of the mask, the resist layer also exhibits a continuous decrease in the completeness of its exposition towards the non-exposed areas. The exposed resist remains after developing, showing the inverted profile, an undercut. This ensures that the metallization applied on the wafer surface in the next step is isolated from the metallization on the resist surface or the resist itself. This guarantees a clean lift-off. In an annealing process the sample is heated in several stages and the metalization melts. Gold and germanium form an alloy and diffuse into the heterostructure. The Germanium as an n-type dopant reduces the Schottky barrier between metal and semiconductor, giving the contacts the ohmic behaviour. This is a low-ohmic contact resistance and a linear I-V- curve following Ohm's law. Figure 3.3 (2) shows optical microscopy of the annealed ohmic contacts on the mesa structure. The ohmic contacts are bonded with gold wires on a chip carrier later, seen in Fig. 3.3 (3). The structure has a central conducting region with a diameter of 30 µm for fabrication of the lateral quantum dot structure itself (Fig. 3.4).

3.1.2.2 Local anodic oxidation

Local anodic oxidation (also: local oxidation nanolithography) is a tip-based nanofabrication method which is a widely used approach for micro- and nano-patterning of metal- and semiconductor surfaces [66–68]. Local oxidation of the surface of GaAs-AlGaAs heterostructures with AFM is used for structuring of the 2DEG of the heterostructure [69–74]. An AFM [75] is a scanning probe microscope with a nanometer-scale tip for scanning a surface in nanometer- or even atomic scale. Also, surface structuring can be performed. For fabrication of the lateral quantum dot structures, an AFM

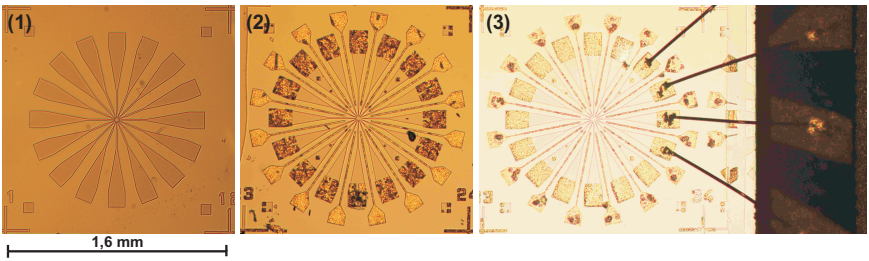

Figure 3.3: Optical microscopy of the described steps of sample processing: (1) Etched mesa structure. (2) Ohmic contacts after transfer of the contact structure, metalization and annealing. (3) Contacts bonded with gold wires on a chip carrier.

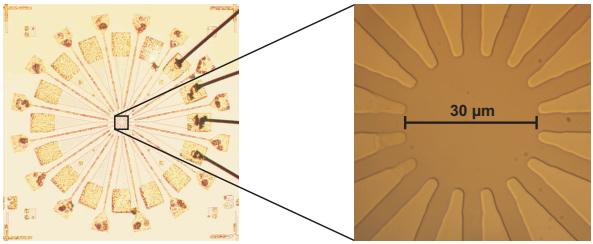

Figure 3.4: Optical microscopy of the central region of the sample structure. The conductance paths meet at a central conducting region with a diameter of 30 µm.

tip is brought into immediate proximity to the sample surface [70, 71]. A voltage is applied between tip (cathode) and the grounded sample (anode), which ensures a water film on the substrate under sufficiently rich water vapor ambient conditions. This leads to the formation of a water meniscus (electrolyte) between tip and surface. Altogether, a small electrolytic cell is formed. The GaAs surface is locally oxidized under the tip (Fig. 3.5). The chemical reaction of the electrolysis is [76]

$$2\mathrm{GaAs} + 12\mathrm{H}^+ + 10\mathrm{OH} \rightarrow \mathrm{Ga_2O_3} + \mathrm{As_2O_3} + 4\mathrm{H_2O} + 2\mathrm{H}^+. \qquad (3.1)$$

The water molecules are dissociated after applying a voltage, the OH^- ions travel to the surface and react with the GaAs to oxide. The resulting $\mathrm{Ga_2O_3}$ reaches a few nm height and at the same time grows a few nm into the

bulk. In this way the GaAs layer thickness is decreased there. The sample thickness decreases and the interface moves closer to the to the 2DEG. In GaAs the Fermi energy at the surface is pinned near the middle of the band gap of GaAs due to a large surface state density already mentioned above. [77] Consequently, the potential well is lifted with respect to the Fermi energy and is ultimately located completely above it, so that the 2DEG is depleted. Thus, by writing oxide lines on the surface of the heterostructure the 2DEG is depleted locally underneath the oxide lines and an insulating barrier is formed [71–73].

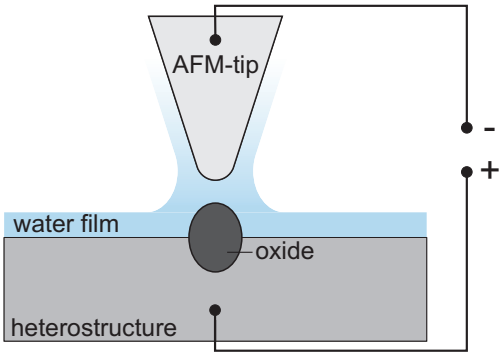

Figure 3.5: Functional principle of the local anodic oxidation procedure. With the help of a water film on the sample surface a small electrolytic cell is formed by applying a voltage between tip and sample. The heterotructure surface is locally oxidized under the tip. The oxide reaches a few nm into the bulk.

The size of the water bridge determines the spatial confinement for oxidation of the surface. The small number of active ions in it allows for a good control of the dimensions of the oxide dot. As the electrical field distribution is strongly localized near the tip oxide dots of nanometer size can be made. The shape of the induced potential in the 2DEG is determined by the aspect ratio of the oxide lines, controlled by parameters like humidity, tip geometry, applied voltage, writing speed etc. The depth of the potential notch and thereby the tunneling barrier height for the electrons in the 2DEG is determined by the penetration depth controlled by the height of the oxide line. The width of the potential and thus the capacitance between the two isolated areas is determined by the width of the oxide lines. Consequently, a high but thin oxide line is required in order to obtain a sufficiently high

tunneling barrier and to induce a large field effect on one side of the line by a small voltage on the other side. This corresponds to a large capacitor. [43]

This gate fabrication technique produces in-plane gates being part of the semiconductor wafer material. This makes the gates robust and the samples less sensitive to electric discharges than metallic top-gate structures fabricated by electron-beam lithography. [78] Additionally, the LAO gate structures are simpler to extend and the oxides lines provide a confining potential even without applied voltages so less gates are needed in general.

3.2 Charge detection with a quantum point contact

The charge configuration is an important parameter of a quantum dot. In order to measure the change of the charge state with a non-invasive method, quantum dots [79, 80] or quantum point contacts [81, 82] are commonly used in transport spectroscopy. They are located near the system under investigation.

A quantum point contact (QPC) is a short and narrow constriction in a 2DEG, which has a variable width being comparable to the Fermi wavelength and is much shorter than the mean free path for impurity scattering, so that electronic transport is ballistic. Due to its width it exhibits size quantization. [83, 84] In a 2DEG such a one-dimensional constriction can be realized by suitable electrostatic potentials induced by top gates [81, 85] or structures produced by LAO [39, 86, 87]. The potential of the confinement can be approximated with a saddle-point potential and has a one-dimensional density of states. These one-dimensional sub-bands are energetically separated transport channels. These are, in assumption of a harmonic one-dimensional confinement potential, equidistant and have a conductance of $2\,e^2/h$ each in case of perfect ballistic transport and spin degeneracy. Hence the conductance of the one-dimensional constriction is quantized in units of $2\,e^2/h$ [88, 89]. The confinement couples to the 2DEG at both sides. This forms the leads of the QPC, the source S_{QPC} and the drain D_{QPC}. Each transport channel which lies within the transport window defined by the chemical potentials of the leads contributes to transport. A gate G_{QPC} is located next to the confinement to lower and raise the saddle potential of the confinement and thus the potential barrier. In this way

the number of participating transport channels is varied. As a result the conductance through the QPC as function of the voltage U_{GQPC} is a step function with plateaus at $2\,\mathrm{e}^2/\mathrm{h}$ and steep transitions in between, see Fig. 3.6.

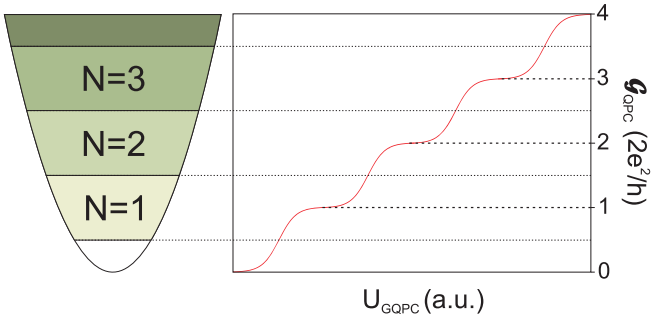

Figure 3.6: Schematic of the one-dimensional harmonic confinement potential of the QPC with sub-bands N=1,2,3 and the corresponding conductance $\mathcal{G}_{\mathrm{QPC}}$ through the QPC in dependence of the gate voltage U_{GQPC}. The steps in conductance correspond to the contribution of an additional transport channel.

The spatially well defined confinement potential is very sensitive to small changes in charge in its environment as the capacitive interaction changes the shape and strength of the confinement. Charge variations shift the conductance of the QPC with respect to U_{GQPC}. At the steep transitions between the conductance plateaus the detector is most sensitive as a small shift results in a strong variation of conductance. Thus, the optimal operating point is a steep slope in the $\mathcal{G} - U_{\mathrm{GQPC}}$-characteristic of the detector. In this way charge differences down to fractions of the elementary charge can be detected, like for example the movement of an electron towards or away from the detector by charge redistribution in the quantum dot system. These do not necessarily cause a current between source and drain of the dot system and consequently are not detectable by transport measurements. As the quantum point contact just reacts to potential shifts in its surrounding while being disconnected from transport through the dot system and carrying no localized charge itself, the detection of a change in charge by a quantum point contact is called non-invasive [81].

Figure 3.7 shows the signature of a change of the charge state in a quantum dot. The current through the QPC I_{QPC} is measured in dependence of a gate voltage U_{G}. In the chosen operating point I_{QPC} rises nearly linearly to the change in gate voltage. At the same time U_{G} influences the potential at the quantum dot, so that at $U_{\mathrm{G}} \approx 113\,\mathrm{mV}$ one more electron can occupy the dot. This additional negative charge shifts the original detector characteristic curve to less negative values of U_{G} by an amount proportional to the change in charge. The change in gate potential compensates for the additional negative potential coming from the added electron on the dot. Thus, the shift in gate voltage is a measure for the change in charge in the system. The shift happens over a certain range in gate voltage. The reason is that the tunneling probability on and off the dot is non-zero for $\mu_{\mathrm{N}} < \mu_{\mathrm{S}},\mu_{\mathrm{D}}$ and $\mu_{\mathrm{N}} > \mu_{\mathrm{S}},\mu_{\mathrm{D}}$ near the resonance due to temperature broadening of the states. The used measuring instrument integrates over the probability of occupancy of the quantum dot during a certain time interval.

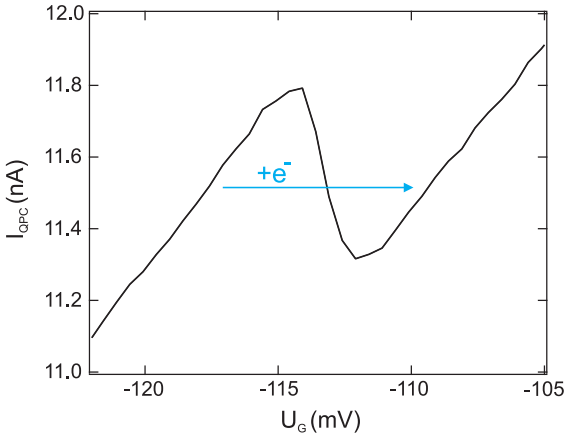

Figure 3.7: Example measurement of the current I_{QPC} through the QPC in dependence of a gate voltage U_{G3} on a quantum dot system, where the quantum dot is charged by one electron. I_{QPC} acts linearly on U_{G3}. The charging is marked by a shift of the current curve to higher values of U_{G3}, compensating for the additional negative potential coming from the added electron on the dot. With one more electron on the dot the same current through the QPC is achieved for a higher gate voltage.

Spectroscopy of the dot system by measuring the differential conductance always strongly depends on the tunneling barriers in the system. The fact that charge measurements with a detector are independent of a current flow in the quantum dot system itself makes them a tool for extending the measurement range to higher tunneling barriers in the system. The measurement of the differential conductance is based on measuring the current I_{AC} for an applied voltage U_{AC}. The observation of small currents is limited by the signal-to-noise ratio. Increasing the voltage means decreasing the energy resolution of the measurement. This is limited by the energetic width of the Coulomb peaks $3.53k_{\mathrm{B}}T$, which should not be undercut by the resolution. The differential conductance through the system significantly depends on the tunnel couplings in the system. In order to discharge the quantum dot by sweeping the gate voltages to higher negative values in case of a LAO structured gates, the tunnel couplings of the dot to the leads are affected as well and are decreased. At a specific gate voltage the differential conductance falls below the detection threshold of the current measurement device. QPC measurements however clearly show that at larger negative gate voltage values the dot is emptied further, as seen in the example of a transport and detector measurement in Figure 3.8.

Instead of I_{QPC} the differential signal $\mathrm{d}I_{\mathrm{QPC}}/\mathrm{d}U_{\mathrm{G}}$ is usually plotted to simplify or even enable the analysis of the detector signal for one- or multi-dot systems in dependence of two gate voltages. Steps in conductance of the QPC appear as lines of high differential conductance in this case. Independent of the arrangement of the dots (series or parallel) in a multiple quantum dot system the whole charging lines of each of the dots in the system are visible. The change in charge of all of the dots can be seen even if they do not participate in transport as it is the case for dots being only capacitively coupled to the transport path. On the contrary, in transport measurements of serial dots conductance is only observed at the resonances between the dots. This can be well seen in Fig. 3.8. Thus, a QPC measurement makes it easier to identify and characterize the dots and analyze the formation of multiple-dot resonances. The QPC measurements can be compared to transport measurements and support their analysis.

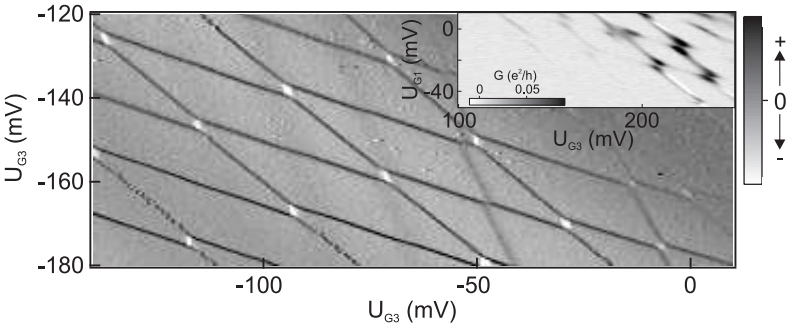

Figure 3.8: Comparison of an exemplary transport and QPC measurement on the triple quantum dot system where each transport path consists of a tunnel coupled double quantum dot with a capacitively coupled third dot. Insert: Transport measurement of one of the paths with dots A and B. For gate voltages below $U_{\mathrm{G3}} \approx 120\,\mathrm{mV}$ and $U_{\mathrm{G1}} \approx 10\,\mathrm{mV}$, the Coulomb peaks are not detectable anymore as the tunnel couplings along the path have become sufficiently small. Resonances of dots A and B are detectable. Big picture: The QPC measurement for the same parameter region but more negative values of U_{G1}, U_{G3} shows that the quantum dots are not empty yet. Changes in the charge of the dots even for larger negative values of U_{G1}, U_{G3} are detectable with unchanged clarity. Also, changes in charge of all three dots of the device are seen directly by charging lines.

3.3 Transport measurements

The measurement and analysis of quantum dot spectra is a standard method to analyze a quantum dot system. As already introduced in section 2.3.2 the differential conductance $G = \mathrm{d}I_{\mathrm{SD}}/\mathrm{d}U_{\mathrm{S}}$ of a quantum dot system is a useful measurand for the investigation of such a spectrum. The differential conductance $G = I_{\mathrm{AC}}/U_{\mathrm{AC}}$ can be measured directly by a lock-in technique. A small AC voltage U_{AC}, typically of around $10\,\mu\mathrm{V}$ and with a small frequency of the order of Hz from the internal oscillator of the lock-in is applied to the source of the sample. The response of the system is detected by measuring I_{AC} by the lock-in and G is calculated and output by the measurement program (Fig. 3.9). Thereby the outcome corresponds to the differential conductance obtained by $\mathrm{d}I_{\mathrm{DC}}/\mathrm{d}U_{\mathrm{S}}$ [40].

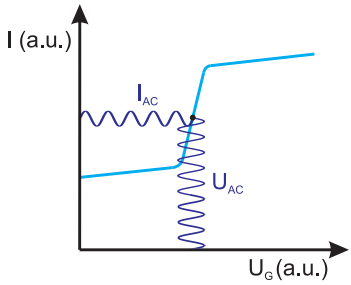

Figure 3.9: Schematic showing the measurement technique of the differential conductance. The reaction of the system to a small applied AC voltage in form of the AC I_{AC} is measured.

3.4 Experimental setup

This section describes the setup used to perform measurements on the quantum dot sample. Subsection 3.4.1 describes the cryogenic setup used for cooling down the sample to enable the observation of quantum mechanical effects. It covers the functional principle of a ^{3}He^{4}He dilution refrigerator which is used within the scope of this work. The electrical setup for transport and QPC measurements is shown in section 3.4.2.

3.4.1 Cryogenic setup

Very low temperatures are required for the resolution of quantum dot energy spectra, as described in section 2.3.2. Temperatures in the order of mK are commonly produced in a dilution refrigerator. The measurements within the scope of this work were performed in a Oxford Instruments Kelvinox 300 and a Kelvinox TLM ^{3}He^{4}He dilution refrigerator, which both achieve temperatures of around 10 mK by cooling in several stages. The functional principle of a dilution refrigerator in general and of the Kelvinox 300 in particular will be presented here shortly. The interior of a cryostat is uncoupled from room temperature by several vacuum shields, a liquid nitrogen cooling shield (77 K) in some cases and a liquid helium cooling shield (4.2 K), the so-called main bath. The insert of the cryostat itself has basically two cooling stages. The insert is enclosed by an inner vacuum chamber (IVC) to minimize heat exchange with the ^{4}He bath. Figure 3.10 shows a schematic

of the functional principle of a dilution refrigerator. The first cooling stage is the so-called 1K-pot. This chamber is partly filled with liquid ^{4}He drawn from the main bath through a flow restriction. The gaseous phase of ^{4}He is continuously pumped out, the vapor pressure is reduced, which in turn cools the liquid ^{4}He down to 1.5 K. The lowest temperatures are achieved in the mixing chamber, the second cooling stage. It contains a ^{3}He^{4}He-mixture which exists separated in a ^{3}He-rich (concentrated) phase and a ^{3}He-poor (dilute) phase below 860 mK. The lower temperature is achieved by pumping. The binding forces between ^{3}He atoms are smaller than the binding forces between ^{3}He and ^{4}He atoms because of the higher zero point energy of the lighter ^{3}He isotop. The kinetic energy of ^{3}He atoms increases with their particle number density as they follow the Fermi statistics, and thus their effective binding energy is reduced with increasing density. At very low temperatures their binding energy is so low that a phase separation into two phases with different ^{3}He-concentration is energetically preferred. Important to mention is, that even at $T = 0$ K a certain solubility of ^{3}He in ^{4}He remains.

Due to the fact that ^{3}He is lighter than ^{4}He, the ^{3}He-rich phase swims on top of the ^{3}He-poor phase. The cooling principle is cooling by evaporation of ^{3}He out of the liquid ^{3}He-rich phase into the superfluid ^{3}He-poor phase. ^{3}He atoms in the ^{3}He-poor phase have a higher enthalpy as ^{3}He atoms in the ^{3}He-rich phase. An evaporation of ^{3}He from the ^{3}He-rich phase into the ^{3}He-poor phase thus leads to effective cooling based on this difference in enthalpies.

This cooling mechanism is implemented into a closed loop. By continuously extracting ^{3}He out of the ^{3}He-poor phase osmotic pressure is induced due to the concentration gradient. This leads to ^{3}He atoms crossing the phase separation line from the ^{3}He-rich phase into the ^{3}He-poor phase to maintain the solution equilibrium which in turn leads to the cooling. This extraction of ^{3}He out of the ^{3}He-poor phase happens in a separate evaporation chamber, the still, connected with the ^{3}He-poor phase in the mixing chamber and located above the mixing chamber. The still is heated to a temperature of around 0.7 K, where ^{3}He has a significantly higher vapor pressure than ^{4}He. It works as a distillation chamber and almost pure ^{3}He gas can be pumped out of the still although the ^{3}He concentration is $\leq 1\%$ in the ^{3}He-poor liquid phase. After being cleaned in nitrogen and helium cold traps and pre-cooled at the 1K-pot, the gas is condensed again by high pressure in a flow impedance. Afterwards it passes a heat exchanger to

use the heat exchange with the ^{3}He-poor phase on its way from the mixing chamber to the still. The ^{3}He is fed back into the ^{3}He-rich phase in the mixing chamber. [90] In the Kelvinox 300 the sample is thermally coupled to the mixing chamber by a cold finger while it is directly immersed in the mixing chamber in the Kelvinox TLM.

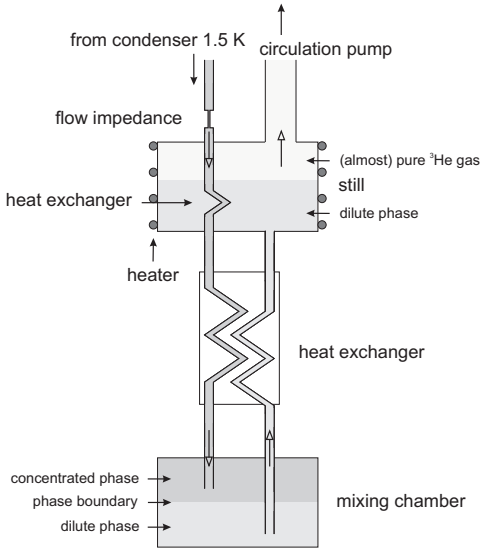

Figure 3.10: Schematic setup and working principle of a dilution refrigerator and its cooling mechanism. [90]

3.4.2 Electrical measurement setup

The measurement setup for the transport and QPC measurements is shown in Fig. 3.11.

Automated instrument control and data collection is achieved via GPIB (General Purpose Interface Bus) and USB. The data is automatically collected and partly processed to some extend by LabView programs specific for the respective measurement type. For the transport measurements the DC gate voltages U_{G1}-U_{G4} and also the DC voltages for the sources U_{S1}, U_{S2} and are generated with a homemade DAC (digital-to-analog converter)

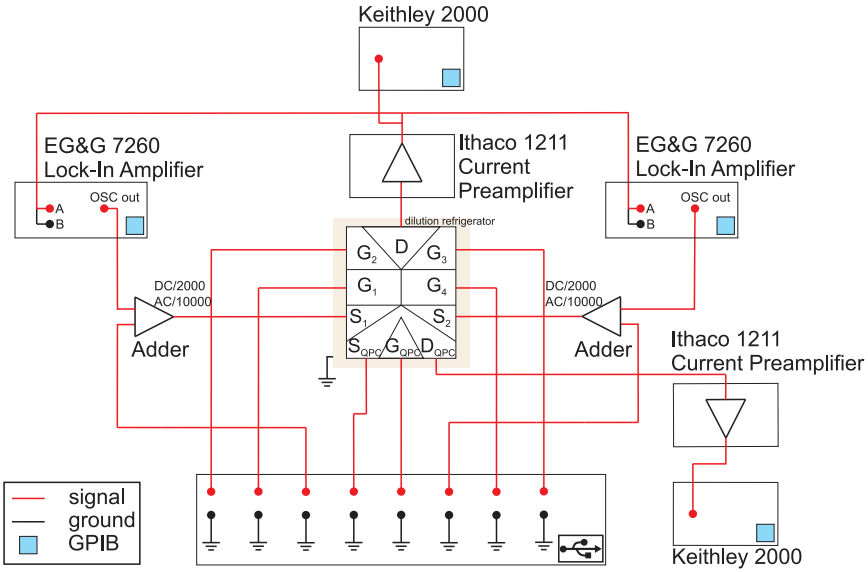

Figure 3.11: Schematic of the electrical measurement setup for transport and detector measurements. The gates of the sample, G_1-G_4, G_{QPC} as well as S_1, S_2, S_{QPC} are driven by DC voltages generated by a DAC. The conductance through the two transport paths of the system S_1-D and S_2-D is measured at the drain lead D via a lock-in technique by additionally applying two different AC voltages at S_1 and S_2.

based on a AD5791 chip (or two iotech DAC 488HR/4). The DAC has galvanically isolated outputs with a voltage range of $\pm 10\,\mathrm{V}$ with a resolution of 20 Bit ($\equiv 19.073\,\mu\mathrm{V}$). The reference potential is given by the ground of the signal cables. The DC source voltages U_{S1}, U_{S2} and $U_{\mathrm{S,QPC}}$ are divided by a factor of 2000 using a voltage divider between DAC output and lead.

In case of measurements with bias a small AC voltage U_{AC} is applied additionally to the DC voltage U_{S} at the source contacts. For the AC voltage, the internal oscillator of an EG&G 7260 DSP Lock-In Amplifier is used. In order to apply AC voltages with two different frequencies at the two sources for distinguished paths at the drain we use one lock-in per source lead. We use a frequency of $f_1 = 83.3\,\mathrm{Hz}$ at source 1 and a frequency of $f_2 = 18.3\,\mathrm{Hz}$ at source 2 both with an amplitude of $U_{\mathrm{AC}} = 10\,\mu\mathrm{V}$. The

amplitude of the AC voltage of the oscillator output is divided by a factor of 10000 by using a voltage divider between lock-in and lead. The sum of U_{AC} and U_{S} is applied at the source contacts, U_{AC} with frequency f_1 and U_{S1} at source 1, U_{AC} with frequency f_2 and U_{S2} at source 2.

The AC and DC current (I_{AC}, I_{DC}) are measured at the drain contact D. The signal at the drain is amplified by an Ithaco DL 1211 current preamplifier by a factor of 10^7. The amplifier is also grounding the drain contact. Thus, the drain contact is the reference potential of the sample. The DC part of the signal, I_{DC}, is measured by a Keithley 2000 Multimeter. The ac part of the signal, I_{AC}, is fed into both of the lock-ins. The measured I_{AC} can be directly converted into the differential conductance G by $G = I_{\mathrm{AC}}/U_{\mathrm{AC}}$. For very small bias voltages $U_{\mathrm{SD}} \approx 0\,\mathrm{mV}$ the differential conductance is equal to the conductance $I_{\mathrm{DC}}/U_{\mathrm{SD}}$.

The quantum point contact is operated by applying a DC voltage $U_{\mathrm{SD,QPC}}$ at source S_{QPC} and $U_{\mathrm{G,QPC}}$ at G_{QPC} via a DAC. At D_{QPC} the DC I_{QPC} is amplified by a DL 1211 and measured by a Keithley 2000. The potential at D_{QPC} is the reference potential of the QPC. It is possible to use the whole QPC as a gate for the TQD by applying a voltage at both G_{QPC}, S_{QPC} and D_{QPC}.

In the grounding concept ground loops are avoided. The cryostat itself serves as center ground.

4 Characterisation of the triple quantum dot system

Within this chapter the TQD sample setup itself and its basic transport properties are presented. The sample is characterized in outline by charge and transport measurements of both transport paths, which are common techniques for this purpose.

The following section 4.1 presents the setup of the TQD sample concerning the arrangement of the dots, leads and gates as well as their couplings. It also explains the dot and lead setup with regard to the measurement purposes. In section 4.2 charge measurements are presented and analyzed as the first step in sample characterization. The dependence of the measurement outcome on the tunneling rates within a transport path is shown. The tunnel barriers in one of the two transport paths are tuned asymmetric so that the path becomes drain decoupled. The arising charging effects and their utilization is explained. In section 4.3 the sample is investigated regarding its basic transport properties. Stability diagrams and Coulomb diamonds of both transport paths separately are shown, analyzed and compared.

4.1 Triple quantum dot sample

Within the scope of this work a lateral TQD sample based on a structured 2DEG within a GaAs/AlGaAs-heterostructure is investigated. Figure 4.1 shows an AFM image of the sample and Figure 4.2 a schematic of the sample setup. The sample was manufactured by M.C. Rogge [24]. It is structured by LAO (see section 3.1.2.2) on the GaAs/AlGaAs-heterostructure presented in Fig. 3.2. The three dots A, B and C are arranged in a triangular geometry with each dot situated next to the other two and one lead attached to each dot. Dots A and B as well as A and C are capacitively and tunnel coupled, whereas the coupling between dots B and C is only of capacitive nature, since the channel between them is too narrow to be opened for transport [24, 38].

The leads S_1 and S_2 are connected to dots B and C respectively and are used as source contacts and the lead D is connected to dot A and used as a drain contact. Thus, two transport paths are formed with two serial double dots, dot A and B in path 1 and dot A and C in path 2. The sample allows a variable measurement setup. Transport through two dots in series with a capacitively coupled third dot can be measured separately in both paths and can be compared or combined. Accordingly, this structure provides the opportunity of investigating double and triple dot physics simultaneously, whereas in serial triple dots double dot resonances can not be detected in transport. In the given system one can thus conveniently study triple dot physics based on the well understood double dot system by investigating transitions from double dot to triple dot resonances in transport. Former work on this system covers the basic transport properties and uses two of the leads as drain contacts and the lead at dot A as a source contact [24]. In the configuration of two-path transport with two sources and one drain, the electrons from the different paths compete for the occupation of dot A. By applying two different frequencies at S_1 and S_2 and using a standard lock-in technique to distinguish the paths at the drain, transport through the paths can be measured simultaneously and separately. With this setup interactions between the paths manifest themselves in transport and can be studied for the zero bias case as well as for different bias voltages at the sources.

The sample has four in-plane gates $G_1 - G_4$ to control the potential of the dots and the inter-dot- and dot-lead couplings. As a result of the setup and small distances in the sample, the dot potentials and the couplings are tuned by a complex cooperation of gate voltages. A quantum point contact (QPC) sensitive to all three dots is located next to dots B and C to perform charge measurements. The QPC has its own source (S_{QPC}) and drain (D_{QPC}) lead and is tunable via gate G_{QPC}.

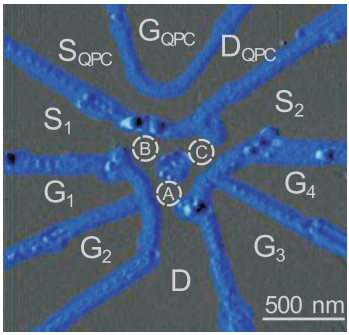

Figure 4.1: AFM image of the TQD sample with in-plate gates $G_1 - G_4$ and a QPC for charge measurements. The blue lines are oxide lines fabricated by LAO (see section 3.1.2.2) and form insulating barriers. [24, 91]

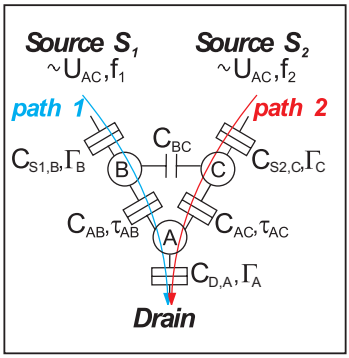

Figure 4.2: Schematic of the TQD setup with dots A, B, and C. The two source leads S_1 and S_2 are connected to dots B and C, respectively, and the drain lead D is connected to dot A. The capacitive couplings between leads and dots are denoted by $C_{S1,B}$, $C_{S2,C}$ and $C_{D,A}$, the tunneling rates by $\Gamma_B, \Gamma_C, \Gamma_A$. Dots A and B as well as A and C are tunnel coupled via τ_{AB} and τ_{AC}, respectively, and capacitively coupled via C_{AB} and C_{AC}, respectively. Dots B and C are capacitively coupled via C_{BC}. This forms two transport paths, path 1 (serial dots A and B) and path 2 (serial dots A and C). Distinguishability between both paths in the drain signal is achieved by different AC-voltages U_{AC}, f_1 and U_{AC}, f_2 applied to S_1 and S_2, respectively. Similar schematic has been published in [91].

4.2 Charge measurements

Charge measurements on a multiple dot system are a common tool for the investigation of basic electrostatic properties of the system: The number of quantum dots, the capacitive inter-dot couplings, gate capacitances as well as the tunability in and out of dot resonances. These system properties can even be investigated for a parameter regime where no transport through the system is observable because of a current below the detection limit due to too large tunneling barriers.

Since a TQD system consists of three linearly independent energy spectra the stability diagram of a TQD is three-dimensional (see section 2.3.1). From a two-dimensional cut through the stability diagram however one can already deduce the electrostatic properties of the system regarding two of the gate voltage parameters of the system.

Figure 4.3 shows an excerpt of such a cut through the three-dimensional charging diagram of the TQD. The derivative of the detector signal $\mathrm{d}I_{\mathrm{QPC}}/\mathrm{d}U_{\mathrm{G3}}$ is plotted as a function of gate voltages U_{G1} and U_{G3} and shows a pattern of lines with three different slopes (see section 3.2). They indicate charging events, where the electron number in the corresponding dot is changed by one. The different slopes result from the different gate-dot capacitive coupling due to their respective distance (Fig. 4.1). Based on the different gradients of the charging lines the quantum dots can be identified. In the charging diagram in Figure 4.3 a large gradient originates from a small coupling of a dot to G_1 and a large coupling to G_3, the line is thus attributed to dot C. Lines with a small gradient stem from a much stronger coupling of a dot to G_1 than to G_3 and are consequently attributed to dot B. The lines with intermediate slope can then be ascribed to the charging of dot A. Where two charging lines meet, they shift due to the capacitive coupling between the dots. These anticrossings mark resonances between two dots. Resonances between dot A and B (red circle), A and C (yellow circle) and B and C (blue circle) are observed. In all the charge measurements the measurement direction goes from negative to positive gate voltage values, sweeping U_{G3} and stepping U_{G1}. In case of the charging lines of the dots the derivative of the detector current is negative, as electrons are added to the system in sweeping direction towards more positive U_{G3}. The triple points of the resonance between dots A and B are connected by a dark blue charge reconfiguration line, a positive derived detector signal. One electron

is moved from dot B to dot A in measurement direction, thus moving away from the detector which then detects a decrease in charge. Analogously the positive charge reconfiguration lines at the other double dot resonances can be explained. A resonance condition for all three dots is achieved, where the double dot resonances coincide (black circle). Here we can identify a point where four charge configurations meet, a quadruple point (QP).

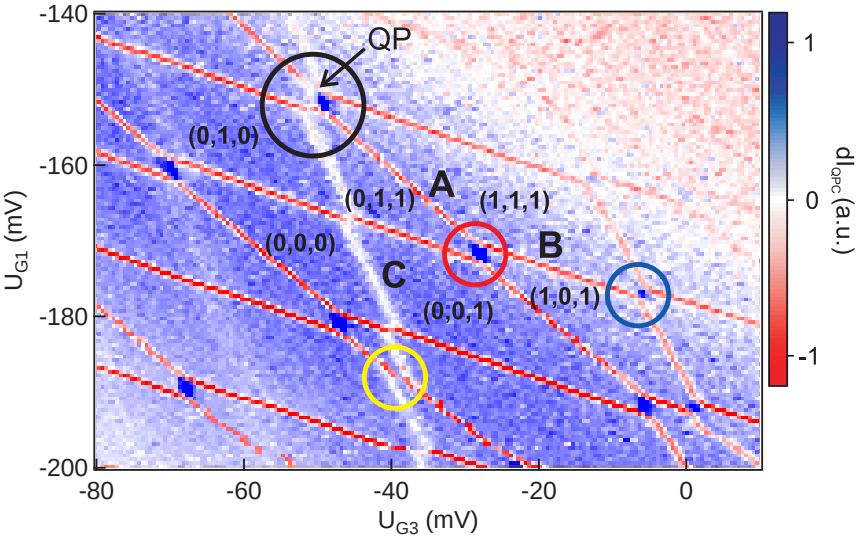

Figure 4.3: Excerpt of a charge measurement using the QPC. Double dot resonances between dots A and B (red circle), A and C (yellow circle), and B and C (blue circle) are observed. Additionally, a triple dot resonance (black circle) with a quadruple point (QP) being clearly visible is seen within this measurement range.

The charge configurations are denoted as $(N_\mathrm{A}, N_\mathrm{B}, N_\mathrm{C})$, where the numbers N_i are the occupations of dots A, B, C. In N_i the electrons in the core of the dots are not taken into account, the values N_i are given relative to (0,0,0), which is fixed individually to support the analysis. This is true for all notations of charge configurations of the system given within the scope of this thesis. The intensity of the charging lines of dot C decreases for

increasing negative gate voltage U_{G3} and the charging lines additionally become broader. This can also be observed in the charging diagrams in Fig. 4.4 and Fig. 4.5 covering a wider gate voltage regime. This is a hint for an increasing coupling between dot C and its lead S_2 (seen in transport in Eq. (2.109), Eq. (2.110) and in section 3.2). By increasing the negative potential at U_{G3} dot C is shifted towards the tunneling barrier to S_2. This leads to an increasing distance between dot C and the other dots which in turn decreases the capacitive inter-dot couplings between them. This can be observed in the decrease of the shift of the charging lines in the resonances between dot C and A, B. For large negative gate voltages at U_{G3} no interaction between the charging lines of dot C and the other two dots is observed. Additionally, the distance between the lines is reduced at the same time, best observable in Fig. 4.4 and Fig. 4.5. Here it is clearly visible that they have a constant but reduced spacing of $\Delta U_{G3} = 18\,\mathrm{mV}$ between them for $U_{G3} < -40\,\mathrm{mV}$, while for $U_{G3} > -40\,\mathrm{mV}$ the spacing is $\Delta U_{G3} = 34\,\mathrm{mV}$. A decreasing spacing between the charging lines in dependence of U_G results from a decreasing ratio C_G/C_Σ (Eq. (2.33)). An increasing sum capacitance thus leads to a smaller spacing between the lines in the charging diagram. A larger sum capacitance of the dot can originate from a shift with respect to the other gates and leads. The increased capacitance could mainly result from the stronger coupling of dot C to S_2. This is also suggested by the observation that the intensity decreases strongly in the transition region where the distance between the lines is reduced.

The capacitive couplings $C_{G1,A}$, $C_{G1,B}$, $C_{G1,C}$ between the dots A, B, C and gate G_1 and the couplings $C_{G3,A}$, $C_{G3,B}$, $C_{G3,C}$ between the dots and G_3 can be directly extracted from the charging diagram by measuring the distance between the charging lines of the respective dot in U_{G1} and U_{G3} sweeping direction using Eq. (2.57). The extracted values are listed in table 4.1. They refer to this certain measurement range as the capacitances change with the size of the dots, but can still be used as an approximation in other regimes. We can deduce for the size of the dots that B > A > C in this parameter regime.

4.2.1 Drain decoupled system

By varying the gate voltages of the device the inter-dot and dot-lead tunneling rates can be tuned into a regime where they are very asymmetric within a transport path. For increasing negative values of U_{G1} and especially U_{G3},

Gate	Dot A	Dot B	Dot C
1	$C_{\mathrm{G1,A}} = 6.5$	$C_{\mathrm{G1,B}} = 12.8$	$C_{\mathrm{G1,C}} = 2.2$
3	$C_{\mathrm{G3,A}} = 5.5$	$C_{\mathrm{G3,B}} = 4.3$	$C_{\mathrm{G3,C}} = 5.3$

Table 4.1: Capacitive couplings in aF between the dots and G_1 and G_3 extracted from Figure 4.3.

the tunneling barrier between dot A and drain is increasing relative to the others in the transport path. Thus, $\Gamma_{\mathrm{A}} \ll \Gamma_{\mathrm{B}}$ and $\Gamma_{\mathrm{A}} \ll \tau_{\mathrm{AB}}$ is obtained for high negative values of U_{G1} and U_{G3}.

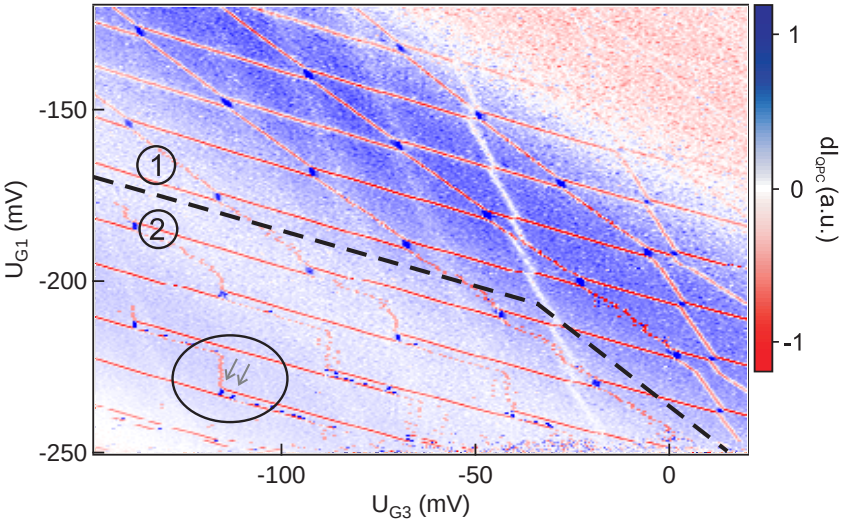

Figure 4.4: Charge stability diagram for $U_{\mathrm{S,QPC}} = 0\,\mathrm{mV}$ QPC bias voltage. Starting from a condition where the dots in path 1 are approximately equally and moderately coupled to their leads (region 1) the tunneling barriers in path 1 are tuned high and asymmetric towards higher negative values of U_{G1} and U_{G3}. For large negative values of U_{G1} and U_{G3} the drain lead becomes decoupled and charging line of dot A is transformed into two lines with different slopes, exemplarly marked with a black circle (region 2). The occurence of multiple charge reconfiguration lines of the resonance between dots A and B is marked with grey arrows expemplarily within this circle.

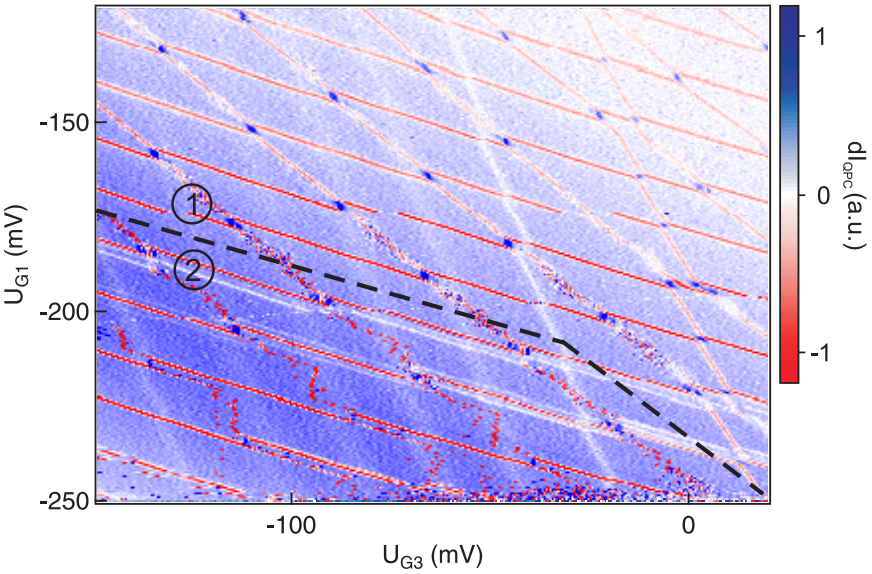

Figure 4.5: Charge stability diagram for relatively large ($U_{\mathrm{S,QPC}} = 1\,\mathrm{mV}$) QPC bias voltage. The tunneling barriers in path 1 are tuned high and asymmetric towards higher negative values of U_{G1} and U_{G3}. This results in a change in the charging lines of dot A from normal charging lines (region 1) towards step-like charging lines (region 2), analogously to Fig. 4.4.

The detector signal derivative is plotted as a function of U_{G1} and U_{G3} for zero (Fig. 4.4) and relatively large ($U_{\mathrm{S,QPC}} = 1\,\mathrm{mV}$) (Fig. 4.5) QPC bias voltage. U_{G1} and U_{G3} are swept from negative to positive values. Both measurements can be divided into two regions, region 1 for lower values of U_{G1} and U_{G3}, region 2 for higher values. They are separated by a black dashed line in Fig. 4.4 and Fig. 4.5. In region 1 the system is in a condition of moderate dot-lead coupling where charging events between both dots and their leads ($\mathrm{A} \leftrightarrow \mathrm{D}, \mathrm{B} \leftrightarrow \mathrm{S_1}$) are significantly faster than the integration time. Typical charging lines of dot A are observed.

The charging lines of dot A become increasingly noisy with increasing negative gate voltages U_{G1} and U_{G3}. This shows that the tunneling barrier between dot A and drain is growing very large. As a result, the tunneling rate for charging events between dot A and the drain lead becomes compara-

ble with the measurement integration time of 500 ms so that the statistical nature of the tunneling processes is revealed. For even higher negative gate voltages $U_{G1} < -180\,\text{mV}$ and $U_{G3} < -20\,\text{mV}$ (region 2 in Fig. 4.4 and Fig. 4.5) the charging lines of dot A marking the charging of A via the drain lead completely disappear. Thus we expect the tunneling barrier between A and drain to be closed in this regime with respect to measurement timescales. Therefore, the drain lead D is decoupled. The system is transformed into a serial double dot connected to one single lead, S_1. Instead of the typical charging line of dot A in a serial double dot system with two leads, now a more complex charging behavior is obtained. A partition of the charging line into two lines with different slopes is obtained: One line with the slope of the charging line of dot B and one with the same slope as the charge reconfiguration line at the resonance between dots A and B (marked in Fig. 4.4). Comparison of Fig. 4.4 and Fig. 4.5 shows that this double slope charging line behaviour is independent of the applied QPC bias voltage. The effect does not disappear for $U_{S,QPC} = 0\,\text{mV}$. It is thus not to be attributed to detector feedback effects [92–94].

Figure 4.6 shows a schematic of a charge stability diagram in this drain decoupled region. The charging lines around an A-B resonance are depicted. As dot C does not contribute to the effect described above, the charge states are only given for the double dot A-B (N_A, N_B) in the following.

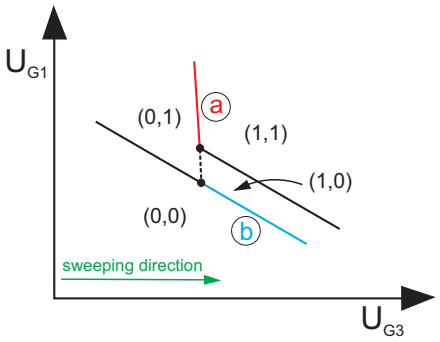

Figure 4.6: Schematic of a charging diagram in case of $\Gamma_A \ll \Gamma_B, \tau_{AB}$. As this effect concerns the double dot A-B only and dot C does not contribute, the charge states are only given for the double dot (N_A,N_B).

Along the charging line marked with (a) the dots A and B are in resonance, as it is an extension of the charge reconfiguration line. To further understand the charging line (a) a schematic picture is presented in Figure 4.7. It shows the configuration of tunneling barriers and chemical potentials in path 1 depicting the particular two-step sequential tunneling process which leads to the charging of dot A along line (a). Dot A has an empty energy level, which was not occupied when it was in resonance with drain at more negative U_{G3} as the tunneling barrier to the drain lead is closed. When dots A and B come into resonance below the chemical potential of the leads, dot A can be charged via dot B. Each time one additional electron occupies dot A the energy levels of dot B are shifted to higher energies by $\Delta = \Delta\mu_B = e^2 C_{AB}/(C_{\Sigma A} C_{\Sigma B})$ (Eq. (2.68)) due to Coulomb repulsion according to the capacitive coupling between the dots. The empty energy level of dot B still being energetically below the chemical potential of the leads, is then charged by one electron via source S_1. Thus, crossing line (a), the charge configuration of the system changes from (0,1) to (1,1) as dot A is charged over dot B which is immediately refilled via S_1.

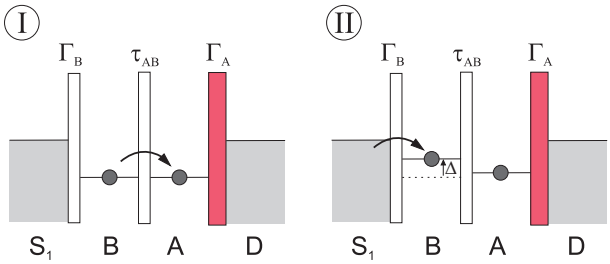

Figure 4.7: Schematic of the tunneling process leading to the charging line part (a) (Fig. 4.6). The tunneling barrier highlighted in red is assumed to be closed within measurement timescales.

Figure 4.8 shows a schematic of the configuration of tunneling barriers and chemical potentials in path 1 with the two-step sequential tunneling process leading to the charging of dot A along line (b). Along the charging line marked with (b) dot B is in resonance with the leads. Dot A, which has an empty energy level below the chemical potential of the leads as the tunneling barrier to drain is closed, can be charged from source S_1 over dot B. When dot A is charged by one electron, the energy levels of dot

B are again shifted to higher energies by Δ according to the capacitive coupling between the dots. The energy level of dot B which was in resonance with the leads before is now Δ in energy higher than the chemical potentials of the leads. For more positive gate voltages, when the energy levels of dot B are shifted by $-\Delta$, a charging line parallel to line (b) appears, where the energy level of dot B is again in resonance with the leads and dot B is charged with one electron. According to Eq. (2.69) this distance in gate voltage is $\Delta U_{\mathrm{G1}} = eC_{\mathrm{AB}}/(C_{\mathrm{G1,B}}C_{\Sigma\mathrm{B}})$ in direction of U_{G1} and $\Delta U_{\mathrm{G3}} = eC_{\mathrm{AB}}/(C_{\mathrm{G3,B}}C_{\Sigma\mathrm{B}})$ in direction of U_{G3}.

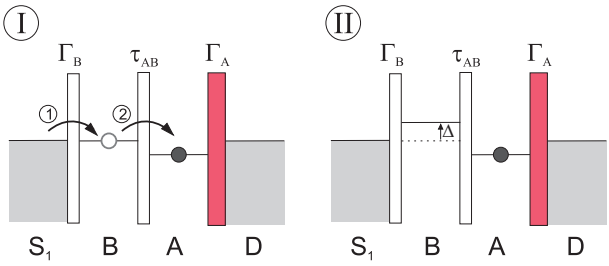

Figure 4.8: Schematic of the tunneling process leading to the charging line part (b) (Fig. 4.6). The tunneling barrier highlighted in red is assumed to be closed within measurement timescales. The numbers 1, 2 indicate the order of the tunneling events.

The noisiness of the two charging lines (a) and (b) shows, that τ_{AB} is comparable to the integration time as well.

In some regions in the drain decoupled regime multiple parallel charge reconfiguration lines of the one separating the states (0,1) and (1,0) are detected independent on QPC bias voltage. Figure 4.9 shows a cut through such a region, marked in Figure 4.4. As the drain lead at dot A is basically decoupled so that the electron can not escape through the drain within the measurement time, back- and forth transitions of the electron between dot A and dot B can be detected within this time. The reason can be a rectification effect [95] due to external frequency noise in the kHz-GHz regime [96, 97].

When increasing U_{G3} at constant U_{G1} to transfer the system from charge

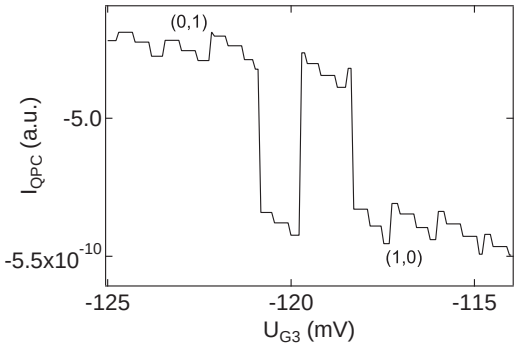

Figure 4.9: Perpendicular cut across a double charge reconfiguration line (marked in Fig. 4.4 with gray arrows). Shown is the QPC current I_{QPC} with respect to the gate voltage U_{G3}. Three fast transitions between the states (0,1) and (1,0) can be identified.

state (0,0) to (1,0), the end state (1,0) can not be achieved until the so-called controlling voltage U_{G3} is sufficiently large, meaning significantly more positive than the value expected in thermal equilibrium. In analogy to the transitions occurring for increasing U_{G3} (Fig. 4.7 and Fig. 4.8), we can deduce the transitions for decreasing U_{G3}. A schematic of the charging diagram for decreasing U_{G3} is shown in Fig. 4.10.

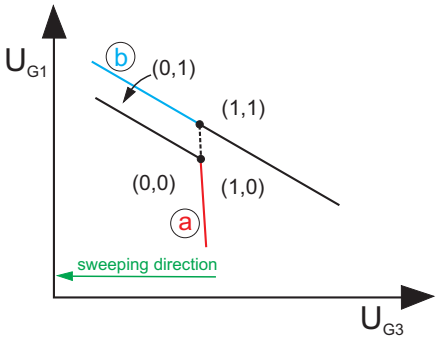

Figure 4.10: Schematic of the charging diagram in case of $\Gamma_{\mathrm{A}} \ll \Gamma_{\mathrm{B}}, \tau_{\mathrm{AB}}$ for reverse U_{G3}-sweeping direction from positive to negative U_{G3}.

The corresponding tunneling processes leading to the distinct features (lines (a) and (b)) are sketched in Fig. 4.11 and Fig. 4.12, respectively.

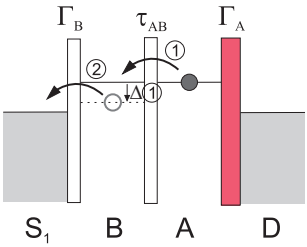

Figure 4.11: Schematic of the tunneling process leading to the charging line part (a) (Fig. 4.10). The numbers 1, 2 indicate the order of the tunneling events.

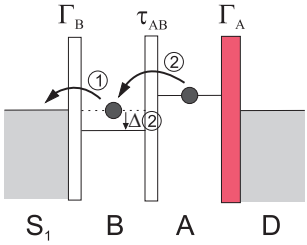

Figure 4.12: Schematic of the tunneling process leading to the charging line part (b) (Fig. 4.10). The numbers 1, 2 indicate the order of the tunneling events.

In contrast to the processes where U_{G3} is swept to more positive values and dot A is charged (Fig. 4.7, Fig. 4.8), dot A is discharged over dot B in this case. Note that whenever dot A is discharged, the potential of dot B is shifted by $-\Delta$ to smaller values due to the capacitive inter-dot coupling. The stability diagrams for the two sweeping directions of the controlling gate voltage U_{G3} are different. The charge configuration of the dot system depends on the history of its charge configuration. While the charging lines belonging to the charging events of dot B are not affected by the direction of the U_{G3} sweep, the position of the charging lines which belong to the charging events of dot A ((a) and (b)) depends on the sweeping direction.

This hysteretic behavior stems from the fact that dot A can only be charged via dot B. The controlling voltage U_{G3} has to be reversed to an extend that dot A can be discharged again via an energy level of dot B. Due to this effect of Coulomb blockade in dot B and the capacitive inter-dot coupling between dots A and B, which causes the shift of $\pm\Delta$ in the chemical potentials of dot B whenever dot A is charged (+) or discharged (-), the charging events of dot A underlie a hysteresis. This hysteretic behaviour was previously described by Yang et al. [98] for a double dot system for which they observed this effect in a small region of the stability diagram.

In case of a large τ_{AC} between the dots the hysteretic effect vanishes, since a large tunnel coupling leads to a significant probability of cotunneling [44, 55] (see section 2.3.2.3 and Eq. (5.25) in section 5.3) between source S_1 and dot A. Cotunneling and the described sequential tunneling process coexist, where cotunneling can become dominant [98]. Varying the gate voltage U_{G1} does not only shift the energy levels but also influences the tunnel barrier between the dots A and B. An increasing negative U_{G1} decreases the strength of the tunnel coupling between dot A and B. This in turn decreases the probability of cotunneling events. Additionally, increasing negative U_{G1} and especially U_{G3} leads to a decreasing tunnel coupling between dot A and drain. Since tunneling rates below the measurement speed are a necessary condition to establish the non-equilibrium initial state, this increases the probability to observe the described sequential tunneling processes of charging dot A via dot B. Consequently the hysteretic effect gradually becomes more pronounced with increasing negative potential at G_1 and G_3 (Fig. 4.4 and Fig. 4.5).

This hysteretic behavior regarding the electronic occupations of the dot system can be utilized for the implementation of a single-electron Set/Reset memory latch [98, 99]. Such a single-electron memory device typically has two inputs, *Set* and *Reset*, and two outputs, the logic states Q and Q^*. State Q^* is the inverse of Q. It is operated such, that the *Set* input sets Q=1, the *Reset* input sets Q=0.

The hysteretic charge transitions of the device can be controlled by the controlling gate voltage U_{G3}. This enables the implementation of these set/reset operations, as depicted in Fig. 4.13. The memory consists of three different states: *Reset*, *Hold* and *Set*. Starting in the *Reset* condition with the system being in the logic state Q $\equiv$ (0,0), by sweeping U_{G3} to more

positive values, the *Hold* region is reached where the previous system state is preserved, at even more positive values of U_{G3} the system is set into a new state $Q^* \equiv (1,0)$ by entering the *Set* region (Fig. 4.13 (a)). To reset the system, U_{G3} has to be swept back, whereby the system again keeps the set state during the *Hold* region and is only reset when entering the *Reset* regime (Fig. 4.13 (b)). The hysteresis of the system ensures the *Hold* condition for both *Set* and *Reset* operations. In our case, by sweeping the system between *Set* and *Reset*, the electron number on dot A changes by one. These latch transitions are also possible for different electron numbers on dots A and B, as given for larger values of U_{G1} and U_{G3}, as long as the described requirements for the tunneling barriers are fulfilled.

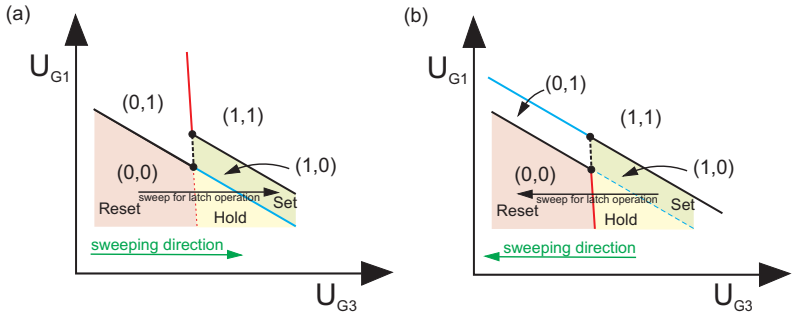

Figure 4.13: Schematic of latch operations between the charge states $Q \equiv (0,0)$ (*Reset*) and $Q^* \equiv (1,0)$ (*Set*) [98]. Equivalent latch transitions are also possible at different electron numbers in dot A and B, as long as the requirements for the tunnel barriers are fulfilled.

4.2.2 Detector feedback effects

In order to investigate the feedback of the detector system on the TQD system, the QPC bias voltage $U_{S,QPC}$ is varied. For vanishing bias voltage feedback effects are expected to vanish as well. On the other hand they are expected to be pronounced for a large QPC bias voltage. In Fig. 4.14 the detector current derivative is shown in dependence of U_{G1} and U_{G3} and for different $U_{S,QPC}$.

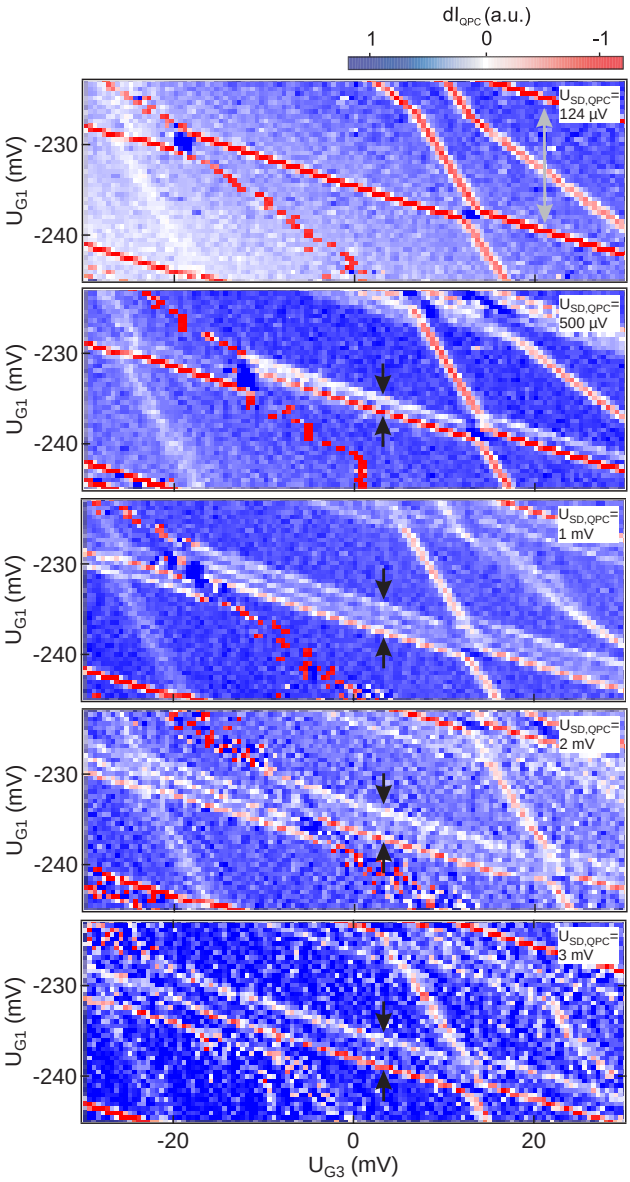

Figure 4.14: Comparison of the feedback effect for $U_{\mathrm{S,QPC}} = 124\,\mu\mathrm{V}$, $U_{\mathrm{S,QPC}} = 0.5\,\mathrm{mV}$, $U_{\mathrm{S,QPC}} = 1\,\mathrm{mV}$, $U_{\mathrm{S,QPC}} = 2\,\mathrm{mV}$, and $U_{\mathrm{S,QPC}} = 3\,\mathrm{mV}$. Multiple charging lines of dot B appear for $U_{\mathrm{S,QPC}} \geq 0.5\,\mathrm{mV}$ and for N and N-1 electrons on dot B.

For a QPC bias voltage of $U_{\mathrm{S,QPC}} = 0.5\,\mathrm{mV}$ a double charging line of dot B instead of a single one is present for a certain number of electrons N and, much less pronounced, also for N-1 electrons on dot B. One additional line in a very small distance to the charging line of dot B appears. At $U_{\mathrm{S,QPC}} = 124\,\mu\mathrm{V}$ this effect is not present, which indicates that it is a feedback effect, induced by $U_{\mathrm{S,QPC}}$. For $U_{\mathrm{S,QPC}} \geq 1.0\,\mathrm{mV}$ multiple charging lines appear as well, also clearly for N-1 electrons on dot B. Two additional charging lines arise, doubling the region where multiple charging lines of dot B are visible with respect to the measurement with $U_{\mathrm{S,QPC}} = 0.5\,\mathrm{mV}$. The regions is marked with black arrows in Fig. 4.14. For even larger QPC bias, $U_{\mathrm{S,QPC}} = 2.0\,\mathrm{mV}$ and $U_{\mathrm{S,QPC}} = 3.0\,\mathrm{mV}$ the size of this region is the same as for $U_{\mathrm{S,QPC}} = 1.0\,\mathrm{mV}$. To sum up, the effect appears for $U_{\mathrm{S,QPC}} \gtrsim 0.5\,\mathrm{mV}$, the region where multiple charging lines of dot B are visible grows for increasing $U_{\mathrm{S,QPC}}$ and stays constant for $U_{\mathrm{S,QPC}} \gtrsim 1.0\,\mathrm{mV}$.

Coulomb interaction between fluctuating charge carriers as an exchange mechanism in mesoscopic systems is prevalent at low temperatures [100]. In our system such a direct exchange mechanism can take place between statistically fluctuating charge carriers in the QPC and the electrons in the quantum dot system. The maximum energy being available from a biased QPC as an energy source for electron excitations in the dot system is $E_{\mathrm{max}}^{\mathrm{QPC}} = e\,|U_{\mathrm{S,QPC}}|$. [92, 93] The energy can be absorbed by electrons on the quantum dots by Coulomb interaction, leading to charge fluctuations in an otherwise Coulomb blockaded dot. The size of this charge fluctuation region can then be identified with the energy the dot can absorb in one process, which in turn is determined by the energy provided by the non-equilibrium electrons in the QPC, $E_{\mathrm{max}}^{\mathrm{QPC}}$.

The maximum provided energy $E_{\mathrm{max}}^{\mathrm{QPC}}$ and the energy E_{max} absorbed by the system measured as energy differences between the ground state resonance line of dot B and the outer parallel line (marked by black arrows in Fig. 4.14) is shown in dependence of the applied QPC bias energy, E^{QPC} in Figure 4.15. In Fig. 4.14 in the measurement with $U_{\mathrm{S,QPC}} = 500\,\mu\mathrm{V}$ it is $E_{\mathrm{max}}^{\mathrm{QPC}} = 0.5\,\mathrm{meV}$. After conversion from gate voltage to energy scales (Eq. (2.34)) with $C_{\mathrm{G1,B}} = 10.3\,\mathrm{aF}$ extracted for this measurement regime (see Fig. 4.14) and the sum capacitance $C_{\Sigma\mathrm{B}}$ from table 5.1 we obtain for the distance between the parallel lines $E_{\mathrm{max}} \cong 0.5\,\mathrm{meV}$, being in agreement with the maximum energy being available from the QPC, $E_{\mathrm{max}}^{\mathrm{QPC}}$. For $U_{\mathrm{S,QPC}} = 1.0\,\mathrm{mV}$ we have $E_{\mathrm{max}}^{\mathrm{QPC}} = 1.0\,\mathrm{meV}$ and the energy distance between

the lines is $E_{\max} \cong 1.0\,\mathrm{meV}$, which is also in agreement. A systematic error source in the calculation of $E_{\max}$ is the sum capacitance used in the energy conversion, which changes with respect of the gate voltages and was not measured for this parameter region where the dots are quite small. It is expected for $C_{\Sigma \mathrm{B}}$ to be slightly smaller. Consequently $E_{\max}$ might be a bit underestimated. Thus, the distance between the ground state resonance line and the outer parallel line above (marked by black arrows in Fig. 4.14) can be identified with the energy the dot can absorb in one process, which in turn is determined by the maximum energy provided by the non-equilibrium electrons in the QPC, $E_{\max}^{\mathrm{QPC}}$. Within this region ebwteen the two lines the charge of dot B fluctuates due to the energy provided by the QPC. Dot B is excited which enables charge fluctuations of the Coulomb blockaded dot B over S_1.

For $U_{\mathrm{S,QPC}} = 2.0\,\mathrm{mV}$ and $U_{\mathrm{S,QPC}} = 3.0\,\mathrm{mV}$, where $E_{\max} = 2.0\,\mathrm{meV}$ and $E_{\max} = 3.0\,\mathrm{meV}$, respectively, are expected, no change in the size of the charge fluctuating region is observed (Fig. 4.15). This can not be explained in terms of a direct back-action mechanism where a linear dependence on $U_{\mathrm{S,QPC}}$ is expected.

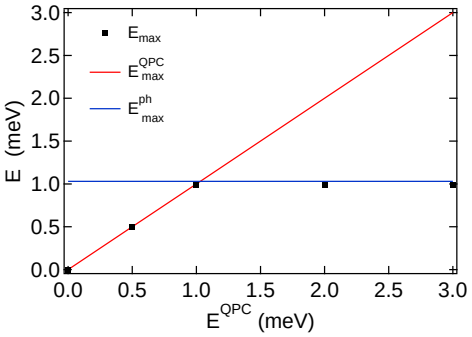

Figure 4.15: Comparison of the relevant energies, $E_{\max}^{\mathrm{QPC}}$, $E_{\max}^{\mathrm{ph}}$ and $E_{\max}$ in dependence of the bias energy applied to the QPC, E^{QPC}. The measured $E_{\max}$ rises linearly as $E_{\max}^{\mathrm{QPC}}$ and saturates at around $E_{\max}^{\mathrm{ph}}$.

Indirect back-action mechanisms can account for this behaviour. These mechanisms between a biased QPC and a quantum dot system involve the relaxation of non-equilibrium charge carriers via emission of acoustic phonons,

photons, 1D-plasmons, or electron-electron interaction [92, 94, 101]. A common indirect back-action mechanism is the emission of acoustic phonons by hot electrons in the leads of a biased QPC, which relax into ground state via this emission [92, 93, 100, 102, 103]. The emitted phonons can propagate through the potential barrier between the QPC and the quantum dot system and be absorbed by electrons on the quantum dots. This can cause charge fluctuations within the dots via excited states. The size of the region within which charge fluctuations can take place is limited by the energy the dot absorbs in one process, which in turn is determined by the phonon energy in this back-action mechanism [92].

An electron of momentum $\hbar k_e$ can emit an interface acoustic phonon of momentum $k_{\mathrm{ph}} \lesssim 2\hbar k_e$ due to energy and momentum conservation law during the back-scattering process [100]. Consequently, the momentum an equilibrium electron at the Fermi energy can reabsorb from an interface acoustic phonon is also limited to $2\hbar k_F$. Thus, an electron in a quantum dot can be lifted to excited states in $\Delta E \lesssim 2\hbar k_F v_s$ distance from its respective ground state [92], with v_s being the sound velocity for acoustic phonons in the semiconductor.

In order to estimate this maximum energy $E_{\mathrm{max}}^{\mathrm{ph}} = 2\hbar k_F v_s$, which can be transferred by an interface acoustic phonon in this back-action mechanism for our system, k_F is calculated by $k_F = (2\pi n_e)^{1/2}$ for a 2DEG with the electron density of $n_e = 3.47 \cdot 10^{15}\,\mathrm{m}^{-2}$ (Fig. 3.2). With this and the maximum sound velocity of $v_s = 5300\,\mathrm{m/s}$ for longitudinal acoustic phonons in bulk GaAs ((110)-direction) [104] we obtain $E_{\mathrm{max}}^{\mathrm{ph}} \cong 1.03\,\mathrm{meV}$.

In the measurements Fig. 4.14 the size of the charge fluctuating region, E_{max}, bounded by the outer line parallel to the usual ground state resonance line of dot B, stays constant with increasing QPC bias for $U_{\mathrm{S,QPC}} \geq 1.0\,\mathrm{mV}$. This maximum size of the charge fluctuating region is $E_{\mathrm{max}} \cong 1.0\,\mathrm{meV}$. This corresponds very well to the maximum acoustic phonon energy of $E_{\mathrm{max}}^{\mathrm{ph}} \cong 1.03\,\mathrm{meV}$ calculated for this system, as clearly visible in Figure 4.15, and indicates that phonon-mediated back-action can play a role in the presented charge measurements. A source of error results from the estimation of the maximum phonon energy in this system and from the described slight inaccuracy expected for E_{max}. The upper bound found for the transferred energy E_{max} in the observed back-action process reflects the existence of phononic back-action in this device and its domination. [100] The observed

bias dependence of $E_{\max}$ can be explained by a domination of this indirect back-action process. The phonon energy increases in proportion to the provided QPC energy $E_{\max}^{\mathrm{QPC}}$ [93] and has an upper bound at $E_{\max} \cong 1.0\,\mathrm{meV}$. The excitation of dot B giving rise to the charge transfer while the dot is in Coulomb blockade can thus be explained by an indirect energy transfer mediated by phonons. The observed clear bound of $E_{\max}$ indicates a relatively low proportion of direct Coulombic back-action, however, the significance of this analysis is limited by the measurement resolution. Especially at high bias votages the indirect back-action can be dominant in relation to direct back-action mechanisms. [105] Similar non-equilibrium charge fluctuations in a dot system caused by energy quanta emitted from a biased QPC leading to charge fluctuating regions have been reported in [94, 101]. For systems where the observed back-action between QPC and dot system is attributed to be mediated by acoustic phonons a linear increase of E_{max} with the bias voltage is detected [93] and a maximum phonon energy is identified [92, 100].

In summary, the triple quantum dot system was characterized within this section by charge measurements using a QPC as a detector. The system is analyzed electrostatically by deriving the capacitive couplings between the dots A, B, C and gates G_1 and G_{G3}. In dependence of gate potentials different charging mechanisms of dot A situated at the drain contact are observed. The system is driven into a drain-decoupled condition where two different tunneling sequences to charge dot A over the source lead take place which are clearly observed in a wide gate parameter region. The capacitive coupling between dots A and B leads to a hysteretic behaviour when reversing the sweeping direction, so a utilization of this effect in a Set/Reset memory latch is conceivable. Observed back-action effects are discussed regarding their energy source considering direct Coulombic and indirect phononic back-action giving indications of a dominant indirect phonon-mediated meachanism.

4.3 Path-resolved transport measurements

4.3.1 Linear transport regime

To characterize the TQD system regarding its basic transport properties the differential conductance G is measured along path 1 (Fig. 4.16) and path 2 (Figure 4.17) simultaneously but separately as a function of U_{G1} and U_{G3}. The gate voltage U_{G1} is mainly controlling the dot potentials and couplings in the left path and U_{G3} is mainly controlling the ones in the right path. The further course of this thesis will focus on the reaction of the system transport on the variation of the potentials of these two gates. During transport measurements the QPC is not in use to avoid the possibility of backaction.

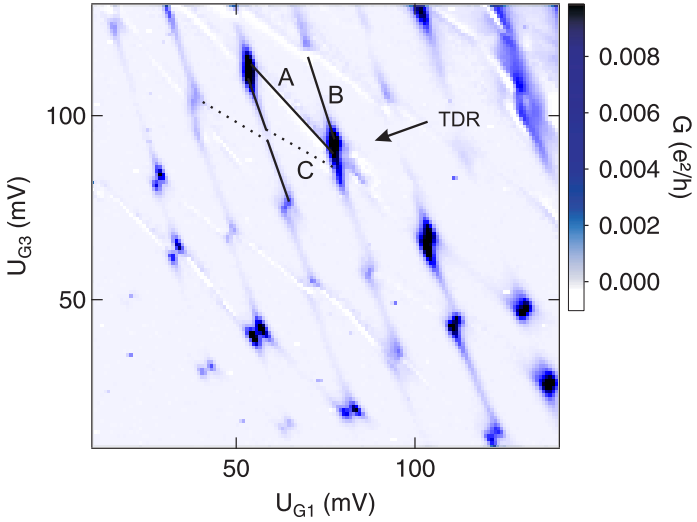

Figure 4.16: Transport through path 1. The differential conductance G is shown in dependence of the gate voltages U_{G1} and U_{G3}. Charging lines of dots A and B (solid lines) are observed. Charging of dot C (dotted line) is observed by a shift of the charging lines of dots A and B.

Transport features of all three dots are detected. Double dot physics are

observed in the stability diagrams of both transport paths with additional signatures of a capacitively coupled third dot. Transport through one path is possible at the triple points, when the dots located in this path are in resonance.

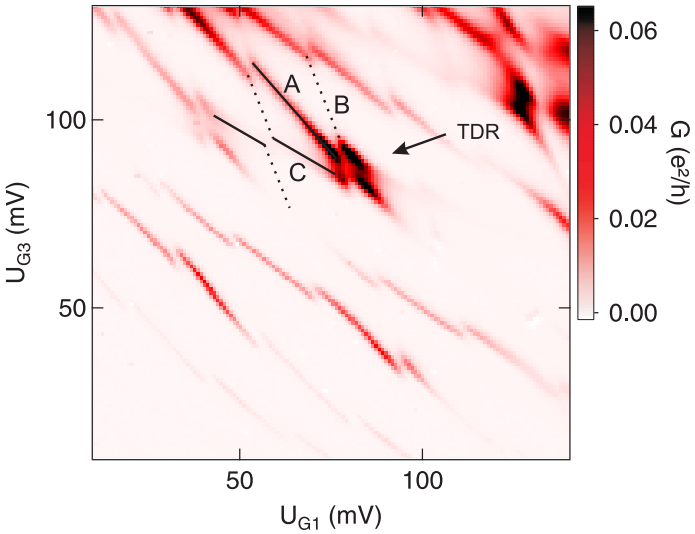

Figure 4.17: Transport through path 2. The differential conductance G is shown in dependence of the gate voltages U_{G1} and U_{G3}. Charging lines of dots A and C (solid lines) are observed. Charging of dot B (dotted line) is observed by a shift of the charging lines of dots A and C.

In path 1 we find high differential conductance at the triple points where dots A and B are in resonance. Analogously to the charge measurement (see section 4.2), we can identify the dots by their expected couplings to the gates derived from their location. Dot B is coupled much stronger to G_1 than to G_3 and is charged along the lines with highest slope. The charging lines of dot A have intermediate slope and the charging lines of dot C have the smallest gradient as the coupling between dot C and G_1 is much smaller than between C and G_3. As dot C is not located in this transport path, but capacitively coupled to dot A and B, its charging is observable by a shift of the charging lines of dot A and B where it comes

into resonance. Analogously in path 2 resonances between dots A and C and shifts of their charging lines marking the charging of dot B are visible. Only one charging line of dot C is visible in this measurement. The bending of the charging lines and the resulting change in distance between them stems from a varying dot-gate coupling. For conditions where we have a double dot resonance in both paths the resonance condition for all three dots is fulfilled and a triple dot resonance is formed (marked with an arrow in Fig. 4.16 and Fig. 4.17).

For small U_{G1}, U_{G3} the differential conductance vanishes as the tunnel rates are too small to allow detectable current through the dots. The rounded broadened shape of the conductance region at the triple points in both paths is a coherence effect due to a strong inter-dot tunnel coupling (see section 2.3.2.4). The triple points in path 1 become increasingly rounded and broadened (Fig. 4.16) as the inter-dot tunnel coupling between dot A and B increases with increasing U_{G1}. The same is true for the tunnel coupling between dots A and C increasing with the gate voltage U_{G3} in path 2, visible in transport in Fig. 4.17. The electrons are rather delocalized between the dots occupying molecular states. An effect also contributing to non-zero differential conductance in the vicinity of the triple points is temperature broadening of the dot energy levels. In path 2 strong finite differential conductance is visible along the whole charging line of dot A. This is a consequence of second-order tunneling, cotunneling, between S_2 and dot A across the off-resonant dot C (see section 2.3.2.3). It becomes even more pronounced for increasing U_{G3} as this increases the tunnel coupling between dots A and C. For large values of U_{G1} high differential conductance along the whole charging line of dot B between two triple points in path 1 can be observed as well. Analogously to path 2 cotunneling between dot B and drain across the off-resonant dot A can contribute to this effect in this region of strong inter-dot tunnel coupling. The cotunneling in the double dots visible in transport, especially concerning the interplay between the transport paths, is shown and explained in more detail within section 5.3.

The capacitive couplings $U_{G1,A}$, $U_{G3,A}$, $U_{G1,B}$, $U_{G3,B}$, $U_{G1,C}$, and $U_{G3,C}$ extracted from the stability diagrams (Eq. (2.57)) are shown in table 4.2. They correspond well to the capacitances extracted from the charge measurements (table 4.1). The differences stem from the variation of the couplings caused by different gate potentials.

capacitive couplings		
$C_{\mathrm{G1,A}} = 6.8$	$C_{\mathrm{G1,B}} = 8.0$	$C_{\mathrm{G1,C}} = 3.3$
$C_{\mathrm{G3,A}} = 6.6$	$C_{\mathrm{G3,B}} = 2.6$	$C_{\mathrm{G3,C}} = 5.1$

Table 4.2: Capacitive couplings C in aF between the dots and the gates G_1 and G_3.

4.3.2 Non-linear transport regime

Non-linear transport is investigated separately for the two transport paths as well. In Fig. 4.18 the differential conductance is shown for path 1 and 2 for varying bias voltage at path 1, U_{S1}, and gate voltage U_{G3}. Since the bias voltage is varied across transport path 1 with serial dots A and B, in the transport of path 1 Coulomb diamonds (see section 2.3.2.2) of dots A and B are visible.

The Coulomb diamond measurements are analyzed by comparison with the stability diagrams measured in gate-gate space for the same parameter region (see Fig. 4.18 (a), bottom and (b), bottom). The diamonds dominating the observed features can be ascribed to dot A. Where there is high differential conductance visible in both paths at $U_{\mathrm{S1}} = 0\,\mathrm{mV}$, a region of a quadruple point is crossed by the measurement plane, where all three dots are in resonance. This is the case for around $U_{\mathrm{G3}} = 260\,\mathrm{mV}$ and $U_{\mathrm{G3}} = 278\,\mathrm{mV}$. In the region around $U_{\mathrm{G3}} = 210\,\mathrm{mV}$ the dots are very close to a triple dot resonance as well, as visible best in the conductance features in Fig. 4.18 (b), bottom. As there are two serial dots within a path, we expect a sawtooth-like pattern of Coulomb diamonds (see section 2.3.2.4). In the measurements this is observed at a rudimentary level basically in the upper part of the transport measurement of path 1, as mostly rather an overlay of the Coulomb diamonds of the single dots in each path is seen. Where non-zero conductance is visible at $U_{\mathrm{S1}} = 0\,\mathrm{mV}$ we expect a triple point, where the dots in the respective path are in resonance. However, we see small non-zero conductance whenever dot A is in resonance with the leads, as observable at $U_{\mathrm{G3}} = 243\,\mathrm{mV}$. This behaviour stems from coherence effects or cotunneling due to the strong inter-dot coupling. These effects are obvious in both stability diagrams in Fig. 4.18, where high differential conductance along the charging lines of dots A and B are observed.

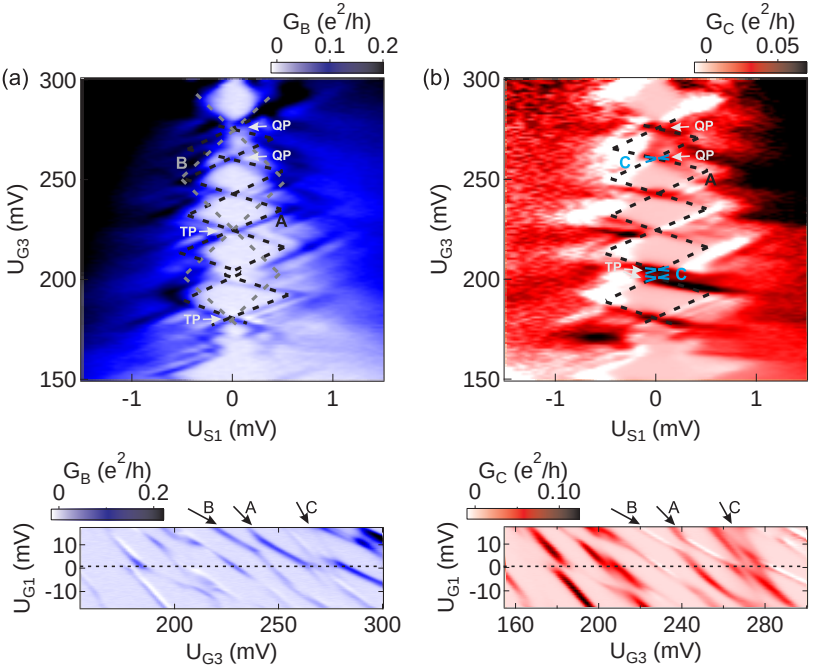

Figure 4.18: Transport through path 1 (a) and path 2 (b). The differential conductance G is shown in dependence of the bias voltage U_{S1} and the gate voltage U_{G3}. Coulomb diamonds of the dots which can be identified in the measurement are marked by dotted lines. In path 1 resonances of dot A and B with the leads are seen. In path 2 signatures of resonances between dot A and the leads can also be identified, as well as resonances between dots A, C and the leads. For comparison the corresponding stability diagrams for path 1 ((a), bottom) and 2 ((b), bottom) are shown, where all dots can be identified due to resonances between them. The Coulomb diamond measurements are performed at $U_{G1} = 1.5\,\mathrm{mV}$ (dashed line).

This results in non-zero conductance at $U_{S1} = 0\,\mathrm{mV}$ also for the system being near a triple point. Triple points are characterized by high conductance through one path only. They are observed at $U_{G3} = 179\,\mathrm{mV}$ and $U_{G3} = 224\,\mathrm{mV}$ in path 1, where dots A and B are in or close to resonance, and at $U_{G3} = 199\,\mathrm{mV}$ and $U_{G3} = 204\,\mathrm{mV}$ in path 2, belonging to the same resonance of dots A and C. This latter resonance however is close to a triple dot resonance, as explained above.

Two kinds of resonance lines crossing at the triple and quadruple points can be observed in the transport of path 1. Their slopes correspond to the coupling between the leads and dots A and B, respectively. In this way Coulomb diamonds of dot A and B can be identified. The Coulomb diamonds are marked in Fig. 4.18 with dashed lines as a guide to the eye. While the edges of the Coulomb diamonds of dot A are clearly visible due to cotunneling via the off-resonant dot B, the resonances with dot B and the leads are only seen in the upper part of the diagram of path 1, between $U_{\mathrm{G3}} = 250\,\mathrm{mV}$ and $U_{\mathrm{G3}} = 300\,\mathrm{mV}$, due to cotunneling.

Figure 4.18 (b) shows the transport through path 2 in dependence of U_{S1}. Across path 2 the bias voltage is set to $U_{\mathrm{S2}} = 0\,\mathrm{mV}$. Thus, transport will occur for values of U_{G3} where both dots A and C are in resonance with the leads. For non-zero bias voltage at path 1 resonance lines of dot A with the drain and the source lead S_1 are visible. The non-zero slope of these resonance lines stems from the influence of the varying potential of the source lead S_1 on the energies of dots A and C. The resonance lines of dot A with the drain lead exhibit small positive differential conductance, the transport originating from significant cotunneling across the off-resonant dot C. The resonance lines of the dot with the drain lead have the same slope as the ones seen in transport through path 1, as the slope of the resonance lines with drain stem from the capacitive coupling between dot A and S_1. Where dot A is in resonance with the source lead S_1 and transport through path 1 is consequently strong, lines of negative differential conductance are clearly visible. The negative differential conductance lines originate from the interaction between the paths only, as no transport signature is supposed to be observed in path 2 in case of resonances in path 1. This interaction and its signature, the negative differential conductance, is analyzed in more detail in section 5.3. The same signatures of intra-channel resonances and inter-channel interaction is observed for investigation of the transport in dependence of the bias voltage at path 2, U_{S2}, as seen and discussed in Fig. 5.21 in section 5.3.

The half-width of the Coulomb diamonds is identified with the charging energy of the respective dot (Eq. (2.61)). For dot A and dot B $E_{\mathrm{C}} \cong 0.5\,\mathrm{meV}$ is obtained and thus with Eq. (2.25) a sum capacitance of $C_{\Sigma\mathrm{A}} \cong C_{\Sigma\mathrm{B}} \cong 320\,\mathrm{aF}$ is calculated. Dot C can not be characterized for this measurement range as the Coulomb diamonds can not be clearly

identified in the transport measurements of path 2 with varied bias voltage U_{S2}. With the large positive potential at U_{G3} the dots are relatively large, leading to small charging energies. The extracted charging energies are only valid for the shown gate voltages and have to be adjusted for other values, as the size of the dots and the couplings to the leads change with varying potential at the gates. Additionally, from the slopes of the edges of the Coulomb diamonds the capacitive coupling between dot and source lead can be calculated with knowledge of the capacitive coupling between dot and the varied gate voltage (Eq. (2.60)). The capacitances between dots and gate G_3 for this parameter regime are extracted from the height of the Coulomb diamonds of dot A and B, respectively (Eq. (2.57)). With $C_{G3,A} \cong 9\,\mathrm{aF}$ we obtain $C_{S1,A} \cong 109\,\mathrm{aF}$ and for dot B with $C_{G3,B} \cong 5\,\mathrm{aF}$ we get $C_{S1,B} \cong 138\,\mathrm{mV}$ for this gate voltage regime. This corresponds well to the location of the dots with respect to S_1.

Lines of finite differential conductance parallel to the edges of the Coulomb diamonds of dot A stem from resonances of excited states of the dot and source (positive slope) or drain (negative slope). The distance between ground state resonance and the excited state resonance with respect to U_{S1} is $\Delta U_{S1} \cong 0.2\,\mathrm{mV}$, corresponding to an energy difference of $\Delta E = 0.07\,\mathrm{meV}$ (Eq. (2.33)), calculated by considering the capacitive influence of U_{S1} on the dot potentials. With a distance between ground state resonance and the excited state resonance of $\Delta U_{S1} \cong 5.5\,\mathrm{mV}$ with respect to U_{G3} an energy difference of $\Delta E = 0.07\,\mathrm{meV}$ is obtained, calculated by considering the capacitive influence of U_{G3} on the dot potentials.

To sum up, the triple quantum dot system was characterized by transport measurements within this section. Basic two-path transport properties are investigated showing triple points in the transport of the paths and the tunability of the system into triple dot resonances. The capacitive couplings between dots A, B, C and gates G_1 and G_3 are derived as electrostatic properties of the system. Coherence effects are detected in the transport measurements of both paths, verifying a strong inter-dot coupling. Additionally, indictations of cotunneling within the double dot paths are observed. Non-linear transport is analyzed for varying the bias voltage at path 1 showing Coulomb diamonds of dot A and B and giving insight into capacitances and charging energies of the dots in this regime. Inter-channel interaction manifests itself in the transport through path 2 while the bias voltage is varied across path 1.

5 Two-path transport

In this chapter the transport through the system is analyzed in more detail. Hereby we focus on the properties originating from the existence of the two different transport paths in the TQD sample.

A first basic property of the setup is that by using two source leads and one common drain lead of the transport paths the electrons coming from path 1 and 2 have to be distinguished at the drain to measure the current through the two paths separately, contrary to the measurement setup with one source lead and two drain leads implemented before [24]. Moreover, the electrons coming from the two paths are expected to be interacting in some way at dot A in this measurement setup. Section 5.1 describes the properties of the system arising from the electron interaction and distinction. Measurements where the electron current through path 1 and 2 is distinguished by applying an AC voltage with different frequencies to S_1 and S_2 are compared with measurements where the electrons coming from the two paths are not distinguished. Thereby we want to investigate whether interferences between the paths are prevented by distinguishing the paths, which would be detected in transport otherwise.

In section 5.2 we first introduce a quantum mechanical model of the TQD for a simulation of the system and thereby a further analysis of the properties of the system in continuation of chapter 4.

The subsequent sections 5.3 - 5.5 discuss the transport through the system without applied bias voltage at the source leads, where we expect linear transport through a dot, and with applied bias voltage, where we expect the transport to be in the non-linear regime. The described transport properties in section 5.3 and 5.5 are unique and characteristic for a multiple quantum dot system with two joint transport paths with two source leads.

5.1 Properties of path-resolved measurements

The triangular dot configuration using two source leads enables a variety of measurement setups. As already described in section 3.4.2 the current through the system is detected at the common drain lead of the two transport paths. At the source leads of the system a DC voltage with an additional AC voltage can be applied. The resulting total DC through the system, meaning the DC through path 1 and path 2, is measured at the drain lead. The AC is also measured (by lock-in amplifiers) at the drain lead. The AC voltage is used to have the possibility to distinguish the current of path 1 and path 2 by using different AC voltage frequencies at S_1 and S_2, f_1 and f_2, respectively, and two lock-ins to filter the current frequency-dependent at the drain (Fig. 3.11). In the following distinguishing the paths means distinguishing the electrons coming from path 1 and path 2.

In this section the differences in the measurement outcomes of these different measurement setups are investigated. The setups are:

a) The measurement of the DC through the whole system without applied AC voltages to the transport paths. The paths are not distinguished.

b) The measurement of the DC through the whole system while two different AC voltages are additionally applied to the transport paths. The paths are not distinguished, although the electrons carry this information.

c) The measurement of the AC of path 1 and path 2 simultaneously but separately. Two different AC voltages are applied to the transport paths. The measurement resolves the paths.

In both cases (a) and (b) we measure the whole system, the only difference is, that in (a) we do not have the possibility to distinguish the paths and in (b) we have the possibility, but do not measure this information. In case (c) the paths are resolved. We have a case differentiation between electrons coming from path 1 and electrons coming from path 2 by measuring the current with AC frequency f_1 and measuring the current with AC frequency f_2 simultaneously but separately at the drain. However, not the isolated paths are measured, as the measurement outcome of the single paths includes information about whole system. The measured subsystem when measuring the conductance through path 1 (2) separately is a double dot

A,B (A,C) with a capacitively coupled third dot C (B). The two subsystems are measured simultaneously, so both of them carry electron current which can interact at dot A.

The electrons coming from path 1 are expected to interfere at dot A with the electrons coming from path 2. The question is, whether in these different measurement setups (a), (b), (c) interferences between the electrons coming from path 1 and path 2 at the drain are possible. Interferences between the electrons coming from the two transport paths are a unique feature of this transport direction having two sources and one common drain. When measuring the transport through the system using one of the leads, in this sample design the contact at dot A, as a source lead and two of them as drains with a respective detector, no interference effects are possible.

One important general requirement for the existence of interference is that the particles are indistinguishable in the respective measurement setup. Here, the consideration of the setup as a realization of a double slit experiment is helpful. The transport paths, path 1 and path 2, of the TQD setup correspond to the slits 1 and 2 in the double slit setup. The detector in our setup corresponds to a detector in the double slit experiment [106], which can also be simply realized with a screen in case of photons. The experiment has also been performed with both single electrons [107] and an electron beam [108]. The double slit experiment shows that the pattern seen on a detector is dependent on whether the particles passing the slits are indistinguishable or not. When measuring which slit (path) a particle passed, the particles become distinguishable for us so the particles do not interfere and we do not see an interference pattern according to laws of quantum mechanics. The measurement destroys the phase coherence needed for the interference. When the electrons are undistinguished in the measurement setup we see an interference pattern at the detector behind the slits.

In mesoscopic systems the phase coherence length of the electrons exceeds the system size, meaning the typical system length scales, for low temperatures in the sub-kelvin regime. The phase coherence length is the length an electron can travel without loosing its phase coherence. At these low temperatures where electron-electron and electron-phonon scattering limiting the electron phase coherence length is low, quantum interference effects are of significance in the system properties [47]. Phase coherence is needed for the appearance of interference effects and leads to behaviour such

as the Aharonov-Bohm effect, the Quantum Hall effect, or the quantized transport through a QPC. From the electron concentration of the 2DEG of $n_e = 3.47 \cdot 10^{15}\,\mathrm{m}^{-2}$ and an electron mobility of $\mu_e = 42.1\,\mathrm{m}^2/\mathrm{Vs}$ (see Fig. 3.2) a mean free path of $l_e \cong 4\,\mu\mathrm{m}$ is obtained, as a lowest estimate for the phase coherence length in the system. With system length scales of around $500\,\mathrm{nm} < l_e$ (see Fig. 4.1) quantum interference effects are generally expected to be observed in this system (see also [109]). Additionally, the electrons tunneling into the two transport paths are expected to obtain a defined phase relation from the start. Further on, coherent inter-dot tunneling in the paths is a condition for interference between electrons from different paths. In the characterization of transport (section 4.3) the stability diagrams of the two paths (Fig. 4.16 and 4.17) show signatures of strong coherence between the on-site states of the dots due to a strong inter-dot tunnel coupling. Indications for contributions of phase-coherent transport to the transport through a triple quantum dot system have been shown in [36, 110].

In the experiment we measure a current I and consequently have an averaged signal. The AC frequencies applied to the source contacts are in the Hz range and thus very small. This means, that we average over many electrons. The number of electrons is defined by $n = I \cdot t/e$ and is $n \approx 7 \cdot 10^6$ for $I = 0.2\,\mathrm{nA}$ and a frequency of $f_1 = 83.3\,\mathrm{Hz}$ (see section 3.4.2). A further signal integration over $t_c = 500\,\mathrm{ms}$ leads to a measurement averaged over $n \approx 3 \cdot 10^8$ electrons. For the observability of interferences the averaged intensity is relevant. The averaging over many electrons leads to a stable and observable signal.

In the TQD setup we have the two transport paths where we can either measure the AC of each path and thus detect the electrons path-resolved (setup (c)), or measure the DC which carries no information about the paths of the electrons and thus do not distinguish the electrons by their path (setups (a) and (b)). The measurement outcomes of setups (a) and (b) are expected to be equivalent, as in both cases the DC through the total system is measured. The paths are not distinguished in both measurements. Based on the laws of quantum mechanics shown in the comparison with the double slit experiment above we predict the measurement outcome of setup (c) to be different from (a) and (b), as in (c) the electrons coming from the two paths are distinguished by measuring the AC of the paths separately so

that coherences between the paths are destroyed and no interference effects are observed.

Figure 5.1 (a), (b) shows the DC differentiated by U_{S1}, dI_{DC}/dU_{S1}, through the system measured at the drain contact in dependence of U_{S1} and U_{G3} using setup (a) and using setup (b), respectively.

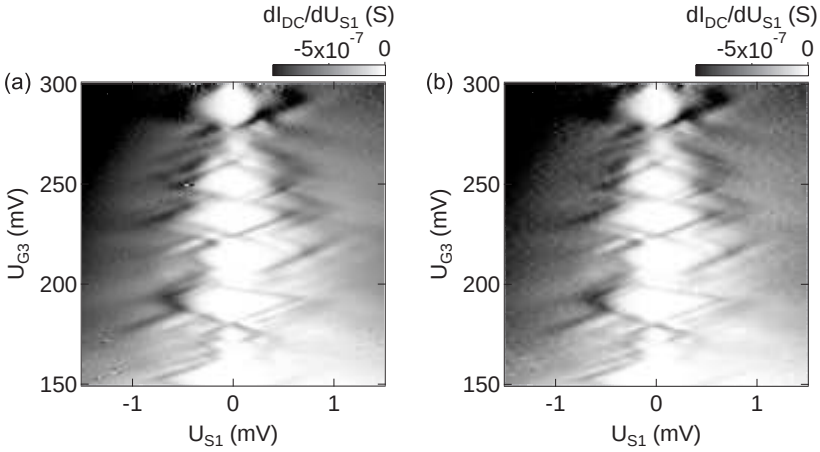

Figure 5.1: Differentiated DC of the system at the drain contact in dependence of U_{S1} and U_{G3} (a) for setup (a) without additional AC applied and (b) for setup (b) with additional AC applied to the paths.

The measurements show the same situation as shown and analyzed in Fig. 4.18, where the differential conductance of the two paths measured separately is presented. Mainly Coulomb diamonds of dot A are seen. The measurement outcomes of setups (a) and (b) show no significant differences exceeding the noise, which is consistent with the prediction. This is also observed in Fig. 5.6 (a), where the difference signal between the measurement outcomes of setups (a) and (b) is shown. The few structures which are visible can stem from noise in the resonances or a slight shift between the measurements. A cut at $U_{S1} = -0.1\,\mathrm{mV}$ (Fig. 5.2) makes it easier to compare the two measurement outcomes. A cut at a small bias voltage is chosen for the comparison, so that we have a well defined current

through the system. We see no additional features in setup (a) without additional applied AC voltage compared to the setup (b) with additional AC voltage applied to the paths, as in both cases only the DC without the path-information is measured. Thus, in this sense the setups are quantum mechanically equivalent.

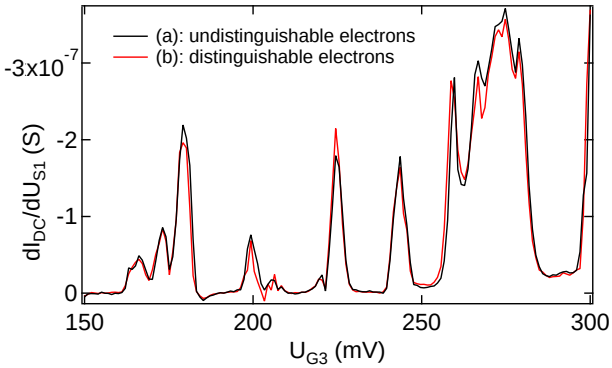

Figure 5.2: Cuts at $U_{S1} = -0.1\,\mathrm{mV}$ through Coulomb diamond measurements of setups (a) and (b) (Fig. 5.1). The differentiated DC shows no significant differences.

In order to analyze the interference features between the electrons expected to be included in these DC measurements (setups (a) and (b)), we compare their measurement outcomes with those of the single separate paths added up afterwards. As interference effects are not included in the sum of the conductance of path 1 and 2 recorded separately (setup (c)), as explained above, a comparison identifies signatures of interference.

For this purpose the measurement outcome of setup (b), the DC, is compared with setup (c), the sum of the AC of both paths, in the following. As done above, we again want to compare the respective measurement outcome in form of the differential conductance in dependence of U_{S1} and U_{G3}. While the differential current for setup (b) is calculated from the DC by dI_{DC}/dU_{S1}, the differential conductance for setup (c) I_{AC}/U_{AC} is calculated from I_{AC} measured by lock-in technique. The conductances derived from

both methods are comparable for the used small AC frequencies as explained in section 3.3. After adding up the measurement outcomes $I_{\mathrm{AC}}/U_{\mathrm{AC}}$ of the two paths, we plot the sum in one graph, Fig. 5.3 (b). As this is a simple summation of the conductance values of the two paths we can not expect to see all physical effects of the whole TQD system. Interference effects between the electrons from the two paths cannot be observed. If there are interference effects seen in measurement setups (a) and (b) we expect their measurement outcomes to be unequal to the simple calculated sum of the conductance values of the two paths. Figure 5.3 shows this comparison. Already at first sight differences in the transport features are visible.

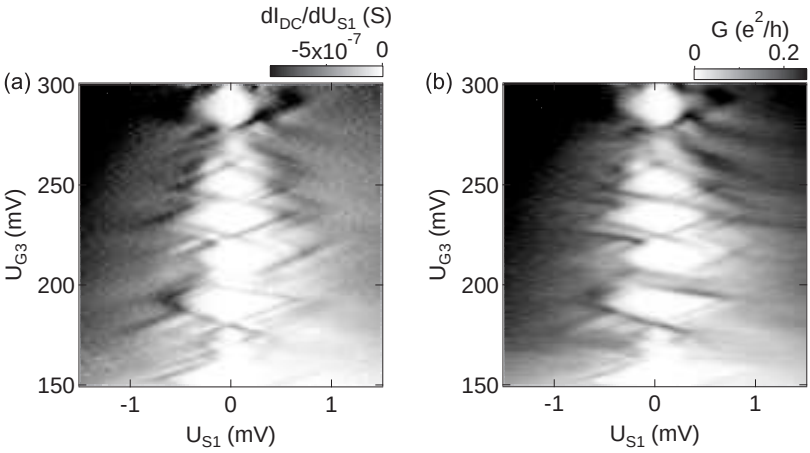

Figure 5.3: (a) Differentiated DC of the system at the drain contact in dependence of U_{S1} and U_{G3}. It corresponds to the measurement outcome of setup (b), where the paths are not distinguished. (b) Added differential conductance G of path 1 and path 2 in dependence of U_{S1} and U_{G3}. It corresponds to the measurement outcome of setup (c), where the path-information is included.

Figure 5.4 shows how the added measurement outcome of setup (c) is composed of the conductances of the separate paths for cut at $U_{\mathrm{S1}} = -0.1\,\mathrm{mV}$. Knowledge about the attribution of the Coulomb peaks to resonances between the dots stems from the analysis of the same Coulomb diamond

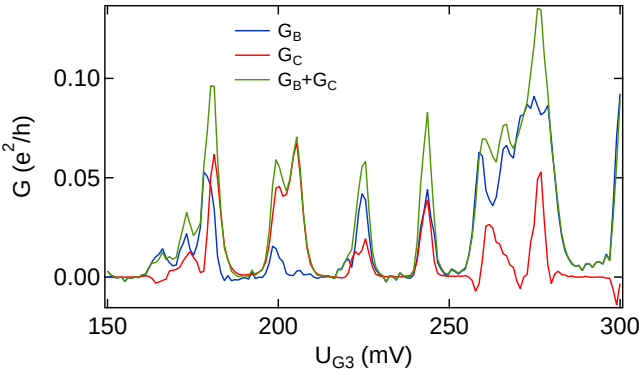

Figure 5.4: Cuts at $U_{S1} = -0.1\,\text{mV}$ through Coulomb diamond measurement of setup (c) for transport path 1 and 2 separately, as well as their sum.

measurement in section 4.3.2, Figure 4.18. Around $U_{G3} = 179\,\text{mV}$ a triple point of a resonance of dots A and B is present in path 1, so there is high conductance in path 1, while there is conductance in path 2 as dot C is energetically close. The conductance of path 2 extending in a wider regime around the resonance is a result of the strong coherence between the dots as their tunnel coupling is strong. Analogously, at around $U_{G3} = 200\,\text{mV}$ the triple points of a resonance of dots A and C and resulting high conductance is present in path 2 and dot B is energetically close. The system is very close to a triple dot resonance. At around $U_{G3} = 224\,\text{mV}$ dots A and B are in resonance. Path 2 also shows small differential conductance, but a comparison with the analysis of the corresponding stability diagrams in Fig. 4.18 shows that the system is quite far away from a triple dot resonance. Second-order tunneling tunneling processes can be significantly contributing to this transport through path 2 far from the resonance. Around $U_{G3} = 243\,\text{mV}$ dot A is in resonance with the leads and dots B and C are energetically close, so there is conductance in both paths, and around $U_{G3} = 260\,\text{mV}$ and $U_{G3} = 278\,\text{mV}$ quadruple points are present with resulting conductance in path 1 and 2.

The added measurement signal of setup (c) is compared with a cut at the same bias voltage through the measurement outcome of setup (b) in

Figure 5.5. For a better comparison $dI_{\mathrm{DC}}/dU_{\mathrm{S1}}$ is converted into a conductance in units e^2/h.

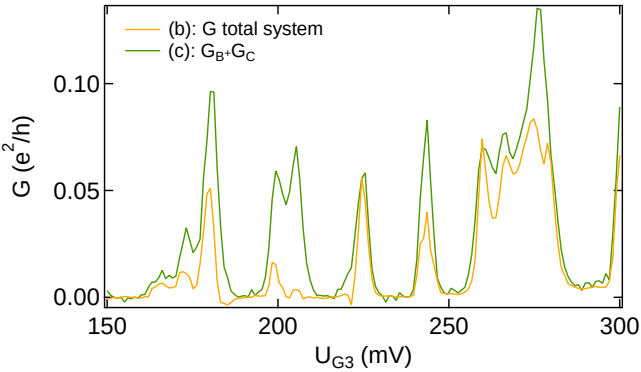

Figure 5.5: Cuts at $U_{\mathrm{S1}} = -0.1\,\mathrm{mV}$ through Coulomb diamond measurements of setups (b) and (c) (Fig. 5.3). Differences in the two measurement outcomes are due to destructive interference between electrons from the two paths visible in the measurement outcome of setup (b). At $U_{\mathrm{G3}} = 200\,\mathrm{mV}$ and $U_{\mathrm{G3}} = 240\,\mathrm{mV}$ suppression of resonances in the measurement outcome of setup (b) are obvious.

Clear deviations of different strength between the measurement outcomes can be observed. The conductance measured for the total system, where the paths are not distinguished, is suppressed for most resonance peaks of the system. For a better analysis of the differences the difference signal of the measurement outcomes of setups (b) and (c) is calculated by subtracting the measurement outcome of (b), where no interferences are expected, from the one with the peak suppression, (c). As a result the deviations between the measurement outcomes become directly visible. The result is shown in Figure 5.6 (b) and for the cut at $U_{\mathrm{S1}} = -0.1\,\mathrm{mV}$ in Figure 5.7.

In Fig. 5.6 (b) structures reproducing the resonances in detail are clearly visible. The differences can be analyzed conveniently in more detail in the cut in Fig. 5.7.

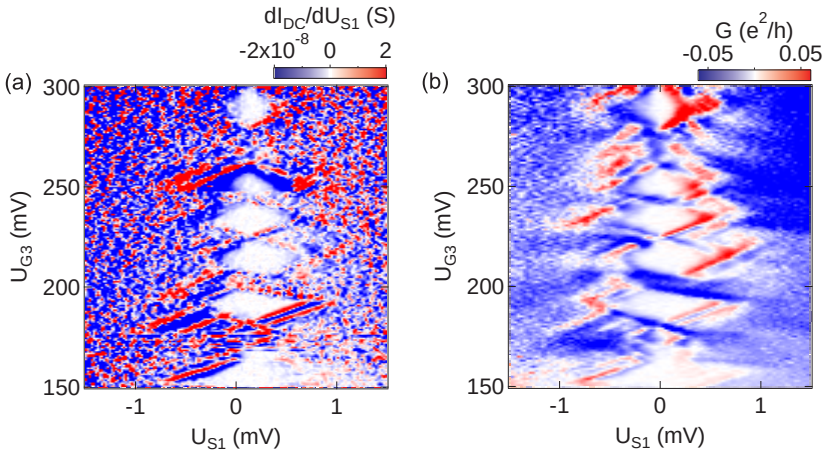

Figure 5.6: Difference signal of (a) the measurement outcomes of setups (a) and (b) (Fig. 5.1) and (b) of the measurement outcomes of setups (b) and (c) (Fig. 5.5).

The electrons only interfere at dot A when they are not distinguished at the drain contact. While the electrons are distinguished when the AC through the paths is measured simultaneously but separately, they are not distinguished when the DC through the whole system is measured. In the path-resolved measurement the coherences between the electrons coming from different paths are destroyed. Thus we understand that interferences are observed when the DC through the system is measured and do not observe them when the AC is measured for the paths separately. The detected electron interference between the paths for the measurement without resolving the paths is an evidence of the contribution of coherent tunneling to transport within the dot system. It indicates that the electrons are delocalized in the TQD and occupy coherent states involving all three on-site states of the single dots. After normalization and subtraction of noise the difference in the areas under the curves is around 20%. This can give a rough measure for the strength of the interference in the system.

Strong deviations are observed around $U_{G3} = 179\,\mathrm{mV}$ and $U_{G3} = 200\,\mathrm{mV}$ as well as $U_{G3} = 243\,\mathrm{mV}$ and $U_{G3} = 279\,\mathrm{mV}$. In these regions the system is close to a triple dot resonance, as explained above and also seen in the

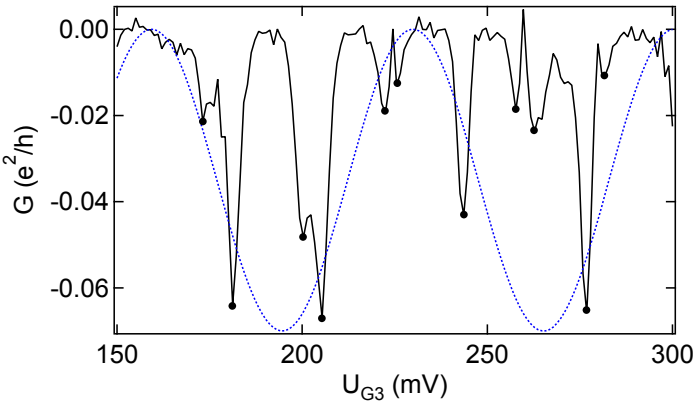

Figure 5.7: Difference signal of the measurement outcomes of setups (b) and (c) (Fig. 5.5) for the cut at $U_{S1} = -0.1\,\mathrm{mV}$ (Fig. 5.5). Large deviations are seen for relatively small and relatively large U_{G3}, whereas the difference signal is only small around $U_{G3} = 225\,\mathrm{mV}$. The mimima are marked with black dots to highlight the peak modulation. The dashed blue line serves as a guide to the eye to identify this additional oscillation period of around 70 mV.

full Coulomb diamond measurement (Fig. 5.3). Here, coherent transport through the whole system takes place. Interference of the electrons from the two paths at dot A is observed. The suppression of the resonance peaks in the measurement of the DC through the system can be explained in terms of destructive interference between the electronic wave functions coming from the two paths. At medium U_{G3}, $U_{G3} = 224\,\mathrm{mV}$, values only two dots are in resonance with the leads, or close to a resonance where the cut is made, so there no coherent state involving all three dots is formed. When the dots are off-resonant first order tunneling is strongly suppressed, making higher-order tunnel processes become significant. Especially at non-zero bias voltage non-coherent higher-order processes gain relevance (see section 2.3.2.3). Consequently, the absence of interference in this region can be explained by a domination of non-coherent transport resulting from second-order tunneling processes. By varying the gate voltage U_G the phase coherence in the system is modulated from mostly coherent transport to a region where statistically less electrons tunnel coherently, to again mostly coherent transport.

In the difference signal of setups (b) and (c) (Fig. 5.7) an oscillation with a large period is observed. An enveloping function with a period of around $\Delta V_{\mathrm{G3,meas.}} \cong 70\,\mathrm{mV}$ is obtained. Such a behaviour can also be explained for a system where the transport is fully coherent in the measured regime. If two waves with slightly different frequencies interfere, a beat signal with periodically increasing and decreasing amplitudes results. This effect might play a role in this experiment, as the electrons tunneling coherently through path 1 and path 2 and interfering at dot A are expected to have a changing but defined phase difference. The measurement outcome of setup (b) indeed shows a variation in the suppression of the Coulomb peaks. The difference signal between a beat signal and a regular oscillation alternates between regions of suppression and strong amplitudes. Such a behaviour is observed in the difference signal in Fig. 5.7, where small amplitudes at medium U_{G3} and large amplitudes at low and high U_{G3} are observed.

Another common quantum interference effect which can be used to discuss this behaviour is Aharonov-Bohm oscillations. The Aharonov-Bohm effect [111] is a quantum mechanical phenomenon where the wave function of a charge gathers an additional phase by traversing through a space where the magnetic or electric field is zero and there is consequently no classical force. The effect is caused by the magnetic vector potential (magnetic Aharonov-Bohm effect) or electric scalar potential (electric Aharonov-Bohm effect) in this region of the nearby magnetic or electric field. In a quantum ring with an enclosed magnetic flux the electrons in one arm move parallel, the ones in the other arm anti-parallel to the magnetic vector potential. This leads to a phase difference between the electrons in the two paths and causes an interference pattern at the drain lead of the ring, the Aharanov-Bohm oscillations. Analogously to this magnetic effect, the electric Aharonov-Bohm effect in a quantum ring leads to oscillations which stem from a phase difference due to one transport path being effected by an additional electric potential [112–114]. Aharonov-Bohm interferometers were also investigated experimentally with both an embedded quantum dot in one path of the ring [115] and a quantum dot in each of the two paths [116, 117], both observing Aharonov-Bohm oscillations showing that the transport through the quantum dot is partially coherent and that the transmittance phase shifts by π across a Coulomb peak at the dot resonance. Going one step further, triple quantum dot rings have been studied theoretically [118] and ring shaped setups with three embedded quantum dots have been investigated experimentally [36, 109, 110], where Aharanov-Bohm oscillations due to the

presence of a magnetic field have been detected, proving coherent transport through the system. The occurrence of Aharonov-Bohm oscillations verifies a phase-coherent coupling of the quantum dots in the system [36]. As the tunnel coupling between the dots in our system is large, coherent transport through the system around the triple dot resonances is expected.

During the measurement discussed here the potential at G_3 is varied, which is located next to transport path 2. When moving across this electrostatic potential, the electronic wave function in this path is expected to undergo a phase shift leading to a phase difference between the paths, the electric Aharonov-Bohm effect. As a rough estimation in order to get a feeling for the system the period of the Aharonov-Bohm oscillations expected for a ring without embedded quantum dots is calculated. In this case, the phase shifts by 2π if the gate voltage is varied by $\Delta V_{G3} = hv_F \cdot (e(C_{G3,A}/C_\Sigma)L)^{(-1)}$ [109, 113], with the Fermi velocity v_F and the length L within which the electron experiences the electrostatic potential. Using the electron concentration of the 2DEG to calculate v_F we obtain $\Delta V_{G3} = 70\,\mathrm{mV}$ when assuming a length of around $L = 160\,\mathrm{nm}$ within which the electron travels through the electronic potential caused by G_3. The result corresponds well to the observed oscillation period of $\Delta V_{G3,meas} = 70\,\mathrm{mV}$. Within this approximation the Fermi velocity of the electrons in the 2DEG is used, which describes the behaviour of the electrons in the leads only. Also, the length L can only be estimated roughly from the sample setup (Fig. 4.1). The transport through the system has to be assumed to be coherent over the full U_{G3} sweep. Consequently, this approximation can only serve as a tool to obtain a feeling for the system, as a quantum ring with embedded dots asks for a more complex description. However, for coherent transport through the system, as expected in a wide region around the triple dot resonances due to the strong inter-dot coupling, this approximation can be useful. An observable oscillation of a period this theory predicts as well as an expected strong coherent coupling between the dots as visible in the stability diagrams suggest that the electric Aharonov-Bohm effect might contribute to the observed oscillations.

The formation of dark states also leads to a suppression, ideally a cancellation, of transport through a quantum system. Such quantum interference effects are, for instance, dark states in electronic transport, where in a three level system coherent superpositions lead to destructive interference and block the current flow though the system. This coherent population

trapping effect in electronic transport has been discovered and investigated theoretically in similar triangular triple quantum dot setups [26–29] and also linear dot arrangements [30]. Even if the dark state formation is incomplete and a partial dark state is formed, or decoherence is present in the system, the current can be noticeably suppressed.

To sum up, the separate transport measurements of the paths do not contain the full information of the TQD transport when combined by a simple summation afterwards. We do not obtain the full TQD physics in such a measurement setup. Interferences between electrons coming from different paths do only occur if the electrons are not distinguished by their path at the drain. The DC signal through the system contains such interference effects. Signatures of interference between electrons coming from the two transport paths are observed being a sign of coherent transport throughout the triple dot system involving all three dots, indicating that the dots are coherently coupled. The modulation of their strength with varying gate voltage is ascribed to the modulation of the coherence in the transport through the system. Also, it is possible that other interference effects like the Aharonov-Bohm effect might contribute to the observed features in regions of coherent transport.

5.2 Simulation and characterization of transport

In this section the TQD system is further analyzed in continuation of chapter 4. For this purpose, a quantum mechanical model of the TQD is used (see basics in section 5.2.1), with which the stability diagram of the TQD with the respective steady state occupations and the current through the two transport paths are calculated. As an analytical expression for the current through a triple dot system would be very complex, the current through the system is calculated numerically. With a simulation of the TQD system using this model the stability regions are identified in the measured stability diagram and the inter-dot- and dot-lead tunnel couplings of the system are calculated (see section 5.2.2). Parts of this section include experimental and theoretical results which have been published in [91] in a collaboration with F. Gallego-Marcos from the Instituto de Ciencia de Materiales, CSIC, Madrid, who contributed the numerical simulation which is presented in [91] and in this section.

5.2.1 Quantum mechanical model of the TQD

A quantum mechanical model of the system is used to calculate the differential conductance in order to help to explain the transport properties [91]. The basics concerning this model are explained in section 2.3.3. We have a system consisting of three dots A, B, C with a tunnel coupling τ_{AB} and τ_{AC} between dots A and B and between A and C, respectively. Each dot is coupled to one lead (S_1, S_2, D) with Γ_l (l = A,B,C). The model distinguishes between electrons coming from S_1 and S_2 so that transport through the paths can be modeled simultaneously but separately analogous to the experimental setup. We allow zero to three electrons in the dot system, up to one electron in each dot.

The total Hamiltonian of the system

$$\mathrm{H} = \mathrm{H}_0 + \mathrm{H}_{\mathrm{lead}} + \mathrm{H}_{\mathrm{I}} \tag{5.1}$$

consists of three parts, the Hamiltonian for the dot system H_0, the Hamiltonian for the reservoirs $\mathrm{H}_{\mathrm{lead}}$ and the one describing the interaction between the dot system and the reservoirs H_{I}. H_0 is a three-site Anderson-like Hamiltonian [119]

$$\mathrm{H}_0 = \sum_i \varepsilon_i \hat{c}_i^\dagger \hat{c}_i + \sum_i \tau_{i,i+1} \hat{c}_i^\dagger \hat{c}_{i+1} + \sum_{i<j} V_{ij} \hat{n}_i \hat{n}_j \tag{5.2}$$

with ε_i ($i \in \{\mathrm{A,B,C}\}$) being the chemical potentials of the dots, τ_{ij} being the coherent inter-dot tunnel coupling and V_{ij} being the Coulomb interaction between the electrons in different dots. We do not need to consider the intra-dot coulomb interaction term as we are just considering one electron per dot. $\hat{c}_i^\dagger$ ($\hat{c}_i$) is the fermionic creation (annihilantion) operator for the electrons in dot i and $\hat{n}_i = \hat{c}_i^\dagger \hat{c}_i$ is the particle number operator of dot i.

The Hamiltonian H_0 for zero up to three electrons in the dot system in matrix form reads

$$\mathrm{H}_0 = \left[\begin{array}{c|ccc|ccc|c} E_{|0,0,0\rangle} & 0 & 0 & 0 & 0 & 0 & 0 & 0 \\ \hline 0 & E_{|1,0,0\rangle} & \tau_{\mathrm{AB}} & \tau_{\mathrm{AC}} & 0 & 0 & 0 & 0 \\ 0 & \tau_{\mathrm{AB}} & E_{|0,1,0\rangle} & 0 & 0 & 0 & 0 & 0 \\ 0 & \tau_{\mathrm{AC}} & 0 & E_{|0,0,1\rangle} & 0 & 0 & 0 & 0 \\ \hline 0 & 0 & 0 & 0 & E_{|0,1,1\rangle} & \tau_{\mathrm{AB}} & \tau_{\mathrm{AC}} & 0 \\ 0 & 0 & 0 & 0 & \tau_{\mathrm{AB}} & E_{|1,0,1\rangle} & 0 & 0 \\ 0 & 0 & 0 & 0 & \tau_{\mathrm{AC}} & 0 & E_{|1,1,0\rangle} & 0 \\ \hline 0 & 0 & 0 & 0 & 0 & 0 & 0 & E_{|1,1,1\rangle} \end{array}\right]. \tag{5.3}$$

Each box has a constant number of electrons in the system. The reservoirs are described as a Fermi electron gas

$$\mathrm{H}_{\mathrm{lead}} = \sum_{lk} \epsilon_{lk} \hat{d}^{\dagger}_{lk} \hat{d}_{lk} \tag{5.4}$$

having constant temperature T and a chemical potential μ_l ($l \in \{\mathrm{S}_1,\mathrm{S}_2,\mathrm{D}\}$). The energy continuum in the lead is denoted by the sum over ϵ_{lk}. $\hat{d}^{\dagger}_{lk}$ ($\hat{d}_{lk}$) is the fermionic creation (annihilantion) operator for the electrons in lead l. The coupling between the dots and the reservoirs is modeled by the interaction Hamiltonian

$$\mathrm{H}_{\mathrm{I}} = \sum_{l,i} \gamma_l \hat{d}^{\dagger}_{l} \hat{c}_i + \mathrm{h.c.} \tag{5.5}$$

which contains the hopping parameter γ_l for the interaction between the dots and the leads.

The parameters ε_i, τ_{ij}, V_{ij} are all tuned with the gate voltages $U_{\mathrm{G1}} - U_{\mathrm{G4}}$ and $\mu_l \equiv U_{\mathrm{SD}}$ analogous to the experiment. The transition rates for electrons tunneling from the leads to the dot system (+) and vice versa (-) are given by Fermi's golden rule $\Gamma^{(+)}_{i\leftarrow l} = 2\pi/\hbar|\gamma_l|^2 f(\mu_l - \varepsilon_i)$ and $\Gamma^{(-)}_{l\leftarrow i} = 2\pi/\hbar|\gamma_l|^2[1 - f(\mu_l - \varepsilon_i)]$, with the Fermi distribution function $f(\alpha) = 1/(e^{-\alpha/(k_{\mathrm{B}}T)} + 1)$ (see section 2.3.3). As the dot-lead tunnel coupling $\Gamma_l \equiv 2\pi/\hbar|\gamma_l|^2$ is smaller than the inter-dot tunnel coupling τ_{ij}, the Born-Markov approximation (see section 2.3.3.1) can be applied for the interaction between the dot system and its leads.

We obtain the master equation

$$\frac{\partial \rho(t)}{\partial t} = \mathcal{L}\rho(t) \tag{5.6}$$

for the system. The reduced density matrix $\rho(t)$ is deduced from the Von Neumann equation Eq. (2.82) with the time evolution of the full system by tracing over the degrees of freedom of the baths Eq. (2.84). The elements of $\rho(t)$, $\rho_i(t)$, are the occupation probabilities of the state i of the system. $\mathcal{L}$ is the Liouvillian superoperator which comprises all information about the dot system H_0 and the dot-lead tunnel rates $\Gamma_{i\leftrightarrow l}$.

As we want to analyze the system in the vicinity of zero bias, we have to work in the delocalized basis so the Hamiltonian H_0 (Eq. (5.3)) needs to be diagonalized. As a result we get three coherent states $|\Phi_i\rangle$ ($i \in \{1,2,3\}$) for one electron in the system, three for two electrons in the system, $|\Psi_j\rangle$ ($j \in \{1,2,3\}$), and $|0\rangle$ and $|1\rangle$ for zero and three electrons in the system, respectively:

$$\begin{aligned} |0\rangle &= |000\rangle \\ |\Phi_i\rangle &= a_i\,|100\rangle + b_i\,|010\rangle + c_i\,|001\rangle \\ |\Psi_i\rangle &= d_i\,|011\rangle + h_i\,|101\rangle + l_i\,|110\rangle \\ |1\rangle &= |111\rangle \end{aligned} \tag{5.7}$$

with $i \in \{1,2,3\}$, which are 8 states in total.

As we want to distinguish electrons coming from source S_1 and source S_2, we have to take into account all the possible combinations of electrons in the system. We label the electrons coming from S_1 with B and electrons coming from S_2 with C. We obtain the following coherent states for zero, one and two electrons in the system

$$\begin{aligned} |0\rangle &= |000\rangle \\ |\Phi_{\mathrm{B}i}\rangle &= a_{\mathrm{B}i}\,|\mathrm{B}00\rangle + b_{\mathrm{B}i}\,|0\mathrm{B}0\rangle + c_{\mathrm{B}i}\,|00\mathrm{B}\rangle \\ |\Phi_{\mathrm{C}i}\rangle &= a_{\mathrm{C}i}\,|\mathrm{C}00\rangle + b_{\mathrm{C}i}\,|0\mathrm{C}0\rangle + c_{\mathrm{C}i}\,|00\mathrm{C}\rangle \\ |\Psi_{\mathrm{BB}i}\rangle &= d_{\mathrm{BB}i}\,|0\mathrm{BB}\rangle + h_{\mathrm{BB}i}\,|\mathrm{B}0\mathrm{B}\rangle + l_{\mathrm{BB}i}\,|\mathrm{BB}0\rangle \\ |\Psi_{\mathrm{CC}i}\rangle &= d_{\mathrm{CC}i}\,|0\mathrm{CC}\rangle + h_{\mathrm{CC}i}\,|\mathrm{C}0\mathrm{C}\rangle + l_{\mathrm{CC}i}\,|\mathrm{CC}0\rangle \\ |\Psi_{\mathrm{BC}i}\rangle &= d_{\mathrm{BC}i}\,|0\mathrm{BC}\rangle + h_{\mathrm{BC}i}\,|\mathrm{B}0\mathrm{C}\rangle + l_{\mathrm{BC}i}\,|\mathrm{CB}0\rangle \\ |\Psi_{\mathrm{CB}i}\rangle &= d_{\mathrm{CB}i}\,|0\mathrm{CB}\rangle + h_{\mathrm{CB}i}\,|\mathrm{C}0\mathrm{B}\rangle + l_{\mathrm{CB}i}\,|\mathrm{BC}0\rangle \end{aligned} \tag{5.8}$$

and for three electrons in the system

$$|\mathrm{BBB}\rangle\,,\ |\mathrm{BBC}\rangle\,,\ |\mathrm{BCB}\rangle\,,\ |\mathrm{CBB}\rangle\,,\ |\mathrm{BCC}\rangle\,,\ |\mathrm{CBC}\rangle\,,\ |\mathrm{CCB}\rangle\,,\ |\mathrm{CCC}\rangle\,. \quad (5.9)$$

The total number of states is now 27.

The density vector only taking into account the occupations (diagonal elements of the density matrix) is, analogous to section 2.3.3,

$$\begin{pmatrix} \dot{\rho}_{|0\rangle} \\ \dot{\rho}_{|\Phi_{\mathrm{B}i}\rangle} \\ \dot{\rho}_{|\Phi_{\mathrm{C}i}\rangle} \\ \dot{\rho}_{|\Psi_{\mathrm{BB}i}\rangle} \\ \dot{\rho}_{|\Psi_{\mathrm{CC}i}\rangle} \\ \dot{\rho}_{|\Psi_{\mathrm{BC}i}\rangle} \\ \dot{\rho}_{|\Psi_{\mathrm{CB}i}\rangle} \\ \dot{\rho}_{|\mathrm{BBB}\rangle} \\ \dot{\rho}_{|\mathrm{BBC}\rangle} \\ \dot{\rho}_{|\mathrm{BCB}\rangle} \\ \dot{\rho}_{|\mathrm{CBB}\rangle} \\ \dot{\rho}_{|\mathrm{BCC}\rangle} \\ \dot{\rho}_{|\mathrm{CBC}\rangle} \\ \dot{\rho}_{|\mathrm{CCB}\rangle} \\ \dot{\rho}_{|\mathrm{CCC}\rangle} \end{pmatrix} = \mathcal{L} \cdot \begin{pmatrix} \rho_{|0\rangle} \\ \rho_{|\Phi_{\mathrm{B}i}\rangle} \\ \rho_{|\Phi_{\mathrm{C}i}\rangle} \\ \rho_{|\Psi_{\mathrm{BB}i}\rangle} \\ \rho_{|\Psi_{\mathrm{CC}i}\rangle} \\ \rho_{|\Psi_{\mathrm{BC}i}\rangle} \\ \rho_{|\Psi_{\mathrm{CB}i}\rangle} \\ \rho_{|\mathrm{BBB}\rangle} \\ \rho_{|\mathrm{BBC}\rangle} \\ \rho_{|\mathrm{BCB}\rangle} \\ \rho_{|\mathrm{CBB}\rangle} \\ \rho_{|\mathrm{BCC}\rangle} \\ \rho_{|\mathrm{CBC}\rangle} \\ \rho_{|\mathrm{CCB}\rangle} \\ \rho_{|\mathrm{CCC}\rangle} \end{pmatrix} \quad (5.10)$$

with $i \in \{1,2,3\}$ and $\mathcal{L}$ being a 27×27 matrix with the entries $\mathcal{L}_{ij}$ being

$$\mathcal{L}_{ij} = f(\varepsilon_{ij}) \left| \left\langle \chi_i \left| \tilde{\mathcal{J}}^{(+)} \right| \chi_j \right\rangle \right|^2 + (1 - f(\varepsilon_{ij})) \left| \left\langle \chi_i \left| \tilde{\mathcal{J}}^{(-)} \right| \chi_j \right\rangle \right|^2 \quad (5.11)$$

with $\{|\chi_n\rangle\}$ and $n \in \{1,2,...,27\}$ being the coherent states of the system and $\varepsilon_{ij} = |\lambda_i - \lambda_j|$ being the energy difference between state $|\chi_i\rangle$ and $|\chi_j\rangle$. $\mathcal{J}$ is a 27×27 matrix containing the tunnel couplings γ_{S1}, γ_{S2} and γ_{D} from the dots to the respective leads. Each entry $\mathcal{J}_{ij}$ couples two states with the appropriate coupling parameter γ and if there is no possibility to go directly from one state to another, $\mathcal{J}_{ij} = 0$. $\mathcal{J}^{(+)}$ describes the tunneling of electrons from the leads to the dots and $\mathcal{J}^{(-)}$ the tunneling from the dots to the leads.

The steady state occupations ρ_{ss} are calculated by solving the kernel of the master equation

$$\rho_{\mathrm{ss}} = \ker[\mathcal{L}]. \tag{5.12}$$

With ρ_{ss} and the tunneling rates between dots and leads Γ_{A}, Γ_{B}, Γ_{C} the total current through the two paths can be calculated by

$$I = \sum_{i,j=0}^{1} \rho^{\mathrm{ss}}_{|1,i,j\rangle} \Gamma^{-}_{|0,i,j\rangle \leftarrow |1,i,j\rangle} - \rho^{\mathrm{ss}}_{|0,i,j\rangle} \Gamma^{+}_{|1,i,j\rangle \leftarrow |0,i,j\rangle}. \tag{5.13}$$

In the calculation of the partial current through path 1 or path 2 one has to distinguish between the electrons coming from source 1 and source 2. We get

$$I_{\mathrm{S1}} = \sum_{i,j=\{0,\mathrm{B},\mathrm{C}\}} \rho^{\mathrm{ss}}_{|\mathrm{B},i,j\rangle} \Gamma^{-}_{|0,i,j\rangle \leftarrow |\mathrm{B},i,j\rangle} - \rho^{\mathrm{ss}}_{|0,i,j\rangle} \Gamma^{+}_{|\mathrm{B},i,j\rangle \leftarrow |0,i,j\rangle} \tag{5.14}$$

for the current through path 1 and

$$I_{\mathrm{S2}} = \sum_{i,j=\{0,\mathrm{B},\mathrm{C}\}} \rho^{\mathrm{ss}}_{|\mathrm{C},i,j\rangle} \Gamma^{-}_{|0,i,j\rangle \leftarrow |\mathrm{C},i,j\rangle} - \rho^{\mathrm{ss}}_{|0,i,j\rangle} \Gamma^{+}_{|\mathrm{C},i,j\rangle \leftarrow |0,i,j\rangle} \tag{5.15}$$

for the current through path 2, with $I = I_{\mathrm{S1}} + I_{\mathrm{S2}}$. The indices B and C represent an electron coming from source 1 or source 2, respectively. The differential conductance is calculated by $\mathrm{G}_{\alpha} = dI_{\alpha}/dV$, $\alpha \in \{\mathrm{B},\mathrm{C}\}$.

This theoretical model considers the inter-dot coupling between the on-site states of the dots to be fully coherent. The electrons are delocalized in the TQD occupying coherent molecular states. The molecular states consist of the complex weighted on-site states of the single dots. The simulation thus includes all electronic correlations within the dot system and is able to describe the quantum mechanical dynamics in the dot system. If the current through path 1 and 2 is calculated separately, the coherences between electrons coming from the different paths are broken. This is discussed in more detail in section 5.3.

5.2.2 Stability diagram

In order to analyze the charge stability regions of the system we focus on a region near a triple dot resonance in the following. Figure 5.8 shows the differential conductance G in dependence of the gate voltages U_{G1} and U_{G3}.

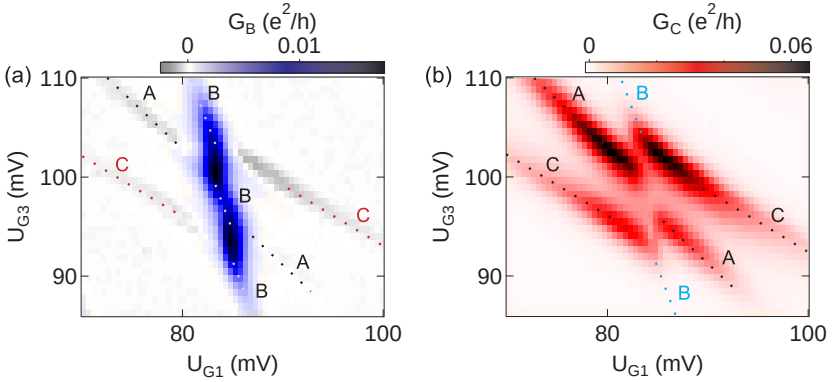

Figure 5.8: Differential conductance of path 1 (a) and path 2 (b) in dependence of the gate voltages U_{G1} and $UG3$. In path 1 resonances between dots A and B are visible, in path 2 resonances between dots A and C. The charging lines in path 1(2) are shifted in gate-space where dot C(B) is charged due to capacitive coupling between the dots. The charging lines of the dots are marked with dashed lines for clarity.

In path 1 we observe the resonances between dots A and B, in path 2 between dots A and C. In both paths the charging lines of the dots are shifted due to charging of the respective dot in the other path, where it comes into resonance. For both paths we see a stability diagram for a serial double dot but broken by a shift in gate voltage where the capacitively coupled third dot is charged. In path 1 negative differntial conductance values are observed, colored in grey here for a better visibility and distinguishability.

We can combine the data in one color plot encoding the paths in different colors to identify them. Doing so, triple dot physics is observed. Contributions of both transport paths can be directly compared. Figure 5.9 shows such a combined transport measurement near the triple dot resonance. We have three double dot resonances, A and B, A and C, B and C, in close vicinity to each other. Regions of high differential conductance are observed

in each of the paths, but at slightly different gate voltages U_{G1} and U_{G3}. In path 1 along the B charging line one can appreciate two vertical resonance lines where dot A is in resonance with dot B. The stability regions which can be clearly identified in this measurement are denoted in the diagram.

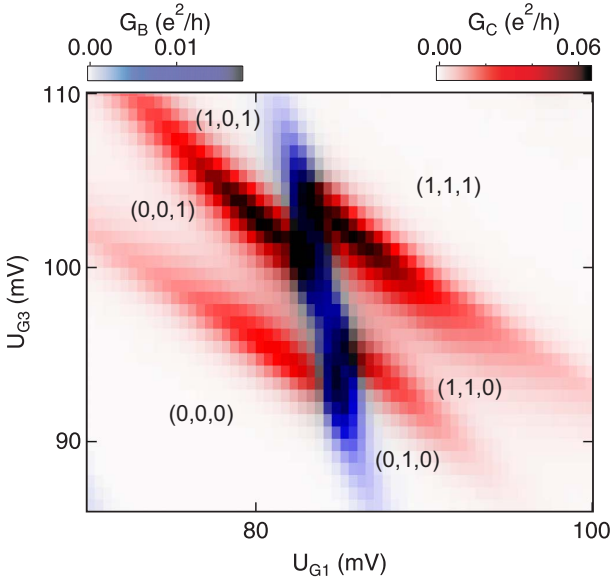

Figure 5.9: Combined color plot of the differential conductance through path 1 (red) and 2 (blue) with denoted charge configurations of the stability regions which can be identified in the measurement. A similar combined plot can be found in [91].

In order to obtain a more detailed understanding of the location of the stability regions in the stability diagram in Fig. 5.9, we calculate the steady state occupation probabilities ρ_i^{ss} of each state i. It is done by solving the kernel of the master equation of the system $\rho^{\mathrm{ss}} = \ker[\mathcal{L}]$ (Eq. (5.12)). This simulation of the system was implemented by Fernando Gallego-Marcos from the Instituto de Ciencia de Materiales, CSIC, Madrid [91].

With the capacitive couplings between the dots and the gates the influence of the gate voltages on the dot energies is calculated by Eq. (2.31). The

capacitive couplings			
dot-lead			inter-dot
$C_{\mathrm{G1,A}} = 6.8$	$C_{\mathrm{G1,B}} = 8.0$	$C_{\mathrm{G1,C}} = 3.3$	$C_{\mathrm{AB}} = 5.5$
$C_{\mathrm{G2,A}} = 5.2$	$C_{\mathrm{G2,B}} = 3.8$	$C_{\mathrm{G2,C}} = 1.1$	$C_{\mathrm{AC}} = 19.8$
$C_{\mathrm{G3,A}} = 6.6$	$C_{\mathrm{G3,B}} = 2.6$	$C_{\mathrm{G3,C}} = 5.1$	$C_{\mathrm{BC}} = 6.3$
$C_{\Sigma\mathrm{A}} = 69.9$	$C_{\Sigma\mathrm{B}} = 27.0$	$C_{\Sigma\mathrm{C}} = 53.0$	

Table 5.1: Capacitive couplings C in aF from the dots to the gates G_1, G_2, and G_3.

used capacitances are shown in table 5.1. The capacitive couplings between the dots A, B, and C and the gates G_1 and G_3 are extracted from the stability diagrams (see section 4.3, table 4.2). The coupling between the dots and G_2 is taken from former measurements [19]. It is only used to shift the simulation outcome to overlap with the measurement outcome. The couplings between the dots and gate G_4 are not determined as they are not used. The sum capacitances of the dots are obtained by matching them to the experimental result to obtain the appropriate effect of the gates on the energies, taking the ones from [19] as starting values. With these sum capacitances charging energies of the dots of $E_{\mathrm{C,A}} = 2\,\mathrm{meV}$, $E_{\mathrm{C,B}} = 6\,\mathrm{meV}$, and $E_{\mathrm{C,C}} = 3\,\mathrm{meV}$ are obtained.

The capacitive inter-dot couplings (table 5.1) are calculated using Eq. (2.69). We get

$$\begin{aligned} C_{\mathrm{AB}} &= \frac{C_{\mathrm{G1,A}} \cdot C_{\Sigma\mathrm{B}}}{e} \cdot \Delta U_{\mathrm{G1,AB}} \\ C_{\mathrm{AC}} &= \frac{C_{\mathrm{G1,A}} \cdot C_{\Sigma\mathrm{C}}}{e} \cdot \Delta U_{\mathrm{G1,AC}} \\ C_{\mathrm{BC}} &= \frac{C_{\mathrm{G1,B}} \cdot C_{\Sigma\mathrm{C}}}{e} \cdot \Delta U_{\mathrm{G1,BC}} \end{aligned} \tag{5.16}$$

with $\Delta U_{\mathrm{G}i,\mathrm{XY}}$ (XY $\in$ {AB,AC,BC}) being the shift of the charging lines of dot X in $U_{\mathrm{G}i}$-direction when dot Y is charged by one electron, extracted from the stability diagrams. They are converted into the electrostatic inter-dot coupling energies by

charging energies		
$E_{\mathrm{C,A}} = 2$	$E_{\mathrm{C,B}} = 6$	$E_{\mathrm{C,C}} = 3$

Table 5.2: Charging energies E_{C} of the dots A, B, and C in meV.

$$E_{\mathrm{XY}} = K \cdot (C_{\Sigma\mathrm{Z}} C_{\mathrm{XY}} + C_{\mathrm{XZ}} C_{\mathrm{YZ}}) \tag{5.17}$$

from [23], with

$$K = \frac{e^2}{C_{\Sigma\mathrm{A}} C_{\Sigma\mathrm{B}} C_{\Sigma\mathrm{C}} - 2C_{\mathrm{AB}} C_{\mathrm{AC}} C_{\mathrm{BC}} - C_{\Sigma\mathrm{C}} C_{\mathrm{AB}}^2 - C_{\Sigma\mathrm{B}} C_{\mathrm{AC}}^2 - C_{\Sigma\mathrm{A}} C_{\mathrm{BC}}^2}.$$

To set up the Master equation we first extract the inter-dot tunnel couplings τ_{AB} and τ_{AC} and the dot-lead tunnel couplings Γ_{A}, Γ_{B}, and Γ_{C} from the transport measurements for the case of resonance between the dots. Fig. 5.10 shows a transport measurement in a region where double dot resonances between dots A, B and A, C are observed. By fitting a cut through the resonant line between the states $|101\rangle$ and $|011\rangle$ in path 1 with a Lorentzian function we obtain τ_{AB} and $\Gamma \equiv \Gamma_{\mathrm{A}} \equiv \Gamma_{\mathrm{B}}$ and by fitting a cut through the resonant line between the states $|011\rangle$ and $|110\rangle$ in path 2 with a Lorentzian function we obtain τ_{AC} and $\Gamma \equiv \Gamma_{\mathrm{A}} \equiv \Gamma_{\mathrm{C}}$.

We treat the system as two separate double dots as an approximation as we analyze the current through the transport paths separately. The resonance peaks are described with the current formula for a dot system with infinite bias voltage (Eq. (2.108)) with weighted tunneling rates Γ between dot and leads by the Fermi function of the respective lead to take account of the finite bias voltage (see section 2.3.3.3). The double dot system should be described in the delocalized basis due to the strong inter-dot coupling in comparison with the dot-lead coupling and the small bias voltage (see section 2.3.3.3). However, the current expression is too complicated to express it analytically for such a system. Thus we take the current expression derived from the description of the system in the localized basis as an approximation for the current through a transport path. The larger the energy level detuning between the dots, the better this approximation for the current is (see

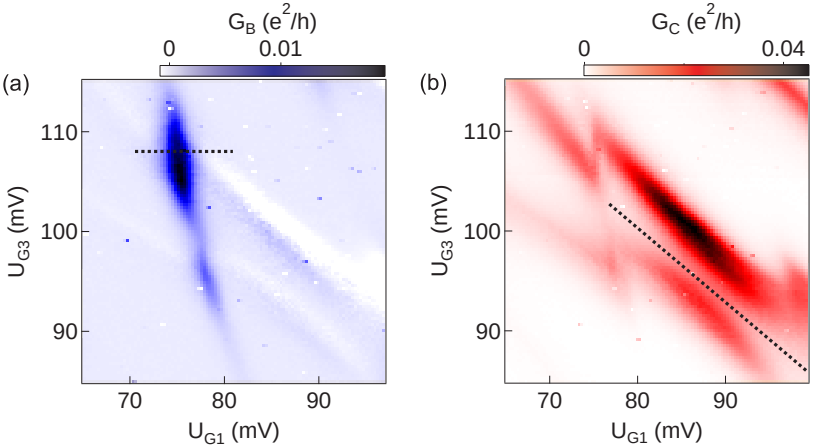

Figure 5.10: Transport through path 1 (a) and 2 (b) with a bias voltage of $U_{S2} = 0.5\,\mathrm{mV}$. The cut across the resonant line between the states $|101\rangle$ and $|011\rangle$ is performed on the transport measurement of path 1 and the cut across the resonant line between the states $|011\rangle$ and $|110\rangle$ is performed on the transport measurement of path 2.

section 2.3.3.3). We expect to obtain deviations in the conductance peak position x_0. It is sufficient to approximate the tunnel rates for the system as they merely serve as start values for the later simulation of the system transport. The stationary current peak has a Lorentzian shape (see Eq. (2.108))

$$I(x) = \frac{I_0(x)W^2(x)}{W^2(x) + (x - x_0)^2}. \tag{5.18}$$

The height of the Lorentz peak I_0 (see Eq. (2.109)) is given by

$$\begin{aligned} I_0(x) =& e\Gamma_\mathrm{B} f(x)\Gamma_\mathrm{A} f(x_0) \\ & * \frac{4\tau_\mathrm{AB}^2}{4\tau_\mathrm{AB}^2(\Gamma_\mathrm{A} f(x_0) + 2\Gamma_\mathrm{B} f(x)) + \Gamma_\mathrm{B} f(x)\Gamma_\mathrm{A}^2 f^2(x_0))} \end{aligned} \tag{5.19}$$

for path 1, and the half width at half maximum W (see Eq. (2.110)) is

$$W^2(x) = \frac{4\tau_{\mathrm{AB}}^2(\Gamma_{\mathrm{A}} f(x_0) + 2\Gamma_{\mathrm{B}} f(x)) + \Gamma_{\mathrm{B}} f(x)\Gamma_{\mathrm{A}}^2 f^2(x_0)}{4\Gamma_{\mathrm{B}} f(x)} \tag{5.20}$$

with the Fermi function

$$f(x) = \frac{1}{\exp(\frac{x-x_0}{T}) + 1}. \tag{5.21}$$

The parameter x_0 is the peak position. For the Coulomb peaks in path 2 the same equations apply, but with the inter-dot tunnel rate τ_{AC} and the dot-lead tunnel rate Γ_{C} between dot C and S_2. In case of infinite negative bias $f(x) = 1$ and $f(x_0) = 0$. These values are used for the measurements with applied bias voltage (Fig. 5.10). In the case of a neglectably small bias voltage applied to the system $f(x_0) = 1/2$ is used for the drain lead to account for a ratio of occupied to unoccupied states the tunneling electron interacts with and $f(x)$ is inserted for the source lead so that the temperature dependence is included.

The temperature T is estimated by fitting the Lorentzian function to the charging line of dot A (Fig. 5.11) from a measurement with a bias voltage around zero. Thus, $f(x_0) = 1/2$ for the drain and $f(x)$ for the source lead is inserted. After a translation from applied gate voltage into energy by the translation parameter $\alpha = 0.0041 \pm 0.0001$ (Eq. (2.34)) and conversion to K by k_{B} an electron temperature of

$$T = 87 \pm 45\,\mathrm{mK}, \tag{5.22}$$

is obtained, which is reasonable with regard to the cryostat bath temperature of around 15 mK. A possible source of error is noise, which is also broadening the Coulomb charging lines, increasing the calculated electron temperature. The other fit parameters, the rates, obtained from these fits, averaged from both fits and converted into energies with α, are $\Gamma_{\mathrm{A}} = 1 \pm 2\,\mu\mathrm{eV}$, $\Gamma_{\mathrm{C}} = 3 \pm 6\,\mu\mathrm{eV}$, and $\tau_{\mathrm{AC}} = 0.012 \pm 0.006\,\mathrm{meV}$.

As we have two equations, Eq. (5.19) and Eq. (5.20), we decrease the number of parameters to two, τ and Γ, with $\Gamma = \Gamma_{\mathrm{A,B}} = \Gamma_{\mathrm{A}} = \Gamma_{\mathrm{B}}$ for path 1. We get

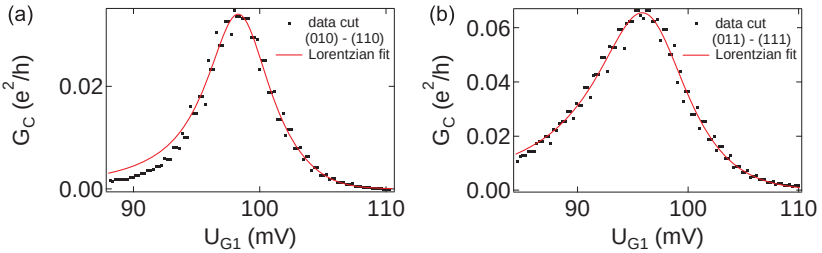

Figure 5.11: (a) Cut (longitudinal) through the resonant line between the states $|010\rangle$ and $|110\rangle$, the charging line of dot A. (b) Cut (longitudinal) through the resonant line between the states $|011\rangle$ and $|111\rangle$, the charging line of dot A, for one more electron on dot C. Both cuts are fitted using the Lorentzian function Eq. (5.18).

$$I_0 = e\Gamma_{\mathrm{A,B}} \frac{4\tau_{\mathrm{AB}}^2}{12\tau_{\mathrm{AB}}^2 + \Gamma_{\mathrm{A,B}}^2} \tag{5.23}$$

and

$$W^2 = 3\tau_{\mathrm{AB}}^2 + \frac{1}{2}\Gamma_{\mathrm{A,B}}^2 \tag{5.24}$$

for path 1.

For path 2 the equations are analogous, but with the inter-dot coupling τ_{AC} and the dot-lead coupling $\Gamma_{\mathrm{A,C}} = \Gamma_{\mathrm{A}} = \Gamma_{\mathrm{C}}$.

For the extraction of the tunnel rates in path 1, τ_{AB} and $\Gamma_{\mathrm{A,B}}$, a cut through the resonant line between the states $|101\rangle$ and $|011\rangle$ (Fig. 5.10 (a)) is fitted with the Lorentzian function (Eq. (5.18)). We use $\alpha = \frac{C_{\mathrm{G1,A}}}{C_{\Sigma\mathrm{A}}} - \frac{C_{\mathrm{G1,B}}}{C_{\Sigma\mathrm{B}}}$ with the capacitances from table 5.1 as a conversion parameter to convert the gate voltage U_{G1} into energies in eV. From the fit (Fig. 5.12 (a)) we obtain $I_0 = 0.0161 \pm 0.0004\,\mathrm{e}^2/\mathrm{h}$, $W = 0.192 \pm 0.006\,\mathrm{meV}$, and $x_0 = -14.997 \pm 0.004\,\mathrm{meV}$.

In order to extract the tunnel rates in path 2, τ_{AC} and $\Gamma_{\mathrm{A,C}}$, a cut through the resonant line between the states $|011\rangle$ and $|110\rangle$ (Fig. 5.10 (b)) is fitted

analogously. As a conversion parameter from gate voltages to energies we use $\alpha = \left(\frac{C_{\mathrm{G3,C}}}{C_{\Sigma\mathrm{C}}} - \frac{C_{\mathrm{G3,A}}}{C_{\Sigma\mathrm{A}}}\right) \cdot \sin(\pi/4) + \left(\frac{C_{\mathrm{G1,C}}}{C_{\Sigma\mathrm{C}}} - \frac{C_{\mathrm{G1,A}}}{C_{\Sigma\mathrm{A}}}\right) \cdot \cos(\pi/4)$ with the capacities from table 5.1. We obtain $I_0 = 0.01414 \pm 5 \cdot 10^{-5}\,\mathrm{e}^2/\mathrm{h}$, $W = 0.1297 \pm 0.0007\,\mathrm{meV}$, and $x_0 = -2.03\,\mathrm{meV}$ (fixed). The fit is shown in Figure 5.12 (b).

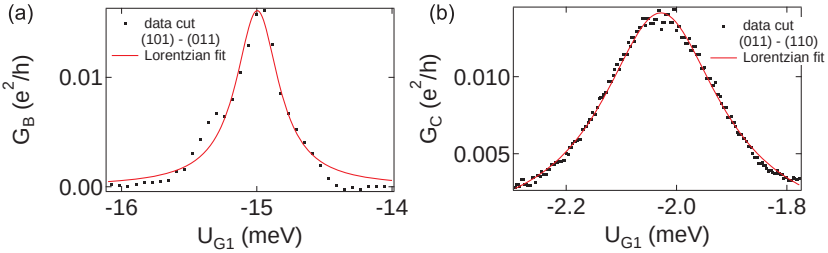

Figure 5.12: (a) Cut across the resonant line between the states $|101\rangle$ and $|011\rangle$ in path 1 in Fig. 5.10 (a) and a fit using the Lorentzian function Eq. (5.18). (b) Cut across the resonant line between the states $|011\rangle$ and $|110\rangle$ in path 2 in Fig. 5.10 (b) and a fit using the Lorentzian function Eq. (5.18).

From solving Eq. (5.23) and Eq. (5.24) we obtain the tunnel coupling parameters $\tau_{\mathrm{AB}} = 0.11\,\mathrm{meV}$ and $\Gamma_{\mathrm{A,B}} = 0.04\,\mathrm{meV}$ as well as $\tau_{\mathrm{AC}} = 0.07\,\mathrm{meV}$ and $\Gamma_{\mathrm{A,C}} = 0.04\,\mathrm{meV}$ as start guide values for a first numerical calculation of the current through the system. Then the simulation result is in detail fitted to the experimental conductance data and we obtain the tunnel couplings shown in table 5.3.

The tunnel couplings of path 2 are larger than of path 1, which is consistent with $\mathrm{G}_{\mathrm{path1}} < \mathrm{G}_{\mathrm{path2}}$ we observe in the measurements (Fig. 5.8 and Fig. 4.16, 4.17). Especially, we obtain $\tau_{\mathrm{AB}} < \tau_{\mathrm{AC}}$. We further get a weaker coupling between the dots and the leads, Γ, than between the dots, τ, which is a requirement for the master equation ansatz used later.

In order to obtain the steady state occupations the kernel of the master equation (Eq. (5.6)) has to be solved, $\rho^{\mathrm{ss}} = \ker[\mathcal{L}]$ (Eq. (5.12)). In this way the steady state properties of the system are obtained. The sys-

tunnel couplings	
inter-dot	dot-lead
$\tau_{AB} = 0.012\,\text{meV}$	$\Gamma_B = 0.003\,\text{meV}$
$\tau_{AC} = 0.020\,\text{meV}$	$\Gamma_C = 0.006\,\text{meV}$
	$\Gamma_A = 0.008\,\text{meV}$

Table 5.3: Tunnel couplings between the dots τ and between the dots and the leads Γ.

tem parameters in table 5.1 and table 5.3 are used as the best fit to the experiment. In Fig. 5.13 the numerical result of ρ^{ss} is shown. With this information the location of each charge stability region of the system can be determined. The state $|0,0,0\rangle$ is occupied for small U_{G1} and U_{G3}, the state $|1,1,1\rangle$ is occupied for large U_{G1} and U_{G3}. The states with one electron in the system are connected by the small stability region of state $|1,0,0\rangle$ and the states with two electrons in the system are connected by the small stability region of state $|0,1,1\rangle$. State $|0,0,1\rangle$
For larger values of U_{G3}, above the stability region of state $|0,0,0\rangle$, state $|0,0,1\rangle$ with one more electron in dot C becomes occupied. For larger values of U_{G1}, on the right side of the stability region of state $|0,0,0\rangle$, state $|0,1,0\rangle$ with one more electron in dot B becomes occupied. Going to smaller values of U_{G3}, below the stability region of state $|1,1,1\rangle$, state $|1,1,0\rangle$ with one less electron in dot C becomes occupied. For smaller values of U_{G1}, on the left side of the stability region of state $|1,1,1\rangle$, state $|1,0,1\rangle$ with one less electron in dot B becomes occupied. These calculated stability regions correspond very well to the regions which could already be identified in the measurement (Fig. 5.9). Both of these regions are not really seen in the measurement, as they are very small with lower occupation probability. They contain two triple points of path 1 and two triple points of path 2. A quadruple point is formed if two triple points of the system coincide.

The measured stability diagram (Fig. 5.9) is analyzed in more detail with the help of this calculation of the steady state occupations. The degenerate states for each of the four triple points of path 1 are determined, they are: ($|0,0,0\rangle$, $|0,1,0\rangle$, $|1,0,0\rangle$), ($|1,1,0\rangle$, $|1,0,0\rangle$, $|0,1,0\rangle$) and ($|0,0,1\rangle$, $|0,1,1\rangle$, $|1,0,1\rangle$), ($|1,1,1\rangle$, $|1,0,1\rangle$, $|0,1,1\rangle$). The last two triple points and the first two are equal. The pairs differ from each other by one electron in dot C,

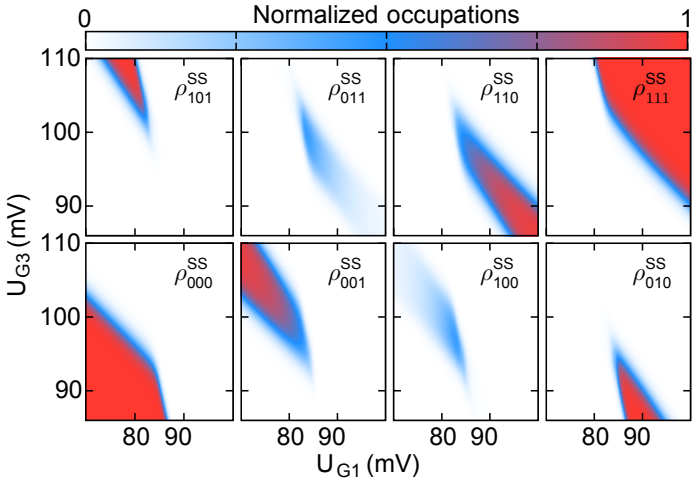

Figure 5.13: Calculated steady state occupation probabilities ρ_i^{ss} of each state i of the system, implemented by F. Gallego-Marcos. The states $|1,0,0\rangle$ and $|0,1,1\rangle$ have low occupation probability in a small region which is situated between the charge stability regions of $|0,0,1\rangle$, $|0,1,0\rangle$ and $|1,0,1\rangle$, $|1,1,0\rangle$, respectively. A similar diagram can be found in [91].

which shifts the energy of the degenerate states due to Coulomb interaction. In path 2 high differential conductance is observed at the triple points with the degenerate states ($|0,0,0\rangle$, $|0,0,1\rangle$, $|1,0,0\rangle$), ($|1,0,1\rangle$, $|0,0,1\rangle$, $|1,0,0\rangle$) and ($|0,1,0\rangle$, $|0,1,1\rangle$, $|1,1,0\rangle$), ($|1,1,1\rangle$, $|0,1,1\rangle$, $|1,1,0\rangle$), which have one more electron in dot B. Thus, in both paths we see resonances of the dots in the respective path for two different electron numbers in the dot present in the other path. The location of the triple points is marked in the stability diagram of the total TQD system in Figure 5.14.

The triple points marked with a and a* correspond to the resonance A-B with N electrons in dot C and the triple points marked with b and b* to the resonance A-B with N+1 electrons in dot C. The triple points marked with c and c* correspond to the resonance A-C with N electrons in dot B and the triple points marked with d and d* to the resonance A-C with N+1 electrons in dot B. In path 1 (2) a splitting of the resonance between the dots A and B (A and C) is observed due to the interaction with dot C (B).

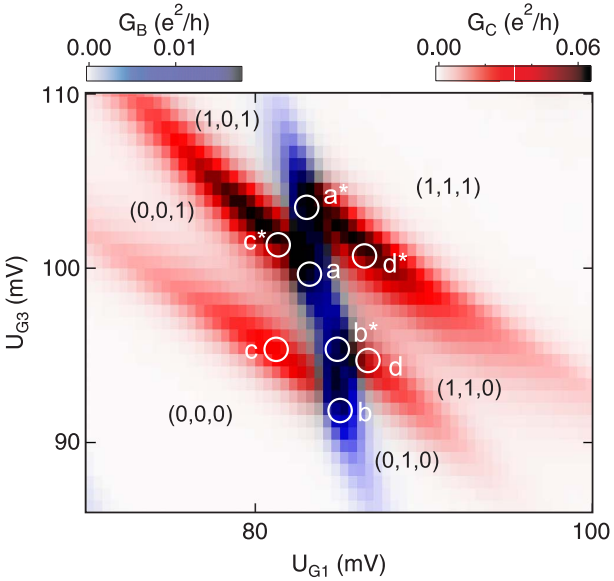

Figure 5.14: Combined color plot of the differential conductance of path 1 (red) and path 2 (blue) with denoted charge configurations and location of the triple points a, a* and b, b* in transport through path 1 and c, c* and d, d* in transport through path 2 as extracted from the calculation of the steady state occupation probabilities (Fig. 5.13).

The shift between the triple points a and b and between c and d is clearly visible. The resonance between the dots in one path is shifted to higher gate voltages when the dot in the other path is charged as it comes into resonance. Differential conductance in an extended area along the charging lines of the dots around the triple points and a rounded shape of the triple points is observed due to strong coherence effects near the dot resonances resulting from a strong inter-dot coupling. Also, temperature broadening of the states accounts for the broadening of the triple points. Consequently, the triple points of the resonance between dots A and B merge in transport and and a vertical high differential conductance line is formed.

Schematics of 2D cuts through the stability diagram of the TQD are shown in Figure 5.15 in order to give an idea of the position of the stability re-

gions and triple points in such a configuration close to a triple dot resonance.

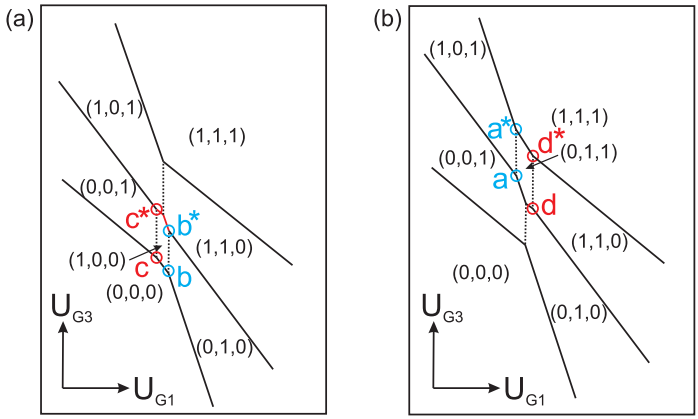

Figure 5.15: Schematic of the 2D stability diagram for two different cuts through the 3D stability diagram of the TQD, so that in (a) the stability region (1,0,0) and in (b) the stability region (0,1,1) is seen. The TP are denoted in the same notation as in Fig. 5.14.

In the measurement we have occupation of both states (1,0,0) and (0,1,1), which is only the case when the TQD system is near a triple dot resonance. In Fig. 5.15 two schematic stability diagrams are shown for slightly different 2D cuts through the 3D stability diagram, one where the stability region (1,0,0) is visible (a), and one where stability region (0,1,1) is seen (b). This way all triple points detected in the transport measurement can be shown in the schematic. The triple points are denoted in the same manner as in Fig. 5.14.

Using the steady state occupations ρ_i^{ss} and the tunneling rates to and from the leads Γ, the current through path 1 is calculated by Eq. (5.14), the current through path 2 by Eq. (5.15). The measured differential conductance and the simulation of transport for the same configuration as in the experiment is shown in Fig. 5.16 through path 1 and 2 separately. The simulation is in very good agreement with the experimental transport features.

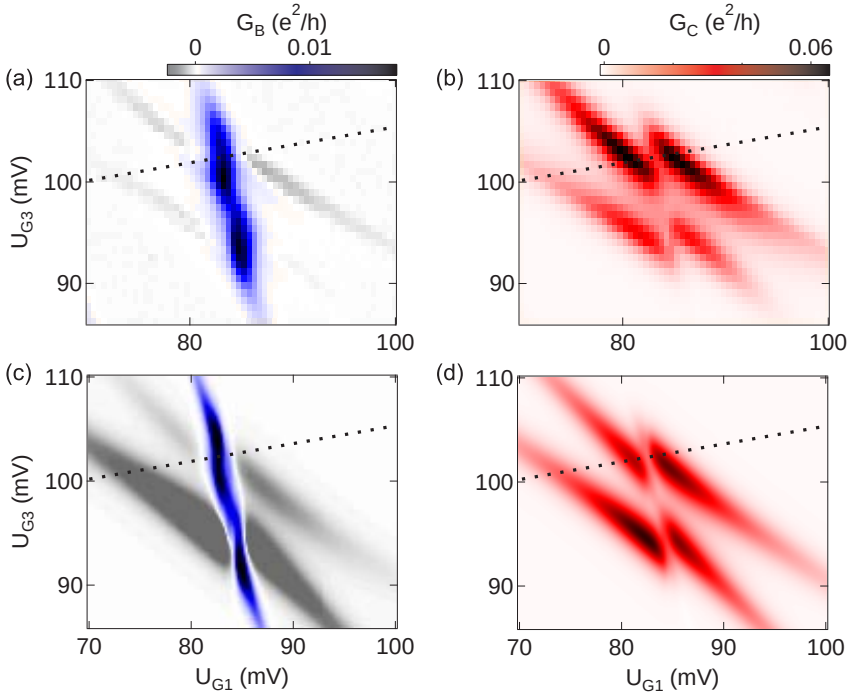

Figure 5.16: Differential conductance in experiment along path 1 (a) and path 2 (b) and in simulation along path 1 (c) and path 2 (d) (implemented by F. Gallego-Marcos). The dotted line indicates the cut shown in Fig. 5.17. Similar plots can be found in [91].

In the measurement and even more pronounced in the simulation we observe negative differential conductance in path 1 where path 2 has high conductance at the triple points. The negative differential conductance is observed in an extended area around the triple points due to strong coherence effects and temperature broadening of the states. The occurrence of negative differential conductance in transport will be analyzed in detail in the following.

To conclude, within this chapter a quantum mechanical model is presented to numerically calculate the steady state occupations of the system and the current through the two paths separately for a detailed analysis of the

transport properties. The system parameters such as capacitances and rough values for the tunneling rates are extracted from the measurements. With the help from the simulation outcome the positions of all stability regions and triple points in the measured stability diagram are determined. The simulated current reproduces the measurement outcome very well. The tunneling rates used in the simulation are treated as knowledge about the system for further investigation of its transport properties.

5.3 Channel blockade

In the following transport features of the two paths are analyzed and compared in more detail. Parts of this section have been published in [91] in collaboration with F. Gallego-Marcos.

A cut crossing the regions of triple points is taken in path 1 and 2 (dotted line in Fig. 5.16) for experiment and simulation outcome and is shown in Fig. 5.17.

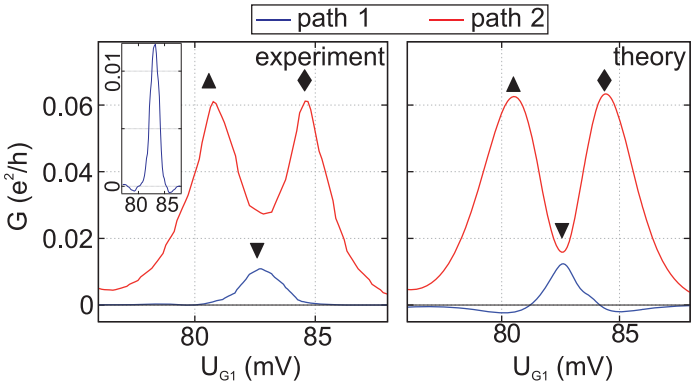

Figure 5.17: Cut through the transport measurement and simulation (dotted line in Figure 5.16) for path 1 and 2. The insert shows the measured differential conductance G of path 1 in dependence of U_{G1} alone and for a slightly different cut in order to clearly show the occurring negative differential conductance. A similar diagram has been published in [91].

The resonance of path 2 splits into two peaks (▲,♦) due to the Coulombic interaction with the third dot located in path 1 as the dots A and B come into resonance at (▼). Thus, the current through path 1 increases, which partially blocks the transport through path 2 and decreases the conductance. This point (▼) is a quadruple point, where four states of the system are degenerate and coexist in the same region of the stability diagram. As the relationship between the tunneling rates of the two paths is $\tau_{AC} > \tau_{AB}$ and $\Gamma_C > \Gamma_B$, transport through path 2 is stronger than through path 1. Consequently, when the quantum dot levels in path 2 are in resonance at (▲,♦) transport through path 1 is fully blocked and its differential conductance is decreased even to negative values. In the experimental data this negative differential conductance is visible in the total stability diagram in Fig. 5.16 (a) and in the insert in Fig. 5.17. A negative differential conductance means a decrease in transport for increasing bias voltage.

This channel blockade effect visible in both experiment and simulation results from the Coulomb interaction between the electrons coming from the two transport channels sharing dot A. The Coulomb interaction in the dots is strong and does not allow double occupancy of the dot energy levels. Thus, if an energy level is occupied by one electron the dot is in Coulomb blockade. When the bias voltage is increased, the path with higher conductance is responsible for the increase of the electron occupation of dot A. This is blocking the access to dot A for the electrons of the other path and is thus decreasing the transport through this path. This behaviour manifests itself in the measurement of the differential conductance of this path by negative differential conductance values.

In the quantum mechanical model of the triple quantum dot (see section 5.2) the Hamiltonian contains coherences among all the on-site states of the system. Only in this way the model is able to reproduce the system, as coherences are important within such a system with strong inter-dot and weak dot-lead coupling. The reason is, that for strong inter-dot coupling the energies of the states with which the dot system is coupled to the leads are not the on-site energies of the dots. Instead, they are the energies of the eigenstates of the Hamiltonian, which contain coherences among all the dots of the system (see section 2.3.3.3). Thus, coherent superpositions between states containing electrons occupying dot B and C are considered as well. However, as the electrons coming from path 1 and path 2 are distinguished, some of the coherences are broken. We call electrons coming from S_1 in

path 1 B-electrons and electrons coming from S_2 path 2 C-electrons. There are no coherences between B- and C-electrons included in the model. This is a consequence of the fact that they are distinguished at the drain which breaks their coherence as explained in section 5.1. We still have coherences between the dots B and C. Consequently, states of the system with one B-electron and states of the system with one C-electron are not coherent. For instance, state $|0,B,0\rangle$, where one electron coming from source S_1, a B-electron, occupies dot B and state $|0,0,C\rangle$, where one electron coming from source S_2, a C-electron, occupies dot C are not coherent. The same is true for $|B,0,0\rangle$ and $|C,0,0\rangle$. As there is no exchange interaction between these states there is no coherence between them. The only interaction between these two states is the Coulomb interaction, which comes from the electrostatic repulsion between the B- and the C-electron at dot A. The experimental results presented in section 5.1 also show that coherences between electrons coming from different paths are broken when they are distinguished at the drain. It directly manifests in transport where signatures of interference are destroyed when distinguishing the electrons. Hence the blockade in transport observed in simulation and experiment is ascribed to the Coulomb blockade in dot A between electrons coming from different paths. Besides, states of the system containing two electrons of different type, for example $|0,B,C\rangle$, $|B,0,C\rangle$, and $|C,B,0\rangle$ are coherent among each other. These coherences however stem from the coherence between the electrons of the same type. The coherence between $|0,B,C\rangle$ and $|B,0,C\rangle$, for example, results from the coherence between $|0,B\rangle$ and $|B,0\rangle$, but with one more electron in C. The same is true for the group $|0,C,B\rangle$, $|C,0,B\rangle$, and $|B,C,0\rangle$.

The dominating and the blocked transport channel for each of the two transport paths and in each resonance (▲,▼,♦) (Fig. 5.17) is identified using the information obtained from the simulation. In this way we can find out which transport sequences play the major role in the blockade effect. The result is implemented in the schematic in Fig. 5.18. The involved initial and final states connected by the two different transport paths are shown. Transport through path 1 is illustrated by blue arrows, transport through path 2 by red arrows. In case of the resonant configurations marked with (▲) and (♦) transport through path 1 is blocked by transport through path 2. In the resonant configuration marked with (▼) both paths are conducting and the occupation of dot A is provided by the transport from both paths. This condition corresponds to that of a quadruple point.

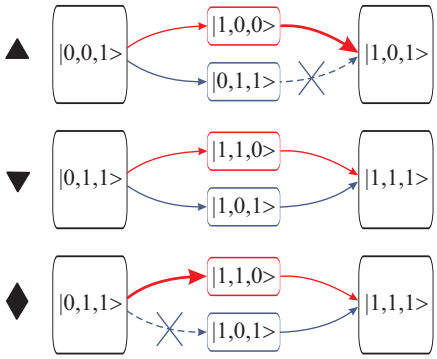

Figure 5.18: Transport mechanism (tunneling sequence) for each resonance seen in Fig. 5.17. In the peaks marked by (▲,♦) path 2 blocks path 1 in transport and in the peak (▼) the occupation of dot A is shared by both paths. A similar schematic has also been published in [91].

In the first peak in conductance of path 2 (▲) the transport sequence $|0,0,1\rangle \rightarrow |1,0,0\rangle \rightarrow |1,0,1\rangle \rightarrow |0,0,1\rangle$ in path 2 blocks the transport sequence $|0,0,1\rangle \rightarrow |0,1,1\rangle \rightarrow |1,0,1\rangle \rightarrow |0,0,1\rangle$ of path 1. The blockade takes place in dot A. In the dip in conductance of path 2 (▼) the transport sequence $|0,1,1\rangle \rightarrow |1,0,1\rangle \rightarrow |1,1,1\rangle \rightarrow |0,1,1\rangle$ in path 1 and the transport sequence $|0,1,1\rangle \rightarrow |1,1,0\rangle \rightarrow |1,1,1\rangle \rightarrow |0,1,1\rangle$ in path 2 share the occupation of dot A nearly equally. In the second peak in conductance of path 2 (♦) the same transport sequences as in the dip of path 2 (▼) are involved. This time the transport sequence in path 2, $|0,1,1\rangle \rightarrow |1,1,0\rangle \rightarrow |1,1,1\rangle \rightarrow |0,1,1\rangle$, blocks the transport sequence in path 1, $|0,1,1\rangle \rightarrow |1,0,1\rangle \rightarrow |1,1,1\rangle \rightarrow |0,1,1\rangle$. In comparison to the first peak in path 2, (▲), in the second peak in path 2 one more electron in dot B is involved, as the splitting of the resonance into two peaks in path 2 is due to the charging of dot B and Coulomb interaction.

Channel blockade is also observed further away from a triple dot resonance in the charging lines of dot A visible in the stability diagram in Fig. 5.19. It shows the differential conductance of path 1 (a) and path 2 (b) in dependence of the gate voltages U_{G1} and U_{G3}. In path 1 we observe resonances between dots A and B and indirect evidence of the charging of

the capacitively coupled dot C. In path 2 we see resonances between dots A and C and indirect evidence of the charging of the capacitively coupled dot B. In path 1 and 2 resonance lines of dot A with the leads are visible, in path 1 with high positive differential conductance and in path 2 with negative differential conductance. We will focus on the triple points of the resonances between dot A and B and the resonance lines of dot A, marked with (1) and (2) in Fig. 5.19, respectively.

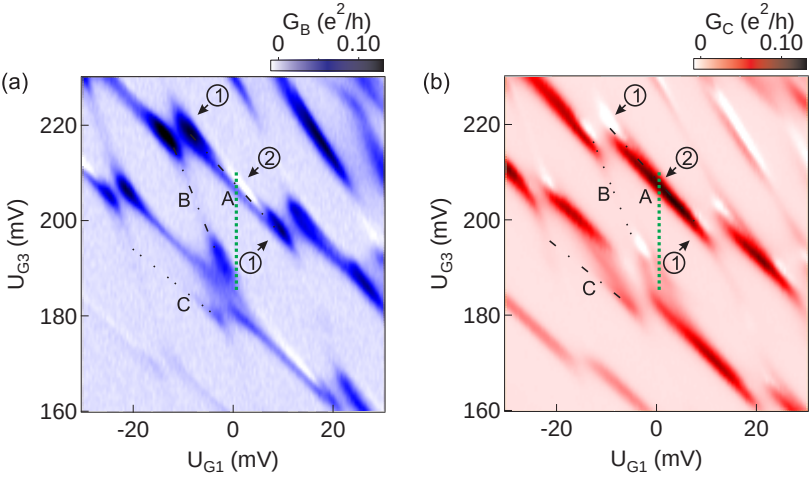

Figure 5.19: Differential conductance of path 1 (a) and path 2 (b) in dependence of the gate voltages U_{G1} and U_{G3}. Channel blockade in transport is seen at the triple points of the resonances between dots A and B in path 1 (1), where the resonant current in path 1 decreases the differential conductance through path 2, at some points even to negative values. Analogously, the cotunneling current in path 2, visible along the charging line of dot A, is blocking the transport through path 1, decreasing its differential conductance to negative values (2).

In path 1 we observe high positive differential conductance at the triple points, as expected, whereas in path 2 we see corresponding negative differential conductance. This can be attributed to the described channel blockade. Along the charging line of dot A in path 2 (2) high differential conductance exhibiting a peak in the middle of the line between two resonances of dot A and dot B for consecutive electron numbers in dot B is observed. Be-

tween the triple points strong decreasing differential conductance due to an exponential decrease of the first-order tunneling rate with the energy level detuning between the dots is expected. We attribute the observed behaviour of strong differential conductance along the charging line of dot A to elastic cotunneling (see section 2.3.2.3) between dot A and source S_2 in path 2, as dot C is out of resonance. The tunneling process is analog to the one depicted in Fig. 2.8 but with cotunneling over a non-resonant state of dot C. It is schematically depicted in Fig. 5.20 (a).

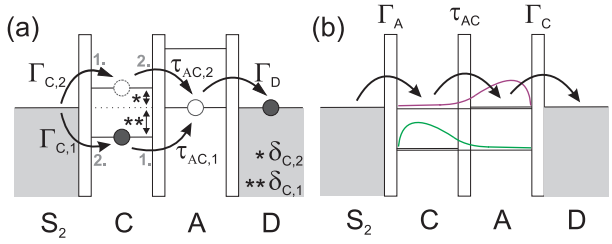

Figure 5.20: Second-order tunneling sequence leading to high differential conductance along the charging line of dot A in path 2. Elastic cotunneling via the virtual state (N+1) or (N-1) of dot C is followed by tunneling via dot A to the drain lead (a). (b) shows a schematic using molecular states to describe the probability of cotunneling via the off-resonant dot C. The electronic occupation probability is schematically depicted in green for the bonding and in purple for the anti-bonding state. Due to a non-zero occupation probability on dot C in the anti-bonding state transport can take place over the double dot.

The detected cotunneling current in path 2 is decreasing towards the triple points of the resonance between dot A and B as it competes with the resonant current through path 1 in this region. In some points the differential conductance even drops to negative values (1). The cotunneling rate from source S_2 to dot A can be expressed as [55, 120]

$$\Gamma_{co} = \Gamma_{C,1}\frac{\tau_{AC,1}^2}{\delta_{C,1}^2} + \Gamma_{C,2}\frac{\tau_{AC,2}^2}{\delta_{C,2}^2} \tag{5.25}$$

The parameters $\Gamma_{C,1}$ and $\Gamma_{C,2}$ are the tunnel rates between source S_1 and the occupied and unoccupied state of dot C, respectively, $\tau_{AC,1}$ and $\tau_{AC,2}$ are the tunnel rates between the occupied and unoccupied state in dot C, respectively, and the state in dot A. The energy difference between the

occupied(unoccupied) state of dot C and the state of dot A is $\delta_{C,1}(\delta_{C,2})$ The cotunneling rate is the sum of two terms, the first (second) one describing the cotunneling over the occupied (unoccupied) state of dot C (see section 2.3.2.3). Thereby the two tunnel processes are assumed to be independent and interferences between them are not taken into account. Equation (5.25) is valid for a large detuning between the dots, $\delta_{C,1} >> \tau_{AC,1}$ and $\delta_{C,2} >> \tau_{AC,2}$, where the first-order tunneling is strongly suppressed. As can be derived from this equation, the smaller the detuning between the dots and the larger the inter-dot tunnel couplings and tunnel couplings between dot C and source, the larger the cotunneling rate becomes. As the inter-dot tunnel rate τ_{AC} and the dot lead tunnel rate Γ_C in path 2 are high, the cotunneling conductance through path 2 is strong. In path 1 the inter-dot tunnel rate τ_{AB} and the dot-lead tunnel rate Γ_B is smaller (table 5.3), leading to a smaller cotunneling probability. Additionally, a larger energy level detuning of dot B than of dot C can contribute to this difference as well. Consequently negative differential conductance is observed between the triple points along the resonance line of dot A in path 1 due to channel blockade. The conductance due to cotunneling in path 2 is high, blocking the transport through path 1.

An alternative approach to this cotunneling through one dot of the serial double dot system is describing the system with molecular states. For a small detuning between the dots compared to the energy level detuning transport through the system can be described as coherent tunneling over a molecular state being delocalized over the two quantum dots (see section 2.3.3.3). In this description the first-order tunneling takes place over the bonding state and the second-order tunneling is the tunneling over the anti-bonding state [120]. This description for the cotunneling current is valid independently of the detuning between the dots and is equivalent to Eq. (5.25) from the localized state description for large energy level detuning. For a non-zero energy level detuning the weight of the occupation probability is strongly unequal between the two dots, but a small occupation probability remains on the other dot, respectively. This is schematically depicted in Fig. 5.20 (b). Due to this non-zero occupation probability there is a finite overlap between the wavefunctions of the electrons in the source lead and the anti-bonding state, leading to a small non-zero tunneling probability from the source lead over the anti-bonding state to the drain lead. This is equivalent to a cotunneling process over the detuned dot C in the picture of fully localized states.

In the parameter regime of the stability diagram in Fig. 5.19 no cotunneling current is observed in the paths when dot B or dot C is in resonance with the leads and dot A is off-resonant. This can be the consequence of a comparatively large charging energy $E_C = \delta_{A,1} + \delta_{A,2}$ of dot A, or of a small tunnel rate Γ_A between dot A and drain in this parameter regime. In the picture of molecular states the latter means a small overlap between the electronic wave function of the anti-bonding state with the wave function of the drain lead.

Channel blockade is also observed in Coulomb diamond measurements of the system. Figure 5.21 shows the differential conductance of path 1 and 2 as a function of the bias voltage at path 2, U_{S2}, and gate voltage U_{G3}. A cut at zero bias voltage through the Coulomb diamond measurement corresponds to a cut at $U_{G1} = 1\,\text{mV}$ in the stability diagram in Fig. 5.19 for $U_{G3} = 185 - 210\,\text{mV}$ (green dotted line). This helps to identify the features seen in the Coulomb diamond measurement.

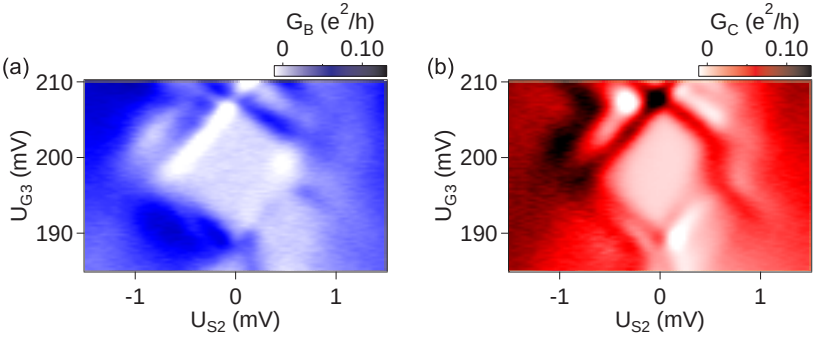

Figure 5.21: Differential conductance in dependence of the bias voltage at path 2, U_{S2}, and gate voltage U_{G3} of path 1 (a) and path 2 (b). A Coulomb diamond of dot A is visible. Channel blockade is clearly observable in path 1 for resonance of dot A with source S_2 in path 2.

Comparison shows that we see a Coulomb diamond of dot A. In path 2 where the bias voltage is varied we observe high differential conductance if dot A is in resonance with the leads. Lines with positive slope are resonances of dot A with source, lines with negative slope resonances of dot A with drain.

The upper and lower crossing point of the Coulomb diamond correspond to the resonance of dot A with the leads only and a configuration close to a quadruple point, respectively. In path 1 corresponding negative differential conductance is observed when dot A is in resonance with the source lead S_2 in path 2 and positive differential conductance for the resonance with the drain lead.

First we will focus on the upper crossing point of the Coulomb diamond at $U_{G3} \approx 208\,\text{mV}$, where by comparison with the stability diagram (Fig. 5.19) only dot A is in resonance with the leads. We see high differential conductance in path 2 in both stability diagram and Coulomb diamond measurement, the described cotunneling between dot A and source S_2 via dot C. The transport through path 1 is weaker and partially blocked by the strong cotunneling conductance through path 2. Similar behavior is observed for the resonance lines of dot A with source S_2 (lines with positive slope). The corresponding differential conductance in path 1 is very low, as the bias across this path is zero and the dots are off-resonant with both leads, S_1 and D. It even drops to negative values, the sign of channel blockade because of strong transport through path 2. For the resonance lines of dot A with the common drain lead D of the two paths positive differential conductance for both paths is observed. We obtain small but positive differential conductance in both paths. The occupation of dot A is shared by both paths as the energy level configurations and thus tunnel probabilities are similar in both paths. The same pattern is observed for varying bias at path 1, U_{S1}, but with channel blockade in path 2 (see Fig. 4.18). Channel blockade is observed in transport path i for resonance of dot A with source S_j ($i,j \in \{1,2\}$; $i \neq j$). With applying a bias voltage in one path a strong blockade of transport in the other path can be induced. In the lower crossing point of the Coulomb diamond at $U_{G3} \approx 188\,\text{mV}$ the system configuration is close to a quadruple point, where all three dots are in resonance. Here the conductance is more equally shared by both paths. In case of a quadruple point a coherent state is formed practically uniformly between all the dots. The occupation of dot A is shared by electrons from path 1 and 2 and no blockade in transport is seen.

Fig. 5.22 shows a cut through the Coulomb diamond at zero bias voltage. It can be clearly observed that the conductance is shared nearly equally by both paths when the system is tuned near a quadruple point ($U_{G3} \approx 188\,\text{mV}$). Channel blockade is occurring when the dots are detuned and the paths have more unequal total tunneling probabilities ($U_{G3} \approx 208\,\text{mV}$). The channel

blockade is dependent on the energy level detuning between the dots and the tunnel couplings. This dependence clearly manifests itself in the different behaviour in the quadruple point and in situations of detuning in the dot system, which is nicely seen in Fig. 5.22.

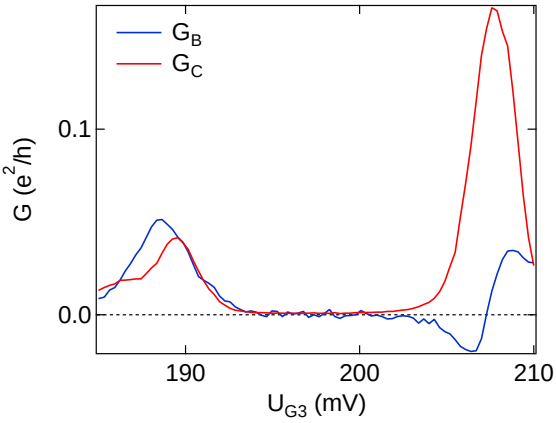

Figure 5.22: Cut through the Coulomb diamond measurement Fig. 5.21 at $U_{S2} = 0\,\text{mV}$. The differential conductance is shown in dependence of U_{G3} for transport paths 1 and 2. Around $U_{G3} \approx 188\,\text{mV}$ the transport is shared equally between the paths (quadruple point) and around $U_{G3} \approx 208\,\text{mV}$ transport through path 2 is stronger, leading to a blockade of transport through path 1.

5.3.1 Non-linearity in transport

The appearance of the channel blockade is dependent on the transport direction in this TQD system, as the way the transport paths interact with each other is transport direction dependent. The two transport directions are depicted in Figure 5.23. For electron transport going from $S_1 \rightarrow D$, $S_2 \rightarrow D$ (Fig. 5.23 (a)), named transport in (+)-direction in the following and corresponding to application of a small positive bias voltage, we encounter channel blockade. For reverse transport direction electron transport is going from $S \rightarrow D_1$, $S \rightarrow D_2$ (Fig. 5.23 (b)), named (-)-direction in the following and corresponding to application of a small negative bias voltage. In this case there is no channel blockade. The reason is, that the transport paths

influence each other in a different way in this transport direction.
In this direction, the electron flow splits at dot A into two paths. This distribution is determined by probabilities which depend on the tunneling rates of path 1 (τ_{AB}, Γ_B) and path 2 (τ_{AC}, Γ_C). For this transport direction no negative differential conductance occurs. Thus, for the observation of channel blockade it is crucial to have two source leads in this system.

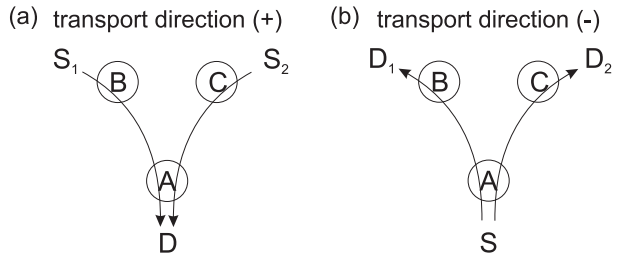

Figure 5.23: Schematic picture defining the (+)- transport direction as transport from the two leads at dots B and C to the lead attached at dot A (a), the (-)- transport direction as transport from the lead at dot A to the leads attached to dots B and C (b).

This difference is shown in a simulation of transport for both transport directions (Fig. 5.24). While for the (+)- transport direction negative differential conductance occurs in path 1 due to channel blockade (Fig. 5.24, (a),(b)), for the (-)- transport direction (Fig. 5.24 (c),(d)) no negative differential conductance is observed. In the latter case, the electrons at dot A see two paths with different tunneling barriers resulting in a corresponding tunneling probability. Therefore, the electron flow splits into two paths with a probability that depends on the tunneling rates of path 1 and 2. The conductance shown in the diagrams depends on this tunneling probability (Eq. (5.13)).

In order to clearly show the difference between the two transport directions and to investigate it in greater depth, the simulated differential conductance G of path 1 and 2 as a function of the ratio between the dot-source couplings Γ_C/Γ_B is analyzed for both transport directions (Fig. 5.25). The ratio is varied by changing Γ_C. The transport direction $S_1 \rightarrow D$, $S_2 \rightarrow D$ is labeled

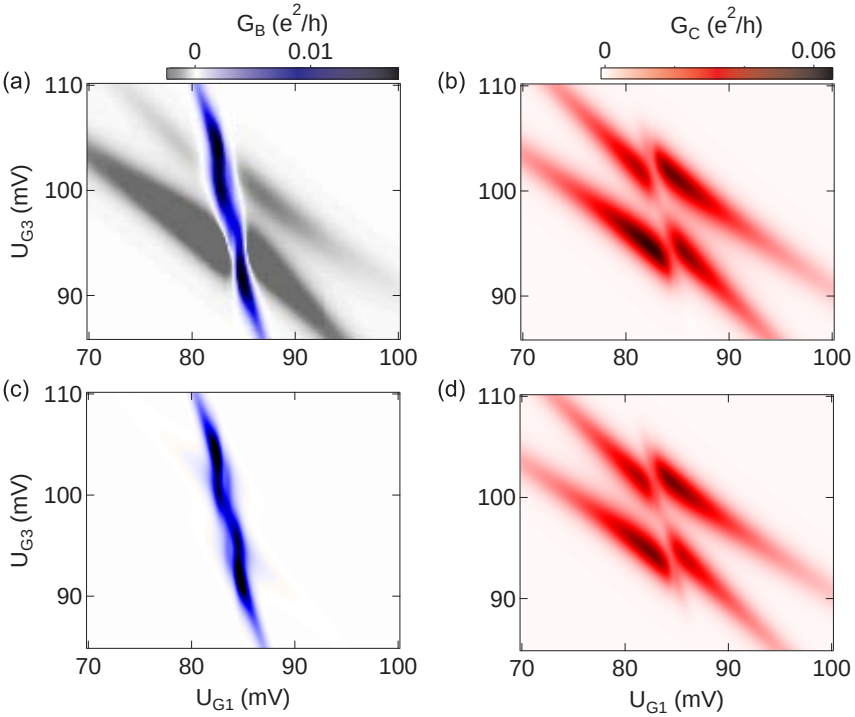

Figure 5.24: Calculated differential conductance of path 1 and 2 in dependence of U_{G1} and U_{G3} for the (+)- transport direction ((a) and (b)) and the (-)- transport direction ((c) and (d)) (implemented by F. Gallego-Marcos). In contrast to the (+)- direction there is no negative differential conductance in path 1 in the (-)- direction as the transport paths influence each other in a different way. [91]

with (+) and the transport direction $S \rightarrow D_1$, $S \rightarrow D_2$ is labeled with (-). The simulation is performed for the situation around a quadruple point, marked with (▼) in Figure 5.17, where the conductance through the paths is almost equal and the paths share the occupation of dot A. The same coupling parameters are used (table 5.3). We observe that for both (+)- and (-)- transport direction the effective tunnel probabilities of the two paths are mutually dependent on each other. For high differential condcutance due to a large tunneling rate in one path we get low differential conductance in

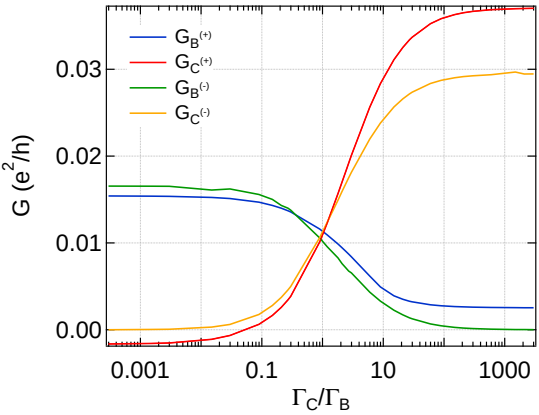

Figure 5.25: Calculated differential conductance G in dependence of the ratio Γ_C/Γ_B, which is varied by changing Γ_C, for path 1 and path 2 and for both transport directions (+) and (-) (implemented by F. Gallego-Marcos). The situation (▼) in Fig.5.17 is here seen at Γ_C/Γ_B=2 (see Table 5.3). For (+)-transport direction we observe negative differential conductance, which is not observed for the (-)-transport direction.

the other and vice versa.

We take a closer look at the differences between the transport directions in the example of Fig. 5.25. First, we analyze the (-)- transport direction (green and yellow line). For path 1 we see strong conductance for large Γ_B with respect to Γ_C and conductance going to zero for large Γ_C with respect to Γ_B. For path 2 it is the other way around. So depending on the tunneling rate along the path, we measure strong or weak transport. For very small Γ_C the tunnel barrier from dot C to the drain is effectively closed. Consequently for path 2 a steady state occupation of dot C over dot A is achieved quickly and no further transport takes place. The system basically behaves like a double dot consisting of path 1 with dots A and B. The conductance of path 1 is only determined by the tunnel rates (τ_{AB}, Γ_B) in this path and saturates at the corresponding maximum value. For increasing Γ_C transport through path 2 becomes more relevant. Dot C is depopulated over S_2 with Γ_C. Now an electron on dot A additionally has the possibility to tunnel to dot C. The larger the tunneling rate of a

dot to the drain becomes, the faster the dot is depopulated and the higher the probability of the electron to tunnel to that dot. For rising Γ_C the probability of the electron tunneling from dot A to dot C is increasing, decreasing the probability of the electron going to dot B. Consequently, the conductance increases through path 2 and decreases through path 1. When Γ_C grows bigger than Γ_B the depopulation of dot C is faster than the depopulation of dot B. Consequently the electron on dot A is more likely to tunnel to dot C than to dot B and thus the conductance of path 2 becomes bigger than the conductance of path 1. In the extreme case of $\Gamma_C >> \Gamma_B$, dot C is depopulated very fast and the probability of the electrons on dot A tunneling to dot C is high. Thus, basically all the electrons will tunnel through path 2 and the conductance of path 2 saturates at a maximum value, determined by τ_{AC}, and the conductance of path 1 goes to zero. As the maximum conductance of path 1 is determined by τ_{AB} and Γ_B and of path 2 determined only by τ_{AC}, as described, the maximum transport through path 1 is smaller than the maximum transport through path 2.

Now we analyze the (+)- transport direction (blue and red line). We see a qualitatively similar behaviour as in the (-)- transport direction. For decreasing Γ_C the conductance through path 2 decreases and the conductance through path 1 increases and for increasing Γ_C vice versa. However, for small values of Γ_C the differential conductance even becomes negative for path 2 in this transport direction. For very large Γ_C the differential conductance of path 1 saturates at a small but finite and positive value. In this transport direction the path with stronger transport due to higher total tunneling probability blocks the transport through the other path in the shared dot A. The blockade is caused by Coulomb interaction between the electrons coming from the two paths competing for the occupation of dot A. The differential conductance becomes negative. As in this simulation the tunnel coupling Γ_C in path 2 is varied, the conductance in path 2 can be driven sufficiently low, so that the transport through this path can be fully blocked. Consequently, only the differential conductance in path 2 becomes negative. For very big values of Γ_C the transport through path 2 becomes strong, but the tunneling probability through path 1 determined by τ_{AB} and Γ_B is high enough for the transport not to be totally blocked.

To sum up, in (+)-transport direction we encounter channel blockade and resulting negative differential conductance in the path with a small total tunneling rate due to a high total tunneling rate in the other path, whereas

in the (-)-transport direction the electron current splits according to the tunneling probabilities through the two paths and no negative differential conductance is possible.

This shows that the two transport directions are in general not equivalent. The channel blockade depends on the strengths of the tunnel couplings and on the detuning between the energy levels which both determine the tunneling probability through the path. Only if the tunneling probabilities of the two paths are equal, there is no channel blockade and the transport directions through the sample are equal. Otherwise the transport directions are non-equivalent and the transport characteristics are non-linear, mediated by inter-channel Coulomb interaction. The total current (Eq. (5.14)) through the system is a function of the tunneling rates between dots and leads Γ and the inter-dot tunneling rates τ which we do not have analytically. The current through one path mainly depends on the tunnel rates to the leads and the inter-dot tunnel rates of the dots in this path. Consequently, in case of a non-equal tunneling probability in the paths we observe non-linear transport even around zero bias voltage. The tunneling probabilities of the paths are equal in the case of a quadruple point if the tunnel couplings in the paths are equal. The transport then is linear around zero bias voltage. In all other cases deviations are obtained. In our system we do not have linear transport through the dot arrangement even when we are at a quadruple point due to the asymmetry in the tunnel couplings within the transport paths. This will be discussed in the following for the example of the resonance condition (▼) (Fig. 5.17). This situation is seen at $\Gamma_\mathrm{C}/\Gamma_\mathrm{B}$=2 in Fig. 5.25.

We consider the case where all three dots are in resonance, a quadruple point. The conductance values $\mathrm{G_B}$ and $\mathrm{G_C}$ of path 1 and 2, respectively, are equal for the (-)-transport direction, $\mathrm{G_B^-} = \mathrm{G_C^-}$, if the tunneling probabilities in the paths are equal. The same is true for the (+)-transport direction. In our case $\tau_\mathrm{AB} < \tau_\mathrm{AC}$, this is why the point where the conductance is equal in both paths as expected in the situation of a quadruple point lies at a value $\Gamma_\mathrm{C}/\Gamma_\mathrm{B} = 0.089 < 1$ for the (-)-transport direction. Here, $\mathrm{G_B^-} = \mathrm{G_C^-} = 0.0106\,\mathrm{e^2/h}$. The point where $\mathrm{G_B^+} = \mathrm{G_C^+} = 0.0112\,\mathrm{e^2/h}$ is shifted to higher values $\Gamma_\mathrm{C}/\Gamma_\mathrm{B} = 1.042 > 1$. This deviation stems from the fact that dots A and C in path 2 are slightly detuned in this considered case ((▼) in Fig. 5.17, dotted line in Fig. 5.16). This decreases the tunneling probability in path 2 and also adds to the difference in the conductance of

the transport directions of a path. As dot C is slightly out of resonance the transport directions are not equal across the tunneling barrier between the dots and across the tunneling barrier between dot C and source S_2. The detuning is such that $G_C^+ < G_C^-$, so the transport through path 2 in the (+)-direction is smaller. Consequently, the crossing point where $G_B^+ = G_C^+$ is shifted to larger values of Γ_C/Γ_B with respect to the point where $G_B^- = G_C^-$.

Around zero bias voltage we would expect the system to be in the linear transport regime (see section 2.3.2.1). For small bias voltages compared to the thermal energy $\Delta\mu_{SD} << k_B T$ the conductance $\mathcal{G}$ of a dot is independent of applied voltage so the current $I = \mathcal{G} \cdot V$ is linear. According to an estimation of the electron temperature of $T \approx 100\,\mathrm{mK}$ (Eq. (5.22)), we would expect this system to be in the linear regime for only small bias voltages $\Delta\mu_{SD} << 9\,\mu\mathrm{eV}$. However, as the slope of the current-bias voltage-characteristic is different for positive and negative bias voltage, as explained, the transport is not in the linear regime around zero bias voltage. Consequently, the transport is non-linear independent of bias voltage. In general, this behaviour is characteristic for a triangular setup of quantum dots where two transport paths share one dot and lead.

The presented measurements (Fig. 5.16 (a),(b)) and also the former ones performed by Rogge et al. [24] with one source at A and two drains at B and C, are all AC measurements, meaning an AC voltage U_{AC} is applied to the source. This is done to measure the differential conductance directly and also, in case of our setup with two sources and only one drain, to allow a distinction between the electrons coming from the two paths at the drain by using two different frequencies. By doing so, interactions between the paths manifest themselves in the transport measurements. In AC measurements we always measure an averaging of the two transport directions. We have to distinguish between the two configurations, the one with one source and the one with two sources and two different applied AC voltage frequencies.

With one source S at dot A and two drains, D_1 at dot B and D_2 at dot C, only one frequency (at S) is applied to directly measure the differential conductance. The electrons move alternately from source to the drains and from the drains to source simultaneously for the two paths. For one source and thus one AC voltage, we get transport from source to the drains ((-)-direction) for the negative half-wave of the sinusoidal AC voltage, and transport from the drains to source ((+)-direction) for the positive half-wave

in both transport paths. In (-)-transport direction the electrons do not encounter a blockade in the common dot A. In the (+)-transport direction one path can be blocked in transport in dot A due to a higher conductance in the other path with higher electron tunneling probability: the described channel blockade. Thus negative differential conductance is possible in this direction. Consequently, when applying an AC voltage U_{AC} to the source the average I_{AC} we measure at the drain is smaller than it would be without the blockade, but always positive. The measurements presented in [24] use this setup. No negative differential conductance is observed, as expected. Interactions between the paths do not clearly manifest themselves in this setup.

In our case, where the system has two source leads S_1 and S_2 and one drain lead D, the possibility is opened up to apply source voltages with different frequencies. If two different AC frequencies are applied to the paths, we have alternating transport from source to drain in both paths, but with a different frequency. Consequently, the transport directions of the two paths are out of phase, so there are more superposition cases of electron current at dot A over time as not always the same half-waves from path 1 and path 2 are superposed at dot A like it is the case with one applied frequency. In all superposition cases the electrons can encounter channel blockade except in the case of superposition of two negative half-waves of the sinusoidal AC voltages from the two paths (transport from the drain to the sources in both paths, (-)- transport direction). Thus, we expect the channel blockade to be more distinct when applying two different frequencies to the paths. Only in this case the interaction between the paths manifests itself clearly in transport via the occurrence of negative differential conductance. To sum up, the setup used within the scope of this work makes the non-linear transport characteristics of the system detectable in the two-path stability diagrams.

The non-linear behavior of transport at zero bias voltage becomes directly apparent in the conductance through the system in dependence of bias voltage. Figure 5.26 shows a Coulomb diamond measurement where the differential conductance is measured in dependence of the bias voltage at source S_1, U_{S1}, and the gate voltage U_{G3}. A Coulomb diamond of dot A is observed. At $U_{\mathrm{G3}} = 180.2\,\mathrm{mV}$ and $U_{\mathrm{S1}} = 0\,\mathrm{mV}$ we see conductance in both path 1 and path 2 and hence are at a region near a quadruple point. Around the region of a quadruple point we have transport in both paths and can thus observe the paths influencing each other in transport by competing for

occupation of dot A. Here we have a similar situation as in the stability diagram measurements around a triple dot resonance (Fig. 5.17). A cut through the area of the quadruple point is shown in Figure 5.27 for path 1, where the bias voltage is varied.

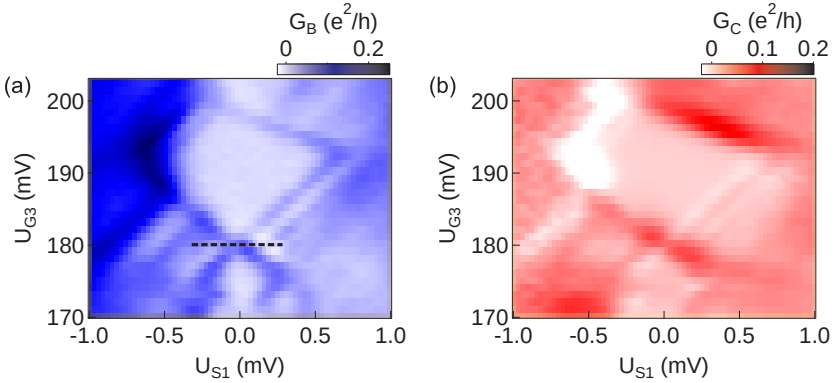

Figure 5.26: Differential conductance of path 1 (a) and path 2 (b) in dependence of bias voltage at S_1 and U_{G3}. At $U_{G3} = 180.2\,\text{mV}$ the system is close to a quadruple point with high conductance in both path 1 and path 2.

In the linear transport regime at zero bias voltage the current, which is the integrated differential conductance signal, is linear around this point and the differential conductance is a peak at zero bias being symmetric in a small range for positive and negative bias voltage. In path 1 where the bias voltage is varied we see an asymmetric Coulomb peak in the relevant regime of $\Delta\mu_{\text{SD}} << k_{\text{B}}T$ around zero bias voltage (bounded by solid lines in Fig. 5.27). This shows that the transport is highly non-linear around zero bias voltage.

Charge transport blockade phenomena of other kinds have been studied theoretically in different other dot setups. It was found in a three-terminal single dot where the interaction between two different spin channels was studied, showing the modulation of one channel by the other [121]. Channel blockade effects involving Coulomb correlations were investigated theoretically for two parallel transport channels with single or double dots in each path and a capacitive coupling between the dots belonging to different paths

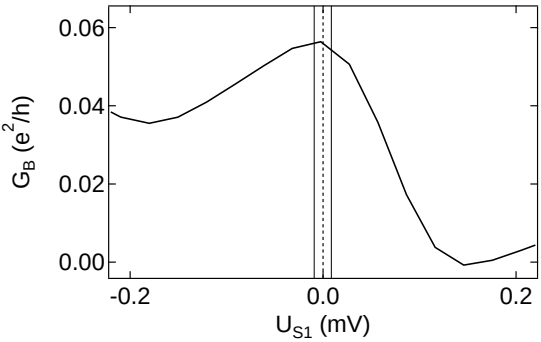

Figure 5.27: Cut across the region near a quadruple point (dotted line in Fig. 5.26) in path 1. It shows a highly non-symmetric Coulomb peak referring to non-linear transport around zero bias voltage. The thermal energy $k_B T$ for $T \approx 100\,\mathrm{mK}$ is marked with solid lines around zero bias voltage.

[122–124]. In our system we have two double dot paths which are connected by one common dot. The dots are coherently coupled forming molecular states involving the on-site states of all three dots so that the electrons are delocalized throughout the TQD. To understand the full transport characteristics in the double path structure it has to be described by quantum mechanical dynamics.

To sum up, the interaction between the paths causes a channel blockade leading to a non-linear transport behaviour of the dot system. Coulomb correlations in the shared dot A between electrons of different paths lead to a blockade of current through one path if the conductance through the other is high. The interaction between the paths gives rise to the possibility to detect current through one path by investigation of transport through the other. The channel blockade manifests itself in the occurrence of negative differential conductance of the blocked path. It is an inherent phenomenon in triangular dot setups with two transport paths and a shared dot and drain lead and occurs for situations where the tunneling probabilities of the transport paths are unequal. The strength of the blockade can thus be modulated by varying the inter-dot detuning. The non-linearity of transport arising from the transport direction dependence of the channel blockade is additionally observed in Coulomb diamond measurements around zero bias

voltage.

5.4 Inelastic cotunneling

Within this chapter a closer analysis of the Coulomb diamonds of dot A is performed. In Figure 5.28 a Coulomb diamond measurement of transport path 1 with dots A and B is presented. The differential conductance G in dependence of bias voltage U_{S1} and gate voltage U_{G3} is shown. Two Coulomb diamonds of dot A are seen right above a triple dot resonance. The left edge of both diamonds at negative bias voltage is filled out with high differential conductance, best seen in the lower diamond, where the dot is in Coulomb blockade.

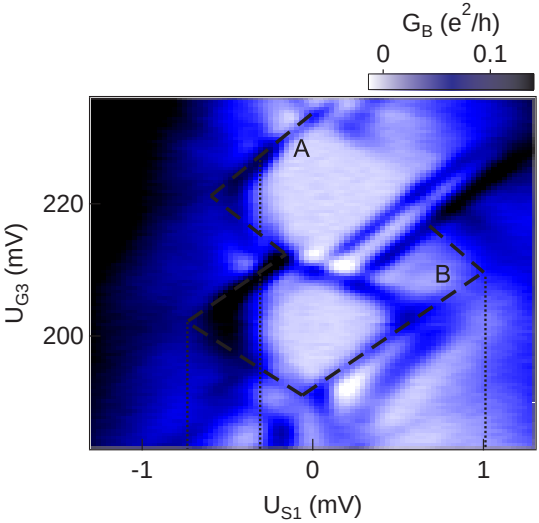

Figure 5.28: Differential conductance of path 1 in dependence of U_{S1} and U_{G3}. Coulomb diamonds of dots A and B are observed, the resonances of the dots with the leads being exemplarily marked with dashed black lines as a guide to the eye. In the edges of both Coulomb diamonds of dot A there is an onset of non-zero differential conductance at negative bias voltage.

If the energy difference of the chemical potential of the leads is equal

or larger than the difference in charging energy E_C of the involved dots, $e\,|U_{S1}| \geq \Delta E_C$, simultaneous tunneling from source S_1 to dot B and from dot A to drain D is possible. This is a non-coherent and inelastic cotunneling process as two electrons are involved and the double dot is left in a state of higher energy than before the tunnel process (see section 2.3.2.3). This onset of inelastic cotunneling results in a current through the otherwise Coulomb blockaded double dot. In the differential conductance to first approximation a step is expected [125], occurring at $e\,|U_{S1}| = \Delta E_C$. This behaviour is different than the one originating from elastic cotunneling through the dots, where residual low constant differential conductance inside the Coulomb diamond is observed. The tunneling process is depicted schematically in Figure 5.29.

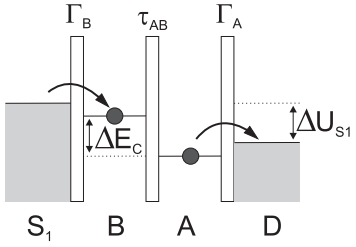

Figure 5.29: Inelastic tunneling process leading to the onset of high differential conductance inside the Coulomb blockaded region of the double dot inside the Coulomb diamond. For $e\,|U_{S1}| \geq \Delta E_C$ energy conservation allows a tunnel current through the double dot by the depicted tunnel sequence of two electrons. The double quantum dot remains in an excited state after this process.

Dots A and B are in Coulomb blockade. In case of $e\,|U_{S1}| \leq \Delta E_C$ no first-order tunneling process through the double dot is possible due the energy conservation law. As the bias voltage at S_1 is increased, the chemical potential of source S_1 is raised above the next energy level of dot B. When $e\,|U_{S1}| \leq \Delta E_C$ the Coulomb blockade is lifted. The half width of the Coulomb diamond belonging to dot A is $\Delta_A = 0.7\,\text{mV}$ and the half width of the Coulomb diamond belonging to dot B is $\Delta_B = 1.0\,\text{mV}$, extracted from this measurement. Thus it is $\Delta E_C = \Delta_B - \Delta_A = 0.3\,\text{mV}$. In the shown Coulomb diamond measurement the finite differential conductance step inside the Coulomb diamond of dot A is observed at $|U_{S1}| = 0.3\,\text{mV}$. Thus, it is $\Delta E_C = |U_{S1}|$ at this point. Consequently, the inelastic cotunneling

process can be responsible for the overcome Coulomb blockade. The non-zero differential conductance fills out the corner of the Coulomb diamond as the probability for the cotunneling process increases with increasing bias voltage. Additionally, the line marking the onset of the inelastic cotunneling connects with a line of first-order tunneling via an excited state, clearly seen for the lower Coulomb diamond, as expected (see section 2.3.2.3). Inelastic cotunneling is only appearing on one side of the Coulomb diamond, for $U_{S1}<0$. This asymmetry stems from the strong inequality of the two transport directions of a detuned double dot system [126]. For the same energy level detuning between the dots the tunneling probability in case of $U_{S1}>0\,\mathrm{mV}$ is very low. This can be deduced from Fig. 5.29 by exchanging the chemical potentials of the leads. The tunneling process then involves a quantum dot acting as a tunneling barrier for both tunneling electrons, which strongly decreases the probability of this process.

Similar cotunneling effect has been frequently observed in a single dot, reported in [127–130], but also in a vertical double dot sample, described in [126].

5.5 Hybridized states

In this section the transport through the system is analyzed for different constant bias voltages applied at the two transport paths. The differential conductance for $U_{S1} = 0\,\mathrm{mV}$ (Fig. 5.30) and for bias voltages of $U_{S1} = -1.0\,\mathrm{mV}$ and $U_{S1} = -1.5\,\mathrm{mV}$ at S_1 (Fig. 5.31) is measured as a function of U_{G1} and U_{G3}. The bias voltage across the other path is zero, $U_{S2} = 0\,\mathrm{mV}$. The device is in a regime where the inter-dot tunnel rates are asymmetric, $\tau_{AC} > \tau_{AB}$ (see table 5.3).

For $U_{S1} = 0\,\mathrm{mV}$ the stability diagram is the same as shown in Fig. 5.8, but for slightly different gate voltage values, so that the weight of the stability regions is slightly different. The stability regions are identified according to Fig. 5.15. If a bias voltage is applied at S_1, a second line parallel to the charge reconfiguration line is observed at the resonances of dots A and B for both N and $N+1$ electrons on dot C. The lines separate the states $|1,0,0\rangle$ and $|0,1,0\rangle$ as well as $|1,0,1\rangle$ and $|0,1,1\rangle$ with one more electron in dot C. A

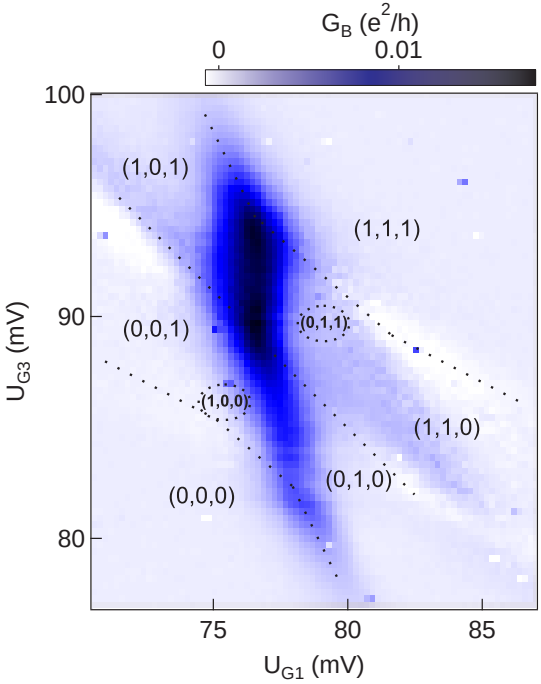

Figure 5.30: Differential conductance of path 1 as a function of gate voltages U_{G1} and U_{G3} for $U_{S1} = 0\,\text{mV}$ in the region of a triple dot resonance. The stability regions are denoted in the diagram.

cut at $U_{G3} = 84.3\,\text{mV}$ and at $U_{G3} = 91.5\,\text{mV}$ across the lines separating the states $|1,0,0\rangle$ and $|0,1,0\rangle$ as well as $|1,0,1\rangle$ and $|0,1,1\rangle$, respectively, is shown in Figure 5.32 for the different bias voltages. For the lines separating the states $|1,0,0\rangle$ and $|0,1,0\rangle$ (lower A-B resonance) an additional peak appears at smaller U_{G1} at the left side of the zero bias peak. For the lines separating the states $|1,0,1\rangle$ and $|0,1,1\rangle$ (upper A-B resonance) the additional peak appears at larger U_{G1} at the right side of the zero bias peak. The distance between the double lines is increasing with increasing bias voltage U_{S1}. The distance between the double lines in U_{G1}-direction is $\Delta U_{G1} = 2.0\,\text{mV}$ for $U_{S1} = -1.0\,\text{mV}$. For $U_{S1} = -1.5\,\text{mV}$ it is $\Delta U_{G1} = 2.4\,\text{mV}$. The same values of ΔU_{G1} are observed for the distance between the parallel lines separating

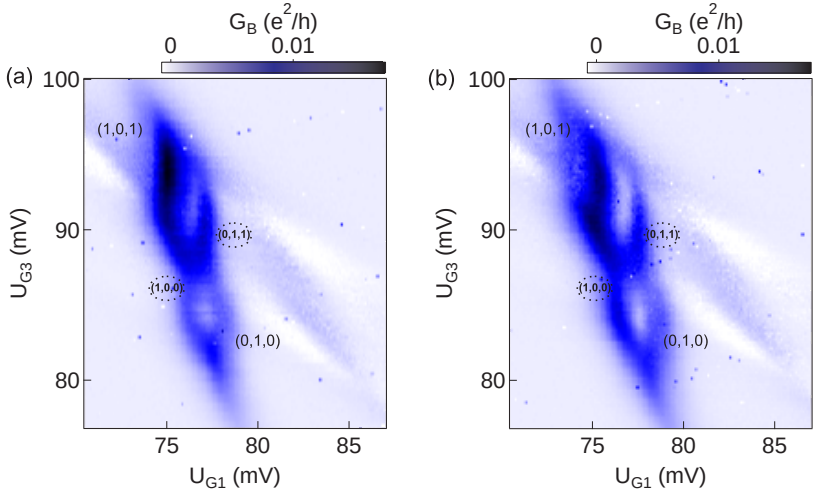

Figure 5.31: Differential conductance of path 1 as a function of gate voltages U_{G1} and U_{G3} for (a) $U_{S1} = -1\,\text{mV}$ and (b) $U_{S1} = -1.5\,\text{mV}$. The stability regions are denoted in the diagram. The data is shifted to compensate the potential shift due to the bias voltage.

the states $|1,0,0\rangle$ and $|0,1,0\rangle$ for the two bias voltages.

In order to find the origin of the double charge reconfiguration lines emerging with non-zero bias voltage, the transport through path 1 is simulated for different values of U_{S1} using the same tunneling rates and capacitances as in the simulations for the stability diagrams in section 5.2.2 (see table 5.3). Figure 5.33 shows the simulated differential conductance of path 1 for bias at path 1 of $\mu_{S1} = 0\,\text{meV}$ (a) $\mu_{S1} = -0.1\,\text{meV}$ (b) and for $\mu_{S1} = -0.2\,\text{meV}$ (c). For zero bias only one charge reconfiguration line is clearly visible. A second parallel line is very faintly visible for larger U_{G1} for the upper and for smaller U_{G1} for the lower A-B resonance. For increasing bias the second parallel line in the lower A-B resonance increases in intensity and becomes clearly visible in the lower A-B resonance. This behaviour of an appearing double charge reconfiguration line for $U_{S1} > 0$ and its location in the lower and upper A-B resonance corresponds to the observation in the experiment.

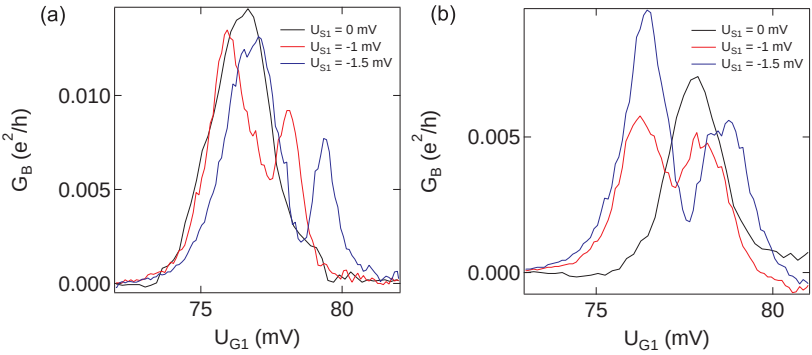

Figure 5.32: Cuts at $U_{G3} = 91.5\,\text{mV}$ (a) and at $U_{G3} = 84.3\,\text{mV}$ (b) through the transport measurements for $U_{S1} = 0\,\text{mV}$, $U_{S1} = -1\,\text{mV}$ and $U_{S1} = -1.5\,\text{mV}$.

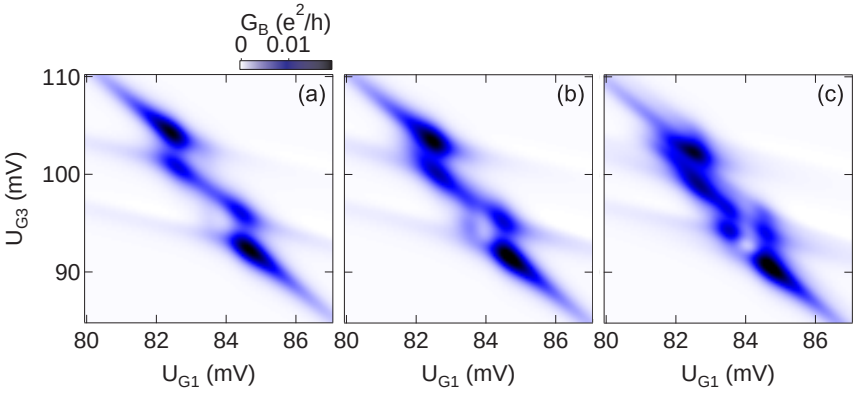

Figure 5.33: Simulated differential conductance of path 1 as a function of gate voltages U_{G1} and U_{G3} for (a) $\mu_{S1} = 0\,\text{meV}$, (b) $\mu_{S1} = -0.1\,\text{meV}$ and (c) $\mu_{S1} = -0.2\,\text{meV}$. The simulation is implemented by F. Gallego-Marcos.

Figure 5.34 shows the variation of the inter-dot tunnel coupling in path 2, τ_{AC}, from the original value of 0.020 meV down to 0.002 meV in the simulation of the differential conductance of path 1 for a cut at $U_{G3} = 95.0\,\text{mV}$ and for $U_{S1} = 0\,\text{mV}$. The cut crosses the double peak in the lower A-B resonance. For $\tau_{AC} = 0.020\,\text{meV}$ a distinct peak at $U_{G1} = 84.5\,\text{mV}$ is visible,

corresponding to the distinct charge reconfiguration line in the 2D stability diagram (Fig. 5.33 (a)). Additionally, a second peak with very low intensity is visible at around $U_{G1} = 83.4\,\text{mV}$. Due to its small peak height is it not appreciable in the 2D plot. For decreasing τ_{AC} the the second peak increases in height and the distance between the two peaks decreases, so that they nearly completely merge for $\tau_{AC} = 0.002\,\text{meV}$. An increase of the separation between the peaks with an increasing A-C inter-dot tunnel coupling suggests that the hybridization between dots A and C is the origin of the double peaks.

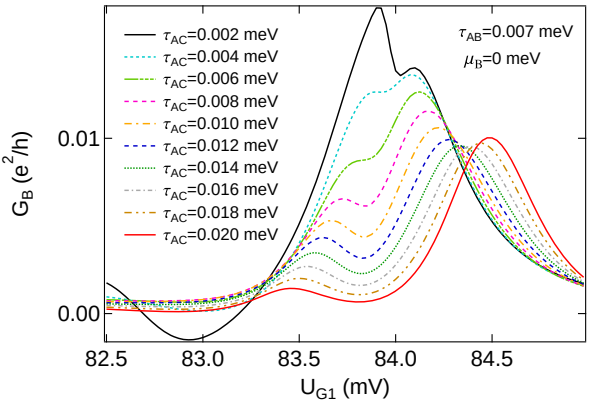

Figure 5.34: Simulated differential conductance of path 1 as a function of U_{G1} for $U_{G3} = 95.0\,\text{meV}$ and $\mu_{S1} = 0\,\text{meV}$ for different tunnel rates τ_{AC}. For increasing τ_{AC} the separation between the two resonance peaks increases and the peak height of the peak at around $U_{G1} = 83.4\,\text{mV}$ decreases rapidly. The simulation is implemented by F. Gallego-Marcos.

The separation between the lines is studied by considering a simplified Hamiltonian only taking into account the hybridization between the dots A and C (see Eq. 2.72):

$$\mathrm{H} = \begin{bmatrix} E_\mathrm{A} & \tau_\mathrm{AC} \\ \tau_\mathrm{AC} & E_\mathrm{C} \end{bmatrix} \Rightarrow E_\pm = \frac{1}{2}\left[(E_\mathrm{A} + E_\mathrm{C}) \pm \sqrt{\Delta_\mathrm{AC}^2 + 4\tau_\mathrm{AC}^2}\right] \tag{5.26}$$

with $\Delta = \sqrt{\Delta_{\mathrm{AC}}^2 + 4\tau_{\mathrm{AC}}^2}$ (see Eq. (2.106)) describing the separation between the hybridized states. $\Delta_{\mathrm{AC}} = E_{\mathrm{A}} - E_{\mathrm{C}}$ describes the energy difference of the localized states of dot A and C. A comparison between the numerical result of the distance between the double lines and the result from equation Eq. (2.106) for different couplings τ_{AC} shows, that Δ perfectly describes the value of the separation between the lines. Consequently, we deduce that the origin of the double charge reconfiguration lines at the resonances between the dots A and B appearing in the numerical transport simulation is a hybridization between dot A and C. An electron which tunnels from dot B to dot A interacts with the two hybrid states of the molecule formed of dot A and C instead of the localized states of dot A. The hybrid states of the A-C molecule consist of the bonding state which is the lower energy state and the anti-bonding state which is the higher energy state. The peak around $U_{\mathrm{G1}} = 84.5\,\mathrm{mV}$ corresponds to the resonance between a single dot energy level of dot B and the anti-symmetric superposition state of the molecule A-C, while the second peak with smaller peak height around $U_{\mathrm{G1}} = 83.4\,\mathrm{mV}$ corresponds to the resonance between a single dot energy level of dot B and the symmetric superposition state of the molecule A-C. The anti-symmetric state is the ground state (bonding state), the symmetric state is the excited state (anti-bonding state) of the molecule. Consequently, the smaller resonance peak corresponds to transport over the excited state. The larger τ_{AC}, the bigger the energy difference of the two hybridized states of dot A and C. The ratio between the inter-dot tunnel couplings in the two transport paths, $\tau_{\mathrm{AC}}/\tau_{\mathrm{AB}}$, has to be large to resolve the hybrid states.

Figure 5.35 shows the variation of the inter-dot tunnel coupling in path 1 from $\tau_{\mathrm{AB}} = 0.020\,\mathrm{meV}$ down to $\tau_{\mathrm{AB}} = 0.002\,\mathrm{meV}$ in the simulation of the differential conductance of path 1 for a cut at $U_{\mathrm{G3}} = 95.0\,\mathrm{mV}$ where the double peak arises. The A-B inter-dot coupling expected for the system and used in the 2D stability diagram (Fig. 5.33) is $\tau_{\mathrm{AB}} = 0.012\,\mathrm{meV}$. For decreasing τ_{AB} the peak width of the two peaks decreases and the peaks become more defined. Additionally, the second peak at around $U_{\mathrm{G1}} = 83.4\,\mathrm{mV}$ which is clearly seen for $\tau_{\mathrm{AB}} = 0.002\,\mathrm{meV}$ is almost vanishing for large τ_{AB}. By reducing the A-B inter-dot coupling the energy levels of dot B more and more resemble single dot states. These localized states probe the hybridized states of the molecule A-C which leads to their visibility in transport. The more localized the state of dot B, the more distinct the resonance peaks with the hybridized states of A-C.

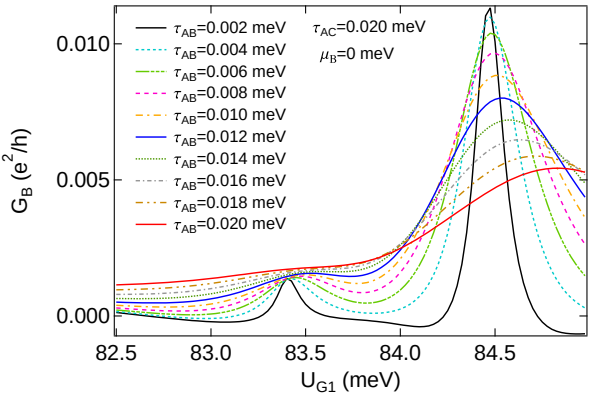

Figure 5.35: Simulated differential conductance of path 1 as a function of U_{G1} for $U_{G3} = 95.0\,\text{meV}$ and $\mu_{S1} = 0\,\text{meV}$ for different tunnel rates τ_{AB}. For increasing τ_{AB} the peak at around $U_{G1} = 83.4\,\text{mV}$ decreases strongly and vanishes for large τ_{AB}. (implemented by F. Gallego-Marcos)

The situation in the experiment for $U_{S1} = 0\,\text{mV}$ corresponds to the transport curve for $\tau_{AB} = 0.012\,\text{meV}$ and $\tau_{AC} = 0.020\,\text{meV}$ in Fig. 5.35. The main resonance peaks at around $U_{G1} = 77.0\,\text{mV}$ (Fig. 5.32 (a)) for N+1 electrons on dot C and at around $U_{G1} = 78.5\,\text{mV}$ (Fig. 5.32 (b)) for N electrons on dot C consequently correspond to the resonance between a localized energy level of dot B and the anti-symmetric hybridized state of the molecule A-C. At the lower A-B resonance for N electrons on dot C the state $|010\rangle$ is in resonance with the anti-symmetric state of the hybridization $|001\rangle \pm |100\rangle$ (Fig. 5.30). At the upper A-B resonance for N+1 electrons on dot C the state $|101\rangle$ is in resonance with the anti-symmetric state of the hybridization $|011\rangle \pm |110\rangle$ (Fig. 5.30). The second line arising for $U_{S1} > 0\,\text{mV}$ (Fig. 5.32 and Fig. 5.31) is the resonance between a localized energy level of dot B and the symmetric hybridized state of the molecule A-C. At the lower A-B resonance for N electrons on dot C it is the resonance of state $|010\rangle$ with the symmetric state of the hybridization $|001\rangle \pm |100\rangle$. It is located at smaller U_{G1} than the resonance with the anti-symmetric hybridized state as the state $|010\rangle$ decreases faster in energy for increasing U_{G1} than the hybridized states $|001\rangle \pm |100\rangle$. This originates from the location of G_1 nearest to dot B.

At the upper A-B resonance for $N+1$ electrons on dot C the state $|101\rangle$ is in resonance with the symmetric state of the hybridization $|011\rangle \pm |110\rangle$. It is located at larger U_{G1} than the resonance with the anti-symmetric hybridized state as the state $|011\rangle$ decreases slower in energy for increasing U_{G1} than the hybridized states $|011\rangle \pm |110\rangle$. These locations of the resonance lines relative to each other are observed in simulation and experimental result.

As shown in Fig. 5.34 and Fig. 5.35 an increase in τ_{AC} and a decrease in τ_{AB} leads to an increasing resolution of the double charge reconfiguration line and thus enhanced visibility of the second resonance peak. In the experiment a strong influence of an applied bias voltage of $U_{\mathrm{S1}} = -1\,\mathrm{mV}$ on the inter-dot tunnel couplings τ_{AB} and τ_{AC} is not expected and also not observable in the transport measurements of path 1 and path 2. As can be deduced from Eq. (2.106), a large ratio between the dot detunings in the paths, $\Delta_{\mathrm{AC}}/\Delta_{\mathrm{AB}}$ leads to a large distance between the hybrid states as well and can thus lead to their resolution in transport. An applied potential at S_1 affects the detuning between the dots A and B. A negative potential at S_1 detunes the dots A and B from their resonance along the charge reconfiguration line, so that a potential difference at U_{G3} is needed to compensate this influence. This effect is observed in a shift of the conductance features in U_{G3} in dependence of S_1, well seen when comparing the Fig. 5.30 and Fig. 5.31). The increased positive potential at U_{G3} for non-zero U_{S1} mostly influences dots A and C as the gate is situated between them. It is expected to change the detuning of their energy levels as well as slightly increase their inter-dot tunnel coupling τ_{AC}. Consequently, this effect can lead to an increase of the resolution of the molecular states of A-C with the bias voltage U_{S1}. However, in the simulation of transport the included influence of the potential change at S_1 on the dot system mediated by the capacitive coupling between S_1 and dots A and B is basically only shifting the measurement outcome in gate-gate space. Excluding this capacitive coupling from the simulation does not change the observed behaviour to the observed extend. The effect of level detuning with the bias voltage is too small to explain the bias dependence of the splitting in experiment alone. The coherent states of the triple dot determine the transport, which remain mostly unaffected. The slight increase in distance between the resonance lines between $U_{\mathrm{S1}} = -1.0\,\mathrm{mV}$ and $U_{\mathrm{S1}} = -1.5\,\mathrm{mV}$ (Fig. 5.32) can result from the described capacitive influence of U_{S1} on the energy levels of the dots affecting Δ_{AC} and τ_{AC}.

The same analysis of transport in dependence of the inter-dot tunnel couplings τ_{AC} (Fig. 5.36) and τ_{AB} (Fig. 5.37) is conducted for non-zero bias at path 1, $\mu_B = -0.1\,\text{meV}$. It is clearly visible in both diagrams that the second peak at around $U_{G1} = 83.4\,\text{mV}$ is larger in height than for zero bias voltage. For increasing τ_{AC} the peak height of the second peak is not decreasing as rapidly as in case of zero bias. The peak height is obviously more robust against changes of the inter-dot couplings. This is most clearly observable for large τ_{AC}, where the second peak is still clearly observable for non-zero bias voltage at S_1. For small τ_{AB} the peak height of the second peak is clearly larger for non-zero bias (Fig. 5.37) than for zero bias voltage.

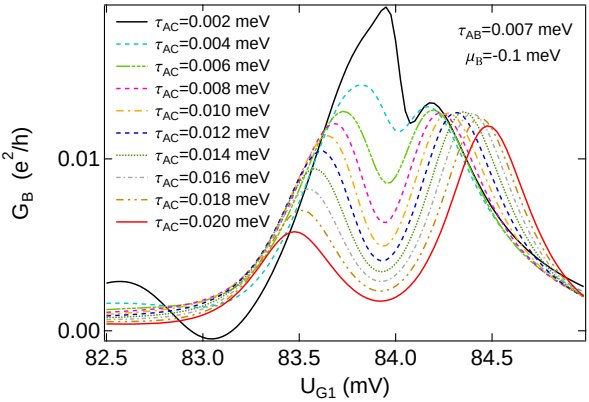

Figure 5.36: Simulated differential conductance of path 1 as a function of U_{G1} for $U_{G3} = 95.0\,\text{meV}$ and $\mu_{S1} = -0.1\,\text{meV}$ for different tunnel rates τ_{AC}. The peak at around $U_{G1} = 83.4\,\text{mV}$ is more appreciable than for zero bias voltage (Fig. 5.34). (implemented by F. Gallego-Marcos)

A comparison between the transport curves for $\mu_B = 0\,\text{meV}$ and $\mu_B = -0.1\,\text{meV}$ for the system parameters $\tau_{AB} = 0.012\,\text{meV}$ and $\tau_{AC} = 0.020\,\text{meV}$ (Fig. 5.35) reflecting the situation in the experiment shows that while for $\mu_B = 0\,\text{meV}$ only one resonance peak (resonance with anti-symmetric molecular state) is clearly visible, for $\mu_B = -0.1\,\text{meV}$ also a second distinct resonance peak (resonance with symmetric molecular state) is observed. The simulation reproduces the experimental result concerning the visibility of only one charge reconfiguration line at $U_{S1} = 0\,\text{mV}$ and the appearance of the second parallel line for $U_{S1} > 0\,\text{mV}$. It can also be appreciated in

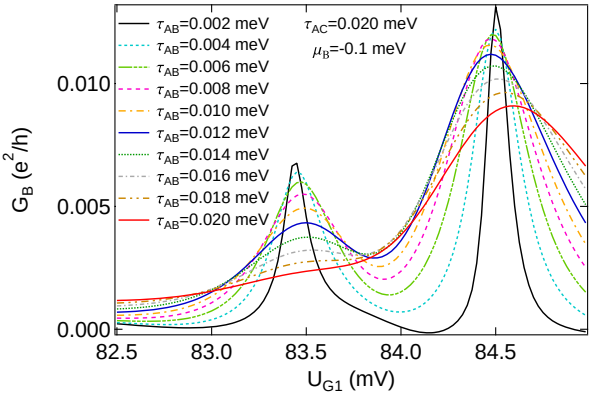

Figure 5.37: Simulated differential conductance of path 1 as a function of U_{G1} for $U_{G3} = 95.0\,\text{meV}$ and $\mu_{S1} = -0.1\,\text{meV}$ for different tunnel rates τ_{AB}. The peak at around $U_{G1} = 83.4\,\text{mV}$ is more appreciable than for zero bias voltage (Fig. 5.35). (implemented by F. Gallego-Marcos)

Fig. 5.33 where the corresponding 2D stability diagrams are shown. While for zero bias voltage only one coherent state of the system contributes to transport around $U_{G1} = 83.5\,\text{mV}$ in the simulation, for non-zero bias voltage a second coherent state enters the transport window and contributes to the transport. The contribution of this additional coherent state to transport leads to the distinct second peak appearing for $U_{S1} = -1.0\,\text{mV}$ in the experiment. A non-zero bias voltage allows for transport via the symmetric (excited) state of the molecule A-C. The resonance of an energy level of dot B with the symmetric state of the A-C molecule results in the second parallel charge reconfiguration line in transport.

The hybridization is also observed in the differential conductance of path 1 measured in dependence of the bias voltage U_{S1} (Fig. 5.38). U_{G1} and U_{G3} are varied to perform a cut through the stability diagram across the charge reconfiguration line between the states $|1,0,1\rangle$ and $|0,1,1\rangle$. U_{G3} is varied from 85 mV to 91 mV and U_{G1} from 73.5 mV to 82.6 mV.

A single peak for zero bias voltage is seen, which splits into two peaks with increasing separation while the negative bias voltage is increased. For

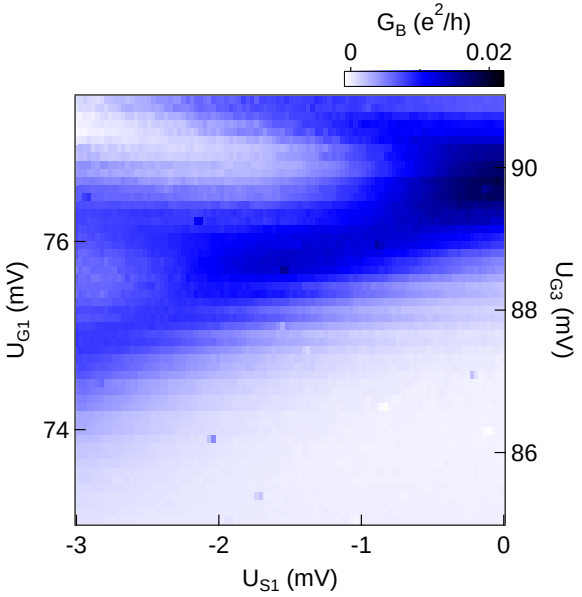

Figure 5.38: Differential conductance of path 1 as a function of the bias voltage U_{S1} and gate voltages U_{G1} and U_{G3}.

$U_{\mathrm{S1}} \gtrsim 1.8\,\mathrm{mV}$ a line parallel to the one with negative slope inside the spanned triangle appears. The line with positive slope corresponds to the resonance of an energy level of dot B with the source lead S_1, the two parallel lines with negative slope correspond to the resonances of the two hybrid states of the A-C molecule with the drain lead. The resonance lines with the drain lead show a non-zero slope due to the influence of the bias voltage U_{S1} on the dot potentials via $C_{\mathrm{S1},i}$, $i \in \{\mathrm{A,B,C}\}$. The capacitive influence of U_{S1} leads to a shift of the cut with respect to the stability diagram of the TQD. A shift in U_{G3}-direction contributes to the visibility of a single peak at zero bias voltage only and the emergence of the double line for $U_{\mathrm{S1}} > 0\,\mathrm{mV}$.

To sum up, the hybridization of electronic states in path 2 is observed in transport through path 1. In the chosen parameter regime dots A and C are strongly tunnel coupled while dot B in the other path is less coupled to them ($\tau_{\mathrm{AC}} > \tau_{\mathrm{AB}}$). The anti-symmetric and symmetric hybrid states

of the A-C molecule are then probed by the localized dot states of dot B. In transport of path 1 instead of one charge reconfiguration line at the A-B resonance, two resonance lines are seen when an energy level of dot B comes into resonance with the A-C hybrid states. The resolution of the molecular states in one path by transport measurements through the other is dependent on the ratio between the inter-dot tunnel couplings in the paths. The impact of this ratio on the resolution of the corresponding resonance peaks is investigated with the help of the numerical simulation of transport through the paths where the resolution is modulated. At zero bias voltage, $U_{S1} = 0\,\mathrm{mV}$, the resonance with the anti-symmetric hybrid state, the lower energy state (bonding state) of the A-C molecule, is visible only. For $U_{S1} > 0\,\mathrm{mV}$ the resonance with the symmetric hybrid state, the excited state (anti-bonding state), becomes visble. The distance between the resonance lines grows for increasing bias voltage. A reason can be the capacitive influence of U_{S1} on the dot energy levels slightly increasing the separation of the hybrid states and their resolution in transport. The main contribution to the visibility of the peak of the anti-bonding state resonance is provided by the opening of the transport window, allowing transport via the anti-bonding state, the excited state of the A-C molecule. The experimental result demonstrates the formation of molecular states in this dot setup and shows their detection by probing them with more localized states within the same device. Making use of the triangular dot setup transport through path 1 thereby serves as a detector for the hybridization in path 2.

6 Summary

This thesis covers an experimental and supportive theoretical approach to electron transport through a triangular-shaped lateral triple quantum dot with two transport paths. The transport through the system was analyzed in detail in a path-resolved manner and it was shown that electronic inter-channel interaction strongly determines the transport properties of such complex multi-dot systems. The results provide a better understanding of the transport properties and coherences and their control in complex dot networks.

The transport properties of a triangular dot distribution were analyzed in a novel configuration using two source contacts and one drain. By applying two different AC voltages to the two sources of the double dot transport paths path-resolved transport measurements are possible and interactions between the paths become observable and can be thoroughly studied in transport.

The TQD sample was characterized by charge measurements using a quantum point contact as a charge detector and by linear and non-linear transport measurements of both paths separately (**Chapter 4**). Electrostatic properties were extracted and the tunability into double and triple dot resonances were shown. With this TQD setup transitions from double to triple dot resonances are observable even in transport measurements. In a regime where the system is in a drain-decoupled condition a serial dot system is formed and two different charging mechanisms of the central dot arise which are clearly observable in a wide gate voltage regime in the charge measurements. This charging behaviour is hysteretic and of particular interest for utilization in a one-bit memory device. In addition, signatures indicating an indirect phononic back-action mechanism between QPC and the dot system have been observed in the detector signal.

The characterization of the sample was complemented and extended by results obtained by a numerical simulation which was implemented by F.

Gallego-Marcos (working group Theoretical Group on Quantum Transport on the Nanoscale, Instituto de Ciencias de Materiales de Madrid, CSIC, Spain). Calculations of the charge stability regions of the system and the path-resolved transport were performed, based on a quantum mechanical model of the system (**Chapter 5**). It was shown that a model which treats the on-site states of the dots coherently coupled is able to reproduce the transport properties of this device in detail. Besides the possibility of investigating the transport through the system in a path-resolved manner, the setup provides the possibility of measuring the total transport through the TQD without distinguishing the paths. In this way signatures of interference occur at the common drain lead of the paths which vanish when distinguishing the electrons by their path. The presence of interference effects in transport verifies coherent transport throughout the dot system. A modulation of the coherent contribution to the tunneling current by tuning the system in and off resonances is reflected in a modulation of the strength of the interference features. Possible other contributions to these features in terms of interference effects were discussed.

Interactions between both paths were further investigated performing path-resolved transport measurements by applying two different AC voltages to the paths. It was found that the transport is substantially influenced by Coulomb correlations in the shared dot. Coulombic interaction between the electrons coming from different paths leads to a blockade of current flow through one path when the current through the other path is strong. Via this inter-channel interaction the transport behaviour of one path can serve as a current detector for the other path within the same dot system. As the channel blockade occurs when the electrons coming from different paths compete for occupation of the shared dot the effect is dependent on the transport direction. This leads to non-linear transport characteristics of the device even around zero bias voltage. The observed properties are inherent and characteristic for triangular dot distributions with two transport paths with a shared dot and drain lead. The experimental findings and interpretations were supported by the simulation of path-resolved transport reproducing the experimental outcome very nicely. The strength of the channel blockade was shown to be dependent on the ratio of the tunneling probabilities of the transport paths and thus is modulated by the resonance condition within the dot system. In addition, combinations of this inter-channel blockade with intra-channel higher-order tunneling effects are found. Elastic and inelastic cotunneling effects are modifying the transport properties of the

device as transport characteristics of the separate double dot paths.

In the last section the detection of hybridized states in one transport path by transport measurements through the other path is discussed. The triple dot system was tuned such that the molecular states of a strongly coupled double dot molecule formed in one path can be probed by a more localized single dot level of the dot in the other path. The experimental results are analyzed with the help of the simulation which reproduces the experimental outcome and shows the dependence of the resolution of the molecular states on the ratio between the inter-dot tunnel couplings. The results give insight into the formation of molecular states in a multi-dot system and show the variability of the device. The triangular setup allows the spectroscopy of coherent states by a more localized states of a quantum dot within the same device.

Further analysis of this triangular TQD system could aim towards the investigation of theoretically proposed quantum interference effects, like the formation of dark states, and different current rectification effects. A requirement for the realization of these ideas is the tunability of the tunneling barriers of the device into the desired configuration. Thus, the realization of these ideas should be supported by an optimization of sample design and tunability of the tunneling barriers and electron numbers on the dots. Additionally, a slightly modified sample setup with a tunnel coupling between all of the dots resulting in a ring geometry with an embedded triple quantum dot molecule would be of high interest for the investigation of coherence and quantum interference effects. This investigation is aiming towards a deeper understanding of significant properties of quantum circuits for an implementation of quantum devices.

Bibliography

[1] G. E. Moore, Electronics **38** (1965), 8.

[2] P. Benioff, Journal of Statistical Physics **22**, 5 (1980), pp. 563-591.

[3] R. Feynman, International Journal of Theoretical Physics **21**, 6 (1982), pp. 467-488.

[4] D. Deutsch, Proceedings of the Royal Society of London A **400**, 1818 (1985), pp. 97-117.

[5] A. Barenco, D. Deutsch, and A. Ekert, Phys. Rev. Lett. **74**, 4083 (1995).

[6] D. Loss and D. P. DiVincenzo, Phys. Rev. A **57**, 120 (1998).

[7] J. A. Brum and P. Hawrylak, Superlattices and Microstructures **22**, 3 (1997), pp. 431-436.

[8] A. I. Ekimov, A. L. Efros, and A. A. Onushchenko, Solid State Communications **56**, 11 (1985), pp. 921-924.

[9] M. A. Reed, J. N. Randall, R. J. Aggarwal, R. J. Matyi, T. M. Moore, and A. E. Wetsel, Phys. Rev. Lett. **60**, 535 (1988).

[10] R. C. Ashoori, Nature **379**, pp. 413 (1996).

[11] K. D. Petersson, J. R. Petta, H. Lu, and A. C. Gossard, Phys. Rev. Lett. **105**, 246804 (2010).

[12] L. Gaudreau, G. Granger, A. Kam, G. C. Aers, S. A. Studenikin, P. Zawadzki, M. Pioro-Ladrière, W. Z. R., and A. S. Sachrajda, Nature Physics **8**, 54 (2012).

[13] D. DiVincenzo, D. Bacon, J. Kempe, G. Burkard, and K. Whaley, Nature **408**, pp. 339 (2000).

[14] E. A. Laird, J. M. Taylor, D. P. DiVincenzo, C. M. Marcus, M. P. Hanson, and A. C. Goosard, Phys. Rev. B **82**, 075403 (2010).

[15] A. Vidan, R. Westervelt, M. Stopa, M. Hanson, and A. Gossard, Appl. Phys. Lett. **85**, 3602 (2004).

[16] M. Stopa, Phys. Rev. Lett. **88**, 146802 (2002).

[17] M. Busl and G. Platero, J. Phys.: Condens. Matter **24**, 154001 (2012).

[18] C. Lent, P. Tougaw, W. Porod, and G. Bernstein, Nanotechnology **4**, 49 (1993).

[19] M. C. Rogge and R. J. Haug, New Journal of Physics **11**, 113037 (2009).

[20] H. Sasakura, S. Adachi, S. Muto, T. Usuki, and M. Takatsu, Sci. Technol. **19**, S409 (2004).

[21] T. Fujisawa, T. Hayashi, R. Tomita, and Y. Hirayama, Science **312**, 5780 (2006).

[22] L. Gaudreau, S. A. Studenikin, A. S. Sachrajda, P. Zawadzki, and A. Kam, Phys. Rev. Lett. **97**, 036807 (2006).

[23] D. Schröer, A. D. Greentree, L. Gaudreau, K. Eberl, L. C. L. Hollenberg, J. P. Kotthaus, and S. Ludwig, Phys. Rev. B **76**, 075306 (2007).

[24] M. C. Rogge and R. J. Haug, Phys. Rev. B **77**, 193306 (2008).

[25] C. Y. Hsieh, Y. P. Shim, M. Korkusinski, and P. Hawrylak, Rep. Prog. Phys. **75**, 114501 (2012).

[26] B. Michaelis, C. Emary, and C. Beenakker, Europhys. Lett. **73**, 677 (2006).

[27] C. Pöltl, C. Emary, and T. Brandes, Phys. Rev. B **80**, 115313 (2009).

[28] M. Busl, R. Sánchez, and G. Platero, Phys. Rev. B **81**, 121306(R) (2010).

[29] C. Emary, Phys. Rev. B **76**, 245319 (2007).

[30] R. Sánchez, F. Gallego-Marcos, and G. Platero, Phys. Rev. B **89**, 161402(R) (2014).

[31] F. Gallego-Marcos, R. Sánchez, and G. Platero, J. Appl. Phys. **117**, 112808 (2015).

[32] M. Busl, G. Granger, L. Gaudreau, R. Sanchez, A. Kam, M. Pioro-Ladrière, S. A. Studenikin, P. Zawadzki, W. Z. R., A. S. Sachrajda, et al., Nature Nanotechnology **8**, 261 (2013).

[33] F. R. Braakman, P. Barthelemy, C. Reichl, W. Wegscheider, and L. M. K. Vandersypen, Nature Nanotechnology **8**, 432 (2013).

[34] R. Sánchez, G. Granger, L. Gaudreau, A. Kam, M. Pioro-Ladrière, S. A. Studenikin, P. Zawadzki, A. S. Sachrajda, and G. Platero, Phys. Rev. Lett. **112**, 176803 (2014).

[35] A. D. Greentree, J. H. Cole, A. R. Hamilton, and L. C. L. Hollenberg, Phys. Rev. B **70**, 235317 (2004).

[36] T. Ihn, M. Sigrist, K. Ensslin, W. Wegscheider, and M. Reinwald, New Journal of Physics **9**, 111 (2007).

[37] C. Y. Hsieh and P. Hawrylak, Phys. Rev. B **82**, 205311 (2010).

[38] M. C. Rogge and R. J. Haug, Phys. Rev. B **78**, 153310 (2008).

[39] M. C. Rogge and R. J. Haug, Physica E **40**, 5 (2008), pp. 1656-1658.

[40] M. C. Rogge, Einzel-, Doppel- und Dreifachquantenpunkte im Transport, Dissertation (2008).

[41] M. C. Rogge and R. J. Haug, Physica E **42**, 4 (2010), pp. 902-905.

[42] A. Kumar, S. E. Laux, and F. Stern, Phys. Rev. B **42**, 5166 (1990).

[43] T. Heinzel, *Mesoscopic Electronics in Solid State Nanostructures* (Wiley-VCH, 3. edition, 2010).

[44] W. G. van der Wiel, S. De Franceschi, J. M. Elzerman, T. Fujisawa, S. Tarucha, and L. P. Kouwenhoven, Rev. Mod. Phys. **75**, 1 (2002).

[45] communication with Dr. K. Roszak, Department of Theoretical Physics, Wroclaw University of Science and Technology (Poland).

[46] L. P. Kouwenhoven, C. M. Marcus, P. L. McEuen, S. Tarucha, R. M. Westervelt, and N. S. Wingreen, Mesoscopic electron transport, NATO ASI Conference Proceedings **Series E 345** (1997).

[47] L. P. Kouwenhoven, G. Schön, and L. L. Sohn, *Introduction to mesoscopic electron transport, in: Mesoscopic electron transport*, vol. Series E: Applied Sciences - Vol. 345 (Springer-Science+Business Media, B.V.; editors: Sohn, L. L. and Kouwenhoven, L. P. and Schön, G., 1997).

[48] D. V. Averin and K. K. Likharev, *Single electronics: A correlated transfer of single electrons and Cooper pairs in systems of small tunnel junctions.* (North-Holland, Elsevier Science Publishers B. V., Amsterdam, Oxford, New York, Tokyo; editors: Altshuler, B.L. and Lee, P. A. and Webb, R. A, 1991), chapter 6, pages 173-271.

[49] P. A. M. Dirac, Proceedings of the Royal Society A **114**, 767 (1927), pp. 243-265.

[50] A. Douglas Stone and P. A. Lee, Phys. Rev. Lett. **54**, 1196 (1985).

[51] M. Büttiker, IBM Journal of Research and Revelopment **32**, 1 (1988), pp. 63-75.

[52] L. L. Chang, L. Esaki, and R. Tsu, Appl. Phys. Lett. **24**, 12 (1974).

[53] S. Datta, *Electronic Transport in Mesoscopic Systems* (Cambridge University Press, 1995), p. 48-51.

[54] J. P. Bird, *Electron Transport in Quantum Dots* (Springer Science+Business Media, LLC, 2003), p. 322-324.

[55] D. V. Averin and Y. V. Nazarov, in Single Charge Tunneling: Coulomb Blockade Phenomena in Nanostructures, eds. H. Grabert and Michel H. Devoret, NATO ASI Series B 294 (New York, Plenum Press) (1992).

[56] D. V. Averin and Y. V. Nazarov, Phys. Rev. Lett. **65**, 19 (1990).

[57] D. K. Ferry, S. M. Goodnick, and J. Bird, *Transport in Nanostructures* (Cambridge University Press, 2. edition, 2009), p. 376.

[58] D. V. Averin and A. A. Odintsov, Phys. Rev. Lett. A **140**, 251 (1989).

[59] B. Küng, C. Rössler, M. Beck, J. Faist, T. Ihn, and K. Ensslin, New Journal of Physics **14**, 083003 (2012).

[60] H. P. Breuer and F. Petruccione, *The Theory of Open Quantum Systems* (Oxford University Press, 2002).

[61] F. Schwabl, *Quantenmechanik (QM 1)* (Springer-Verlag Berlin-Heidelberg, 7. edition, 2007).

[62] M. B. Busl, Nanoscopic Systems Driven by Magnetic and Electric AC Fields, Dissertation (2012).

[63] R. Sánchez Rodrigo, Spin and Charge Transport through Driven Quantum Dot Systems and their Fluctuations, Dissertation (2007).

[64] S. M. Sze, *Semiconductor Devices - Physics and Technology* (John Wiley & Sons, 1985).

[65] S. Adachi, J. Appl. Phys. **58**, R1 (1985).

[66] J. A. Dagata, Science **270**, 1625 (1990).

[67] H. W. Schumacher, U. F. Keyser, U. Zeitler, R. J. Haug, and K. Eberl, Appl. Phys. Lett. **75**, 1107 (1999).

[68] J. Regul, U. F. Keyser, M. Paesler, F. Hohls, U. Zeitler, R. J. Haug, A. Malavé, E. Oesterschulze, D. Reuter, and A. D. Wieck, Appl. Phys. Lett. **81**, 2023 (2002).

[69] A. Fuhrer, A. Dorn, S. Lüscher, T. Heinzel, K. Ensslin, W. Wegscheider, and M. Bichler, Superlattices and Microstructures **31**, 19 (2002).

[70] R. Held, T. Heinzel, P. Studerus, K. Ensslin, and M. Holland, Appl. Phys. Lett. **71**, 2689 (1997).

[71] R. Held, T. Vancura, T. Heinzel, K. Ensslin, M. Holland, and W. Wegscheider, Appl. Phys. Lett. **73**, 262 (1998).

[72] U. F. Keyser, H. W. Schumacher, U. Zeitler, R. J. Haug, and K. Eberl, Appl. Phys. Lett. **76**, 457 (2000).

[73] K. Matsumoto, S. Takahashi, M. Ishii, M. Hoshi, A. Kurokawa, S. Ichimura, and A. Ando, Japanese Journal of Applied Physics **34**, 1387 (1995).

[74] M. Ishii and K. Matsumoto, Japanese Journal of Applied Physics **34**, 1329 (1995).

[75] G. Binning, C. F. Quate, and C. Gerber, Phys. Rev. Lett. **56**, 930 (1986).

[76] S. K. Ghandi, *VLSI Fabrication Principles* (John Wiley & Sons, 1994), 2nd ed.

[77] U. F. Keyser, Nanolithography with an Atomic Force Microscope: Quantum Point Contacts, Quantum Dots, and Quantum Rings, Dissertation (2002).

[78] M. C. Rogge, C. Fühner, U. F. Keyser, R. J. Haug, M. Bichler, G. Abstreiter, and W. Wegschneider, Appl. Phys. Lett. **83**, 1163 (2003).

[79] C. Barthel, M. Kjærgaard, J. Medford, M. Stopa, C. M. Marcus, M. P. Hanson, and A. C. Gossard, Phys. Rev. B **81**, 16 (2010), p. 161308.

[80] M. R. Delbecq, T. Nakajima, T. Otsuka, S. Amaha, J. D. Watson, M. J. Manfra, and S. Tarucha, Appl. Phys. Lett. **104**, 18 (2014), p. 183111.

[81] M. Field, C. G. Smith, M. Pepper, D. A. Ritchie, J. E. F. Frost, G. A. C. Jones, and D. G. Hasko, Phys. Rev. Lett. **70**, 9 (1993), p. 1311.

[82] J. M. Elzerman, R. Hanson, J. S. Greidanus, L. H. W. van Beveren, S. Franceschi, L. M. K. Vandersypen, S. Tarucha, and L. P. Kouwenhoven, Phys. Rev. B **67**, 16 (2003), p. 161308.

[83] H. van Houten, C. W. J. Beenakker, and B. J. van Wees, *Quantum Point Contacts, in: Semiconductor and Semimetals*, vol. 35 (edited by Reed, M.A. (Academic Press, New York), 1992), 9-112.

[84] H. van Houten and C. W. J. Beenakker, Physics Today **49**, 7 (1996), pp. 22-27.

[85] L. P. Kouwenhoven, N. C. van der Vaart, A. T. Johnson, W. Kool, C. J. P. M. Harmans, J. G. Wiliamson, A. A. M. Staring, and C. T. Foxon, Z. Phys. B - Condensed Matter **85**, pp. 367 (1991).

[86] C. Fricke, M. C. Rogge, B. Harke, M. Reinwald, W. Wegscheider, F. Hohls, and R. J. Haug, Phys. Rev. B **72**, 193302 (2005).

[87] M. Sigrist, S. Gustavsson, T. Ihn, K. Ensslin, D. Driscoll, A. Gossard, M. Reinwald, and W. Wegscheider, Physica E **32**, 5 (2006).

[88] B. J. van Wees, H. van Houten, C. W. J. Beenakker, J. G. Williamson, L. P. Kouwenhoven, D. van der Marel, and C. T. Foxon, Phys. Rev. Lett. **60**, 848 (1988).

[89] D. A. Wharam, T. T. J., R. Newbury, M. Pepper, H. Ahmed, J. E. F. Frost, D. G. Hasko, D. C. Peacock, D. A. Ritchie, and G. A. C. Jones, J. Phys. C **21**, L209 (1988).

[90] C. Enss and S. Hunklinger, *Tieftemperaturphysik* (Springer Berlin Heidelberg, 2000).

[91] M. Kotzian, F. Gallego-Marcos, G. Platero, and R. J. Haug, published on arXiv:1507.03595 (2015).

[92] D. Harbusch, D. Taubert, H. P. Tranitz, W. Wegschneider, and S. Ludwig, Phys. Rev. Lett. **104**, 196801 (2010).

[93] G. Granger, D. Taubert, C. E. Young, L. Gaudreau, A. Kam, S. A. Studenikin, P. Zawadzki, D. Harbusch, D. Schuh, Z. R. Wegschneider, W. Wasilewski, et al., Nature Physics **8**, 522 (2012).

[94] D. Taubert, M. Pioro-Ladrière, D. Schröer, D. Harbusch, A. S. Sachrajda, and S. Ludwig, Phys. Rev. Lett. **100**, 176805 (2008).

[95] J. Weis, R. J. Haug, K. von Klitzing, and K. Ploog, Semicond. Sci. Technol. **10**, 6 (1995), pp. 877-880.

[96] R. H. Blick, R. J. Haug, D. W. van der Weide, K. von Klitzing, and K. Eberl, Appl. Phys. Lett. **67**, 3924 (1995).

[97] J. Zhang, S. Vitkalov, K. Z. D., J. C. Portal, and A. Wieck, Phys. Rev. Lett. **97**, 226807 (2006).

[98] C. H. Yang, A. Rossi, N. S. Lai, R. Leon, W. H. Lim, and A. S. Dzurak, Appl. Phys. Lett. **105**, 183505 (2014).

[99] N. J. Stone and H. Ahmed, Appl. Phys. Lett. **73**, 2134 (1998).

[100] G. J. Schinner, H. P. Tranitz, W. Wegscheider, J. P. Kotthaus, and S. Ludwig, Phys. Rev. Lett. **102**, 186801 (2009).

[101] V. S. Khrapai, S. Ludwig, J. P. Kotthaus, H. P. Transitz, and W. Wegscheider, Phys. Rev. Lett. **97**, 176803 (2006).

[102] U. Gasser, S. Gustavsson, B. Küng, K. Ensslin, T. Ihn, D. C. Driscoll., and A. C. Gossard, Phys. Rev. B **79**, 035303 (2009).

[103] B. K. Ridley, Rep. Prog. Phys. **54**, 169 (1991).

[104] J. S. Blakemore, Appl. Phys. Lett. **53**, R123 (1982).

[105] H. Li, M. Xiao, G. Cao, C. Zhou, R. Shang, T. Tu, G. Guo, H. Jiang, and G. Guo, Appl. Phys. Lett. **100**, 092112 (2012).

[106] R. P. Feynman, R. B. Leighton, and M. Sands, *The Feynman Lectures on Physics: Quantum Mechanics*, vol. Vol. 3 (Addison-Wesley, 1965), chapter 1.

[107] A. Tonomura, J. Endo, T. Matsuda, T. Kawasaki, and H. Ezawa, Am. J. Phys. **57**, 117 (1989).

[108] R. Bach, D. Pope, S. H. Liou, and H. Batelaan, New Journal of Physics **15**, 033018 (2013).

[109] A. Mühle, Elektronischer Transport in Quanteninterferometern und komplexen Ringstrukturen, Dissertation (2008).

[110] L. Gaudreau, A. S. Sachrajda, S. Studenikin, A. Kam, F. Delgado, Y. P. Shim, M. Korkusinski, and P. Hawrylak, Phys. Rev. B **80**, 075415 (2009).

[111] Y. Aharonov and D. Bohm, Phys. Rev. **115**, 485 (1959).

[112] S. Washburn, H. Schmid, D. Kern, and R. A. Webb, Phys. Rev. Lett. **59**, 1791 (1987).

[113] B. Krafft, A. Förster, A. van der Hart, and T. Schäpers, Physica E **9**, 635 (2001).

[114] P. G. N. de Vegvar, G. Timp, P. M. Mankiewich, R. Behringer, and J. Cunningham, Phys. Rev. B **40**, 3491 (1989).

[115] A. Yacoby, M. Heiblum, D. Mahalu, and H. Shtrikman, Phys. Rev. Lett. **74**, 4047 (1995).

[116] A. W. Holleitner, C. R. Decker, H. Qin, K. Eberl, and R. H. Blick, Phys. Rev. Lett. **87**, 25 (2001).

[117] M. Sigrist, A. Fuhrer, T. Ihn, K. Ensslin, S. E. Ulloa, W. Wegscheider, and M. Bichler, Phys. Rev. Lett. **93**, 066802 (2004).

[118] F. Delgado, Y. P. Shim, M. Korkusinski, L. Gaudreau, S. A. Studenikin, A. S. Sachrajda, and P. Hawrylak, Phys. Rev. Lett. **101**, 226810 (2008).

[119] P. W. Anderson, Phys. Rev. **124**, 41 (1961).

[120] S. Gustavsson, M. Studer, R. Leturcq, T. Ihn, and K. Ensslin, Phys. Rev. B **78**, 155309 (2008).

[121] A. Cottet, W. Belzig, and C. Bruder, Phys. Rev. B **70**, 115315 (2004).

[122] R. Hussein and S. Kohler, Phys. Rev. B **89**, 205424 (2014).

[123] C. Nietner, S. G., C. Pöltl, and T. Brandes, Phys. Rev. B **85**, 245431 (2012).

[124] G. Schaller, G. Kießlich, and T. Brandes, Phys. Rev. B **82**, 041303 (2010).

[125] Y. Funabashi, K. Ohtsubo, M. Eto, and K. Kawamura, Jpn. J. Appl. Phys. **38**, 388 (1999).

[126] A. O. Badrutdinov, S. M. Huang, K. Kono, K. Ono, and D. A. Tayurskii, JETP Letters **93**, 4 (2011), pp. 199-202.

[127] S. Franceschi, S. Sasaki, J. M. Elzerman, W. G. van der Wiel, S. Tarucha, and L. P. Kouwenhoven, Phys. Rev. Lett. **86**, 878 (2001).

[128] D. M. Zumbühl, C. M. Marcus, M. P. Hanson, and A. C. Gossard, Phys. Rev. Lett. **93**, 256801 (2004).

[129] R. Schleser, T. Ihn, E. Ruh, K. Ensslin, M. Tews, D. Pfannkuche, D. C. Driscoll, and A. C. Gossard, Phys. Rev. Lett. **94**, 206805 (2005).

[130] Y. Okazaki, S. Sasaki, and K. Muraki, Phys. Rev. B **87**, 041302 (2013).

List of Figures

Danksagung

An dieser Stelle möchte ich mich bei all jenen bedanken, die mich während der Erstellung dieser Arbeit auf vielseitige Weise unterstützt haben.

Allen voran möchte ich meinem Doktorvater Prof. Dr. Rolf Haug herzlich danken für die Ermöglichung dieser Arbeit unter seiner Leitung und die Bereitstellung dieses interessanten Themas. Ich verdanke ihm darüber hinaus hervorragende Betreuung, Anleitung und freundliche und wertvolle Unterstützung und Diskussionsbereitschaft zu jeder Zeit. Bei Prof. Dr. Gloria Platero möchte ich mich für das Interesse an meiner Arbeit, die gute Zusammenarbeit, den wertvollen Austausch und die fachlichen Anregungen sowie die freundliche Übernahme des Amtes der Zweitgutachterin dieser Arbeit bedanken. Herzlichen Dank auch an Prof. Dr. Stefan Süllow für die Bereitschaft als Drittgutachter und als Prüfer bei meiner Verteidigung zur Verfügung zu stehen.

Besonderer Dank gilt Fernando Gallego-Marcos für die gute und fruchtbare fachliche Kooperation, aus der Teile dieser Arbeit hervorgegangen sind, seine große Unterstützung mit seiner fachlichen Kompetenz, seine stetige Diskussionsbereitschaft, das Korrekturlesen von Teilen dieser Arbeit und den freundlichen Austausch sowohl auf fachlicher also auch auf persönlicher Ebene. Ihm, seiner Arbeitsgruppe im Instituto de Ciencias de Materiales de Madrid (CSIC) und ihrer Leiterin Prof. Dr. Gloria Platero danke ich sehr für die herzliche Gastfreundschaft bei meinem Besuch in Madrid im Rahmen dieser Zusammenarbeit.

Solch eine experimentelle Arbeit wird immer auch erst ermöglicht durch gute Zusammenarbeit innerhalb der Arbeitsgruppe in vielerlei Hinsicht. Vielen Dank an Ronny Hüther und Niels Ubbelohde für die Unterstützung und ihr großes Engagement bei der Lösung verschiedener (mess-)technischer Probleme und Fragestellungen. Yvonne Griep, Florin Riechers und Klara Wernecke danke ich für die Unterstützung in organisatorischen Angelegenheiten und die netten Gespräche.

Mein Dank gebührt auch Maximilian Rogge für die Überlassung der Probe, die Hilfe bei der Einarbeitung in die Thematik und die kompetente Beantwortung meiner zahlreichen Fragen. Bei meinen Bürokollegen im Laufe meiner Tätigkeit in der Abteilung, Nils Scharnhorst und Jan Gerrit Lonnemann möchte ich mich herzlich bedanken für die tolle Atmosphäre in unserem kleinen Büro, die gute Laune und die unterhaltsamen Gespräche, so dass ich mich dort immer sehr wohl gefühlt habe. Den Mitgliedern meiner Arbeitsgruppe und der gesamten Abteilung Nanostrukturen danke ich für die tolle und lockere Arbeitsatmosphäre. Durch sie alle haben Arbeit, Pausen und Konferenzen einfach Spaß gemacht. Danke für die konstruktiven fachlichen Diskussionen, die aufbauenden Gespräche und die unermüdliche Unterstützung beim Handling der Kryostaten unter der Woche und in der Freizeit, insbesondere an Nandhavel Sethubalasubramanian, Alexander Heine, Timo Wagner, Dr. Lina Bockhorn und Johannes Bayer.

Mein Dank gebührt auch all jenen, die sich der mühevollen Arbeit des Korrekturlesens dieser Arbeit gewidmet haben und mir viele Tipps zur Verbeserung gegeben haben. Vielen herzlichen Dank an Johannes Bayer, Dr. Dmitri Smirnov, Timo Wagner, Dr. Lina Bockhorn, Jan-Gerrit Lonnemann, Dr. Jörg Duhme und Martina Kotzian.

Bei meinen Eltern Siglinde und Helmuth und meiner Schwester Martina möchte ich mich ganz besonders herzlich bedanken für ihre uneingeschränkte und liebevolle Unterstützung während meines Physikstudiums und der Promotion und den familiären Rückhalt. Sie haben mir meine akademische Laufbahn erst ermöglicht und mir, ganz besonders in der Endphase, stets den Rücken freigehalten. Dafür bin ich sehr dankbar. Meinen Großeltern Eva, Anna und Josef danke ich herzlich für ihre Geduld, ihr Verständnis und ihr Interesse an meiner Arbeit.

Von ganzem Herzen danke ich meinem Lebensgefährten Jörg Duhme für seine unermütliche emotionale und tatkräftige Unterstützung in allen Bereichen und jeglicher Hinsicht und die liebevolle Aufmunterung und Bestärkung besonders in stressigen Phasen. Er hat mir immer zur Seite gestanden, mir stets Verständnis entgegengebracht und mich durch alle Phasen dieser Dissertation, durch Höhen und Tiefen, mit Liebe begleitet.

Lebenslauf

Name	Monika Kotzian
Date of Birth	February 26th, 1986
Place of Birth	Wolfsburg
Nationality	German
1998-2005	Ratsgynmasium Wolfsburg Degree: Abitur
2005-2008	Studies of Physics (Bachelor) at the Technische Universität Carolo-Wilhelmina zu Braunschweig Bachelor thesis: Magnetisierungsmessungen an Zirkonia als potentieller magnetischer Halbleiter für die Spintronic Degree: Bachelor of Science
2008-2010	Studies of Physics (Master) at the Technische Universität Carolo-Wilhelmina zu Braunschweig Master thesis: Magnetowiderstands- und Hall-Effekt-Messungen an unstöchiometrischen FeSi-Einkristallen Degree: Master of Science
since 2010	Dissertation at the department Nanostrukturen, Institut für Festkörperphysik, Leibniz Universität Hannover supervisor: Prof. Dr. Rolf J. Haug